Österreichische Beiträge zu Meteorologie und Geophysik

ISSN 1016-6254

Heft 10

CONTRIBUTIONS TO SATELLITE AND RADAR METEOROLOGY IN CENTRAL EUROPE

edited by
Veronika Zwatz-Meise
Zentralanstalt für Meteorologie
und Geodynamik, Wien

Wien 1994

Österreichische Beiträge zu
Meteorologie und Geophysik

Heft 10

CONTRIBUTIONS TO SATELLITE AND RADAR METEOROLOGY IN CENTRAL EUROPE

I. Bartha
D. Bižic
I. Čačić
I. Csiszár
M. Diószeghy
F. Dombai
E. Fejes
D. Glasnović
A. Jann
J. Kaňák
L. Kovács
B. Łapeta
S. Moszkowicz
D. Serafin
N. Strelec
J. Vehovar
R. Winkler
V. Zwatz-Meise

Wien 1994

Zentralanstalt für Meteorologie und Geodynamik, Wien

Publ.Nr. 357

ISSN 1016-6254

IMPRESSUM

Herausgeber:	Peter Steinhauser Zentralanstalt für Meteorologie und Geodynamik Hohe Warte 38, A-1190 Wien Austria (Österreich)
Redaktion:	Veronika Zwatz-Meise
Corrigendum:	Ilse Fabian
Graphik und Layout:	Gabriele Seifriedsberger
Druck:	Robitschek & Co.Ges.m.b.H. Schloßgasse 10-12, A-1050 Wien Austria (Österreich)
Verlag:	Zentralanstalt für Meteorologie und Geodynamik

PREFACE

It is a pleasure for me to present the proceedings of the conference on „Remote Sensing Methods in Meteorology and their Application in Nowcasting", held in Vienna, Austria between 11 - 13 October 1993.

This meeting was organized under the auspices of the Central European Initiative (CEI) and was attended by participants from Croatia, Hungary, Poland, Slovakia, Slovenia and Austria.

Intensive discussions during this meeting resulted in plans for joint scientific research projects especially in developing vertical cross sections out of radiosonde and satellite data as well as in the fields of nowcasting and synoptical applications of cloud classification systems.

Last but not least I have to thank all the participants for their involvement and their contributions and especially Dr. Veronika Zwatz-Meise for her enthusiasm and the organization of the meeting.

(Univ.-Prof. Dr. Peter Steinhauser, Director)

SOME ASPECTS OF SATELLITE METEOROLOGY IN THE CEI-COUNTRIES

SOME ASPECTS OF RADAR METEOROLOGY IN THE CEI-COUNTRIES

COMBINED METHODS AND NOWCASTING

VERTICAL CROSS SECTIONS - A PROJECT BETWEEN AUSTRIA AND CROATIA

ANALYSES OF VERTICAL CROSS SECTIONS AND THEIR COMBINATION WITH SATELLITE IMAGES

CONTRIBUTIONS TO SATELLITE AND RADAR
METEOROLOGY IN CENTRAL EUROPE

SOME ASPECTS OF SATELLITE METEOROLOGY IN THE CEI-COUNTRIES

THE USE OF SATELLITE IMAGES IN OPERATIONAL AND RESEARCH WORK AT THE CENTRAL INSTITUTE OF METEOROLOGY AND GEODYNAMICS IN VIENNA

Central Institute for Meteorology and Geodynamics, Vienna, Austria

VERONIKA ZWATZ-MEISE, ALEXANDER JANN, ROLAND WINKLER

ABSTRACT

The report describes the evaluation tools and steps used for operational diagnosis and forecast as well as for research. Several data sources like satellite information, surface and radiosonde measurements and model output are combined interactively. Calculations and evaluation of parameters are done on isobaric as well as on isentropic surfaces. For the latter relative streams utilizing system velocities are computed. Other frequently used tools are vertical cross-sections. One main aim of the whole system is the development and use of conceptual models.

Besides this interactive qualitative use of satellite images quantitative satellite products are used and integrated into the evaluation process, too; at the moment this is true for precipitation probabilities. The introduction of quantitative WV-products like winds and humidity parameters is in a developing stage.

ZUSAMMENFASSUNG

Die Arbeit beschreibt die Hilfsmittel und Methoden einer interaktiven Nutzung verschiedenster meteorologischer Datenquellen für Diagnose, Prognose und Forschung. Verschiedene Datenquellen wie Satellitendaten, Radiosondenmessungen und abgeleitete numerische Parameter werden interaktiv kombiniert. Parameterberechnungen sowie Auswertungen erfolgen sowohl auf isobaren wie auch auf isentropen Flächen. Für letztere werden u.a. relative Ströme unter Verwendung von Systemgeschwindigkeiten berechnet. Ein wesentliches Ziel ist die Entwicklung und Anwendung konzeptioneller Modelle für die in Satellitenbildern beobachteten Wolkensysteme in verschiedenen Größenordnungen.

Neben dieser interaktiven qualitativen Auswertung von Satellitenbildern werden auch quantitative Produkte der Satellitenmessungen bestimmt und in den Diagnoseprozeß integriert. Derzeit bezieht sich dies vor allem auf abgeleitete Niederschlagswahrscheinlichkeiten. Quantitative Produkte aus dem WV-Bild wie Windvektoren und Feuchteparameter sind in Vorbereitung.

1. INTRODUCTION

At the Central Institute for Meteorology and Geodynamics in Vienna satellite images are used in applied synoptic research for the derivation and/or correction of conceptual models (Zwatz-Meise and Mahringer 1990; Mahringer and Zwatz-Meise 1993) as well as for the evaluation of quantitative information. The results of these investigations are applied in the operational weather service within the process of diagnosis and for very short range forecast.

Since June 1992 the basic technical device consists of a PDUS Meteosat receiving station where all images of the European and Atlantic area as well as once per day the total disc are received and archived. This archive before June 1992 consists of the 3-hourly SDUS images and until January 1994 of the 3-hourly PDUS images. From January 1994 on the complete amount of images is stored.

The images can be visualized on SUN workstations in polarstereographic projection which allows superposition of all meteorological observations and parameter fields in use. Examples for this follow later on (figures 3ff). The images can be processed by several filter functions and enhancement curves for a visualization of appropriate false colour images. Figure 1 shows examples for a "shade filter" (figure 1a), an enhancement for cold (figure 1b) and for warm tops (figure 1c) as well as a superposition of VIS and IR signals (figure 1d) which enables separation between low, thick and high clouds.

Pixel values can be extracted for arbitrarily chosen cutlines (compare vertical cross sections; chapter 4.1) and areas (compare precipitation determination; chapter 3.) as well as for time series (compare Project: vertical cross sections).

There are three main steps in analysing satellite images and combining them with other meteorological material:

1. satellite images in combination with meteorological parameters on isobaric surfaces;
2. satellite images in combination with parameters on isentropic surfaces; a form of evaluation which can be divided into two substeps:
   - vertical cross sections
   - relative streams;
3. quantitative evaluations of satellite images.

2. SATELLITE IMAGES COMBINED WITH PARAMETERS ON ISOBARIC SURFACES

2.1 BASIC CONCEPT

The left side of figure 2 shows a flow diagram of the single analysis steps.

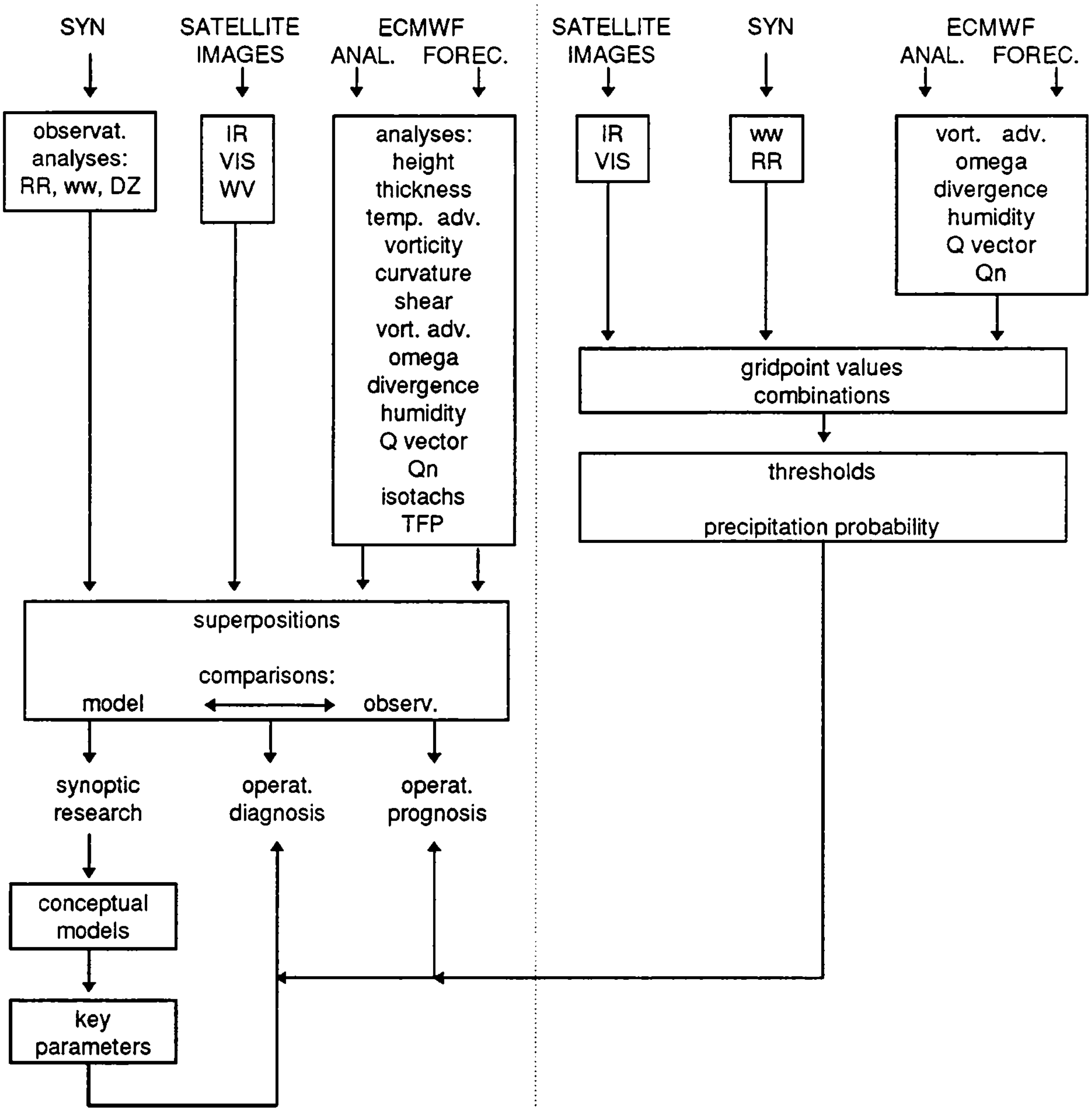

Figure 2: Block diagram part I

Input data are:

- synoptic observations and analyses of precipitation observations as well as precipitation amounts (ww and RR in the synop code);
- PDUS satellite images of Meteosat of all three channels (IR, VIS, WV) in image form as well as in quantitative pixel form;
- fields of derived parameters based on the ECMWF model from analysis and forecast grid point values. The following parameters are computed partly operationally and partly on request on mandatory levels respectively for the layers between:
    - height
    - thickness
    - temperature (thickness) advection

relative vorticity split up into:
    curvature vorticity
    shear vorticity
absolute vorticity advection
vertical motion (omega)
divergence
humidity
isotachs
frontogenesis parameter (Q vector, Qn)
thermal frontparameter

All these data fields can be superimposed and comparisons between the forecast model and the observations are computed which at the moment is done automatically for the 6-hourly precipitation amounts.

The output of this evaluation step can be used in synoptic research, in operational diagnosis and operational prognosis.

There is a feedback between synoptic research and operational work because one of the main aims of research is the derivation of conceptual models for typical physical states of the troposphere. These conceptual models contain the full content of meteorological material which is far too much for an operational application; therefore a few typical and operationally available "key parameters" are chosen as an input for operational diagnosis and prognosis (Zwatz-Meise and Mahringer 1990; Mahringer and Zwatz-Meise 1993).

2.2 EXAMPLE

Figures 3 to 5 present an example for the use of a conceptual model describing the increase of cloudiness and weather events at a cold front cloud band in case a jet streak crosses the front with its left exit region (Uccellini and Johnson 1979; Zwatz-Meise 1991; Mahringer and Zwatz-Meise 1993).

From the conceptual model describing such a situation the following is known: frontal cloudiness is increased and accompanied by intensive weather events (for instance thunderstorms) where the maximum of positive vorticity advection (PVA) which usually exists in the left exit region of a jet streak is superimposed on the frontal cloud band. Furtheron it is known from previous studies that the numerical model of ECMWF underestimates in its forecasts the precipitation amount in the area of the PVA maxima (Zwatz-Meise and Bendl,1992).

Figure 3 contains much of these typical conditions. The satellite image in figure 3a shows a cold front cloud band reaching from Germany across Switzerland and France to Spain. The high cloud fibres at the rear of the cloud band especially over France and the broadening of the cloud band together with very cold tops over the eastern parts of France (around approximately 47N/04E) are a first optical indication for the application of the relevant conceptual jet streak model. Figure 3b contains synoptic measurements with the green and red station-marks standing for precipitation respectively thunderstorms. There are three thunderstorm reports in the area under discussion. Key parameters for a manifestation of the conceptual model are isotachs and vorticity-advection in 300 hPa. Figures 3b, c manifest clearly the coincidence of the cloud phenomenon with a PVA maximum in the left exit region of a jet streak. In figure 3c the yellow lines shows the differences between the precipitation forecast and the measured amounts which demonstrate that the model precipitation does not catch this area very well.

In figure 4 the PVA fields corresponding with the image time (black lines) and those for 6 hours ahead are superimposed and show a northeast propagation of the PVA max from east France across the western parts of Switzerland to the southwesternmost regions of Germany.

According to the experience from the conceptual model this path should be a region of dense cloudiness, high precipitation amounts and thunderstorms during the 6 hours from 06 UTC (figure 3) to 12 UTC (figure 5).

The temperatures respectively colours in figure 5a over the western parts of Switzerland and the southwestern of Germany confirm the cloud intensification within the frontal cloud band accompanied by 3 thunderstorms and a lot of precipitation reports (figure 5b). The coincidence with a PVA maximum in the left exit region of the jet streak is still very distinct (figure 5c) and the precipitation forecast underestimates the situation, the same phenomena as already shown by the conceptual model (Zwatz-Meise and Bendl 1992).

3. QUANTITATIVE EVALUATIONS OF SATELLITE IMAGES

3.1 BASIC CONCEPT

The right side of figure 2 shows the flow diagram of the single evaluation steps.

Input data are:

- IR, VIS and WV pixel values at gridpoints (14 km griddistance, mean value of 9 pixels)
- analyses of precipitation measurements (ww, RR from the synop code) at the same grid as for the pixels
- derived meteorological parameters from ECMWF analysis as well as forecast values at the same grid as for the pixels; from the table in 2.1 only those parameters are selected which are crucial for the condensation process:
    - vorticity advection
    - vertical motion
    - divergence
    - temperature advection
    - Q-vector (normal component)
    - humidity

The basic method used (Lovejoy and Austin 1979; Scofield et al 1984) is the derivation of precipitation probabilities from a combination of IR and VIS signals on the one hand and of IR signals and a relevant meteorological parameter on the other hand. The latter approach has been chosen because of the restricted availability of the VIS image. The results of the statistical evaluations are thresholds for the parameters used for precipitation probabilities. These thresholds can be applied to the actual cases in operational diagnosis as well as prognosis and areas with high precipitation probabilities are marked in the image.

Figure 6 shows the results of the statistical evaluation for a combination of IR signal and 2 parameters (relative humidity and vorticity advection). At present, the data of about half a year are included but the set is updated daily. Both panels show distinct maxima of precipitation probabilities allowing a delineation of a precipitation cluster although the probabilities are not too high up to now (Zwatz-Meise and Stockinger, 1992; Zwatz-Meise et al., 1993).

Areas of high precipitation probability can be computed from analysis values as well as from the forecast values using relative humidity instead of the IR-signal.

3.2 EXAMPLE

Figure 7 presents the same case as figures 3 to 5. The red dotted area is an area where thresholds for 60% precipitation probability from IR- and vorticity advection are exceeded. The yellow dotted area means the same from the forecast values 6 hours ahead with relative humidity instead of the satellite signals. This area of high precipitation probability can be compared to the forecast 6-hourly precipitation amounts and, as is the case in this example, corrections of the precipitation model forecast can be made. The maximum of the precipitation amounts is too far southwest and therefore doubtful for parts of Switzerland and Southwest Germany.

4. SATELLITE IMAGES COMBINED WITH PARAMETERS ON ISENTROPIC SURFACES

4.1 VERTICAL CROSS SECTIONS

4.1.1 Basic concept

Vertical cross sections are the topic of an Austrian-Croatian project which is described later on in more detail. Here only some necessary basic facts and an example shall be added.

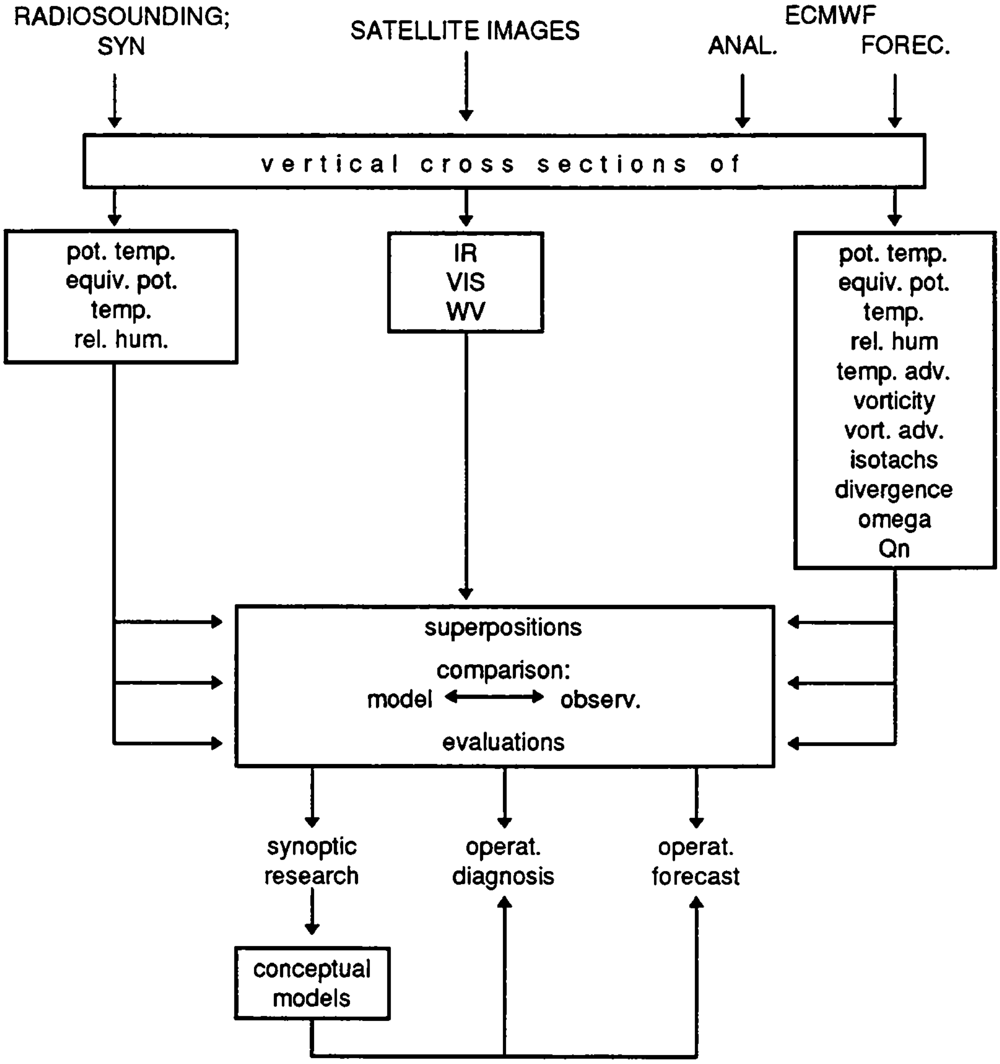

Figure 8: Block diagram part II

Figure 8 shows the block diagram for the single steps. Three types of vertical cross-sections are computed:

- from radio-soundings supplemented with synoptic measurements being within a free chooseable distance from the cutline. The results are:
    - potential temperature
    - equivalent-potential temperature
    - relative humidity;
- from satellite signals for all three channels (IR, VIS and WV);
- from ECMWF analysis as well as forecast fields. Results are profiles of:
    - potential temperature
    - equivalent-potential temperature
    - relative humidity
    - temperature advection
    - relative vorticity
    - absolut vorticity advection
    - isotachs
    - divergence
    - vertical motion (omega)
    - Q-vector (Qn frontogenesis parameter)

All these types of vertical cross sections can be superimposed and comparisons between radiosonde and model data are computed.

This material is used for operational diagnosis and forecasting as well as in synoptic research for the evaluation of conceptual models which are an additional tool for the operational evaluation procedures.

4.1.2 Examples

Figure 9 shows a well-developed cloud spiral which seems to accompany a classical frontal system. Nevertheless, during the analysis process there have been a lot of difficulties and contradictions to classical ideas about fronts. Two vertical cross sections are computed for all three data sources; they are shown in figure 9a, b.

Several interesting phenomena can be derived from figure 10a, b. The west-east cross section (figure 10a) indicates a cold front between Ajaccio (07761) and Rome (16245) being inclined from about 300 hPa down to 900 hPa and extending from there on in form of a shallow layer eastward. It is the cloud mass with rather dark greyshades between Corse, Sardinia and Italy which belongs to this cold front. The north-south cross section (figure 10b) leading through the occlusion-like cloud band over Austria, Hungary, Croatia and Slovenia also shows also a very pronounced frontal surface with high humidity values within and on top of it while low values of humidity exist below the frontal surface. The wettest air can be found above Zagreb (13130) between 800 and 500 hPa.

The same features can be identified from the ECMWF cross sections along the same cutlines (figure 11a, b); the quality of the numerical model can be evaluated from the differences between both data sources shown in figure 12. In this case the model fits quite well.

Another remarkable phenomenon can be identified from both cross sections in figure 10, namely an upper level front between approximately 300 and 400 hPa being bounded by the 318 and 324 K isentropes. This feature can be applied to the pronounced cloud band with very cold tops stretching from Bulgaria to Tunisia.

The figures 13 and 14 contain the superposition of all three types of cross sections for a selection of parameters: equivalent-potential temperature from radiosonde measurements, frontogenesis parameter (figure 13) respectively temperature advection (figure 14) from ECMWF and IR and WV signals from Meteosat data. Interesting results can be derived from the frontogenetic parameter which in the north-south cross section (figure 12b) shows pronounced frontogenesis immediately south of Zagreb (13130) in the middle troposphere between 800 and 600 hPa; in the west-east cross section (figure 12a) frontolysis prevails approximately in the same tropospheric layers of the front between Cagliari (16560), Rome (16245) and eastward to Brindisi (16320).

In the satellite cross sections both areas show rather warm cloud tops compared to the cold tops of the cloud band from Tunisia to the Balcan Peninsula; the rather low cloud tops in the west-east cross section can be related to frontolysis, but attention has to be paid to the frontogenetic area where possibly an increase of cloudiness can be expected.

Besides this, satellite signals clearly show the boundaries of the cold cloud band belonging to the upper level front and the cooling of the tops along the north-south cross section which may be caused by upgliding processes.

This upgliding warm air is manifested also in the temperature advection cross section (figure 14) with warm air advection being very pronounced within the whole frontal surface with distinct maxima in low and middle levels.

For forecast purposes, cross sections from ECMWF forecast values are computed for the next 30 hours, that is for 00, 06, 12 and 18 UTC. Figure 15 is an example for the north-south cross section and the combination of equivalent-potential temperature and the frontogenetic parameter (normal component of Q vector). Frontogenesis is prevalent within the frontal surface during the whole period moving slightly northward as does the frontal surface as a whole.

4.2 RELATIVE STREAMS

4.2.1 Basic concept

The concept of relative streams respectively conveyor belts has shown to be useful for the physical interpretation of cloud configurations (Browning 1986; Carlson 1987; Zwatz- Meise 1991, Mahringer and Zwatz-Meise 1993). Cloudiness tends to align along streamlines relative to the system-movement and so pronounced cloud boundaries and curvatures being the result of air masses of different origin can easily be explained.

Relative streams are those an observer would recognize if moving with the cloud system. So one crucial point of this method is the determination of a system velocity. Three methods are used simultaneously which fulfill also the condition of being available in real time:

1. the displacement of the cloud system in the satellite image by cross correlation methods. In this case the cloud configuration is chosen as representative for the synoptic system.
2. The displacement of centers of curvature vorticity in 500 hPa representing the upper level trough of the system and
3. the wind vector at the maximum of absolute vorticity in 500 hPa, where the latter is regarded as conservative property for the processes under discussion (Steinacker 1985).

A second crucial point for this method is the selection of appropriate isentropic surfaces on which the relative streams are computed. Assuming the physical processes being adiabatic, air masses move on isentropic surfaces which usually are inclined to the isobaric surfaces. Therefore lifting or sinking of the relative stream can be read directly from the charts.

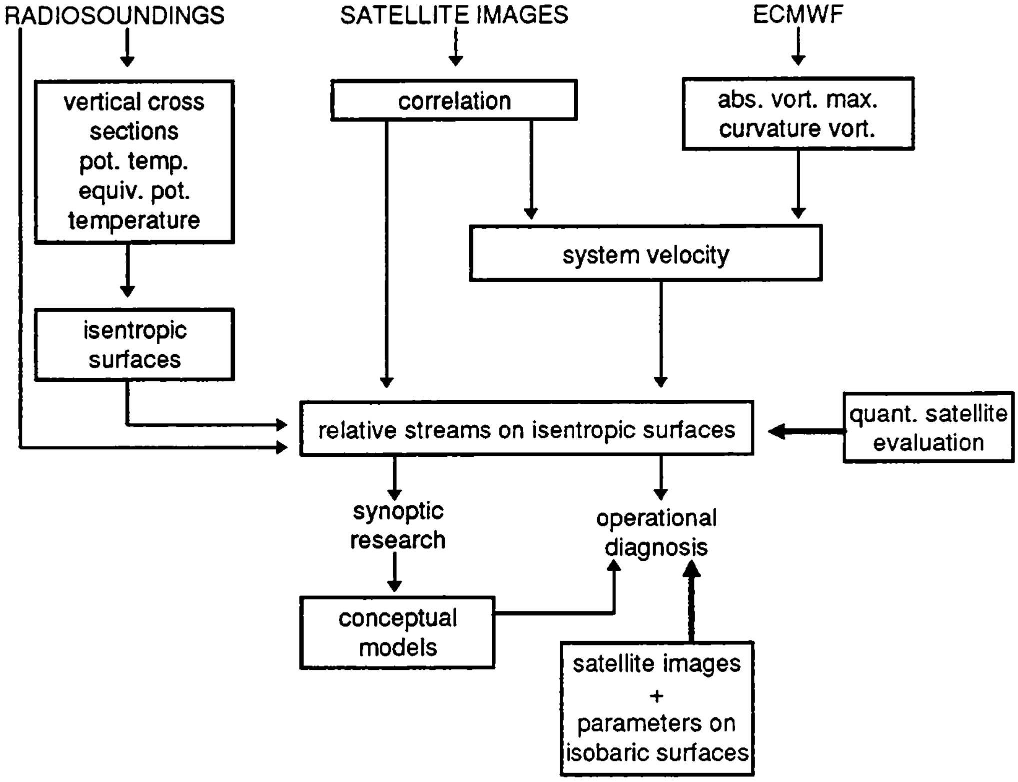

Figure 16: Block diagram part III

Figure 16 shows the block diagram for the single evaluation steps. Basic material is:

1. data from radiosoundings and synoptic measurements for the derivation of vertical cross sections as basis for the selection of relevant isentropic surfaces;
2. consecutive satellite images for the computation of the system velocity with cross correlation methods;
3. fields from ECMWF for the two other computation methods of comparable system velocities.

With the output of these basic steps the relative streams are computed on the isentropic surface and diverse superpositions with satellite images and other data fields (for instance precipitation from synoptic measurements or vertical motion from ECMWF data) can be used.

The results can be used in research and in operational diagnosis with a feedback between both working fields through the conceptual models. At present the evaluation is not yet used for operational forecast because of a reduced availability of forecasted model surfaces. It is intended to find a solution for this problem in the near future.

4.2.2 Example

For the demonstration of relative streams the same case as for the cross sections (figures 9-15) is used. As has already be mentioned there, some difficulties arose during diagnosing because of deviations from classical front models. The form of the cloud configuration (figure 9) gives some indication that the frontal conveyor belt model with warm and cold conveyor belt and upper level stream from southwest (Carlson 1987; Kurz 1990) could describe the physical state in the troposphere better. Two isentropic surfaces are chosen from the vertical cross sections (figure 10): 310K being near the upper boundary of the main frontal zone and 320 K representing the upper level front. The system velocity has been computed as 286°/8m/s with only small deviations between the three methods.

Relative streams on both isentropic surfaces are shown in figure 17; two completely different streams can be discriminated. On the lower layer (310K figure 18a) a relative stream from the southeastern Mediterranean is rising from near the ground level across the Balcan Peninsula and the Adriatic sea up to about 500-400 hPa over Austria and Slovakia where it bends to eastern directions without any further rising. A different relative stream from the southwestern Mediterranean and from a much higher layer of the troposphere (approx. 400 hPa) meets with the first stream over Italy. The limiting streamline between both relative streams is very close to the northern boundary of the cloud band (Austria - Slovakia).
A completely different situation exists on the higher isentropic surface (figure 17b, 320K). An only moderately rising relative stream from southwestern directions is oriented parallel to the pronounced cloud band from Tunisia to the Black Sea. There are some indications from the analoguos computations for 12 UTC that also on this isentropic level two relative streams of different origin meet at the western bondary of the cloud band where also the jet axis can be located. Because of a lack of radiosonde stations over Africa this cannot be verified in this chart.

As a result, one can conclude that there are two cloud systems above each other related to different relative streams transporting different air masses.

A practical application of these investigations can be shown for the area of maximal rising within the Adriatic Sea, Slovenia and Croatia where in the relevant cross sections pronounced frontogenesis has been computed and where there is much more actual precipitation than forecasted by the model. The area of frontolysis between Sardinia and Italy is related to a different relative stream transporting different air masses which are partly sinking in the area under interest.

5. CONCLUSION

The main aim of these evaluation steps is to make an optimal use of satellite material for the synoptic work by combining it with all the other meteorological data fields. This is accomplished by the evaluation of typical structures and their implementation in conceptual models as well as the evaluation of quantitative pixel values for a combination with other material in vertical cross sections and for precipitation probabilities.

REFERENCES

AUSTIN, G., 1990: Objective Methods of Inferring Precipitation. Proceedings of the Workshop on the Use of Satellite Data in Nowcasting and Very Short Range Forecasting. EUMETSAT, EUM P07.

BROWNING, K.A., 1986: Conceptual Models of Precipitation Systems. Weather and Forecasting 1, 23-41.

CARLSON, T.N., 1987: Cloud configuration in relation to relative isentropic motion. EUMETSAT: Satellite and Radar Imagery Interpretaton, 43-61.

KURZ, M., 1990: Synoptische Meteorologie. Leitfäden für die Ausbildung im Deutschen Wetterdienst. Selbstverlag des Deutschen Wetterdienstes.

LOVEJOY, S. and G.L. AUSTIN, 1979: The Delineation of Rain Areas from Visible and IR Satellite Data for GATE and Mid-Latitudes. Atmosph.Ocean. 17 (1) 1979, 77-92.

MAHRINGER, G. and V. ZWATZ-MEISE, 1993: A semi-operational diagnosis method. Contributions to Atmospheric Physics, Vol 66, No 1-2, 89-106.

SCOFIELD, R.A., E. LEROY and J.R. SPAYD, 1984: A Technique that uses Satellite, Radar and Conventional Data for Analysing and Short-Range Forecasting of Precipitation from Extratropical Cyclones. NOAA Technical Memorandum NESDIS 8.

SCOFIELD, R.A. and XIE JUYING, 1989: Satellite-Derived Rainfall Estimates and Propagation Characteristics Associated with Mesoscale Convective Systems (MCSs). NOAA Technical Memorandum NESDIS 25.

STEINACKER, R., 1985: On the Interpretation and Motion of Synoptic Systems. Arch. Met. Geoph. Biokl.,Ser. A, 34, 59-83.

UCCELLINI, L.W. and D.R. JOHNSON, 1979: The Coupling of Upper and Lower Atmospheric Jet Streams and Implications for the Development of Severe Convective Storms. Mon. Wea. Rev.,107,682-703.

ZWATZ-MEISE, V. and G. MAHRINGER, 1990: SATMOD: An Interactive System Combining Satellite Images and Model Output Parameters. Wea. and Forecasting, Vol.5,no.2,233-246.

ZWATZ-MEISE, V. and F. HUFNAGL, 1990: Some Results about the Relation between an objective Front Parameter and Cloud Bands in Satellite Images and its Connection to Classical Cold Front Models. Meteorol. Atmos. Phys.,42,77-89.

ZWATZ-MEISE, V., 1990: Very Short Range Forecasting Frontal and Non-Convective Weather. Proceedings of the workshop of the use of satellite data in nowcasting and very short range forecasting. EUMETSAT EUM P07.

ZWATZ-MEISE, V., 1991: Use of satellite images for the diagnosis and prognosis of certain jet streak phenomena. Proceedings of the 8th Meteosat Scientific Users Meeting. EUMETSAT; EUM P 08.

ZWATZ-MEISE, V., 1991: Satellite-synoptic aspects of warm fronts. Proceedings of the 8th Meteosat Scientific Users Meeting. EUMETSAT; EUM P 08.

ZWATZ-MEISE, V., 1991: Satelliten-synoptische Jet-Streak Phänomene und ihre Einbeziehung in die Wettervorhersage. Publikationen der Österr. Akademie der Wissenschaften, math.-nat. Kl.,Abt.I 198.Bd,5. bis 10.Heft.

ZWATZ-MEISE, V. and K.BENDL, 1992: PVA-Maxima and their connection to cloud systems in satellite images and to precipitation. Meteorol. Atmos.Phys. 47,145-164.

ZWATZ-MEISE, V. and J. STOCKINGER, 1992: Qualitative and Quantitative Diagnosis of Cloud Images for Use in Weather Forecast. ISY; Munich 1992. ESA ISY-1

ZWATZ-MEISE, V., 1992: Results of a quantitative evaluation of satellite images with respect to precipitation events. 9th Meteosat Scientific Users' Meeting, Locarno 1992. EUM P 11.

ZWATZ-MEISE, V., A. JANN and R. WINKLER, 1993: An Analysis and Forecast Method Including Satellite Images and Parameters on Isobaric and Isentropic Surfaces. Conference Documentation. First European Conference on Applications of Meteorology. Oxford.

Author's address:

VERONIKA ZWATZ-MEISE, ALEXANDER JANN, ROLAND WINKLER
Central Institute for Meteorology and Geodynamics
Synoptical Division
Hohe Warte 38
A-1190 Vienna
AUSTRIA
Phone.: 0043 1 36 44 53/2315, 2316
Fax: 0043 1 36 45 70
E-mail: zwa@zassun3.zamg.ac.at
jann@zassun3.zamg.ac.at

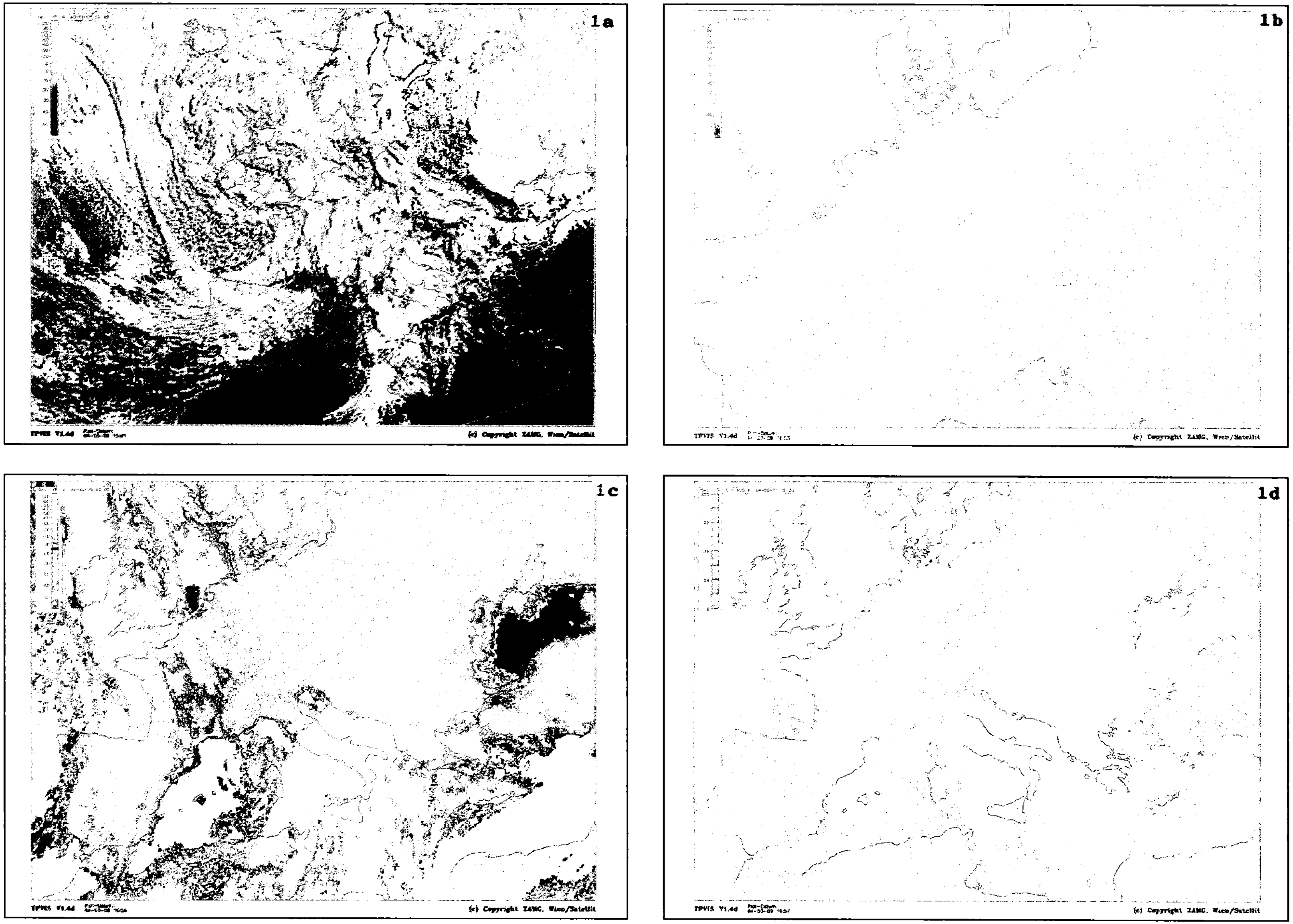

Figure 1:
Examples for image processing

1a:
"shade filter", IR, 1 Oct.1993/ 12 UTC

1b:
5 Aug.1993/ 12 UTC, IR, enhancement of thunderstorm cells

1c:
18 Feb.1994/ 00 UTC, IR, enhancement of warm tops including fog

1d:
18 Feb.1994/ 12.30 UTC, VIS + IR, separation of cloud layers

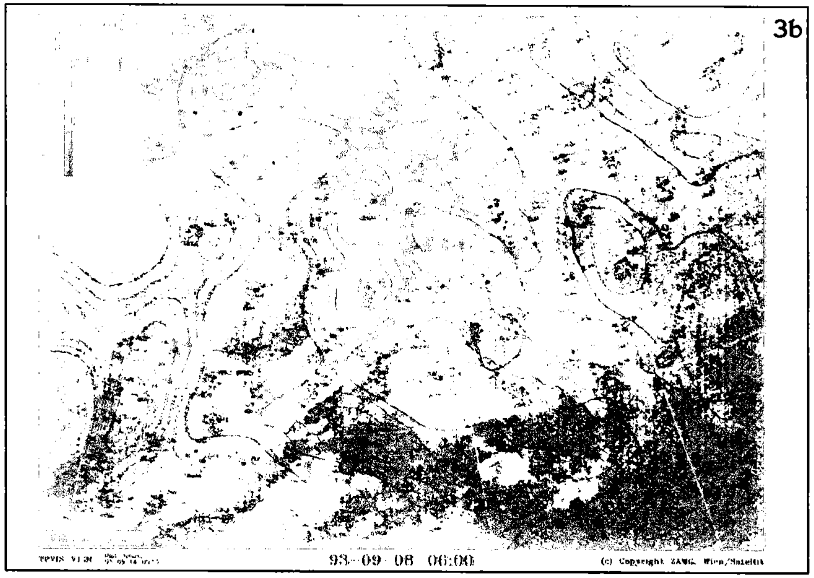

Figure 3:
Example for the use of a conceptual jet streak model: intensification of frontal cloudiness in the left exit region of a jet streak.
8 Sept.1993/
06 UTC; 3a: IR;
3b: IR, synoptic reports (green: actual precipitation, yellow: fog, red: thunderstorm), black lines: PVA 300 hPa
($*10^{-9}s^{-2}$)

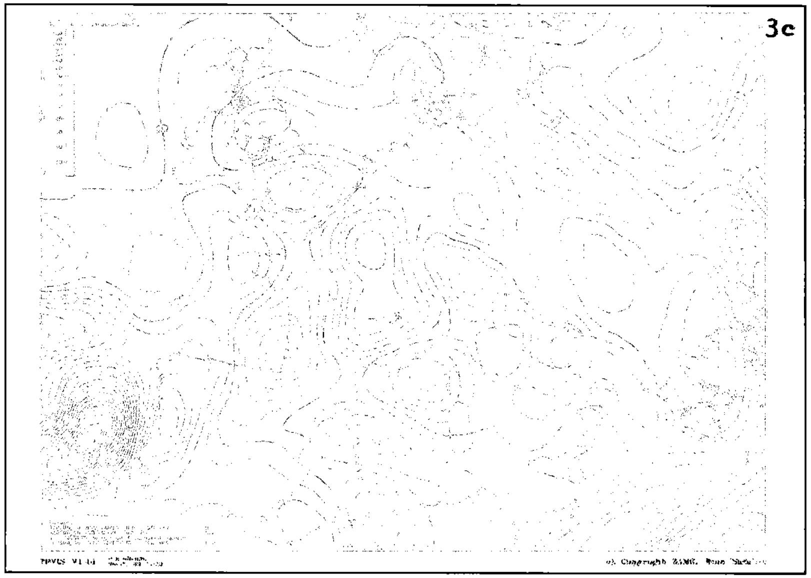

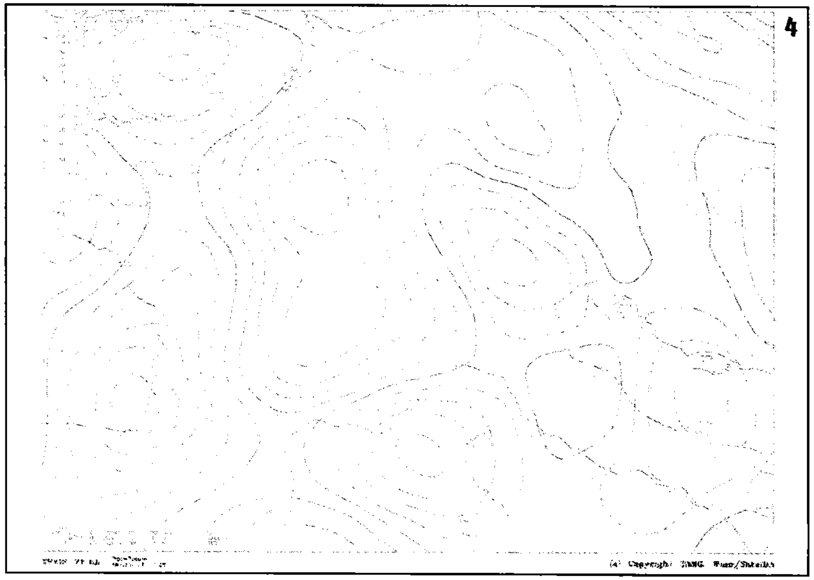

3c: IR, black lines: PVA 300 hPa, red and blue lines: isotachs 300 hPa (m/s), yellow lines: differences of 6-hourly precipitation amounts between actual measurements and ECMWF forecasts (mm/6 hours)

Figure 4:
8 Sept.1993/
6 UTC, black:
PVA 300 hPa/
6 UTC, red: PVA
300 hPa/12 UTC

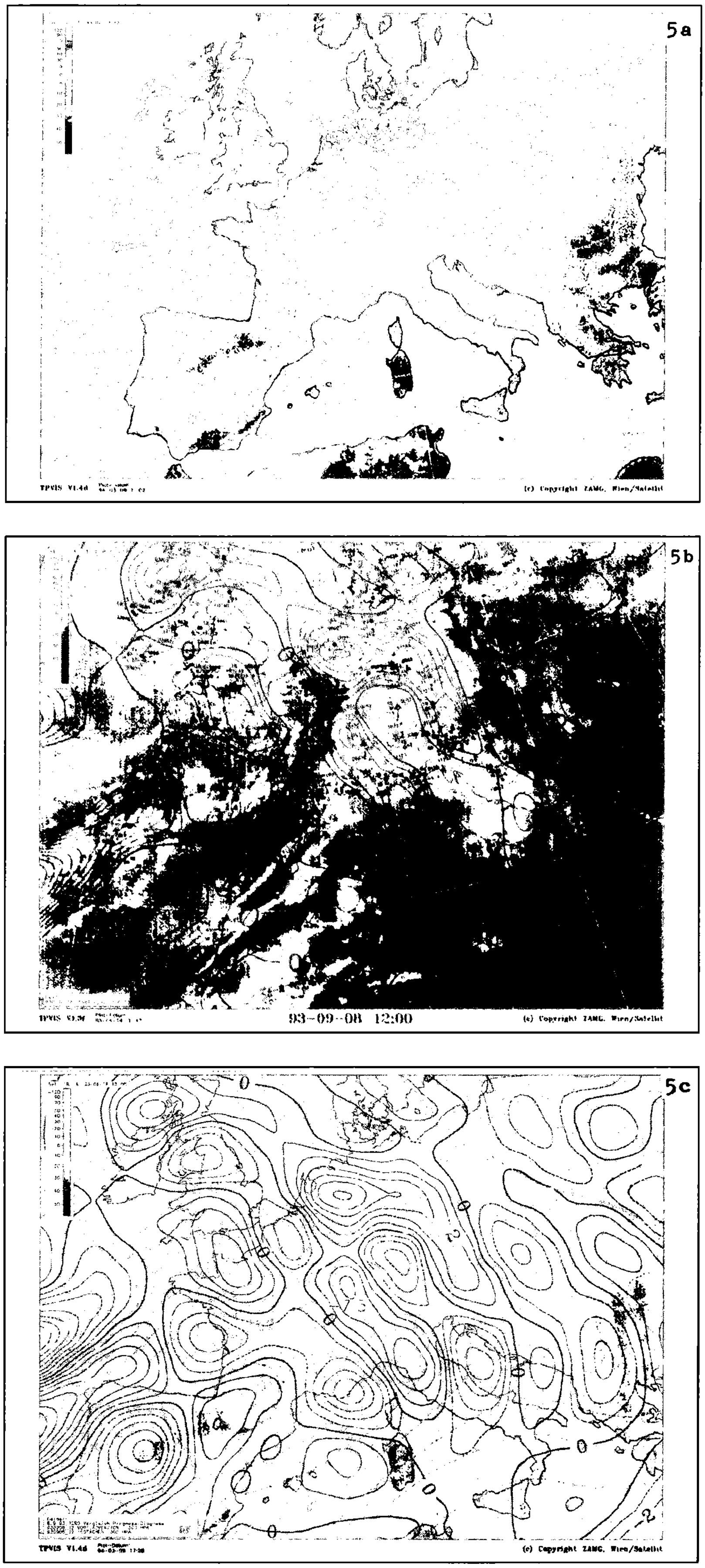

Figure 5: Same as figure 3 for 8 September 1993/12 UTC

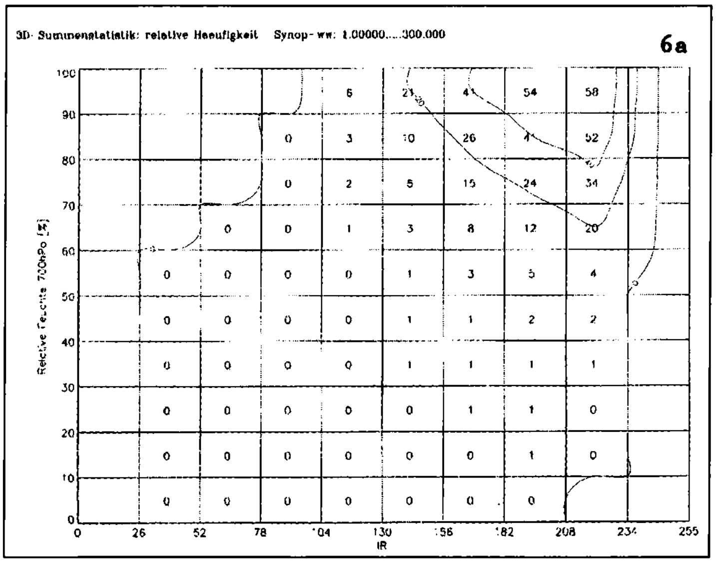

6a

6a: IR and relative humidity 700 hPa

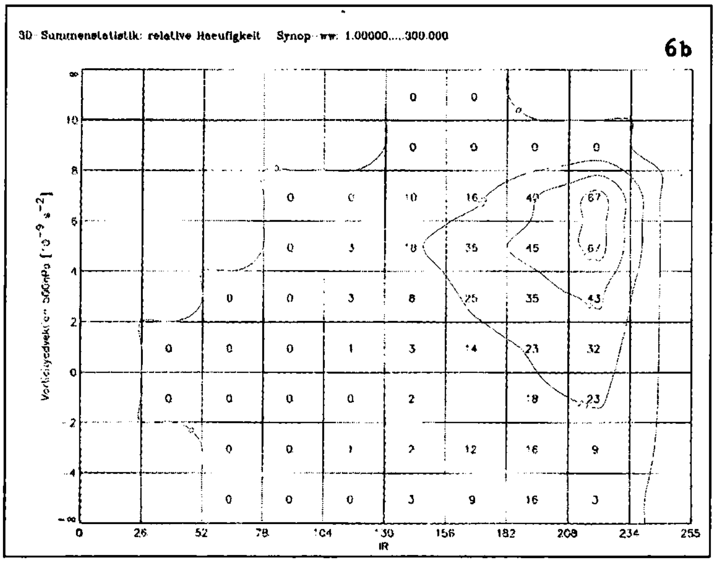

6b

6b: IR and vorticity advection 500 hPa

Figure 6: Precipitation probabilities from a combination of IR-pixels and a numerical Parameter

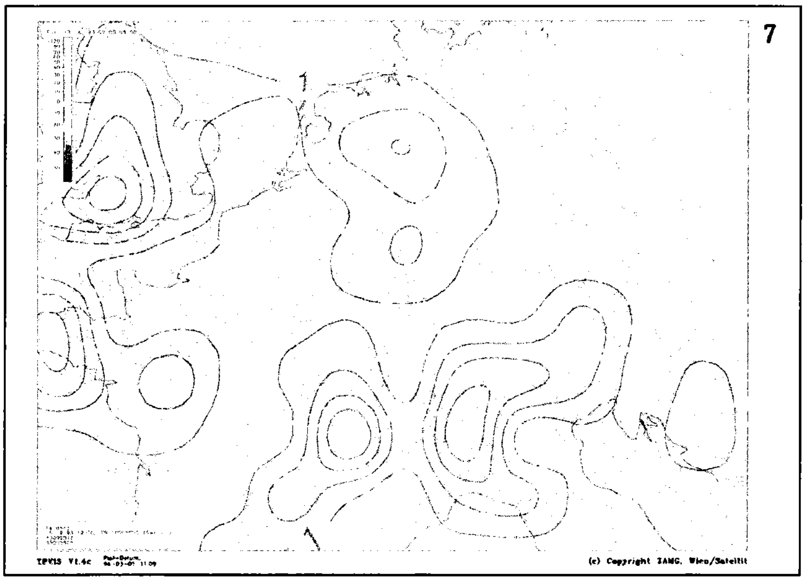

7

Figure 7:
Evaluation of the model precipitation forecast;
9 September 1993/
06 - 12 UTC; IR 06 UTC,
red shaded: high precipitation probability from the combination IR and PVA 300 hPa for 06 UTC; yellow shaded: high precipitation probability from the combination relative humidity 700 hPa and PVA 300 hPa from forecast fields; blue lines: ECMWF forecast of 6-hourly precipitation

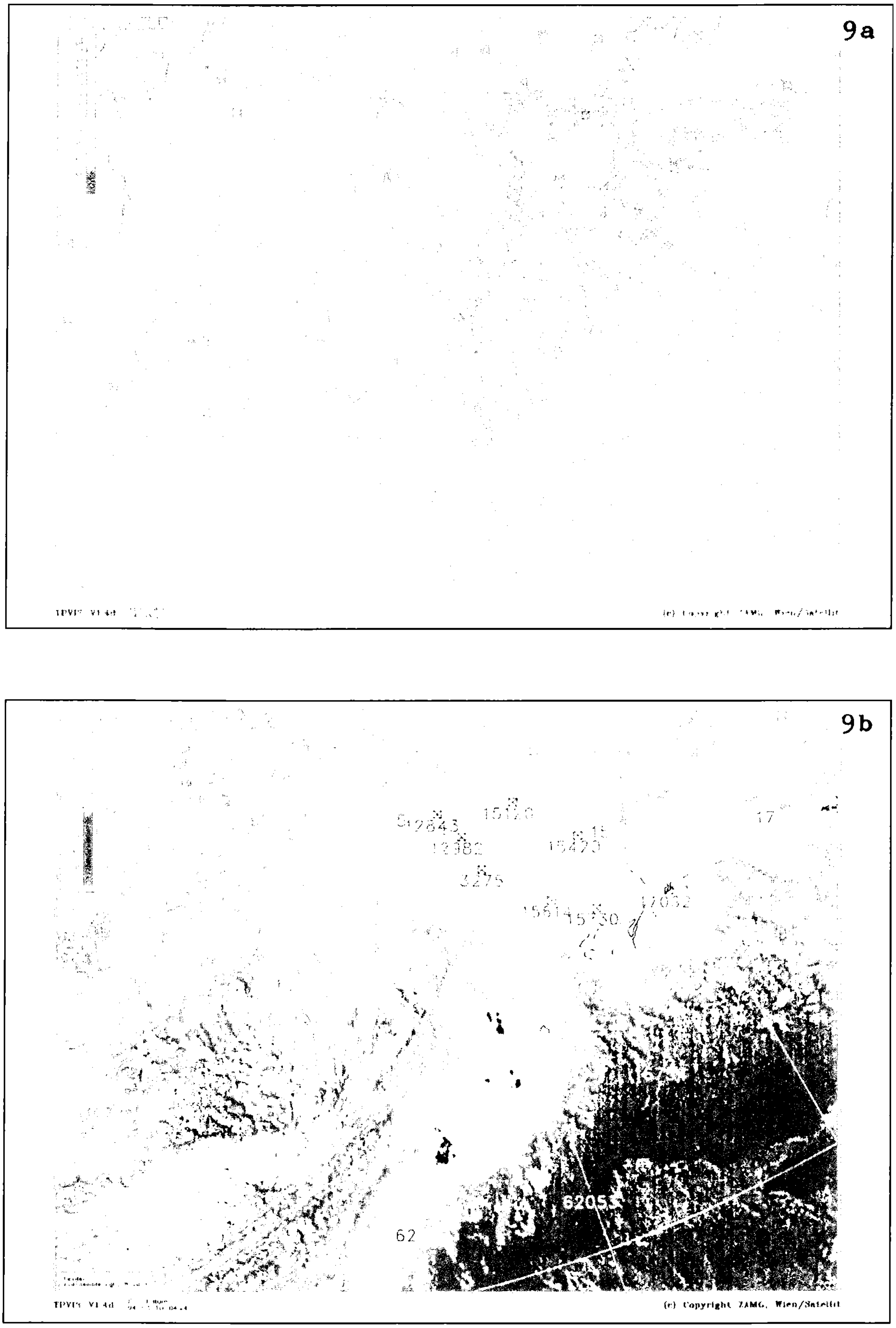

Figure 9: 15 April 1993/00 UTC; 9a: IR, superimposed are radiosonde station numbers and the selected W-E cutline for the vertical cross section; 9b: WV, same as 9a with N-S cutline

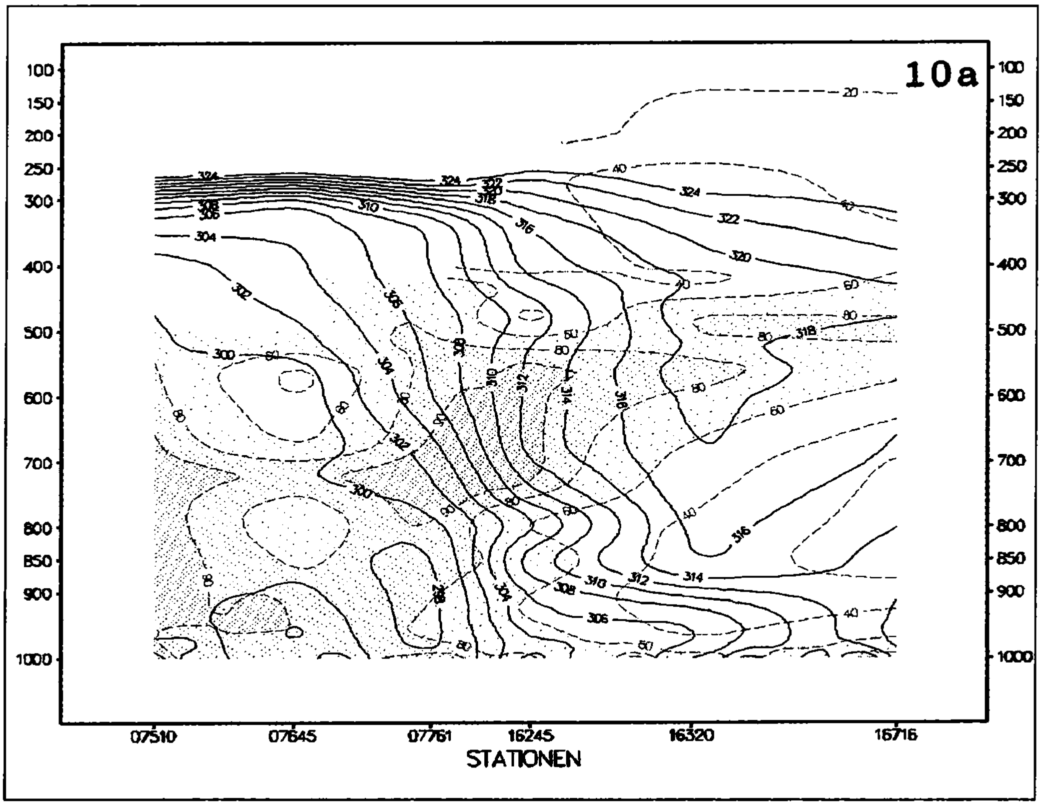

10 a: W-E cross section

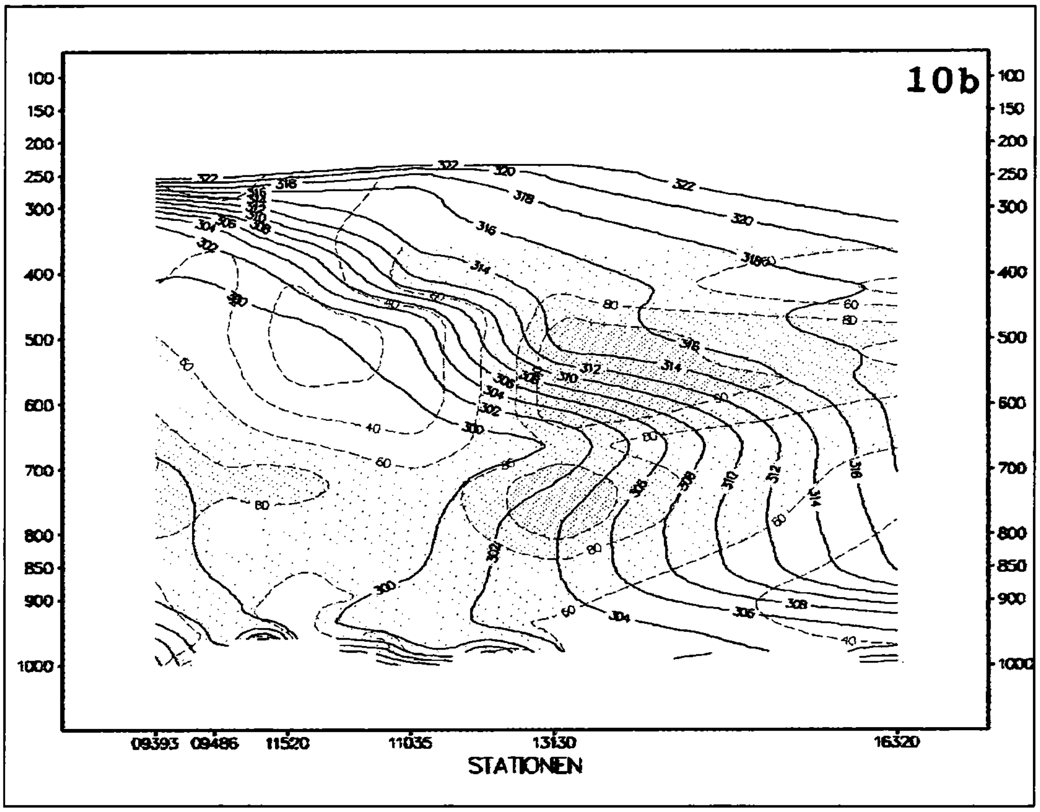

10 b: N-S cross section

Figure 10: Vertical cross sections of equivalent potential temperature (solid lines) and relative humidity (dashed and shaded) from radiosonde data; numbers of radiosonde stations are indicated on the abscissa

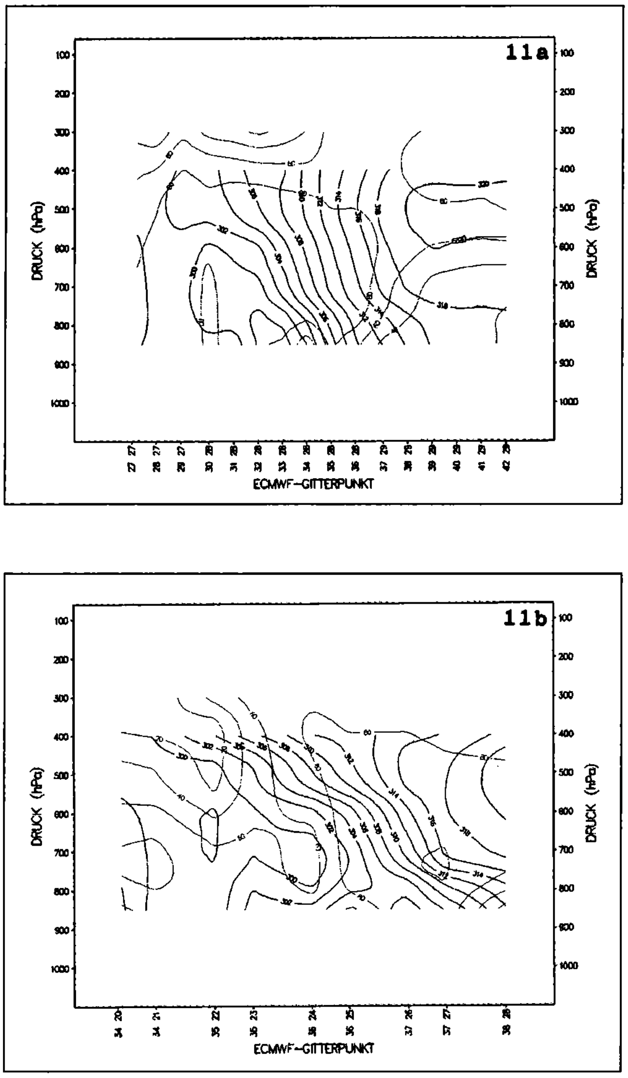

Figure 11: Same as figure 10, but from ECMWF analysis grid point values; numbers of grid points are indicated on the abscissa

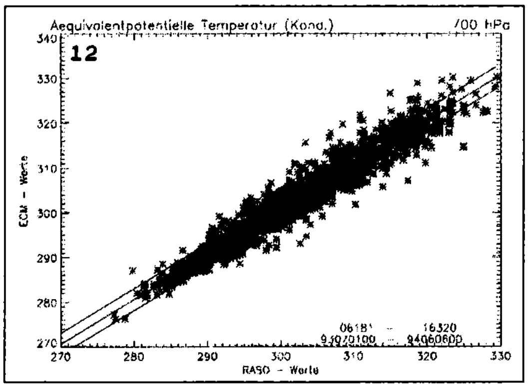

Figure 12: Comparison between radiosonde and ECMWF data within the cross sections. Black crosses: all available data; green dots: values of 15 April 1993/00 UTC

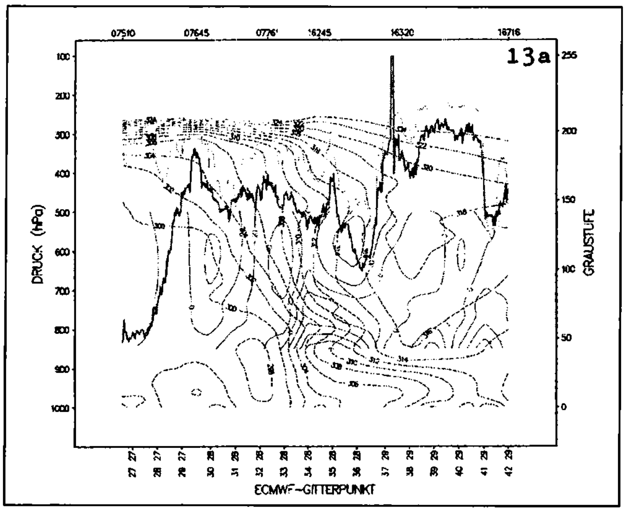

13a: W-E cross section

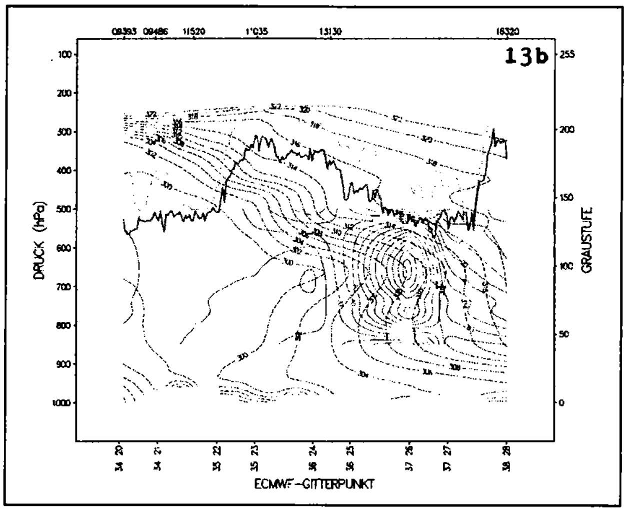

13b: N-S cross section

Figure 13: 15 April 1993/00UTC, dashed: equivalent potential temperature from radiosonde data; violet: frontogenesis parameter (normal component of Q vector) from ECMWF grid point analysis data; orange: IR pixel values; green: WV pixel values

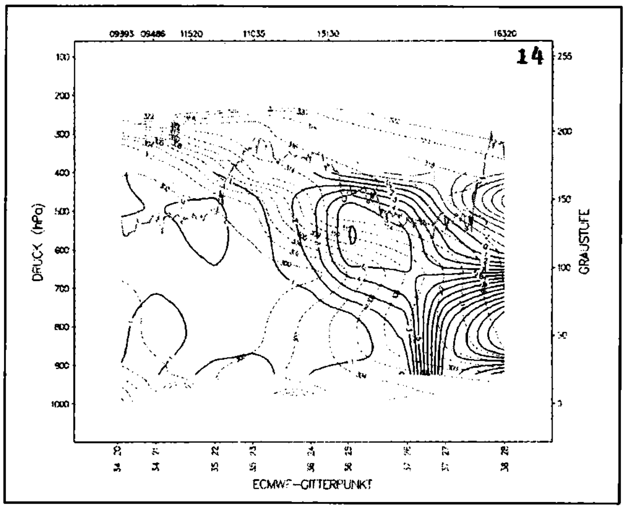

Figure 14:

15 April 1993/00 UTC; dashed: equivalent potential temperature from radiosonde data; blue: temperature advection from ECMWF grid point analysis data; orange: IR pixel values; green: WV pixel values

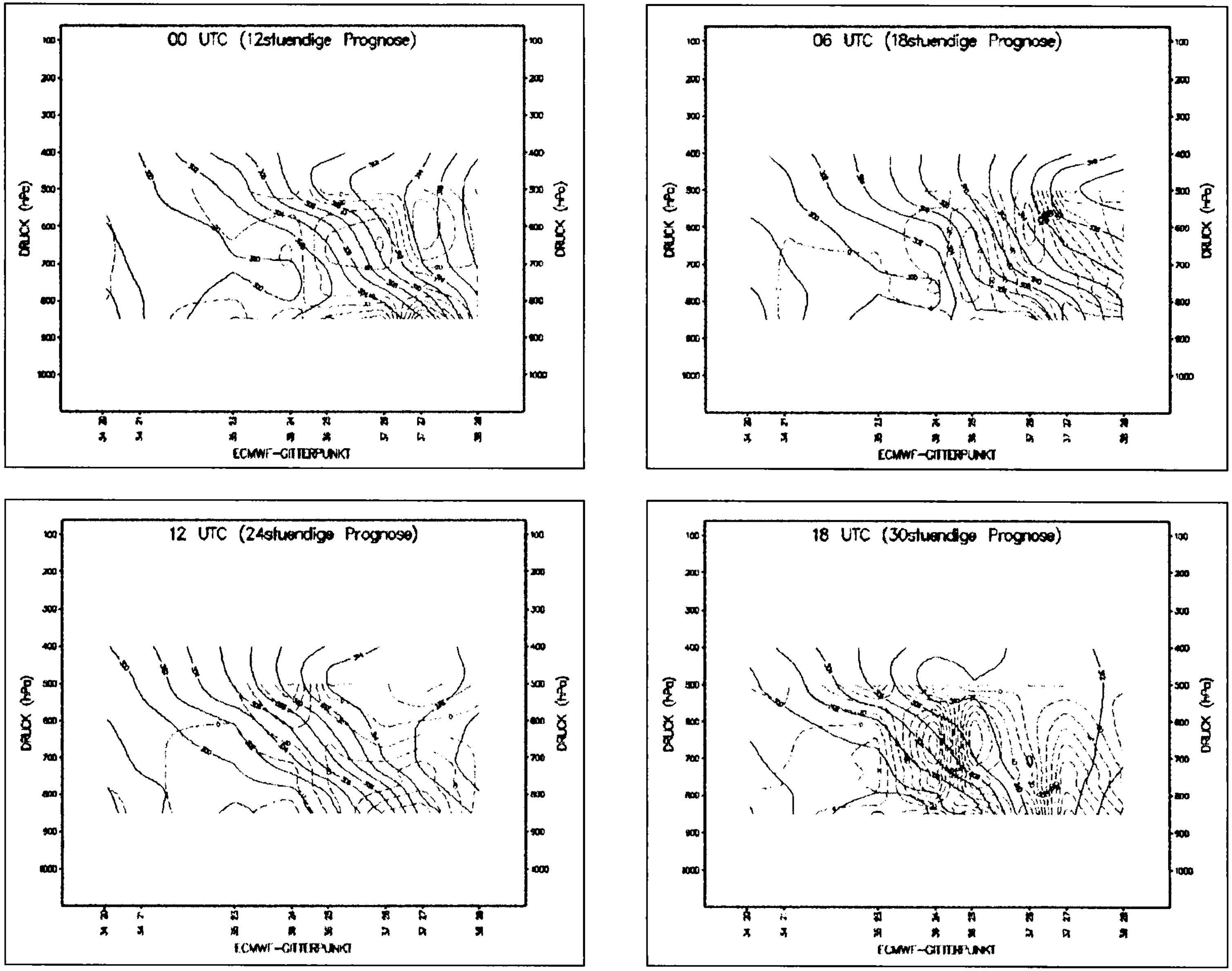

Figure 15:

15 April 1993; N-S cross section; ECMWF forecast values; forecasts for

left side:
00 UTC
(12-hourly forecast)

right side:
06 UTC
(18-hourly forecast)

left side:
12 UTC
(24-hourly forecast)

right side:
18 UTC
(30-hourly forecast); solid black: equivalent potential temperature, violet dashed: frontogenesis parameters

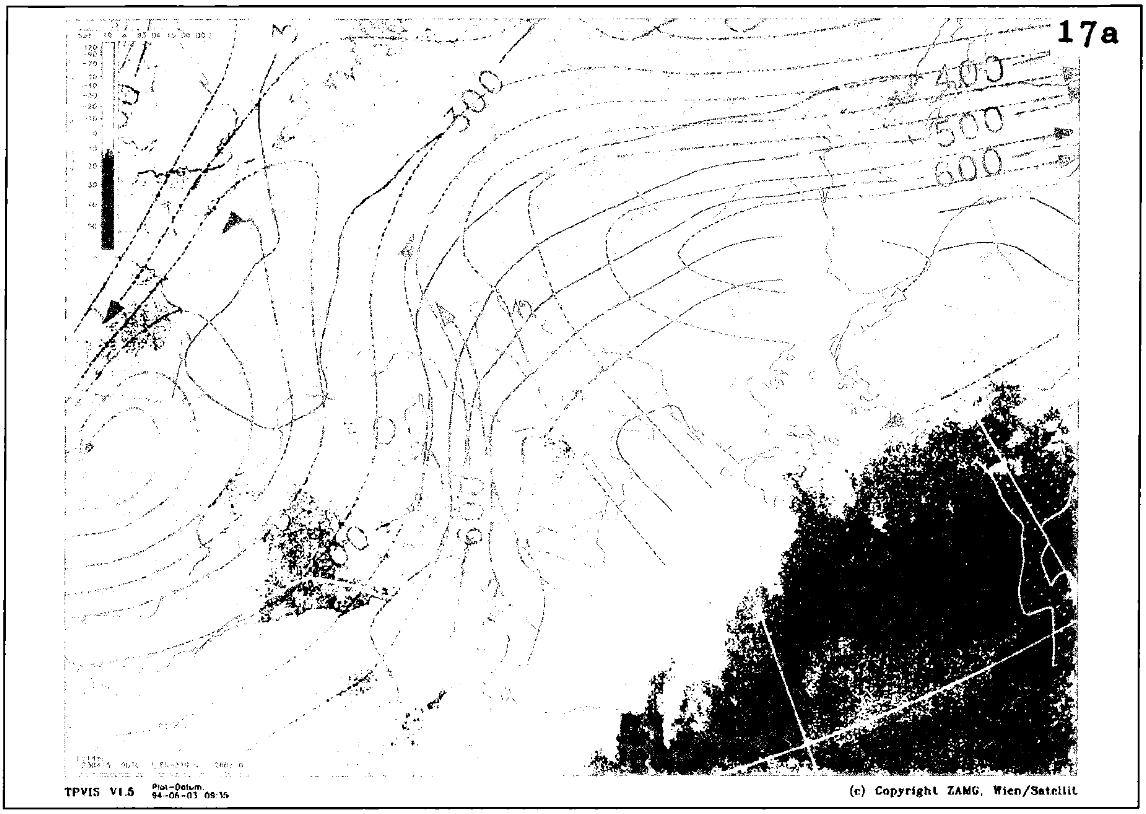

17 a: 310 K

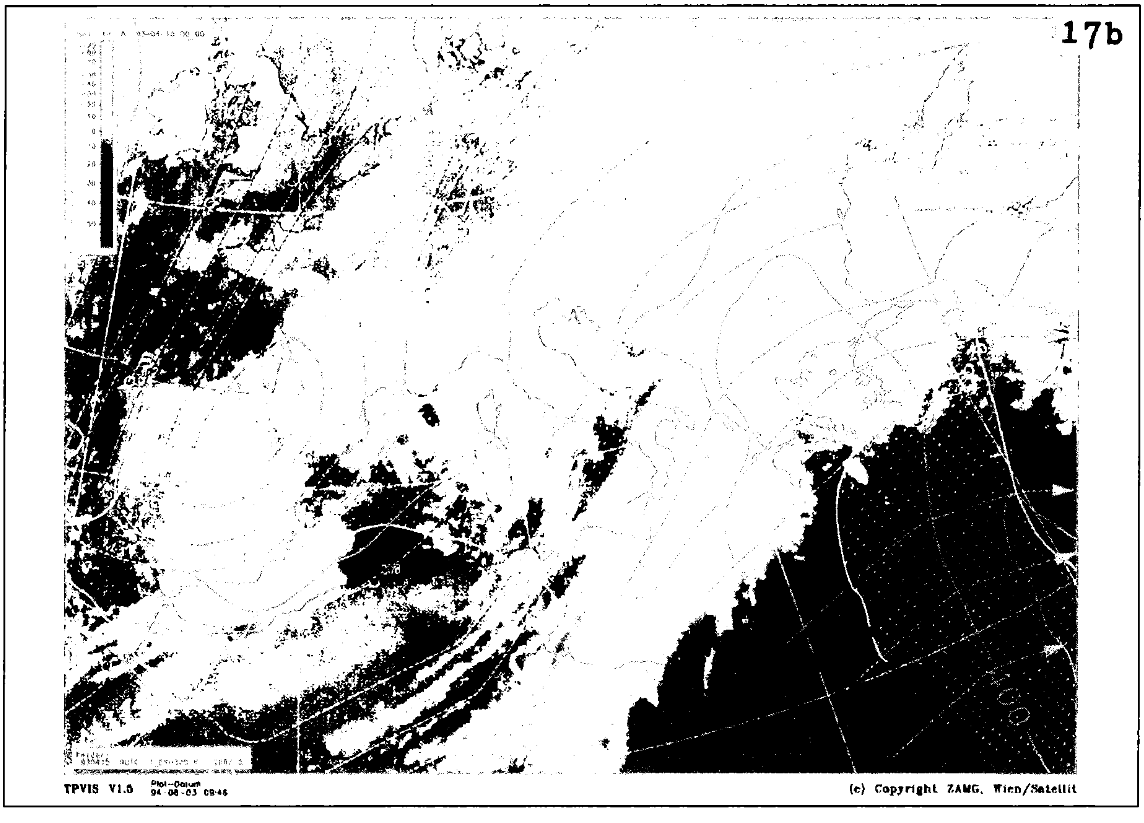

17 b: 320 K

Figure 17: 15 April 1993/00 UTC; IR; relative streams for system velocity 286°/8 m/s; solid blue: isobars; dashed blue: relative streamlines; green shaded: areas with rising (only qualitatively)

CLOUD CLASSIFICATION TECHNIQUES AT THE HUNGARIAN METEOROLOGICAL SERVICE

Satellite Research Laboratory of HMS, Budapest, Hungary

MÁRTA DIÓSZEGHY and EDINA FEJES

ABSTRACT

After the first attempts to find appropriate thresholds for cloud classifications from satellite images a statistical method of cluster analysis is chosen which can find the natural partition of a data set without any preliminary information. A bi-dimensional (visible and infrared) frequency histogram of the brightness values for a 15-day-long period is computed. The cloud classes are separated on the histogram by dynamic cluster analysis. The method was tested for data of May and September 1992, comparing the results to surface observations and visual nephanalyses.

ZUSAMMENFASSUNG

Nach ersten Versuchen zur Bestimmung geeigneter Schwellwerte für eine Wolkenklassifikation aus Satellitenbildern wurde eine statistische Methode der Clusteranalyse gewählt, bei der eine automatische Abgrenzung eines Datensatzes ohne zusätzliche Informationen möglich ist. Ein zweidimensionales (visible und infrared) Histogramm der Grauwerte wird für eine 15tägige Periode berechnet. Die Wolkenklassen werden im Histogramm durch eine dynamische Clusteranalyse getrennt. Die Methode wurde für Daten des Mai und September 1992 durch Vergleich mit Bodenbeobachtungen und Nephanalysen getestet.

1. THRESHOLD METHODS

At the Hungarian Meteorological Service (HMS), the first attempt to determine cloud amounts and types by digital satellite information was made by Tänczer (1990; 1992) even before the operational receipt of digital satellite pictures.

The case study was performed using visible and infrared digital images taken over Europe on July 26th, 1988 by the Japanese satellite MOS-1. It was decided to use threshold values based on histograms of signal intensities for distinguishing between cloudy and cloud-free pixels. The cloud amounts were estimated for a grid of 25x25 pixels (area of approximately 2500 km²). An investigation was carried out to which degree the cloud amounts computed from the visible and the infrared images coincide. In 68 % of the cases the difference was within ± 10% . The cloud types were defined for squares of 5x5 pixels, with spatial resolution of about 100 km² using visible and infrared images simultaneously. Three thresholds for each channel were determined to separate the cloud types according to different albedo values and heights. In addition, a coherence test was carried out in the infrared image: the cumuliform and layer clouds were separated by comparing the standard deviation around the pixel with a given threshold. Altogether 15 cloud and surface types were differentiated (Table 1).

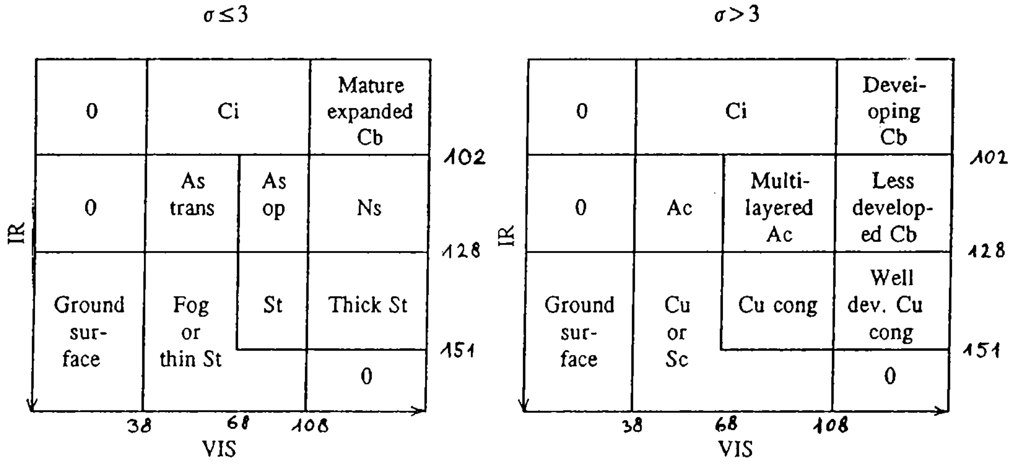

$\sigma \leq 3$

0	Ci		Mature expanded Cb
0	As trans	As op	Ns
Ground surface	Fog or thin St	St	Thick St
			0

$\sigma > 3$

0	Ci		Developing Cb
0	Ac	Multi-layered Ac	Less developed Cb
Ground surface	Cu or Sc	Cu cong	Well dev. Cu cong
			0

Table 1: Cloud types on the basis of the combined threshold method (from Tänczer, 1992)
On the left (right) side types with high (low) coherence can be found

In September 1991 the digital METEOSAT receiving system was installed at the Satellite Research Laboratory of the HMS and Fejes et al. (1992) worked out a program package for image processing. This package involved a cloud classification module as an application of the above mentioned method. The authors introduced a correction in the visible channel for the solar zenith angle. The method calculates the sun elevation for each pixel - or above grid points - and after that the brightness values are transformed for a constant sun elevation (45°).

Because of the few channels on METEOSAT there are no possibilities for a combination of different channels (adding or extracting brightness values). This fact makes it very difficult to determine appropriate thresholds for a partitioning. To avoid this problem another cloud classification process based on the statistical method of cluster analysis was worked out.

2. CLUSTER ANALYSIS

2.1 DESCRIPTION OF THE METHOD

The cluster analysis can find a natural partition of the data set without any preliminary information. In the final classification the objects of the same cluster are close to each other according to a resemblance measure, while distant objects belong to different clusters. The best partition can be reached by finding the minimum of the similarity function. The Euclidean distance is chosen as a resemblance measure, the formula of the similarity function will be the following:

$$W = \sum_{l=1}^{K} \frac{1}{|C_i|} \sum_{x \in C_i} \upsilon(\underline{x}) \rho(\underline{x}, \overline{x_i})$$

where

K	is the number of the clusters
Ci	is cluster i
|Ci|	is the number of objects in cluster i
$\nu\ (\underline{x})$	is the frequency value of the object on the histogram
$\rho\ (\underline{x},\ \overline{x_i}\ )$	is the distance of the object from the centre of gravity of cluster i.

There are several types of clustering techniques (Diday and Simon,1976) from which the dynamic cluster algorithm is chosen. In this method the symbolic description of a class is the centre of gravity. After choosing initial centres for the clusters (random points or local maxima) all of the objects have to be assigned to the nearest centre recomputing the centre of gravity of the chosen cluster at the same time. When all of the objects are classified, the similarity function can be computed and eliminating the classes with too few elements - a new iteration can be started. Ideally the process is finished when the centres of gravity show the same distribution as in the former iteration or the similarity function reaches its minimum value. Practically it is enough to reach a relatively stable distribution of centres which does not differ too much from the former one according to an appropriate threshold.

In case of cloud classification the cluster analysis has to be applied to the frequency histogram of the brightness values in the chosen channels, because the different cloud types appear as different peaks on the histogram.

In the method described here the infrared (IR, 10.5-12.5 μm) and visible (VIS, 0.4-1.1 μm) channels of METEOSAT images are used and the bi-dimensional histogram is partitioned. The main steps of the algorithm are the following:

I. Preparation process

1. Selection of the region of interest from the IR, VIS images (450x150 pixels)
2. Polar stereographic projection (of the cuts)
3. Computation of the bi-dimensional histogram of the brightness values

II. Cluster analysis

1. Choice of the inital centres of the classes
2. Assignment of the objects to the nearest centre and recomputation of the centre of gravity (point by point)
3. Computation of the similarity function
4. If the next iteration is necessary go to II.2. (elimination of classes with few elements) if not go to III.

III. Classification

1. Assignment of the indices (results of the cluster analysis) to the brightness values of the images
2. Visualisation of the classified image

Developing the method some technical problems arose. Theoretically the method does not depend on the choice of the initial centres; but practically the program should not be too slow. Therefore the method of Porcú and Levizzani (1992) who divided the histogram into bi-dimensional intervals and defined the local maxima as initial centres is used. Four times as many intervals (16x16) are used as by the Italian scientists because it was proved by Gallaudet and Simpson (1991) that more initial clusters lead to a more stable partition. In this way the process starts with 50-70 centres (centres with less than 5 elements are eliminated).

When two centres of clusters are too close to each other (according to a given threshold) then the two clusters are merged.

Eliminating classes with too few elements means that only the centres of clusters are neglected, the points assigned to those clusters are again classified in the next iteration. The elimination threshold was defined by Porcú and Levizzani as 1/20 of the total number of pixels but this proved to be too strict for the first few iterations. Therefore the threshold is chosen as a function of the number of iterations as follows:

$$\text{threshold} = 1/K$$

$$K = -4I+100 \qquad \text{if } I < 20$$

$$K = 20 \qquad \text{if } I \geq 20$$

where I is the ordinal number of the iteration.

According to the investigations of Debois and Seze (1987), the alteration of brightness values as a function of the solar zenith angle differs about three times as much in case of latitudes as in case of longitudes. Therefore the region of interest is a rectangular box (450x150 pixels). To avoid the correction of brightness values - mainly because of the difficulties in the infrared channel - the panels are rather small. Because of this, time-cumulated histograms for 15 days are coumputed using only pictures of the same time of the day.

2.2 RESULTS

The method was tested for two months, May and September of 1992. Although there was great interest in cumulonimbus detection, the archives of June and July were not complete and in August there were hardly any clouds over Hungary. From the 11 UTC images 5, 15 and 30 day histograms were calculated but the cluster analyses showed that the 15 day period was the most usable as the convergence of the similarity function was suitable (< 5%) and the number of separated classes was reasonable (8-12).

Finally, the cloud type of a cluster was determined by the location of the clusters on the histogram and by comparison out of the classified image to surface observations (taken at 12 UTC) and visual nephanalyses.

The results obtained for the first half of September are presented showing only the most interesting cloud fields. In figure 1 the partitioned histogram can be seen and table 2 shows the characteristics of the different classes: the brightness values (VIS, IR) of the centres of clusters (on the scale of 0-255) and the names of the classes. On 1st September (figure 2) the cloud field of a well developed cold front can be seen. The cumulonimbus clouds (green) are well separated from the frontal nimbostratus area (white). The contaminated pixels appear at the edges of the clouds (yellow). Unfortunately the cold land surface areas (eastern part of Carpathian Mountains) were put into the same class as the Adriatic Sea (blue). On 4th September (figure 3) it is worth to look at the cirrostratus (ochre), on the visible image no cloud appeared at that place. In the eastern part of the picture there are bigger patches of contaminated pixel with agreement to the cumulus and cumulus congestus clouds observed from the ground. On 7th September (figure 4) a large area was classified as cumulonimbus (green) but it is evident from spatial characteristics that it must be something else. In fact, there were cirrus clouds overlapping dense nimbostratus with the same brightness values - both in VIS or IR channels - as cumulonimbus clouds normally have.

A further investigation of standard deviation fields will hopefully solve this problem and it can also help to avoid the confusion of sea and very cold land surface areas.

	COLOUR	VIS	IR	SURFACE/CLOUD TYPES
1	blue	43	150	sea surface
2	red	46	163	land
3	ochre	60	110	dense Cs
4	brown	53	138	thin Ci
5	yellow	77	128	contaminated pixels
6	grey	90	99	less developed Ac, As
7	pink	119	101	well developed Ac, As
8	white	153	90	As or Ns
9	green	132	62	Cb or Ns overlapped by Ci

Table 2: Coordinates of the centres of classes and names of the cloud classes

2.3 CONCLUSION AND FUTURE PROSPECTS

The main advantages of the method are that it is applicable for METEOSAT images without any other information and that it is quite fast. Once the histogram is separated into clusters the images can be classified with the same index field for 1-2 weeks. The process separates the cloud types according to different thickness and heights relatively well. Unfortunately the separated classes are hardly comparable to the traditional classifications and it is difficult to differentiate between cumuliform and layer clouds with the same brightness values in case of multilayered cloud systems.

For these reasons work involving the standard deviation fields of VIS, IR images is going on. It will hopefully lead to a better separation of cumuliform and layer clouds. As a further dimension the water vapor absorption band can be include into the process. It is planned to run the cluster program for a longer period (years) to build up a bank of indices for every half month which can be used directly for the classification.

REFERENCES

DEBOIS, M., SEZE, G. (1987): Cloud Cover Analysis from Satellite Imagery Using Spatial and Temporal Characteristics of the Data. J. Clim. Appl. Meteor., **26**, 287-303.

DIDAY, E., SIMON, J.C. (1976):Clustering Analysis. Digital Pattern Recognition (Ed. K.S. Fu), Springer Verlag, Berlin, Heidelberg, New York, 47-94.

FEJES, E., KERÉNYI, J., VÁRNAI, T. (1992): Processing and Application of Digital METEOSAT images at the Hungarian Meteorological Service. Proc. of 9th METEOSAT Users' Meeting, Locarno, EUM P 11, 421-426.

PORCÚ, F., LEVIZZANI, V. (1992): Cloud classification using METEOSAT VIS-IR imagery. Int. J. Remote Sensing, **13**, 893-909.

TÄNCZER, T. (1990): A felhözeti mezö bispektrális komplex analízise digitális mûholdadatok alapján. OMFB Press, Budapest.

in English:
TÄNCZER, T. (1992): A combined bispectral cloud analysis using digital data from MOS-1. Idöjárás, **96**, 3, 146-158.

Author's address:

MÁRTA DIÓSZEGHY and EDINA FEJES,
Satellite Research Laboratory of the
Hungarian Meteorological Service,
P.O.Box 39, H-1675 Budapest,
HUNGARY
Phone: +36-1-290-0163
Fax: +36-1-290-7387
E-mail: h10356muh@huella.bitnet

FIGURES

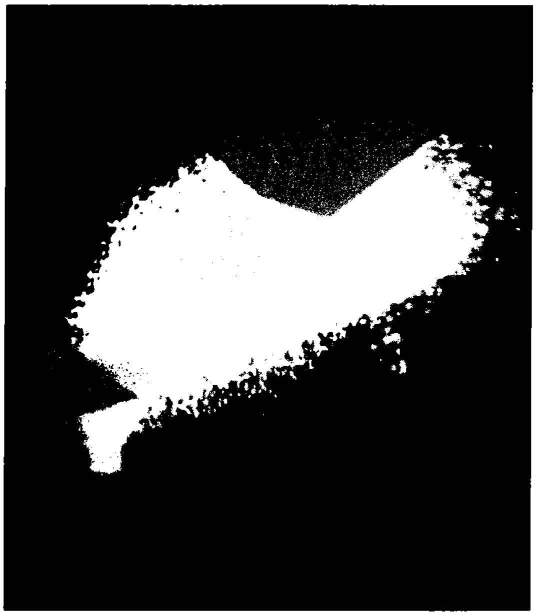

Figure 1:
The bi-dimensional histogram of the brightness values (abscissa: IR, ordinate: VIS) separated into cloud clusters

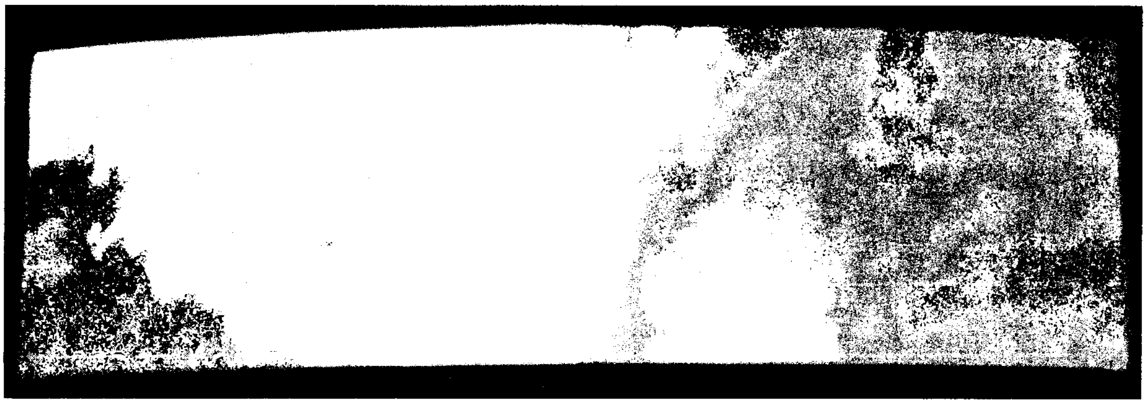

Infrared image

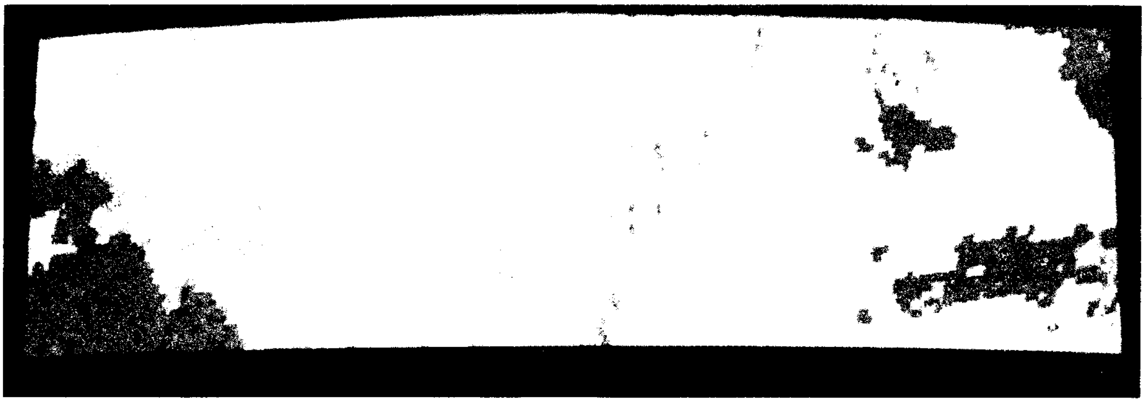

Classified image

Figure 2: 1 September 1992/11 UTC

Infrared image

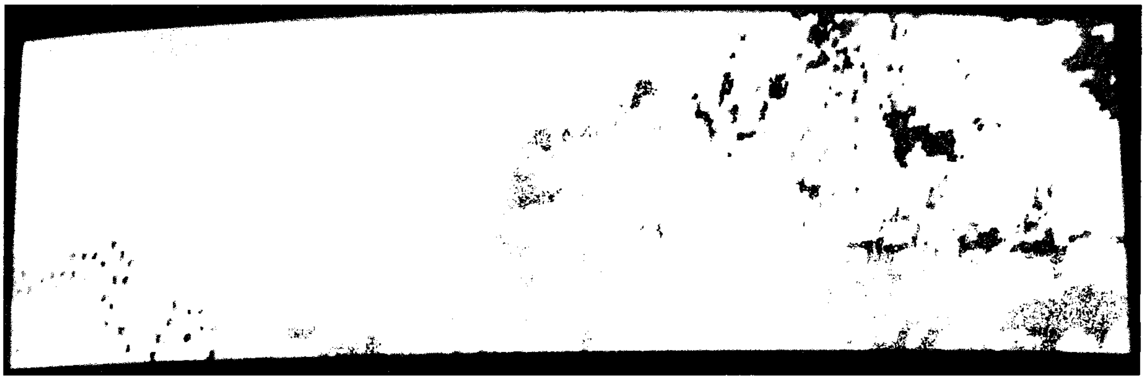

Classified image

Figure 3: 4 September 1992/11 UTC

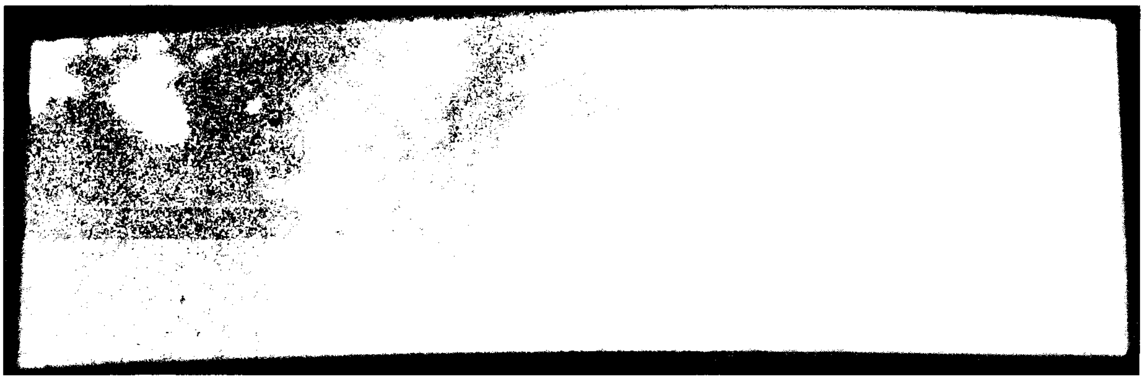

Infrared image

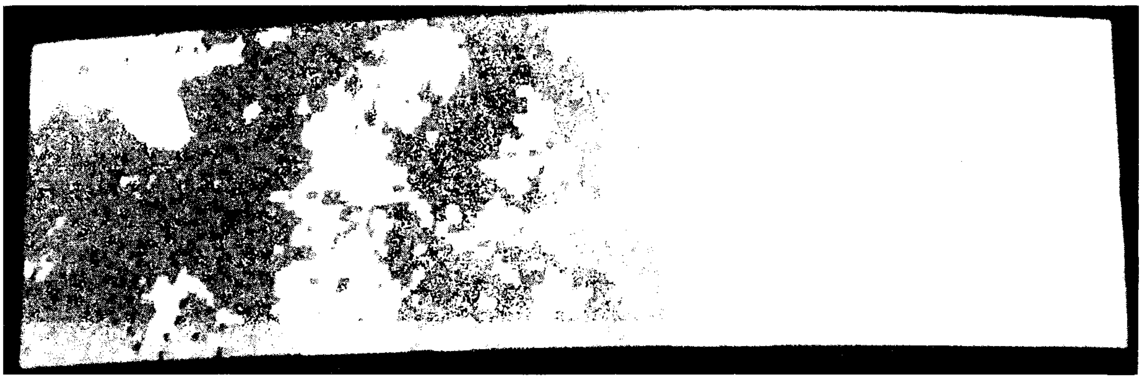

Classified image

Figure 4: 7 September 1992/11 UTC

APPLICATION OF TOVS DATA AT THE HUNGARIAN METEOROLOGICAL SERVICE

Hungarian Meteorological Service, Budapest

I. CSISZÁR AND L. KOVÁCS

ABSTRACT

In recent years the installation of a direct-readout satellite receiving station and the improving computational capabilities have allowed the quasi-operational use of the TIROS-N Operational Vertical Sounder (TOVS) data at the Hungarian Meteorological Service. In this paper results of two investigations are presented. First the derivation of vertical temperature and humidity profiles from TOVS and their impact on the accuracy of a limited area numerical weather prediction model is discussed. A positive impact was only found in the middle troposphere, where the TOVS soundings have relatively good quality. In the second part an improved multiple regression algorithm for the calculation of the total atmospheric ozone content is described. Comparisons with coincident ground-based and ozonesonde measurements have shown that the use of regression coefficients determined seperately for five satellite-derived airmasses in most cases provides a better ozone retrieval accuracy.

ZUSAMMENFASSUNG

Durch die Installation einer geeigneten Satellitenempfangsanlage sowie durch verbesserte Rechenkapazitäten ist in den letzten Jahren eine quasi-operationelle Anwendung der TOVS-Daten (TIROS-N Operational Vertical Sounder) im Ungarischen Meteorologischen Dienst möglich geworden. In dieser Arbeit werden die Ergebnisse zweier Untersuchungen präsentiert. Zuerst wird die Ableitung vertikaler Temperatur- und Feuchteprofile aus TOVS-Daten sowie ihr Einfluß auf ein LAM-Vorhersagemodell diskutiert. Nur für die mittlere Troposphäre, für die die TOVS-Daten relativ gute Qualität aufweisen, konnte ein positiver Einfluß festgestellt werden. Im zweiten Teil der Arbeit wird ein verbesserter Regressionsalgorithmus für die Berechnung des totalen Ozongehaltes der Atmosphäre beschrieben. Vergleiche mit Boden- und Ozonsondenmessungen haben gezeigt, daß die Verwendung von Regressionskoeffizienten, die getrennt für fünf aus Satellitendaten abgeleiteten Luftmassen bestimmt werden, in den meisten Fällen eine höhere Genauigkeit der Ozonbestimmung gewährleisten.

1. INTRODUCTION: THE SATELLITE SOUNDING

The HRPT (high resolution picture transmission) transmission from the polar orbiting NOAA series consists of the Advanced Very High Resolution Radiometer (AVHRR) and the TIROS Operational Vertical Sounder (TOVS) data. The TOVS includes 3 instruments: The High-resolution Infrared Radiation Sounder (HIRS), the Microwave Sounding Unit (MSU) and the Stratospheric Sounding Unit (SSU). HIRS performs measurements at 20 channels, MSU at 4 channels and SSU at 3 channels. Table 1 provides more detailed information on these channels. This table shows that the weighting functions of these channels (i.e. the partial derivatives of the transmittance function with respect to the pressure or height) have their maximum values at different levels. So these channels are sensitive to different layers of the atmosphere. Therefore this measurement is called satellite sounding. The regular reception of the HRPT transmission from the satellites NOAA - 11 and 12 began at the Satellite Research Laboratory of the Hungarian Meteorological Service (HMS) in January 1992. Possibilities of an operational application of the TOVS data, which have been archived and processed quasi-operationally since then, are investigated.

channels	wave long	active gas	maximum of weighting function
HIRS 1	15.00 µm	CO$_2$	30 hPa
HIRS 2	14.70 µm	CO$_2$	60 hPa
HIRS 3	14.50 µm	CO$_2$	100 hPa
HIRS 4	14.20 µm	CO$_2$	400 hPa
HIRS 5	14.00 µm	CO$_2$	600 hPa
HIRS 6	13.70 µm	CO$_2$/H$_2$O	800 hPa
HIRS 7	13.40 µm	CO$_2$/H$_2$O	900 hPa
HIRS 8	11.10 µm	window	surface
HIRS 9	9.70 µm	O$_3$	25 hPa
HIRS 10	8.30 µm	H$_2$O	900 hPa
HIRS 11	7.30 µm	H$_2$O	700 hPa
HIRS 12	6.70 µm	H$_2$O	500 hPa
HIRS 13	4.57 µm	N$_2$O	1000 hPa
HIRS 14	4.52 µm	N$_2$O	950 hPa
HIRS 15	4.46 µm	CO$_2$/N$_2$O	700 hPa
HIRS 16	4.40 µm	CO$_2$/N$_2$O	400 hPa
HIRS 17	4.24 µm	CO$_2$	5 hPa
HIRS 18	4.00 µm	window	surface
HIRS 19	3.70 µm	window	surface
HIRS 20	0.70 µm	window	cloud
MSU 1	5.96 mm	window	surface
MSU 2	5.58 mm	O$_2$	700 hPa
MSU 3	5.45 mm	O$_2$	300 hPa
MSU 4	5.18 mm	O$_2$	90 hPa
SSU 1	15.00 µm	CO$_2$	15 hPa
SSU 2	15.00 µm	CO$_2$	4 hPa
SSU 3	15.00 µm	CO$_2$	1.5 hPa

Table 1: Some selected information about TOVS channels

2. CALCULATION OF TEMPERATURE AND WATER VAPOR PROFILES

These profiles are derived from TOVS data by the ITPP 4.02 model developed at the Cooperative Institute for Meteorological Satellite Studies (CIMSS). The principle of this model is the following (Smith et al. 1985): (1) contains the perturbation form of the radiative transfer equation.

$$\delta T_b = \int_0^{p_s} \delta W \frac{\partial \bar{T}}{\partial p}\frac{\partial \tau}{\partial W}\frac{\frac{\partial B}{\partial T}(\bar{T})}{\frac{\partial B}{\partial T}(\bar{T}_b)}\,dp - \int_0^{p_s} \delta T \frac{\partial \tau}{\partial p}\frac{\frac{\partial B}{\partial T}(\bar{T})}{\frac{\partial B}{\partial T}(\bar{T}_b)}\,dp + \delta T_s \frac{\frac{\partial B}{\partial T}(\bar{T}_s)}{\frac{\partial B}{\partial T}(\bar{T}_b)}\tau_s \tag{1}$$

where T_b is the brightness temperature, T_s is the surface-skin temperature, T is the air temperature, B is the Planck radiance, τ is the transmittance, p is the pressure and W is the precipitable water vapor which is obtained from the water vapor mixing ratio m by the equation

$$W(p) = \frac{1}{g}\int_0^{p} m(p)\,dp \tag{2}$$

where g is the gravitational acceleration.

The perturbation δ is with respect to an a-priori estimated or mean condition which is represented with overlined symbols. If this equation is written for all of the TOVS channels and the perturbation profiles are described as a linear combination of the weighting functions, which include statistical information about the given profile, the equation is in matrix form. The solution of this equation leads to the coefficients of the linear combinations. In this way the temperature and water vapor profiles can be determined simultaneously at 56x100 TOVS pixels which means a resolution of about 50 km at the subsatellite point.

3. ASSIMILATION OF TOVS PROFILES IN THE HUNGARIAN NWP

The applied model is a 12σ-level primitive equation limited area numerical weather prediction model (NWP) which was developed at the Swedish Meteorological and Hydrological Institute and adopted by the HMS (Undén 1982). A 36 hour model forecast is processed in a 60 hour assimilation cycle which contains assimilation of radiosonde data and surface observations.

In a first experiment, it was investigated if the assimilation of TOVS profiles has any effect on the NWP and what sort of effect this is. A five-day experiment was performed starting on 31st October 1992. Limited by the calculation capacity available at that time the profiles were determined for only 200 pixels, preferably above the Central European area. The forecast products of the Hungarian NWP were considered as an a-priori estimation for the ITPP 4.02 model. The TOVS profiles were processed in the assimilation by the objective analysis scheme. Some improvement of the 500 hPa temperature fields above the Central European area was found where the TOVS profiles had the best quality. However, there was a negative impact for the other fields. For the quantitative evaluation of the effect of TOVS retrievals, brightness temperature fields were calculated from the NWP data also by a forward radiative transfer model (Csiszár and Kovács 1993). In order to decrease the time gap between the forecast and the satellite overpasses +3 and +15 hour forecast fields were used in this calculation. The standard deviation of the NWP brightness temperature from the TOVS brightness temperature was derived (see figure 1). Some positive impact for a carbon-dioxid channel (HIRS 5) and a water vapor channel (HIRS 12) was found. Both of them were sensitive around 500 hPa.

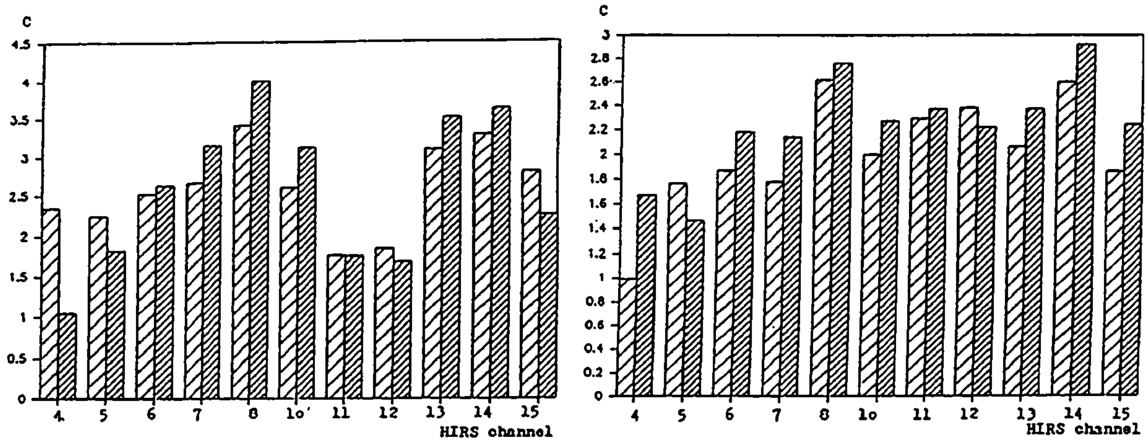

at +3 hour forecast

at +15 hour forecast

Figure 1: TOVS-NWP standard deviation

▨ in case of assimilation without TOVS data

▩ in case of assimilation with TOVS data

In a second experiment the TOVS profiles were assimilated over the Atlantic Ocean where the amount of radiosonde data is insufficient. At that time a workstation could be used, so the profiles could be caculated for all the 56x100 TOVS pixels. Preferably TOVS profiles were assimilated in cloudfree and partly cloudy cases. In that case some improvement also in the lower troposphere was found, but sometimes the forecast "blew up". The reason for this is the following: The ITPP 4.02 model calculates the profiles at every single pixel independently. So it happens frequently that there is a 2-5 °C temperature difference between two neighbouring pixels. This big temperature gradient often causes the "blowing up" of the forecast.

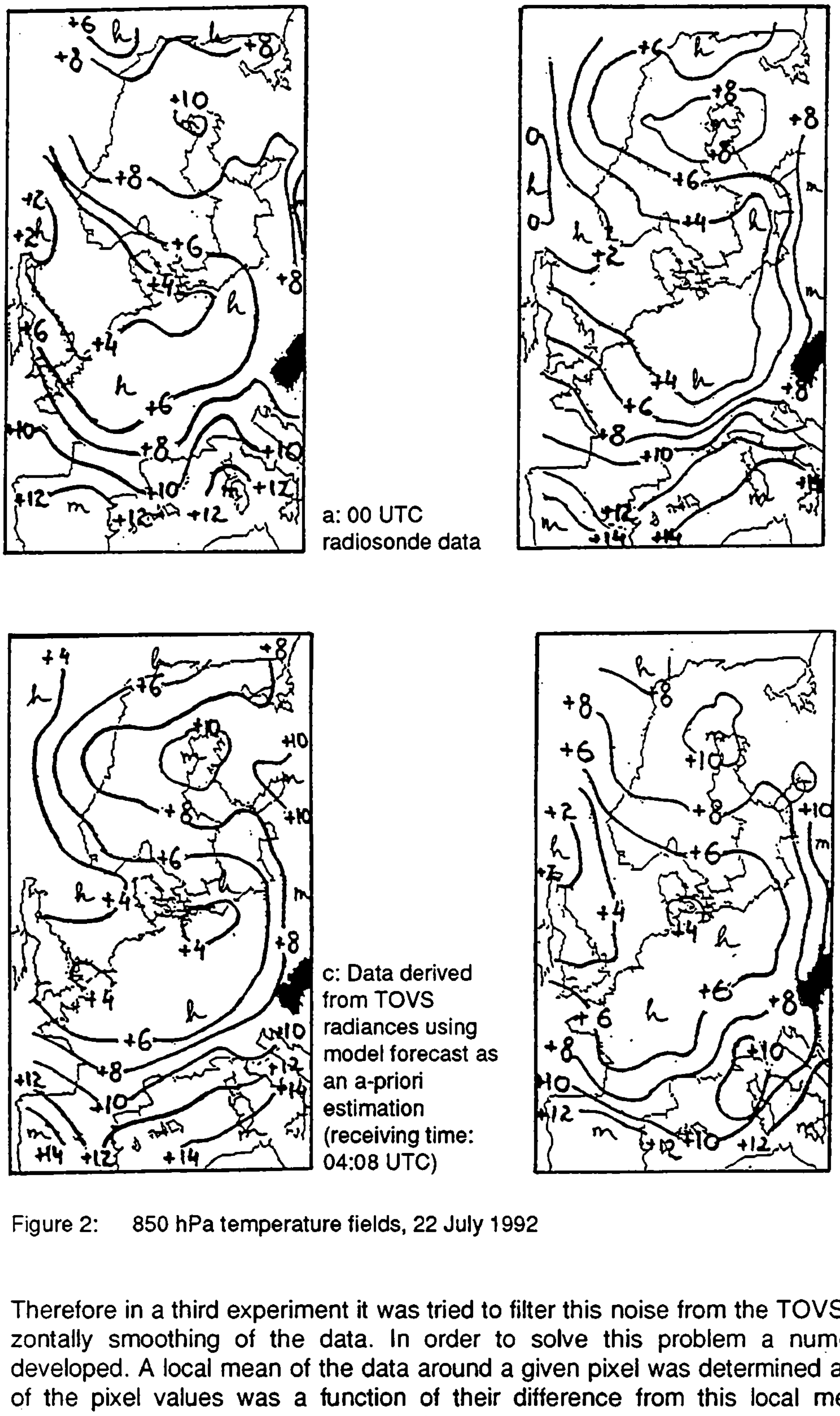

a: 00 UTC radiosonde data

b: Data derived from TOVS radiances using climatological mean as an a-priori estimation (receiving time: 04:08 UTC)

c: Data derived from TOVS radiances using model forecast as an a-priori estimation (receiving time: 04:08 UTC)

d: 12 UTC radiosonde data

Figure 2: 850 hPa temperature fields, 22 July 1992

Therefore in a third experiment it was tried to filter this noise from the TOVS profiles, by a horizontally smoothing of the data. In order to solve this problem a numerical method was developed. A local mean of the data around a given pixel was determined and the modification of the pixel values was a function of their difference from this local mean. In this way a successful smoothing could be carried out. In this experiment 24 satellite overpasses were processed, 12 oceanic and 12 Central European. All of them were processed using climatological mean and model forecast as an a-priori estimation of the profiles for the ITPP 4.02 model. In order to demonstrate the results some fields are represented in figures 2 and 3.

In figure 2 the 850 hPa air temperature fields can be seen. The radiosonde data (figure 2a) show cold air advection over the Central European area and warm air advection in the North. This is reflected in the data derived from TOVS radiances (figure 2 b, c) as well but using a climatological mean as an a-priori condition leads to the under-estimation of the air temperature field (figure 2b). In the upper troposphere, the same process can be observed (figure 3). In that case, temperature data derived from TOVS radiances using climatological a-priori estimation are less accurate than in the lower troposhere.

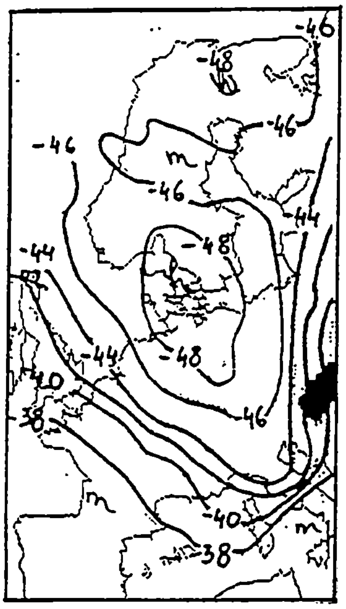

a: 00:00 UTC radiosonde data

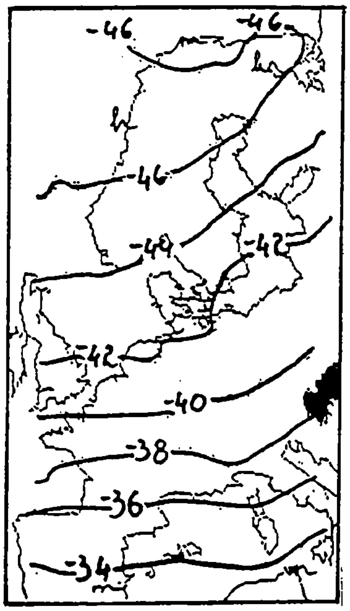

b: Data derived from TOVS radiances using climatological mean as an a-priori estimation (receiving time: 04:08 UTC)

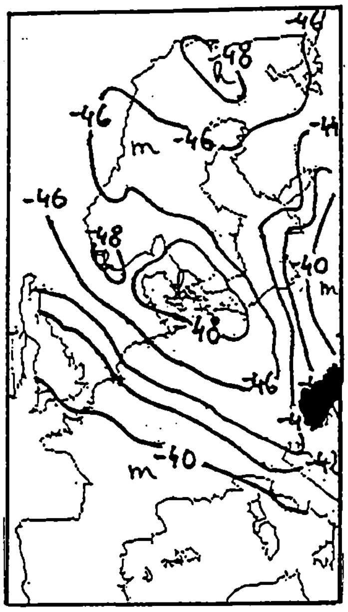

c: Data derived from TOVS radiances using model forecast as an a-priori estimation (receiving time: 04:08 UTC)

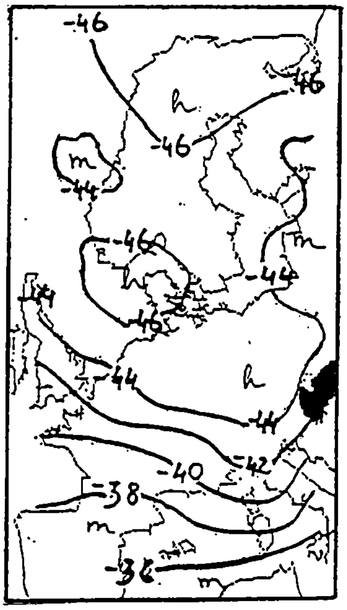

d: 12:00 UTC radiosonde data

Figure 3: 300 hPa temperature fields, 22 July 1992

The conclusion of these experiments is the following:

1. Assimilation of the data derived from TOVS radiances can have a positive effect on the numerical forecast where the amount of radiosonde data is insufficient (e.g. above sea surface).
2. Especially in cloudfree cases a good approximation of air temperature and water vapor data can be obtained.
3. The derived profiles can lead to the "blowing up" of the forecast if these data are not horizontally filtered.
4. These profiles depend on the a-priori estimation very strongly.

4. TOTAL OZONE CONTENT RETRIEVAL

Two major problems are connected with the retrieval of ozone from TOVS. First, due to the fact that there is only one ozone channel in the 9.6 µm absorption band (HIRS 9), no information can be obtained about the vertical profile of ozone. Second, the ozone channel is contaminated by the emission of the surface and the absorption by water vapour in the lower troposphere.

The methods for deriving total ozone content from TOVS measurements can be grouped into two categories: Statistical and physical methods. The statistical methods (Planet et al., 1984; Lienesh, 1988) use the brightness temperature of various HIRS channels as predictors for a multiple regression estimation. The predictors are chosen to account for the effects mentioned above and for the good correlation between the total ozone amount and the stratospheric temperature. The physical methods (Prabhakara et al., 1970; Ma X. et al., 1984; Lefevre et al. 1991) use the radiative transfer equation either in an iterational approach or to derive the transmittance of the ozone channel. However, even these methods use multiple regression either to derive a first-guess ozone profile or to determine the temperature of the ozone layer.

The applied algorithm is partially based on and incorporated into the 3I (Improved Initialization Inversion) program package developed at the Laboratoire de Météorologie Dynamique (LMD) in Palaiseau, France (Chedin et al., 1985). In this package the retrieval of the three-dimensional fields of temperature, humidity and other atmospheric parameters is carried out by the selection of first-guess profiles from TIGR (Thermodynamic Initial Guess Retrieval), a statistical data set of 1761 atmospheric situations grouped in 5 air mass categories according to the vertical profile of the virtual temperature (Achard, 1991). For each atmospheric situation and different observational conditions (10 satellite viewing angles, 19 surface pressures and two surface emissivities) the corresponding outgoing radiance values and transmittances in the spectral intervals of the TOVS instruments are computed by a line-by-line radiative transfer model (4A: Automatized Atmospheric Absorption Atlas, Scott and Chedin, 1981). TIGR contains information on the atmospheric ozone content obtained from ozonesonde data and measurements of the total ozone amount by ground-based instruments (Dobson, Brewer spectrophotometers) and by TOMS (Total Ozone Mapping Spectrometer) on board of the Nimbus-7 satellite. In the latter cases a climatological adjustment of the ozone profiles was made.

It was decided to apply a modified version of the algorithm described by Lefevre et al. (1991). In this approach, first the transmittance of the ozone layer is determined from the radiative transfer equation:

$$\tau(O_3) = \frac{R_9 - B_9(O_3)}{B_9(T_8) - B_9(T_{O_3})} \tag{3}$$

where $\tau(O_3)$ is the ozone layer transmittance, R_9 is the measured radiance in HIRS channel 9, B_9 represents the Planck function for the wavelength of channel 9 and T_8 is the brightness temperature of HIRS channel 8. T_{O_3} is the temperature of the ozone layer which can be estimated by a multiple regression formula:

$$T_{O_3} = a_1 T_2 + b_1 T_6 + c_1 T_8 + d_1 T_9 + e_1 \tag{4}$$

Here T_k denotes the brightness temperature of the k-th HIRS channel. Then, the total ozone value is calculated from the equation:

$$[O_3] = -f \ln(\tau(O_3)) + a_2 T_2 + b_2 T_6 + c_2 T_8 + d_2 T_9 + e_9 \tag{5}$$

The regression coefficients, in addition to being generated for each set of viewing angle, surface pressure and surface emissivity, were also determined for each air mass type separately. Since there is a good correlation between the vertical temperature and the ozone profiles, the dependence of the ozone absorption on the altitude (or mean pressure) of the ozone layer could be taken into account in this way. The basis for these calculations is the TIGR data set.

In order to be able to investigate the effect of the air mass-dependent regression coefficients, a set of them was derived without making distinction between the air masses. Then the statistics calculated for the whole TIGR data set from the air mass-dependent and air mass-independent regressions were compared. This comparison showed a decrease of the error standard deviation of about 15 % (from 18.9 DU to 15.5 DU) as an impact of the air mass-classification.

The ozone retrieval program can be run after the 3I inversion. It uses the cloud-cleared radiances and the air mass flag stored in the 3I output file. The regression coefficients are interpolated according to the viewing angle of the actual satellite observation. The isothermal cases (when the estimation of the ozone layer transmittance is unstable) are omitted. These situations are defined by a difference of less than 20 K between the ozone layer temperature and the brightness temperature of channel 8. The cases with retrieved cloud top pressure less than 423 hPa seem to have poor quality and are also omitted.

Preliminary comparisons were carried out between the retrieval products and an independent set of ground measurements. This data set consists of 197 Dobson data in the European region in March 1987, archived at the World Ozone Data Center in Downsview, Ontario, Canada. The coincident TOVS radiances were taken from the global Pathfinder 3I output products for satellite NOAA-10. Unfortunately, most cases belonged to one of the mid-latitude air masses and thus it was not possible to derive separate statistics for each air mass. However, the overall statistics gave an opportunity for the first evaluation of the algorithm.

Table 2 shows some of the verification statistics. It can be noted that the use of air mass-dependent regression coefficients introduced an improvement of about 1.5 DU in the error standard deviation of the data when the coefficients were derived at once for the whole TIGR data set. Also, by omitting the cases at the borders of the air masses (where the total ozone value may have a big spatial and temporal variability), an additional significant improvement can be observed. However, a larger amount of verification data would be necessary to give a proper and detailed evaluation of the results.

Table 2: TOVS-Dobson verification statistics for the March 1987 data set

Air mass class.	Air mass borders	Corr.	Error std. dev.
no	retained	0.848	22.188
no	omitted	0.909	17.797
yes	retained	0.850	20.797
yes	omitted	0.926	16.273

Also ozonesonde measurements were investigated from the EASOE (European Arctic Stratospheric Ozone Experiment), with the aim of a detailed study of the stratosphere to monitor the processes that lead to the decrease of the ozone content. The measurements were taken in a 5-month period during the winter of 1991-1992. From these data and available 31 output files for NOAA-11 it was possible to find 19 TOVS-ozonesonde coincidences, representing 9 stations in the Northern European area (table 3).

Table 3: Ozonesonde stations from EASOE used for the comparisons

STATION	LONGITUDE	LATITUDE
Aberystwyth, Wales (AB)	52.7 N	4.1 W
Athens, Greece (AT)	38.0 N	24.0 E
Gardemoen, Norway (GA)	60.1 N	11.0 E
Hohenpeissenberg, Germany (HO)	47.5 N	11.0 E
Kiruna, Sweden (KI)	67.9 N	21.1 E
Lerwick, Scotland (LE)	60.1 N	1.2 E
Lindenberg, Germany (LI)	52.1 N	14.1 E
Reykjavik, Iceland (RE)	64.0 N	22.6 W
Sodankyla, Finland (SO)	67.4 N	26.6 E

To be comparable to values of other instruments (Dobson or Brewer spectrophotometers, TOMS or TOVS), the integrated ozone amounts calculated from ozonesonde measurements have to be corrected in two steps (Kyro 1989). First, the integrated value X_t has to be increased by the residual ozone contribution above the burst level of the balloon calculated by the formula:

$$x_r = 7.9\, p_{O_3} \qquad (6)$$

where p_{O_3} is the ozone partial pressure in mPa at the burst level. Second, this integrated value has to be corrected by a correction factor depending on the value of the Brewer or Dobson Measurement X_b:

$$C = \frac{x_b}{x_t + x_r}$$

Unfortunately, C was not available for most of the balloon measurements, partly due to the fact that during the arctic winter only focused moon measurements can be performed by the spectrophotometers. Because of this and the small sample size a statistical analysis could not be carried out. However, these soundings were valuable for a qualitative evaluation with special respect to the shape of the ozone profile.

Table 4: Coincident TOVS-ozonesonde measurements. The orbit numbers refer to NOAA-11. Explanation see text.

DATE	UTC	ST.	BURST A.	X_T+X_R	CORR.F.	TOVS	ORBIT	BORDER
27/12/91	10	GA	6.7	203	-	248	16776	no
	11	LE	8.1	230	-	267	16777	no
	11	LI	6.3	318	-	332	16776	no
15/01/92	09	HO	6.9	257	1.045	279	17044	yes
16/01/92	12	KI	3.7	334	-	375	17058	no
	17	SO	12.4	343	-	389	17058	no
17/01/92	06	HO	10.1	239	0.942	274	17066	no
20/01/92	08	HO	5.9	249	1.013	325	17115	yes
27/01/92	11	AB	6.7	284	-	277	17214	yes
	10	GA	10.2	212	-	244	17214	yes
	09	HO	5.6	352	1.169	357	17214	no
	11	LI	15.8	265	-	305	17214	no
	11	RE	8.8	278	-	342	17215	yes
31/01/92	11	LI	8.5	270	-	291	17270	no
	07	HO	5.3	267	1.243	300	17270	no
20/03/92	11	GA	7.3	325	-	329	17962	no
	11	KI	11.3	300	-	407	17962	yes

Table 4 shows all the coincidences. The correction factors given for the Hohenpeissenberg station and those given for Sodankyla by Kyro (1989) are in the interval between 0.95 and 1.25, tending to have a value bigger than one. It is assumed that these data are representative for the other balloon measurements, most of the TOVS retrieval values are acceptable. However, in certain cases the big overestimation cannot be explained in this way (e.g. the TOVS retrievals overestimate the balloon measurements by more than 25%). These cases seem to correspond to measurements at the borders of air masses, where the high variability of the ozone content may lead to big differences if there is no good temporal coincidence. On the other hand, at the borders different air masses may be stratified above each other in a vertical column. This can produce double-peaked ozone profiles, with significant ozone amounts in the lower stratosphere. Such profiles were found, for example, in Reykjavik on 27 January and in Kiruna on 20 March. As was pointed out by Achard (1991), the channel 9 radiance is sensitive to the shape of the ozone profile. Here the secondary maxima, due to the increase of absorption with pressure, produce absorption comparable to that of bigger ozone amount in the higher stratosphere. Since the regression algorithm assumes a climatological single-peaked profile with a maximum at around 25 km, such cases can be expected to be overestimated. The situation is particularly complicated in the case of Kiruna, where the 3I boxes are assigned to four different air masses in a small region around the measurement site. This underlines again the caution required at the evaluation of the retrieval products in such areas.

ACKNOWLEDGEMENTS

We are grateful to Dr. N.A. Scott and Dr. C. Claoud at LMD for the valuable discussions about 3I. We also wish to thank the Pathfinder team at LMD (B. Bonnet, S. Dardaillon, P. Bouster and J. P. Chaboureau) for providing the 3I output files, Dr. Husson for her image display software, the Centre National de Recherches en Météorologie for the Dobson measurement data and Dr. J. Ovarlez for making available the ozonesonde measurements taken by Mr. Reid, Howells, Braathen, Pommerau, Borchers, Gernandt, Cacho, Gil, Kyro, Varotros and Claude. The computations were carried out on the computers of CIRCE (Centre Interregional de Calcul Electronique, CNRS).

REFERENCES

ACHARD V.,1991: Trois problemes cles de l'analyse tridimensionelle de la structure thermodynamique de l'atmosphere par satellite: mesure du contenu en ozone, classification des masses d'air, modelisation hyperrapide du transfert radiatif. PhD dissertation (in French), Universite Pierre et Marie Curie. Available from Laboratoire de Météorologie Dynamique, Ecole Polytechnique, 91128, Palaiseau Cedex, France.

CHEDIN A., N.A.SCOTT, C.WAHICHE, P.MOULINIER,1985: The Improved Initialization Inversion method: a high resolution physical method for temperature retrievals from satellites of the TIROS-N series, J. Clim. Appl. Meteorol., 24,124-143.

CSISZÁR I., L. KOVÁCS,1993: Use of TOVS data in numerical weather prediction at the Hungarian Meteorological Service, Proceedings of the VIIth International TOVS Study Conference.

KYRO E.,1989: Measurement of vertical ozone profile by Vaisala MicroCORA sounding system, Vaisala News, No.120.

LEFEVRE F., D.CARIOLLE, S.MULLER, F.KARCHER, 1991: Total ozone from the TIROS Operational Sounder during the formation of the 1987 ozone hole, J. Geophys. Res., 96,12843-12911.

LIENESCH J.H.,1988: Evaluation of an improved set of predictors for derivation of total ozone from TOVS measurements, J. Atmos. Oceanic. Technol., 5, 625-630.

MA, X., W.L. SMITH, H.A. WOOLF, 1984: Total ozone from NOAA satellites-A physical model for obtaining measurements with high spatial resolution, J. Clim. Appl. Meteorol., 23,1309-1314.

PLANET W.G., D.S.CROSBY, J.H.LIENESCH, M.L.HILL, 1984: Determination of total ozone amount from TIROS radiance measurements, J. Clim. Appl. Meteorol., 23,308-316.

PRABHAKARA C., B.J.CONRATH, R.A.HANEL, 1970: Remote sensing of atmospheric ozone using the 9.6 micron band, J.Atmos. Sci., 26,689-697.

SMITH W.L., H.M.WOOLF, C.M.HAYDEN, A.J.SCHREINER, 1985: The simultaneous retrieval export package. Technical Proceedings of The Second International TOVS Study Conference, Igls, Austria, 18-22 February, 1985, 224-253.

SCOTT N.A., A.CHEDIN, 1981: A fast line-by-line method for atmospheric absorption computation: The Automatized Atmospheric Absorption Atlas, J. Appl. Meteor., 20, 802-812.

UNDEN P., 1982: The Swedish Limited Area Model. SMHI reports, RMK 35.

Author's address:

I. CSISZÁR and L. KOVÁCS
Hungarian Meteorological Service
Satellite Research Laboratory
P.O.Box 32
H-1675 Budapest
HUNGARY
Phone/fax: + 1585/351

MODEL OF CLOUD CLASSIFICATION USING MULTISPECTRAL AVHRR DATA

Department of Regional Forecasts, Institute of Meteorology and Water Management, Kraków, Poland

DANUTA SERAFIN

ABSTRACT

A method of multispectral analysis of satellite data from the Advanced Very High Resolution Radiometer (AVHRR), on the polar orbiting satellites NOAA, is developed at the Department of Regional Forecast in Cracow. The meteorological products derived from digital AVHRR data are presented using the SysVision - image processing system for PC computers. The SysVision system gives the possibility of operational processing and the data handling capacity necessary for a classification of AVHRR data. The cloud classification model is based on a thresholding procedure in a five-dimensional spectral feature space. The classification algorithm has been trained and tested for the central European region in summer season, when the sun elevation is high. Operational tests start at the beginning of 1994.

ZUSAMMENFASSUNG

In der Abteilung für Regionalvorhersage in Krakau wird eine Methode für eine multispektrale Analyse der Daten des Advanced Very High Resolution Radiometer (AVHRR) der Polarbahnsatelliten NOAA entwickelt. Es werden meteorologische Produkte der digitalen AVHRR Daten mittels des SysVision - Bildaufbereitungssystems für PC präsentiert. Das SysVision System bietet die Möglichkeit einer operationellen Aufbereitung ebenso wie die Kapazität, die für eine Klassifikation der AVHRR Daten nötig ist. Das Wolkenklassifikationsmodell basiert auf der Bestimmung von Schwellwerten in einem 5-dimensionalen Raum bestehend aus den Werten der 5 Spektralkanäle. Der Klassifikationsalgorithmus wurde für den Bereich von Zentraleuropa sowie für Sommerdaten mit hohem Sonneneinfallswinkel entwickelt und getestet. Operationelle Tests beginnen 1994.

1. INTRODUCTION

The need for information concerning clouds for climate and forecasting models has increased in the last years. Satellites provide the most suitable data from which an extraction of cloud parameters can be attempted. This is primarily due to their global coverage and temporal continuity. Several authors have developed methods of an automatic cloud classification; methods of derivation of quantitative information about surface and clouds have been tested, they are proving useful in weather forecasting and numerical prediction models. These methods can be separated into two groups:

1) threshold methods (Karlsson and Liljas, 1990) where the cloud detection and analysis are performed on individual pixels using VIS and IR radiance thresholding;

and

2) statistical methods (Ebert, 1992) where these two steps are not performed on each pixel, but globally on image segments, using statistical properties of the VIS and IR radiance.

This paper describes a model for a near–real time cloud classification from digital AVHRR data. The method is based on a thresholding procedure in a five-dimensional spectral feature space. This supervised cloud classification method following almost exactly the Karlsson algorithm, has been tested for Central Europe and is found the most effective in classifying surface and cloud types.

The model forms an important part of the image processing system SysVision, which was created in 1990. The SysVision system works on a PC-386 computer with a SVGA display monitor and offers a wide range of image operations, for example: zooming, quick comparison of images, contrast operations, false colouring. The SysVision permits to calculate from digital data and to display: the brightness temperature in infrared, albedo in visible channels, vegetation index, sea surface temperature, linear function of albedo and temperature from different channels.

2. AVHRR DATA

The AVHRR measures radiance in five spectral bands: two in the visible band (channel 1 → 0.55 - 0.68 μm; channel 2 → 0.73 -1.1 μm), one in the 3.7 μm window region and two infrared window channels (channel 4 → 10.5 - 11.5 μm; channel 5 → 11.5 -12.5 μm), with 1.1 km spatial resolution at the nadir. In order to perform the spectral analysis, the measured radiance is converted into albedo (channels 1, 2 and 3) and brightness temperature (channels 4 and 5). The channel 3 albedo is estimated by subtracting the thermal radiance that would be emitted by a blackbody at the temperature measured in channel 4 from the actually measured radiance. The satellite-measured albedos are normalised by the cosine of the solar zenith angle at each pixel and then scaled with grey levels 0 - 255 representing 0% - 100% respectively.

Supervised training is realised using AVHRR satellite imagery for Central Europe with full spatial resolution; for the classification process data with lower resolution, approximately 4 km (800 x 600 pixels or 640 x 480 pixels dependent on the graphical monitor) are used.

The radiance measured in different channels depends on the characteristics of the object: temperature and reflectivity; it depends also on the following factors:

- sun elevation;
- satellite viewing angle;
- sun-satellite azimuth angle;
- contributions from atmospheric water vapour and aerosols;
- transparency of the object;
- what part of the field of view matches the object.

Some of those factors contribute to the classification solution, others bring some problems. The parameters that are regarded as significant or characteristic for different cloud types are temperature (related to height), reflectivity, transmissivity and emissivity.

3. THE CLASSIFICATION MODEL

The classification process splits up into two parts: training and classifying. The SysVision classification programme allows to perform training with supervision. The analyst selects pixels that represent a chosen class, the system calculates statistics from this sample of pixels and creates a 5 feature signature for the class. The calculated signatures are stored in an actual category file in the database. All defined classes are listed in table 1 and the five-dimensional spectral features are presented in table 2. For each sample in the five-dimensional feature space, the following signatures are computed: maximum and minimum value, standard deviation, median, mean. In using the supervised training, it is possible to create and refine signatures iteratively in order to generate signatures that accurately represent the classes. It is also possible to manipulate the signatures if necessary, for example merge, delete or append signatures from one file to another.

Once a set of reliable signatures has been created and evaluated, the next step is to create the classification algorithm suitable for the season of the year, sun elevation and satellite (NOAA9, NOAA10, NOAA11 and NOAA12). This is the most difficult part of the classification process. The analyst is supported in his analysis by histograms, scatterograms and synoptic charts with cloud observations as ground truth data.

Table 1: Classes of object defined for classification

1.	Sea	11.	Cumulus congestus
2.	Land	12.	Altostratus
3.	Snow	13.	Thin Cirrus over land
4.	Sunglint	14.	Thin Cirrus over sea
5.	Fog over land	15.	Cirrus over clouds
6.	Fog over sea	16.	Cirrostratus
7.	Stratus	17.	Nimbostratus
8.	Stratocumulus	18.	Small Cumulonimbus
9.	Cumulus over land	19.	Cumulonimbus
10.	Cumulus over sea	20.	Not identified

Table 2: Features used in the cloud classification model.

1.	Albedo ch.1	(A1)
2.	Albedo ch.2 - Albedo ch.1	(A2-A1)
3.	Albedo ch.3	(A3)
4.	Brightness temperature ch.4	(T4)
5.	Bright. temp. ch.3 - Bright. Temp. ch.4	(T3-T4)

The algorithm performs a classification of data according to a decision rule. Each pixel is analysed independently. Pixels satisfying the criteria that are established by the decision rule are then assigned to the class relevant for that signature. At present, SysVision provides a parallelepiped decision rule. In the future, other commonly used decision rules will be added: minimum distance and maximum likelihood.

4. RESULTS

The classification model has been tested on AVHRR imagery for the summer season with high sun elevation. The analysis of the imagery permits to create the optimum classification algorithm which maximises the separability of the classes. It is difficult to establish the skill of the human analyst in correctly identifying surface and cloud types. The verification of the classification model described by Ebert (1987) appears to be the best and will be used for the current model in the future. The successive steps in the classification procedure are summarised in table 3.

Table 3: Scheme of the steps in the classification procedure for summer with a high sun elevation angle.

STEP	CLASS SEPARATION	FEATURES
1.	Land / (Sea+Clouds)	(A2-A1)
2.	Sea / Clouds	(A1), (T3-T4)
3.	Water clouds / Ice clouds	(A3)
4.	(St+Cu+Sc) / (Ns+Cb)	(T4)
5.	St / Cu / Sc	(A1)
6.	Ns / Cb	(A1)
7.	Ac / (Ci+Cs+Cb)	(T4)
8.	Ci / Cs / Cb	(A1)

The first threshold classifies the whole imagery (with lower resolution) into two object classes: "land" and "sea+clouds+snow" using feature (A2 - A1). The comparison of the albedo measured in channels 1 and 2 provides the best tool for the identification of cloud free land pixels. Thresholds of the features (A1) and (T3 - T4) are then used to classify all clouds. The difference in brightness temperature (T3 - T4) is useful for the identification of Ci clouds (Allen et al, 1990). In the next step low, middle and thick clouds are separated by using (T4) values. The temperature of middle layer cloud tops lies between the 700 hPa and 500 hPa level temperatures. Water clouds with small particles and sunglint have a very high value of the (A3) feature. Thick Ci , Cs over clouds and Cb are separated using the A1 feature. The algorithm fails to find small amounts of cumulus over land. The classes most difficult to identify with the algorithm are the high cloud overlying low clouds and thin Ci over land/water.

Figure 2 presents an example of cloud type classification maps derived by the method from the multispectral AVHRR image. The case study has been performed on the 04 June 1992 pass of NOAA11. Figure 1 shows channel 2 analysed image.

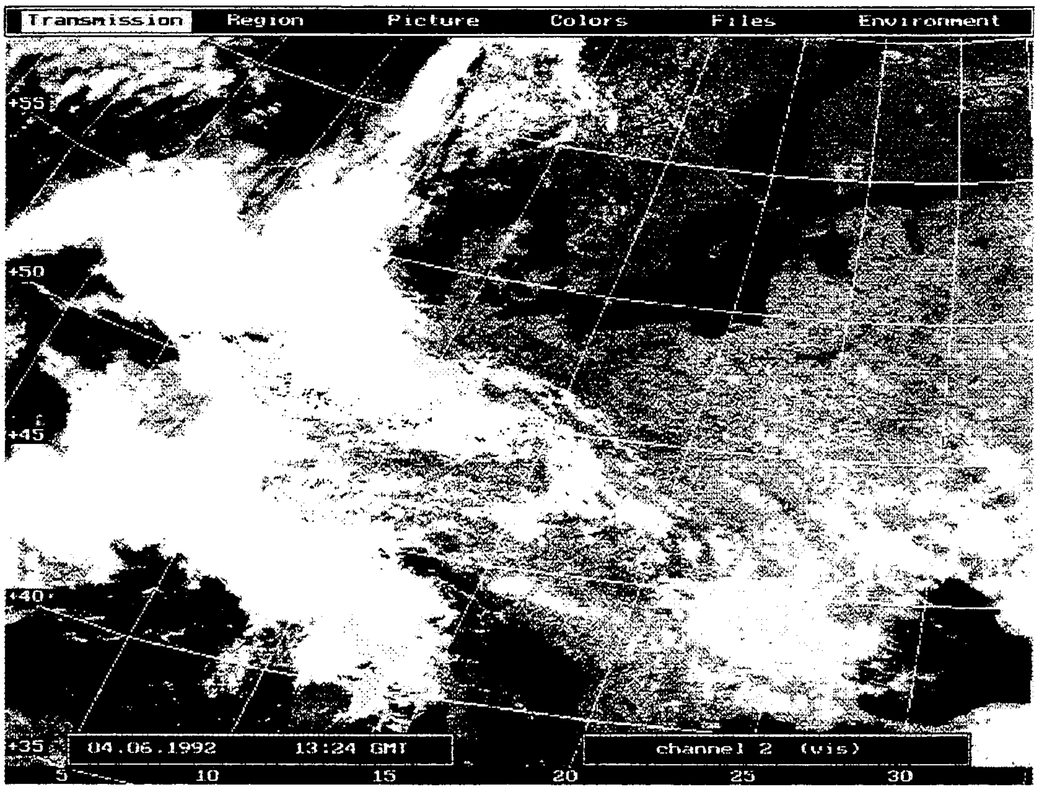

Figure 1: Channel 2 image for NOAA11 AVHRR, 13.24 GMT 04 June 1992.

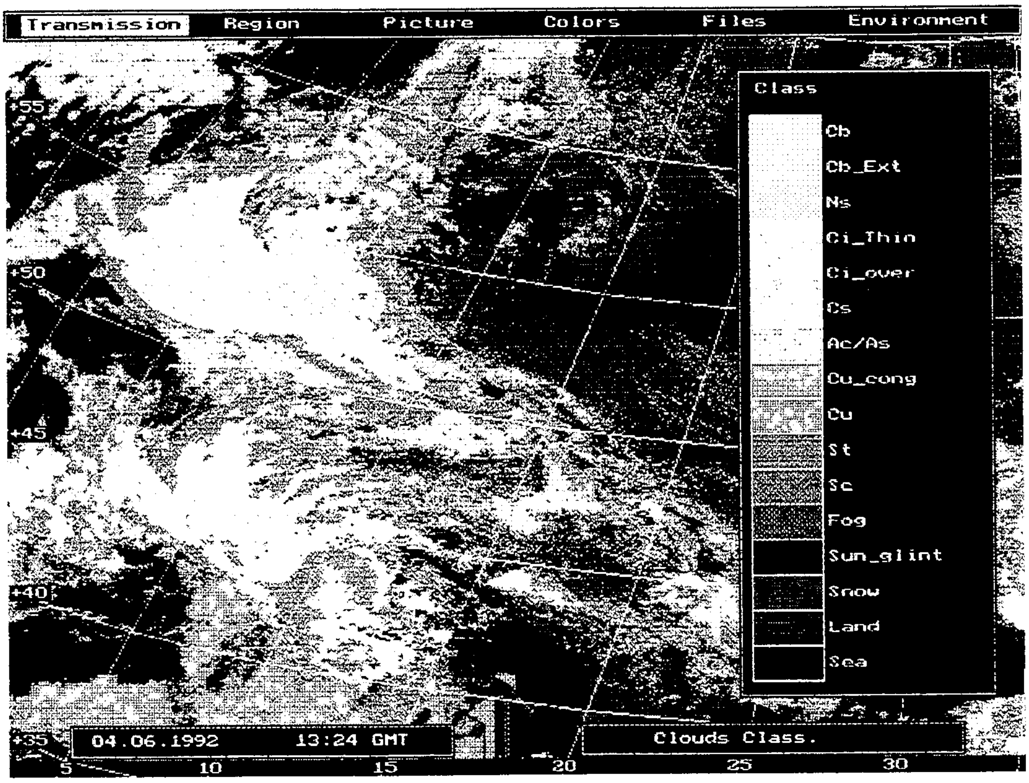

Figure 2: Cloud classification for NOAA11 AVHRR, 13.24 GMT 04 June 1992.

5. DISCUSSION

For the cloud type classification a threshold technique has been applied to the five-dimensional AVHRR data. Although dynamic cluster methods are also applicable, they are too much consuming the computer time to be operationally used (Desbois et al.,1982). On the other hand, the threshold method is adversely affected by partial cloudiness within the field of view. The threshold technique offers the reasonable compromise between efficiency and accuracy and has been used for cloud classification with AVHRR data. The success of a multispectral classification depends on how well it is possible to compensate for diurnal and seasonal variations of radiance. When some temperature information is added and the model takes into consideration the prevailing sun elevations, such a model is believed to offer good perspectives.

Cloud information (such as cloud cover, cloud type, and cloud organisation) retrieved from satellite observations over areas where no conventional observing system is available is very effective for studies of climatology and large scale aspects of atmospheric dynamics. The classification of clouds has many important applications, including studies of the heat budget of the earth-atmosphere system, convective activity and rainfall estimation.

REFERENCES

ALLEN R.C., P.A.DURKEE and C.H.WASH, 1990: Snow/Cloud Discrimination with Satellite multispectral measurements, J.Appl.Meteorol., **29**, 994-1004.

DESBOIS M., G.SEZE and G.SZEJWACH, 1982: Automatic classification of clouds on METEOSAT imagery, J.Appl.Meteorol., **21**, 401-412.

EBERT E.E., 1987: Pattern recognition Technique for distinguishing surface and cloud types in the polar region., J.Climate Appl.Meteor., **26**, 1412-1427.

EBERT E.E., 1992: Pattern recognition analysis of polar clouds during summer and winter., Int.J.Remote Sensing, **13**, 97-109.

KARLSSON K.G. AND E.LILJAS, 1990: The SMHI model for cloud and precipitation analysis from multispectral AVHRR data, Internal Report SMHI, Nr 10.

Author's address:

DANUTA SERAFIN
Institute of Meteorology and Water Management
Dep. of Regional Forecasts
ul. P. Borowego 14
30-215 Kraków
POLAND

TEMPERATURE PROFILE DERIVED FROM HIRS SOUNDING DATA

Department of Regional Forecasts, Institut of Meteorology and Water Management, Kraków, Poland

BOŻENA ŁAPETA

ABSTRACT

The paper presents methods of determining vertical temperature profiles from HIRS data, as carried out in the Department of Regional Forecasts in Cracow. Smith and Chachine iterative schemes have been investigated and the more effective one will be applied operationally. A comparison of satellite profiles and upper-air soundings for some ground stations has been performed and the very first results are depicted.

ZUSAMMENFASSUNG

Der Bericht zeigt Methoden für die Bestimmung vertikaler Temperaturprofile aus HIRS Daten, wie sie in der Abteilung für Regionalvorhersage in Krakau durchgeführt werden. Die Iterationsmethoden von Smith und Chachine wurden auf ihre operationelle Effektivität hin untersucht. Ein Vergleich von Satelliten- und Radiosondenprofilen wurde für einige Stationen durchgeführt, und erste Ergebnisse wurden abgeleitet.

1. INTRODUCTION

Temperature profiles are of great importance both for improving operational weather forecasting and for a retrieval of such atmospheric parameters as e.g. total ozone content.

Temperature sounding from polar orbiting satellites is currently performed by the TIROS Operational Vertical Sounder which consists of three instruments: High-resolution Infrared Radiation Sounder (HIRS), Microwave Sounding Unit (MSU) and Stratospheric Sounding Unit (SSU). HIRS data allow to determine temperature profiles for clear and partly clear spots. For the remaining spots, either no retrievals are made or the MSU data are used to determine temperature in the upper atmosphere.

This paper describes studies concerning vertical temperature profile retrievals from HIRS data for clear areas, which are carried out in the Department of Regional Forecasts in Cracow.

2. DATA

The characteristics of the HIRS unit are summarised by Smith et al. (1979) and described in detail by Schwalb (1978). In this work the first eight HIRS channels are used.

The radiative transfer equation, which forms the base for remote sensing retrieval, assumes that there are no clouds in a satellite field of view, which is not always true. To identify clear areas, radiances are subjected to the surface temperature test and are processed until they give an approximation to those radiances that would be observed in a clear atmosphere, McMillin and Dean (1982).

A grid of 250 km mesh size has been selected as nominal horizontal spacing for temperature soundings. To achieve that, a single sounding is derived from 9 x 7 individual HIRS fields of view (FOV). These boxes contain 9 FOVs across and 7 along the satellite track. For the clear radiances test, individual FOVs are taken into consideration and the clear radiance for the box is obtained by averaging from these fields of view, which have been determined to be clear. If it is too cloudy, no temperature profile is calculated.

3. METHOD

The TIROS Operational Vertical Sounder measures the outgoing radiance in several spectral channels. This can be described by the radiative transfer equation

$$i=1,2,\ldots M \qquad I_i = B_i(T_s)\tau(p_s) + \int_{p_s}^{0} B_i(T)\frac{\partial\tau_i(p)}{\partial \ln p}\, d\ln p \qquad (1)$$

where $I_i = I(\upsilon)$ is the spectral radiance, $B_i(T)$ the Planck function at wave number υ and temperature T(p), p the pressure, τ the atmospheric spectral transmittance from any given level to the top of the atmosphere, T_S the surface temperature and p_S is the surface pressure. For a given set of radiance measurements it would be possible to obtain the temperature profile by solving Eq.(1). Unfortunately, there is no unique solution for a detailed profile for at least two reasons: (1) the observations contained in a set of spectral radiances are not vertically independent, and (2) measurements of outgoing radiance contain errors. Hence, some analytical approaches must be used, Smith (1985).

For the studies under consideration two non-linear solutions proposed by Chachine respectively Smith were applied.

In the Chachine method (1968,1970), by using the mean value theorem and assuming that the contribution to the outgoing radiance of the term $B_i(T_S)$ is (dependant on υ) dominant or negligible, the relaxation equation (3)

$$\frac{\tilde{I}_i}{I'_i} \approx \frac{B_i(T(p_i))}{B_i(T'(p_i))} \tag{2}$$

is obtained, where $T'(p_i)$ is a "guess" temperature profile, p_i the pressure at the level where the weighting function peaks and $\tilde{I}_i$ the radiance measured by the satellite. This leads to the formula

$$B_i(T^n(p_i)) = B_i(T^{n-1}(p_i))\frac{\tilde{I}_i}{I_i^{n-1}} \tag{3}$$

The main disadvantage of the Chachine method is that the number of levels for which temperature is calculated is the same as the number of radiance observations and if the retrieval is not stopped at the point where the convergence criterion is satisfied, the solution will become unstable. The advantage is that the method is rather easy to be programmed and does not require a lot of computer memory.

The generalisation of the Chachine scheme was proposed by Smith. Smith (1970) suggested a solution in which, instead of (2), equation (4) is used:

$$i = 1, 2, \ldots, M;\ j = 1, 2, \ldots, N \qquad B_i(T^n(p_i)) = B_i(T^{n-1}(p_i)) + \tilde{I}_i - I_i^{n-1} \tag{4}$$

where N is the number of the pressure levels.
Then, the temperature at any pressure level can be obtained from:

$$T^n(p_j) = \frac{\sum_{i=1}^{M} T^n_{ij} W_{ij}}{\sum_{i=1}^{M} W_{ij}} \tag{5}$$

where W_{ij} is a weight function that can be modified to provide the best solution.
In contrary to the Chachine scheme, (5) allows to solve for a correct temperature at all levels from the radiance residual in each channel and no interpolation is required. Moreover, the solution is stable in the averaging scheme (5) and one does not have to know the measurement noise.

To calculate the atmosphere transmittance the Smith polynomial representation of carbon dioxide and water vapour transmission, Smith (1969) were chosen. These species are the main absorbents in the chosen HIRS channels.

4. RESULTS

The described schemes have been applied to invert radiance data coming from satellites NOAA 11 and NOAA 9 to temperature profiles. The studies have been done for a few ground stations and for different days. In this paper very first results are presented briefly.

Figure 1 shows the comparison between upper-air sounding temperature profiles and those computed from satellite data, for a corresponding area, by using Chachine respectively Smith schemes.

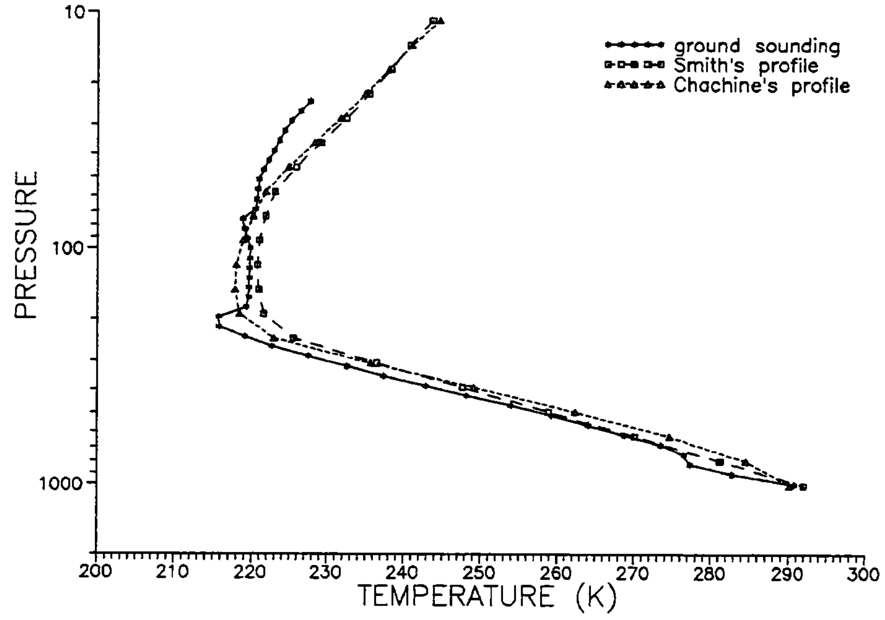

Figure 1: Ground based temperature profile and satellite profiles from NOAA-11 for stations 12425 (01 July 1993)

The US Standard Atmosphere profile, McClatchey et al. (1972), has been used as the initial temperature profile for both methods.

The accuracy of satellite estimations seems to be satisfying but one can easily notice that there are two regions of large errors: the upper stratosphere and the tropopause. The poor accuracy in the upper atmosphere results from the fact that the initial (or mean) profile is not representative of the profiles retrieved at those pressure levels, (Fleming and Smith, 1971).

The tropopause region has always been a difficulty for the remote sensing retrieval of a satisfactory temperature profile, and the problem is very hard to overcome with the poor vertical resolution provided by the weighting functions.

The good accuracy obtained at the surface results from the application of the surface temperature in the retrievals.

Figures 2 and 3 show the different satellite profiles computed for two different initial conditions, for Smith and Chachine schemes, respectively. The standard profile means the US Standard Atmosphere profile and the summer profile corresponds to the mean profile for mid latitude summer, McClatchey et al., (1972).

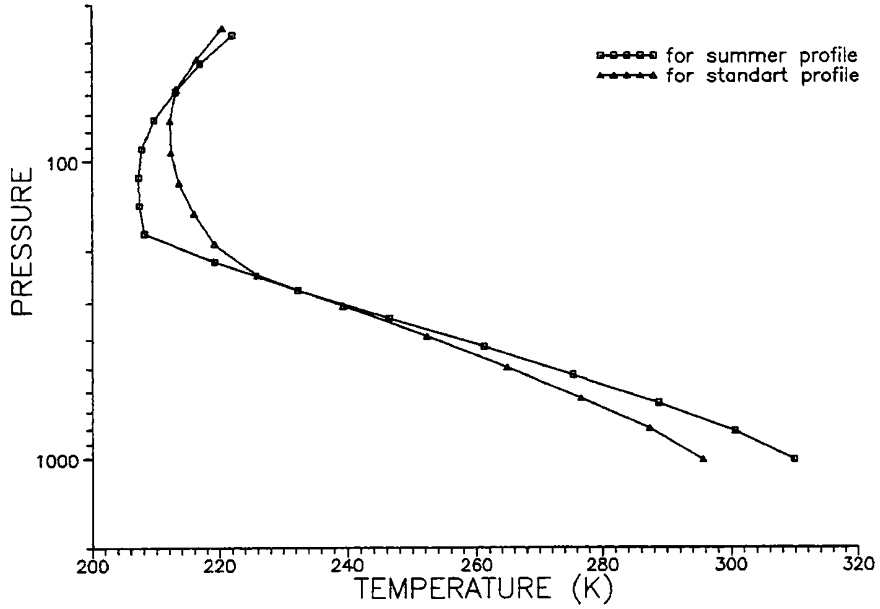

Figure 2: Comparison between Smith's profiles obtained for two different initial profiles (10 May 1993, NOAA 9)

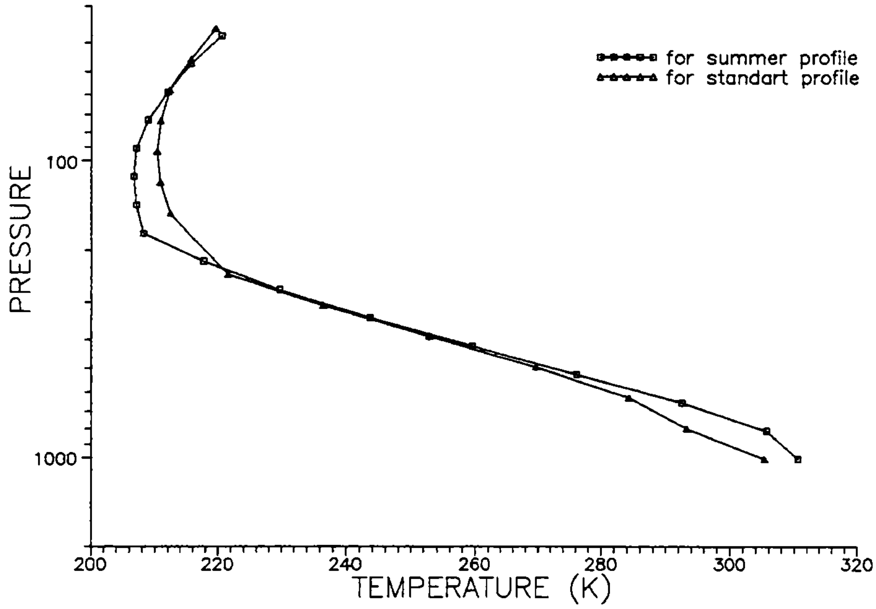

Figure 3: Comparison between Chachine's profiles obtained for two different initial profiles (10 May 1993, NOAA 9)

Significant differences are seen immediately at the tropopause level and near the ground, that corresponds to the problems discussed above (in this case the surface temperature has not been taken into account). It also suggests that a more accurate initial profile might improve the results of the temperature retrievals in these regions.

5. CONCLUSIONS

This paper describes the state of research in temperature profile retrievals based on the HIRS satellite data carried out in the Department of Regional Forecast in Cracow. It also presents very first results of these studies. The comparison between Chachine and Smith methods shows that the generalisation scheme is more useful for operational applications as it does not require interpolation and is more stable.

Obviously, further analysis concerning a data base of the initial profiles should be performed. This will lead to a better solution of the inverse problem as the initial profile plays the crucial role. Next, an operational procedure for the temperature profile retrievals for cloudless areas will be elaborated.

REFERENCES

CHACHINE M.T., 1968: Determination of the temperature profile in an atmosphere from its outgoing radiance., J.Opt.Soc.Amer., **58**, 1634-1637.

_____ 1970: Inverse problem in radiative transfer: determination of atmosphere parameters., J.Atm.Sc., **27**, 960-967.

FLEMING H.E., W.L.SMITH, 1971: Inversion techniques for remote sensing of atmospheric temperature profiles. In Reprints, Fifth Symposium on Temperature. Pittsburgh: Instrument Society of America.

McCLATCHEY R.A. et.al., 1972: Optical properties of the atmosphere. Air Force Cambridge Research Lab. Res. pap., **411**.

McMILLIN L.M., C.DEAN, 1982: Evaluation of a new operational technique for producing clear radiance., J.Appl.Met., **21**, 1005-1014.

SCHWALB A., 1978: The TIROS-N/NOAA A-G satellites series., NOAA Tech. Memo. **NESS 95**, Environmental Science Information Centre (D822), Environmental Data Service, NOAA, 75pp.

SMITH W.L., 1969: A polynomial representation of carbon dioxide and water vapour transmission., ESSA Technical Report NESC **47**, 20pp.

_____ 1970: Iterative solution of the radiative transfer equation for the temperature and absorbing gas profiles of an atmosphere., Appl.Opt.,**9**, 1993-1999.

_____ 1985: Satellites. In: Houghton,D.D., Handbook of Applied Meteorology, John Wiley & Sons, 380-472.

_____, H.M. Wolf, C.M. Hayden, D.Q. Wark and L.M. McMillin, 1979: The TIROS-N operational vertical sounder., Bull.Amer.Meteor.Soc.,**60**, 1177-1187

Author's address:

BOŻENA ŁAPETA
Department of Regional Forecasts
Institute of Meteorology and Water Management
ul. P. Borowego 14
30-215 Kraków
POLAND

COMPUTATION OF CLOUD TOP HEIGHT BY MEANS OF DATA FROM THE SATELLITE METEOSAT

Slovak Hydrometeorological Institute, Bratislava, Slovakia

JAN KAŇÁK

ABSTRACT

The method of Cloud Top Height Computation by means of the total radiation measured by the satellite at the wave length 6.7 µm (Water Vapour channel of Meteosat) and the known shape of the contribution function, which is computed on the basis of the radiation theory and measured temperature and humidity profiles, is presented in this article. The results obtained in experimental conditions are discussed and a possibility to specify the emissivity of cloudiness at the wave length 11.1 µm (Infrared channel of Meteosat) by means of cloud top height is mentioned, too.

ZUSAMMENFASSUNG

Der Artikel präsentiert die Methode zur Bestimmung der Höhe der Wolkenobergrenzen mittels der Gesamtstrahlung, die der Satellit im Wellenlängenbereich 6.7 µm (Wasserdampfkanal von Meteosat) mißt, sowie der bekannten Form der "contribution function" (bestimmt aufgrund der Strahlungstheorie mit gemessenen Temperatur- und Feuchteprofilen). Die unter experimentellen Bedingungen erhaltenen Ergebnisse werden diskutiert und die Möglichkeit aufgezeigt, die Emission der Bewölkung im Wellenlängenbereich von 11.1 µm (Infrarotkanal von Meteosat) mit Hilfe der Höhe der Wolkenobergrenze zu bestimmen.

1. INTRODUCTION

Usually for the computation of Cloud Top Height (CTH) the data from IR channel together with aerological measurements are used. In the case of optically thick clouds (Cu cong., Cb, Ns) CTH is given by the height of the pressure level, the temperature of which is equivalent to the radiation temperature in IR channel. Thin clouds are over-radiated by lower surfaces and it is necessary in the first step to correct their radiation temperature by means of emissivity (e). This parameter is added interactively from other data (e.g. image of VIS channel) by a meteorologist.

This method is rather elaborate for larger territories and it needs long-time experience.

The WV channel is chosen in the water vapour absorption band. It is supposed that in this part of the electromagnetic spectrum clouds (except thin cirrus) act as black bodies and radiation temperature correction is not necessary.

At the SHMI there is a sufficiently precise model for the computation of atmospheric radiances for IR wavelength (1-15 µm) in use. Based on processed aerological measurements the developed program computes CTH from the WV channel and the emissivity in the IR channel from the CTH.

2. PHYSICAL PRINCIPLE

The contributions of the single layers of the clear atmosphere to the total radiance measured by the radiometer sensor are characterized by the contribution function C (log p)

$$C(\log p) = \int_{\lambda_1}^{\lambda_2} A(\lambda).B(\lambda,T).\frac{t(\lambda,\log p)}{\log p}.d\lambda \qquad (1)$$

where:		
	C (log p)	contribution function of the layer around the pressure level p
	A (λ)	spectral sensitivity of WV channel (filter function)
	B (λ,T)	Planck function
	t (λ,log p)	atmospheric transmittance from the pressure level p up to the satellite sensor
	p, T	pressure and temperature in a given level
	λ_1, λ_2	limit wave lengths of the WV channel.

In the case of the cloud top at pressure level p_c the cloud cuts off the contribution function and only the radiation from this cloud surface and from the atmospheric layers above reaches the sensor (figure 1). Then,

$$N_c = \int_{\lambda_1}^{\lambda_2} A(\lambda).B(\lambda,T_c).d\lambda + \int_{p_c}^{0} C(\log p).dp \qquad (2)$$

where N_c is the radiance measured by the satellite.

If the measured radiance is known the height of a cloud top level can be determined.

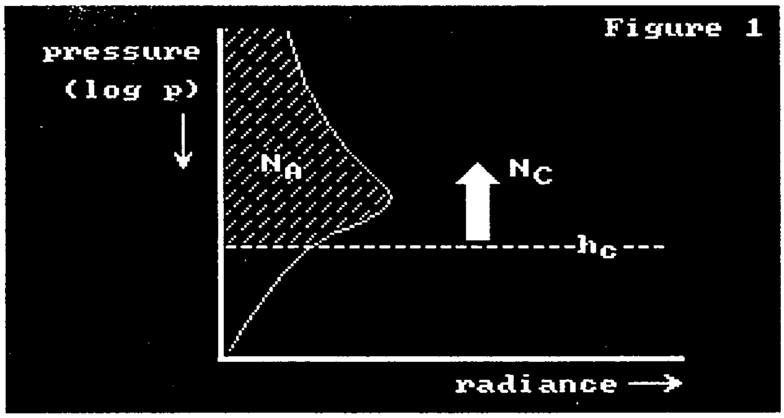

Figure 1: Influence of a cloud upon the radiance in the WV channel
C (log p) - contribution function of the atmosphere
N_A - measured radiance of the atmosphere above a cloud
N_C - radiance of a cloud surface
h_c - cloud top height

In the spectral portion of the IR channel the majority of clouds is over-radiated by radiation from the surface. The measured radiance M_c has two components: one from the cloud surface - $N_{IR}(T_c)$ and one from the earth's surface - $N_{IR}(T_S)$ (figure 2)

$$M_C = e_{IR}.N_{IR}(T_C) + (1 - e_{IR}).N_{IR}(T_S)$$

where e_{IR} is the emissivity which can be expressed as follows:

$$e_{IR} = \frac{N_{IR}(T_S) - M_C}{N_{IR}(T_S) - N_{IR}(T_C)} \tag{3}$$

The amount of the emissivity is given by the microstructure and the thickness of the cloud layer.

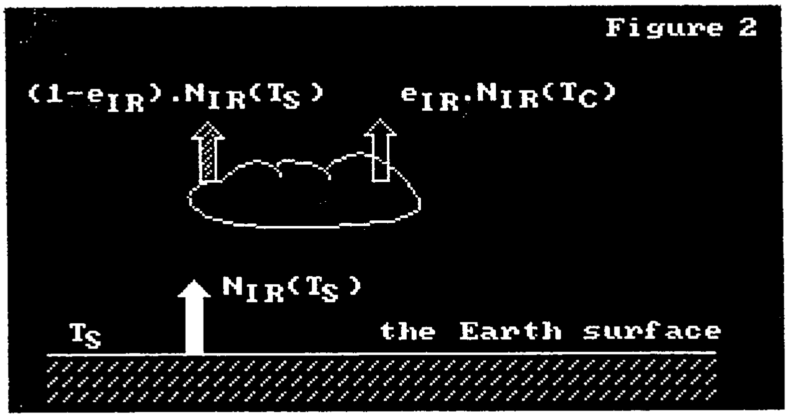

Figure 2: Influence of a cloud on the radiance in IR channel
N_{IR} (T_C), T_C - radiance, resp.temperature of CTH
N_{IR} (T_S), T_S - radiance, resp.temperature of the earth surface
e_{IR} - cloud emissivity

3. COMPUTATION

From the aerological measurements every 6 hours data on the temperature and moisture profile of the atmosphere are available. The area of interest 1024x1024 km^2 (Central Europe) is divided into regions around the stations which have provided sounding data. For every region a temperature and moisture profile is computed.

The atmosphere in the model is divided into 40 levels from which the lower twenty ones (troposphere) are used for this topic. Besides this, the model gives the possibility to compute the influence functions in the spectral interval of the WV channel and of their partial sums N^i

$$N^i = \Sigma_{k-1}^{i} C(\log p_k).\Delta p_k$$

where:

p_k	pressure level in the centre of kth layer
Δp_k	layer thickness expressed by means of pressure

The radiance N_C measured by the satellite is after a correction in respect to noise, compared with the partial sums. In the case of

$$N^i < N_C < N^{i+1}$$

the CTH (=h_C) is computed by interpolation of the heights h^i of the pressure levels

$$h_C = h^i - \frac{N_C - N^i}{N^{i+1} - N^i}.(h^i - h^{i+1}) \tag{4}$$

where: h_i, N_i - height, resp. radiance of ith pressure level.

The CTH computed in such way is compared to the temperature profile; the temperature T_C of the cloud surface is derived and the radiance in the IR channel is computed. Together with the temperature of the earth's surface, computed from ground measurements, the emissivity of the cloud can be computed using (3).

The results are in form of image files, which can be displayed by means of an interactive graphic system in various configurations. Most frequently an output is used which is divided into four quadrants. The original IR and VIS images of Meteosat, cloud top heights and emissivities.

The whole software was developed in FORTAN 77 and runs under the RSX11 operating system.

4. RESULTS

The CTH determination is influenced by maximum and shape of the contribution function in the WV channel, as well as by the quality of the given temperature and moisture profiles. The exact calibration of the WV channel is very important, too.

In well developed convective systems the results are similar to the CTH determined from the IR channel only (based on the assumption that $e_{IR} = 1$) as well as similar to the results of radar measurements. In other situations the method computes heights which differ from those of radar respectively visual observations from aircrafts. As is the case for all satellite methods there is a negative influence by the presence of thin cirrus clouds. They reduce the values of radiances in all channels, but they are difficult to recognize. This may be one reason for the mentioned differences between satellite and non-satellite measurements.

Another reason may be that separate methods work with radiance of various origins (heat radiation, scattered solar and radar radiation) and thus contain other microstructure characteristics of a cloud which probably lead to differently defined CTHs. It is obvious that all inaccuracies which are caused by only partial cloud cover of a pixel or by multi-layered cloudiness are important, too.

The determination of the IR emissivity can also be used as a test of the method. Considerable inaccuracies should lead to meaningless values of emissivity, because data from IR and WV channels are independent from the point of view of measurement as well as of calibration.

REFERENCES

YEARBOOK of WMO AC for Very Short-range Weather Forecasting SHMI, Bratislava, 1988, p. 7 - 8

Author's address:

JAN KAŇÁK
Slovak Hydrometeorological Institute
Centre for Radar and Satellite Meteorology
835 15 Bratislava
SLOVAKIA

STATUS REPORT OF SATELLITE METEOROLOGY RADAR METEOROLOGY AND NOWCASTING

Part I: SATELLITE METEOROLOGY

Hydrometeorological Institute of Slovenia, Ljubljana, Slovenia

JASNA VEHOVAR

ABSTRACT

The existing satellite system at the Hydrometeorological Institute of Slovenia is described and future plans are mentioned.

ZUSAMMENFASSUNG

Das derzeitige Satellitensystem am Hydrometeorologischen Institut Sloweniens wird beschrieben und zukünftige Pläne werden erläutert.

Part I: SATELLITE METEOROLOGY

I.1 ACTUAL STATE

At the Hydrometeorological Institute of Slovenia, satellite data from METEOSAT geostationary meteorological satellite are received by means of a Secondary Data User Station (SDUS). The use of satellite data for further applications is limited because the satellite images received as an analog signal and cannot give the information about absolute pixel values. It only gives information about location and approximate intensity of cloud phenomena.

A signal received by SDUS is digitized and written into BMP format, which is sent to the data base at the Micro VAX. In this way more than one user can receive the image at the same time. The images are visualized at PCs, which are connected to Micro VAX through Ethernet (PCSA) to enable a quicker transfer of satellite images. The software for satellite image presentation is a Microsoft Windows application whith this software it is possible to choose among three spectral channels of satellite data - Infra Red, Visible and Water Vapour. The resolution of the full image is 1000 x 800 pixels, but it is possible to enlarge a detail of the image with a zoom facility. In the zoom mode the resolution of the image remains unchanged, because it is limited by the resolution of the received analog image. An animation loop of a sequence of images is also supported. At the Micro VAX all images of the last day are accessible.

I.2 SATELLITE/RADAR COMBINATION

In the future, satellite and radar data will be combined to estimate regions of precipitation in the satellite image, but before this, a change from a SDUS to a PDUS has to take place. Hopefully a PDUS will be installed in the beginning of 1994.

The fundamental algorithm which will be used for the combination is taken from A. Bellon et al., 1980. It consists of two bivariate frequency distributions from visible and infrared images, colocated with simultaneous radar data in order to discriminate between raining and no-raining clouds. Remapped visible and infrared digital picture and corresponding radar maps form the data base. The radar enables an identifcation of raining (R_R) from the non-raining(R_{NR}) points. For each R_R, the corresponding values (V_R) on the visible and (IR_R) on the infrared image are located. The set (IR_R, V_R) becomes the subscript of a contingency matrix in which all the R_R points are accumulated. Similarly, the pair (IR_{NR},V_{NR}) provides the coordinates of the no-rain matrix for all the radar echo-free points R_{NR}.

These two arrays of bivariate frequency distribution in infrared-visible space are then combined to yield a probability of rain distribution as a function of infrared and visible values, expressed as:

$$PR(IR,V)=\frac{R_R(IR,V)}{(R_R(IR,V)+R_{NR}(IR,V))}$$

R_R(IR,V) is the number of occurences of rain with associated (IR,V) magnitudes and the denominator represents the total number of points in each (IR,V) interval. The above empirical relationship, derived from (IR,V) values within radar range is then assumed to apply over the entire domain of the satellite image. Thus, the underlying assumption used in extracting rain information from satellite data is that those clouds that are thick (i.e., of intense visible brightness) in comparison with their height (as inferred from infrared counts) possess a greater probability of producing rain (from A. Bellon et al, 1980).

For implementation of this algorithm more than one radar would probably be needed. This will be possible by exchanging radar data with surrounding countries, which is planned to start at the end of 1994.

REFERENCES

A. BELLON, S. LOVEJOY and G. L. AUSTIN, 1980: Combining Satellite and Radar Data for the Short-Range Forecasting of Precipitation. Mon. Wea. Rev., 108, 1554-1566.

Author's address:

JASNA VEHOVAR
Hydrometeorological Institute of Slovenia
Meteorological Research Department
Vojkova 1B 61000 Ljubljana
SLOVENIA
Phone.: 386 61/327 461
Fax: 386 61/320 466

CONTRIBUTIONS TO SATELLITE AND RADAR
METEOROLOGY IN CENTRAL EUROPE

SOME ASPECTS OF RADAR METEOROLOGY IN THE CEI-COUNTRIES

OPERATIONAL WEATHER RADAR DATA IN AUSTRIA

**Central Institute of Meteorology and Geodynamics,
Vienna, Austria**

ALEXANDER JANN

ABSTRACT

The article gives an overview of the current Austrian weather radar system. The most important problems are caused by the orography and the method used to reduce the volume of the radar data. The consequences for a few applications are briefly discussed.

ZUSAMMENFASSUNG

Es wird ein Überblick über das operationelle österreichische Wetterrardarsystem gegeben. Probleme ergeben sich einerseits durch die ausgeprägte Orographie in Österreich, andererseits dadurch, daß durch eine Reduktion der Datenmenge ein großer Teil der von den Radars gemessenen Information verloren geht. Als Konsequenz ergibt sich mangelnde Eignung für bestimmte Anwendungen, wie z.B. die Ableitung von Niederschlagsmengen. Von Ombrographendaten können hierfür bessere Ergebnisse erwartet werden. Hingegen ist mit Ausnahme von Westösterreich (Vorarlberg, Nord- und Osttirol, Pinzgau) bei qualitativen Aussagen das Radar durch die bessere räumliche Auflösung im allgemeinen überlegen.

1. INTRODUCTION

At present, the Austrian radar network consists of 4 C-band radars whose locations are: near the airport Wien-Schwechat, near Salzburg, on the Zirbitzkogel in Styria, and on the Patscherkofel near Innsbruck (figure 1). The radar network was designed for the detection of severe weather conditions, which could be dangerous to aircrafts, and it is doubtless appropriate for this purpose. A successful extrapolation of the movement of thunderstorm cells associated with intense rainfall has been reported by Hailzl (1989).

A study about other applications of the Austrian operational radar data has been carried out by Jann (1993). One question was the suitability of the radar data for the derivation of rainfall rates. The present article chiefly recapitulates the most important points of that study.

Figure 1: Locations of the 4 Austrian operational weather radars. It is noteworthy that the altitudes of the radars Zirbitzkogel and Patscherkofel are 2372m and 2454m, respectively.

2. DATA PROCESSING

The rainfall rate R (in mm/h) is derived from the radar reflectivity Z (in mm^6m^{-3}) using the well-known Marshall-Palmer relationship

$$Z = 200\, R^{1.6}$$

The whole range of radar reflectivities respectively corresponding rainfall rates is subdivided into 8 categories including category 0, which represents no rain (see the scale in figure 2).

R is transformed into the corresponding category code already at the radar site. The idea behind this approach is to reduce the data volume that needs to be transmitted. Toward the same aim, the maximum projection method is applied, i.e. only the maximum intensity in x-, y- and z-direction is transmitted. There is no possibility of an access to the full three-dimensional information or to the reflectivity values. This, of course, drastically limits the possible accuracy of any quantitative evaluation, which is discussed later on in section 4.3.

3. AVAILABLE PRODUCTS

Every 10 minutes, each radar produces an image. The horizontal resolution of the images is 2 km, vertical resolution is 1 km. Displayed is a ground view containing the maximum codes of the vertical columns. Two side views show the maximum signals observed in the horizontal columns, the latter running approximately north-south or east-west, respectively. The side views allow the height assignment of the most intense precipitation events. Besides the single images, a composite image combining the information from all 4 radars is available (figure 2). If a point is covered by two or more radars, the maximum measured category code is displayed in the composite image.

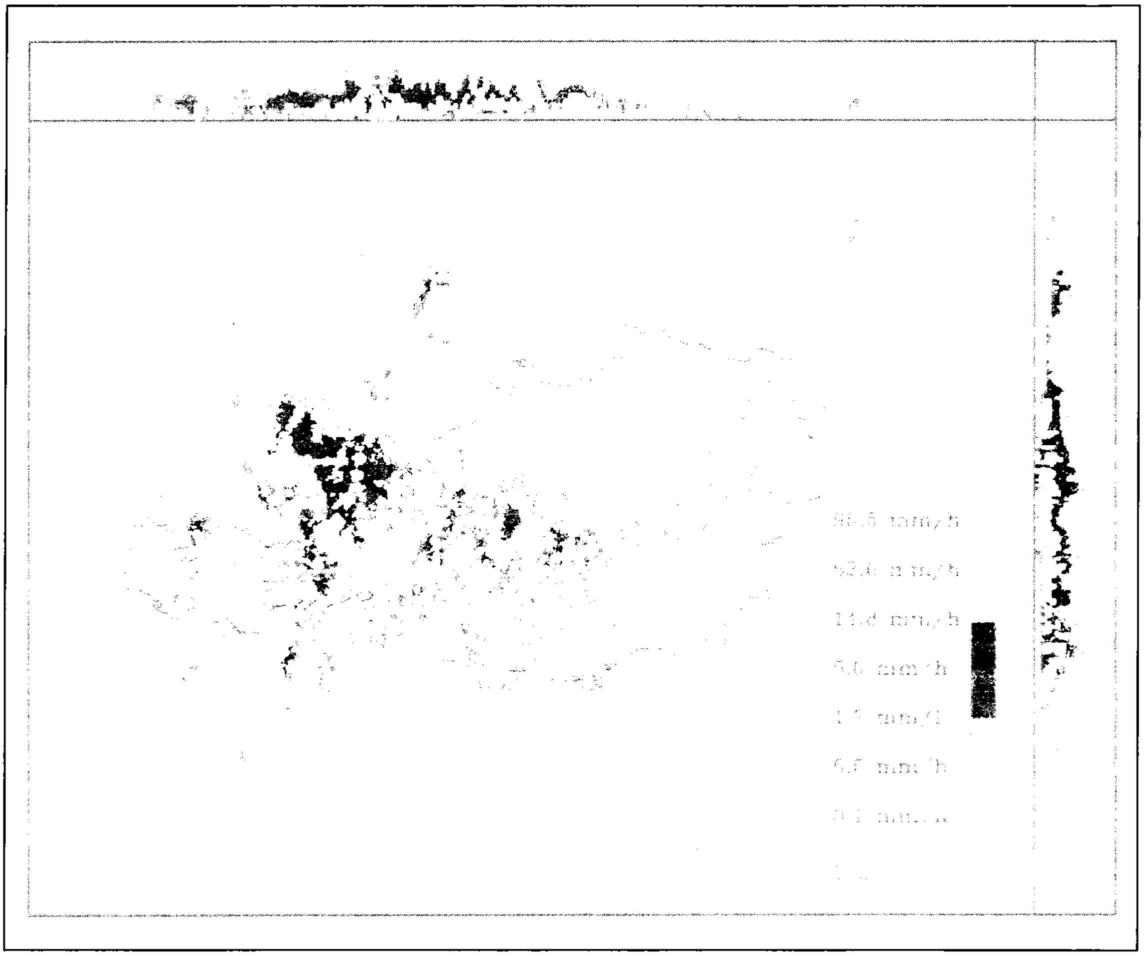

Figure 2: Austrian composite radar image from July 22nd, 1992, 15.55 UTC.

4. PROBLEMS

For a thorough discussion of possible errors of radar measurements, see Clift (1985). Here, only those difficulties are described which are more momentous in Austria than in most other countries.

4.1 CLUTTER

Two radars (Salzburg, Patscherkofel) are equipped with Doppler processors to enable the suppression of clutter. However, the performance is satisfactory only in Salzburg (Randeu, 1994).

The other radars use a three-dimensional clutter map where the pixels contaminated by ground clutter (determined during rain-free periods) are flagged. If there are only contaminated pixels in a vertical column, the minimum measured intensity is displayed. Otherwise the maximum clutter-free information is displayed and the pixel is not reported to be contaminated.

An impression of the usual clutter contamination in an Alpine country like Austria can be obtained from figure 2. It should be emphasized that there may be additional, unrecognized clutter-contaminated pixels.

4.2 SHIELDING

Pronounced shielding occurs in some parts of the country. This is an especially serious problem for the Tyrolean radar on the Patscherkofel, which consequently cannot be used for any other application than the detection of severe weather conditions. The radar Salzburg usually shows a sector to the south-west (central angle approximately 50^o) where hardly any echos are obtained due to shielding. Reference is made to Joss and Waldvogel (1990) who described similar problems occurring in Switzerland.

4.3 LOSS OF INFORMATION CAUSED BY THE DATA REDUCTION

It is obvious that accurate rainfall rates cannot be expected from radar data reduced in the manner described in section 2. Assumptions required to retransform the category code into rain rates are associated with errors, which play a particularly important role when one is forced to avoid averaging over large areas or long periods, as is the case when it is intended to combine precipitation fields and satellite images. For this application, better quantitative results can be expected from an interpolation of gage reports. However, for nowcasting the occurrence of rain or a rough estimate of its intensity, 8-category images might be sufficient (Andersson and Ivarsson, 1991).

The gage-radar comparisons performed by Jann (1993) clearly indicate that the qualitative information of the radar images is very good over flat terrain close to the radar (up to a distance of about 100 km), in most other regions the distinction between rain and no rain is at least better than that attainable with a gage network (for exceptions to that rule, see section 4.2.). It is therefore desirable to incorporate the qualitative radar information for those areas where the radar data seem reliable (i.e. where there is fair agreement between radar image and gage reports), and to decide between rain and no rain on basis of the radar image. Additionally, the gage-based precipitation fields should be modified when the radar image shows a small phenomenon like a thunderstorm cell which a gage network with a comparatively coarse spatial resolution possibly fails to notice. The gage-radar combination is planned to develop during the next two years.

ACKNOWLEDGEMENT

I wish to thank Dr. W. Randeu (Institut für Nachrichtentechnik und Wellenausbreitung der Technischen Universität Graz) for reading the draft and providing information which helped improving the manuscript (in particular the section about clutter suppression).

REFERENCES

ANDERSSON, T. and K.-I. IVARSSON, 1991: Probability nowcasts of accumulated precipitation using radar. Preprints, 25th International Conference on Radar Meteorology (Paris), 87-90.

CLIFT, G.A., 1985: Use of radar in meteorology. WMO Technical Note No. 181, World Meteorological Organization, 90 pp.

HAILZL, G., 1989: Wetterradar I und II. Unpublished manuscript (in German), 46 pp.

JANN, A., 1993: Untersuchung der Verwendungsmöglichkeiten der operationellen österreichischen Radardaten. Diploma thesis (in German), University of Vienna, 157 pp.

JOSS, J. and A. WALDVOGEL, 1990: The influence of shielding demonstrated with operational radar data in Switzerland. In: D. Atlas (Editor), Radar in Meteorology, Amer. Meteor. Soc., 601-606.

RANDEU W., 1994: Scanning strategies and clutter suppression applied in the Austrian weather radar network. COST-75 working document 75/WD/46/A, 5pp.

Author's address:

ALEXANDER JANN
Zentralanstalt für Meteorologie und Geodynamik
Hohe Warte 38
A-1190 Vienna
AUSTRIA
Phone: 0043-1-36 44 53/2316
Fax: 0043-1-36 45 70
E-mail: jann@zassun3.zamg.ac.at

REPORT ON THE WEATHER RADAR MEASUREMENTS IN HUNGARY

Meteorological Service of Republic of Hungary,
Budapest, Hungary

FERENC DOMBAI

ABSTRACT

In this article a comprehensive exposition on the present status of the weather radar measurements in Hungary is provided. The configuration of the weather radar network, brief descriptions of the key elements and digital radar data products, as well as an outlook for the next future are discussed. Following own developments in the past the analog MRL-5 radars used in Hungary are providing regularly digital radar data for the forecasters of the HMS and for other users.

ZUSAMMENFASSUNG

In dieser Arbeit wird ein ausführlicher Überblick über den gegenwärtigen Stand der Wetterradarmessungen in Ungarn gegeben. Es werden die Konfiguration des Wetterradarnetzes, die wichtigsten Elemente und digitalen Radarprodukte sowie eine Vorschau auf die nächste Zukunft beschrieben. In Weiterführung der Entwicklung in der Vergangenheit versorgen in Ungarn die analogen MRL-5-Radars die Prognostiker des HMS sowie auch andere Nutzer regelmäßig mit digitalen Radardaten.

1. THE NETWORK

At present there are two weather radar stations in operation in Hungary. (There was a third one at the Budapest Airport but it was cancelled in 1992). The radar stations are operating since about ten years from the begining of the eighties.

These stations are

SZENTGOTTHÁRD/FARKASFA (1982)	N 46.54.49	E 16.19.01 (327 m)
NYIREGYHAZA/NAPKOR (1983)	N 47.57.45	E 21.53.19 (141 m)

The radar stations are equipped with MRL-5 dual-wavelength (S and X band) weather radars which are automatized with a Weather Radar Processor WRP32C system developed in Hungary (PC and DSP32C based) to produce high resolution digital output (Nyiregyhaza 1991, Szentgotthard 1993).

The network is based on the public telephone network and on the Radar Communication Servers - RCS. The RCSs are placed at the radar stations and at the main users including the Center of the Meteorological Service.

In the case of precipitation events the measurement is repeated every five minutes up to 256 km range using the WRP32C. The digital radar pictures are sent to the Center every 15 minutes. In the Center the measured radar data are stored with full resolution on a server computer of the integrated LAN so they can be accessed at every forecaster's workplace.

Presently the staff of the radar stations (8 or 9 people) makes synoptic observations and manual radar measurements every hour, too. The output of these radar measurements are the radar telegrams that contain manually coded rainfall intensity values (0-9). The radar telegrams can be sent to the users via telex (this will be cancelled in 1994).

2. THE MRL-5 WEATHER RADAR

The MRL-5 is a conventional analog weather radar with analog intensity output. A special feature of the MRL-5 is the dual wavelength capability. For measuring in two wavelengths simultaneously, the MRL-5 has two transmitters and two receivers but it has only one antenna and display equipment. The main characteristics of MRL-5 radar are:

		X BAND	S BAND
Antenna		4.5 m parabolic	(for X band there is 1.5 m dish also)
	Radome	yes	
	beam width	0.5 degree	1.5 degree
	polarization	vertical	horizontal
	gain	49 dB	40 dB
Transmitter			
	wavelength	3.26 cm (9.5 Ghz)	10.6 cm (2.95 Ghz)
	type	magnetron	magnetron
	peak power	250 kW	550 kW
	pulse length	1 / 2 μs	1 / 2 μs
	losses	5 / 7 dB	5 / 7 dB
	pulses/s	500/250 Hz	500/250 Hz

		X BAND	S BAND
Receiver			
	min. det. signal	-134 dBW	-136 dBW
	type	log	log
	dynamic range	80 dB	80 dB
	attenuators	78 dB	78 dB
	range corr.	yes	yes

3. DIGITAL WEATHER RADAR MEASUREMENTS

3.1 THE WRP32C WEATHER RADAR PROCESSOR

The WRP32C Weather Radar Processor is based on the DSP32C floating point digital signal processor that is hosted in a small computer of the PC/AT type. The system is developed in Hungary by KOSZOFA. The WRP32C has a special interface to the MRL-5 radar taking the status, video, etc. signals and controlling the radar movements.

In the WRP32C the radar video signal is digitized with 8 bit resolution. The minimum sampling distance (maximum sampling rate) is 62.5 m. The first step of the processing is the conversion of the 8 bit digital values into four byte real words. Following this, all calculations are executed with these floating point values. The WRP32C has parameters for taking measurements on X and S band alternatively.

The WRP32C can be controlled interactively but it is able to work without operator interactions fulfilling the preprogrammed measurement tasks. The digital radar data can be displayed on the SVGA color display of the WRP32C and are archived and sent to the Radar Communication Server via the radar station LAN.

A more detailed description of the WRP32C is given in the referenced papers.

3.2 DIGITAL RADAR DATA

The primary radar data products are the arrays of the radar reflectivity factor values in dBZ taken from radar measurements of different types from PPI (horizontal), RHI (vertical) scans and HY-SCAN (combined array from 4 PPI) scans. Every radar data array has 256 rows and 256 columns with 8 bit pixels. The radar reflectivity factor values range from -15 to + 63.5 dBZ with 0.5 dBZ resolution. These data arrays are in a Cartesian coordinate system.

The resolutions are:

	Range	Resolution	A/D sampling
PPI&HY-SCAN	256 km	2.0 * 2.0 km	500 m
	128 km	1.0 * 1.0 km	250 m
	64 km	500 * 500 m	125 m
	32 km	250 * 250 m	62.5 m
RHI	256 km	1.0 * 0.25 km	500 m
	128 km	500 * 125 m	250 m
	64 km	250 * 62.5 m	125 m
	32 km	125 * 31.3 m	62.5 m

3.3 OTHER DIGITAL RADAR DATA PRODUCTS

The reflectivity factor, dBZ arrays measured every 5 minutes is converted into radar rainfall intensity values of the same temporal resolution using the well-known Marshall-Palmer formula. From these values also 1 hour and 6 hour precipitation totals are calculated at the radar site.

3.4 THE RCS - RADAR COMMUNICATION SERVER

The RCS, Radar Communication Server has to transport the digital radar data between two RCS systems via the public switched telephone network. The working modus can be interactively requesting from the remote RCS any radar pictures selected by an operator or automatically fulfilling a preprogrammed data transfer schedule.

The transmission speed can vary from 1200 bps to 9600 bps depending on the line quality and on the installed modems. For transfer purposes the RCS compresses respectively decompresses the raw digital radar data. Usually the transfer of one 256 by 256 radar data array with 8 bit values needs about 0.5 - 1.0 minutes on a 1200 bps line. The RCS is able to display the radar data on its SVGA color display, too.

Now RCSs are working at the radar stations, at the Meteorological Service of Hungary and at two water authorities.

4. FUTURE PLANS

4.1 BUDAPEST RADAR

It is planned to reestablish the weather radar measurements at the Budapest region using a MRL-5 radar which was removed from the hail suppression network cancelled in 1990. This radar will be equipped with WRP32C modification kit to provide digital radar data. The site of this radar will be the Upper Air Observation Station at Budapest. This station should work from the 3rd quarter of 1994. The coordinates of this station will be N 47.26 & E 19.16 (150 m).

4.2 WHOLE VOLUME SCANS - 3D MEASUREMENTS

At present the digital radar data measured automatically every 5 minutes are coming from two dimensional radar scans, from PPI or HY-SCAN scans (RHI is done from time to time). The 3-dimensional measurements shall be introduced in the next future. These 3-dimensional measurements will open the possibility to derive more digital radar data products necessary for deriving the 3-dimensional structure of the cloud-precipitation systems.

4.3 DUAL-WAVELENGTH MEASUREMENTS

It is planned to utilize the special features of a MRL-5 weather radar to further develop the WRP32C system for taking measurements at two wavelengths simultaneously. The significantly different properties of the microwave propagation at the 3 and 10 cm wavelength in heavy rainfall events give the possibility to improve the echo type identification (shower, hail etc.) and the rainfall calculations. This work is going on in the frame of the CEC COST 75 project which has been started in 1993.The following topics will be considered in the next future:

- preparing the radar installation at Budapest for both operational use and research;
- modification of the WRP32C system to make measurements at the two wavelengths simultaneously (new A/D converter board) and embedding of the second DSP32C floating point signal processor for raw video data handling;
- assessment of the algorithms to be used for real-time processing.

4.4 RADAR DATA EXCHANGE

Following the recommendations of the Meeting of the directors of the Central European Meteorological Services an operational radar data exchange via GTS is prepared, which will be finished by the end of 1994. The coordination of this work is done by Austria.

REFERENCES

DOMBAI F., 1991: Using DSP32C Floating Point Signal Processor as Radar Video Processor. In: C.G. Collier, International Weather Radar Networking, Kluwer AP, pp. 41-46

DOMBAI F., 1993: DSP32C based Weather Radar Modification Kit on the Upper Tisza River Catchment. (will be published in the Proceedings of the 2nd Int. Sem. on Hydrological Applications of the Weather Radar - Sept. 1992, Hannover)

Author's address:

FERENC DOMBAI
Hungarian Meteorological Service
Kitaibel Pal u.l.
H-1024 Budapest
HUNGARY
Phone: + 1355/335
Fax: + 1353/180

THE PRESENT STATUS AND FUTURE PLANS OF SATELLITE AND RADAR MONITORING IN CROATIA

Meteorological and Hydrological Service, Zagreb, Croatia

IVAN ČAČIĆ and DUŠAN BIŽIC

ABSTRACT

The monitoring and usage of the satellite and radar data in the Meteorological and Hydrological Service of the Republic of Croatia (hereafter: MHS) is still in the developing stage. This is the reason why the MHS is wide spreading its activity towards Central European Initiative (hereafter: CEI) projects and particularly to the participation in the joint Project "Remote Sensing Methods in Meteorology and their Application in Nowcasting" that is supported by modern informatic and mathematical methods. At the moment the MHS is operating a simple SDUS station and one conventional S-band weather radar near Zagreb. Serious efforts have been made to produce digitized radar pictures as a first step towards the future national composite radar picture. The paper presents the actual and the planned radar network as well as the main characteristics of the radar products.

ZUSAMMENFASSUNG

Monitoring und Verwendung von Satelliten- und Radardaten im Meteorological and Hydrological Service der Republik Kroatien (im folgenden: MHS) sind noch immer in einem Entwicklungsstadium. Das ist ein Grund, warum das MHS seine Aktivitäten innerhalb der Central European Initiative (im folgenden: CEI) Projekte sehr breitgestreut unternimmt; das gilt besonders für das gemeinsame Projekt "Remote Sensing Methods in Meteorology and their Application in Nowcasting", das moderne Methoden der Mathematik einschließt. Im Moment unterhält das MHS eine einfache SDUS Station sowie ein konventionelles S-Band Wetterradar nahe von Zagreb. Als erster Schritt in Richtung eines nationalen Radarbildmosaiks wurden Anstrengungen in Hinblick auf die Erstellung digitalisierter Radarbilder unternommen. Der Bericht präsentiert das aktuelle und geplante Radarnetz sowie die hauptsächlichen Radarprodukte.

1. SATELLITE METEOROLOGY

The usage of satellite data in Croatia is very limited by the lack of professional equipment. At the moment, the MHS is operating a simple SDUS station for the purpose of the Weather Service. Unfortunately, such the receiver serves only the monitoring and storage of WEFAX images. There is no possibility to extract and process the gray levels. Therefore it was decided to purchase a high quality PDUS station as a high priority realization of the strategic plan for the development of the National Meteorological Center-Zagreb (hereafter: NMC). There is a realistic hope that in the 1994 the MHS will have the possibility for the aquisition of the PDUS station "Skyceiver Rainbow" manufactured by the Swiss firm Tecnavia.

First of all, the MHS has in 1993 signed a Cooperation Agreement with the EUMETSAT for the satellite data usage licence and the MDD receiving system which is valid in the period from 1 January 1993 to 31 December 1995.

2. RADAR METEOROLOGY

In Croatia weather radars so far have been used exclusively in the hail suppression program. Radar measurements were performed manually in convective situations only and during the hail suppression season (May-September). In 1993, serious efforts have been made to organize and produce digital radar output useful in other areas of interest (precipitation measurements, nowcasting). The initial impulse for the development of more modern radar data organization and presentation was "Remote Sensing Methods in Meteorology and their Application in Nowcasting", a project within the framework of CEI.

The radar measurements performed in the hail suppression program for the period 1987-1991 were compiled in order to investigate various characteristics of convective clouds (Bižic et al., 1994). Efforts have been made to produce digitized radar picture as a first step towards the future national composite radar picture. So far, the prototype of the digital radar signal processor and display is developed and will be in experimental use in 1994.

At present the Croatian Meteorological and Hydrological Service is operating two S-band weather radars from EEC: one conventional near Zagreb (RC-Sljeme) and one Doppler near Virovimca (RC-Bilogora). The third one (RC-Osijek) is out of function due to serious damage caused during the war. In 1993 hourly measurements of several cloud parameters were performed for the CEI project (Glasnović et al.,1994), including the description of the cloud system.

The new standpoint in the radar network implementation is that all radars are to be used equally in nowcasting and hail suppression. Figure 1 shows the existing as well as the planned radar locations for the period 1994-1996. The Osijek radar will be repaired and the Pula radar will be installed with the financial support of the United Nations Development Program. All radars operate at S-band, and Bilogora and Pula are the third generation Doppler radars.

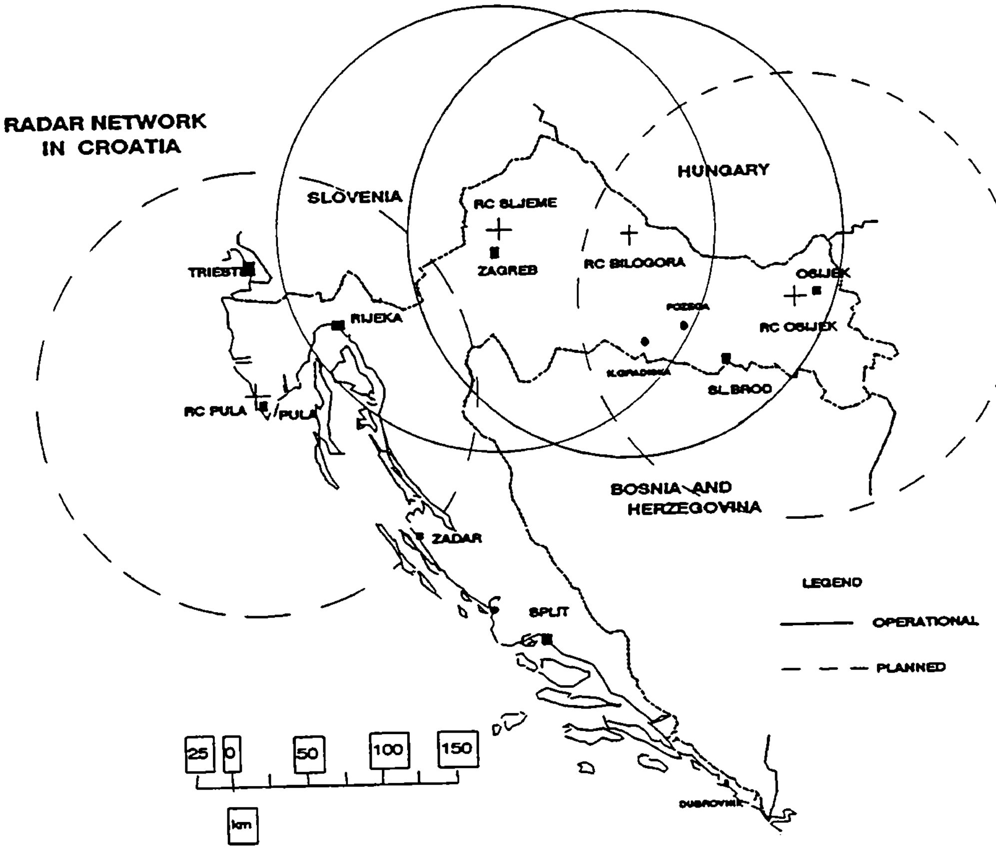

Figure 1: Radar network in Croatia

The national composite radar picture will have the following characteristics:

1) Scanning mode
every 30 min, starting at H00
16 elevations
range: 0-150 km, 1-12 km above m.s.l.

2) Generated product
ground projection and two side projections of
non-cluttered maximum reflectivities
pixel size: 5 x 5 x 1 km, optionally for single
pictures 2.5 x 2.5 x 1 km (range 70 km)
seven precipitation rate intensity levels plus one
"no data" level : <0.3, 0.3, 1, 3, 10, 30, 100 mm/h
using Marshall-Palmer relation $Z \doteq 200\ R^{1.6}$

The pixel size is selected according to the satellite data resolution, so that the implementation of the combined radar-satellite picture could be readily done. The Doppler mode will be used for various research projects, primarily in severe convective and wind situations (bora in Adriatic).

REFERENCES

BIŽIC, D., GERBER, Z. and M. MATVIJEV, 1994: Radar Observations of Convective Clouds in Croatia. (in preparation).

GLASNOVIĆ D., ČAČIĆ I. and N. STRELEC, 1994: Methodology and Application of the High Resolution Isentropic Diagnostic Model HRID. (Published in this Volume).

Author's address:

IVAN ČAČIĆ and DUŠAN BIŽIC
Meteorological and Hydrological Service
Gric 3
41000Zagreb
CROATIA
Phone: +385 41 421 222/279
Fax: +385 41 278 703
E-mail: hrid@madhz.dhz.hr

STATUS REPORT OF SATELLITE METEOROLOGY, RADAR METEOROLOGY AND NOWCASTING

Part II: RADAR METEOROLOGY

Hydrometeorological Institute of Slovenia, Ljubljana, Slovenia

JASNA VEHOVAR

ABSTRACT

The existing radar system at the Hydrometeorological Institute of Slovenia is described and future plans are mentioned.

ZUSAMMENFASSUNG

Das derzeitige Radarsystem am Hydrometeorologischen Institut Sloweniens wird beschrieben und zukünftige Pläne werden erläutert.

Part II: RADAR METEOROLOGY

II.1 EXISTING CAPABILITIES

At present the Slovenian weather radar network consists of only one radar, situated on Lisca Peak, about 70 km east from Ljubljana, and a national radar data acquisition and dissemination center in Ljubljana.The radar is a conventional C-band 1-degree pencil beam radar from EEC, controlled by a PDP-11/44 computer, linked with the center by the fixed 4800-baud telephone line. Volume scans are performed in intervals of 30 minutes (surveillance mode), 15 minutes (nowcasting mode) or 7.5 minutes (precipitation mode) in the range up to 200 km on 16 elevations. An "echo field structure" product is generated, consisting of ground projection and two side projections. All projections consist of non-cluttered maximum reflectivity in the volume of 400x400x12 km. The extent of one volume element is 2x2x1 km. There are six levels used for echo intensity: 16, 24, 32, 40, 48 and 56 dBZ, corresponding to rainfall intensity of 0.3, 1, 3, 10, 30 and 100 mm/h. This product is transmitted to the center and from the center it is disseminated to the primary and secondary users, using fixed and dial-up telephone lines. Primary users are the meteorological service, the Hydrological Service and the Brnik airport. Secondary users consist of 2-3 departments at the hydrological part of the institute. All users are supplied with PC-based low-cost display systems.

II.2 PLANNED STRATEGY

The radar network will be expanded by adding the second Micro VAX, controlled C-band Doppler radar with dual polarization from EEC, on Slavnik Peak in the south-western part of Slovenia. The main products (echo field structure, rainfall intensity, horizontal wind and vertical wind profile) will be transmitted to the center and echo field structure composites will be generated. Both radars will perform volume scans simultaneously every 7.5 minutes, using identical sets of 16 elevations. Scan parameters for the conventional radar will remain unchanged. Doppler radar will operate alternately in "Half-Doppler" mode (reflectivity, Doppler capabilities used for clutter suppression only) and "Full-Doppler" mode (reflectivity, velocity and turbulence products). The number of users will be increased by the Krško Nuclear Power Plant and the national transport authorities.

II.3 WEATHER RADAR DATA ADJUSTMENT

To estimate the instantaneous ground rainfall rate from the radar-measured reflectivity aloft, the following procedure is used:

- The "preliminary" rainfall rate R is calculated using the relation $Z=A^*R^B$, with A=250 and B=1.6. Z is measured in mm^6/m^3 and R in mm/h.

- The "true" ground rainfall rate G is determined using the equation $\log G=a+b^*\log R+c^*\log r$, with a=-0.38, b=0.89 and c=0.37 (r is the distance from the radar). G and R are measured in mm/h and in km. The correction equation was obtained from a multiple regression analysis of the ground-measured and radar-estimated hourly rainfall amounts (one year data set).

Investigations are under way to include two additional regression variables: the height of the zero-degree isotherm and the decorrelation distance of the precipitation field.

As an improvement to the above-mentioned statistical method of adjustment, the following vertical reflectivity profile correction method is being investigated:

- Selection of the "representative" vertical reflectivity profile Z(h) (daily average 5-50 km from the radar at present).
- Estimation of the "true" ground reflectivity from the measured reflectivity aloft and the calculated reflectivity profile.
- Conversion of ground reflectivity to rainfall rate using the standard Z-R relation.

II.4 CURRENT ACTIVITIES

II.4.1 COST-75

Operational radar measurements of rainfall show a systematic range-depending under estimation and a large scattering around raingauge-measured values. In Slovenia, for example, the radar-estimated hourly-accumulations at 100 km are approximately 40% of raingauge values, whereas the average scattering reaches a factor of two. The physical causes for these discrepancies suggest that the discrepancies could possible be diminished, to some extent, by using the vertical reflectivity profiles. Apart from the pioneer work in Switzerland, little research activity has been carried out in this direction. As a contribution to the COST-75 project, is proposed to investigate the use of vertical reflectivity profiles to improve the accuracy of rainfall measurements on an operational basis.

The contract with CEC is already signed. It is expected to construct and implement an "adequate" algorithm for the determination of the vertical reflectivity profiles and, by using it in real time, to improve the accuracy of rainfall measurements on an operational basis.

II.4.2 GORN

There is a participation in the Liaison Group for European Operational Radar Networking (GORN). In this frame the software has to be adopted for international radar data exchange through the GTS/MSS system. All radar data will be exchanged in binary BUFR form. There are already some agreements made with surrounding countries for radar data exchange. The exchange should start in the first quarter of 1994.

Author's address:

JASNA VEHOVAR
Hydrometeorological Institute of Slovenia
Meteorological Research Department
Vojkova 1B61 000 Ljubljana
SLOVENIA
Phone: (386) 61 327 461
Fax: (386) 61 320 466

CONTRIBUTIONS TO SATELLITE AND RADAR
METEOROLOGY IN CENTRAL EUROPE

COMBINED METHODS AND NOWCASTING

DEVELOPMENT OF A DECISION PROCEDURE FOR STORM WARNING AT LAKE BALATON

Storm Warning Observatory of Hungarian Meteorological Service, Siófok, Hungary

IMRE BARTHA

ABSTRACT

As a result of successive investigations an objective decision procedure has been developed which combines methods based on conventional data with the use of radar data. This procedure can be executed interactively on a computer. The permanence of wind hazards was investigated during frontal and convective weather situations using radar data and synoptic observations.The resulting distribution functions of empirical probability for the permanence of wind hazards associated with cumulonimbus can be used for the further optimization of the decision method.

ZUSAMMENFASSUNG

Als Folge ausgedehnter Untersuchungen wurde eine objektive Entscheidungsprozedur entwickelt, bei der Methoden, die auf konventionellem Material aufbauen mit Radardaten kombiniert werden. Die Prozedur kann interaktiv am Computer ausgeführt werden. Die Dauer von Sturmereignissen wurde für synoptische und für konvektive Wettersituationen mittels Radardaten und synoptischen Beobachtungen untersucht. Die resultierende Verteilungsfunktion der empirischen Wahrscheinlichkeiten der Sturmdauer im Zusammenhang mit Cumulonimben kann für eine weitere Optimierung der Methoden benutzt werden.

1. INTRODUCTION

In wind forecasting, one of the most difficult tasks is to predict the degree of wind strengthening associated with cumulonimbus (Cb) for different synoptic situations. (1954) Fawbush and Miller worked out a simple method for the prediction of maximum wind speeds associated with non-frontal thunderstorms. This method is based on the idea that there is a close relationship between the temperature decrease induced by thunderstorms and the maximum wind speed at the surface.

In Hungary, during the 1970s, identification of Cb and qualitative estimation of wind gusts associated with Cb have made use of radar data. However, new problems have arisen concerning the very short range ($t \leq 2$ hours) forecast of the wind speed. In particular, following each radar observation of Cb-echoes, it has been necessary to estimate to which wind category the maximum wind gusts (V_{max} in units of m/s) belong from the point of view of the storm warnings at Lake Balaton: no warning ($V_{max}<12$), alert ($12 \leq V_{max} \leq 17$) or storm warning ($V_{max}>17$).

In the 1990s, an objective decision model has been developed (Bartha,1987) to estimate the maximum wind gusts associated with Cb measured by radar.

2. DECISION METHOD

The decision method that has been developed is based on a combination of radar and upper-air data as well as synoptic observations. The decision system is summarized in the block diagram in Figure 1:

a) It can be seen that the very short range forecast for the region of Lake Balaton serves as basis for the decision-making on storm warning.

b) Whenever precipitation systems detected by satellite and weather radar appear close to the lake and their vertical development and intensity reach or exceed certain threshoulds ($H_{max} \geq$ 4 km; $\lg Z_3 > 0$) more frequent radar observations are initiated. (H_{max} = radar echo top, Z_3 = radar reflectivity factor).

c) Then input data (see Bartha, 1987) are fed into the decision system, classifying the Cb-echoes on the basis of the degree of wind hazard.

d) It is followed by consideration of the actual weather situation that may have influence on the development of Cb. Significant situations are analyzed every one or three hours on meso-synoptic charts. The surface pressure patterns are determined by the hourly change of horizontal pressure gradient (Δp)

e) The decision-making requires the monitoring of changes in the cooling rate (ΔT) as well as in the maximum wind gusts (V_{max}) measured by a telemetry system around Lake Balaton and in the surface pressure gradient (Δp) in the region of West-Hungary.

f) Finally, the decision procedure results in one of the decisions: no warning, alert or storm warning.

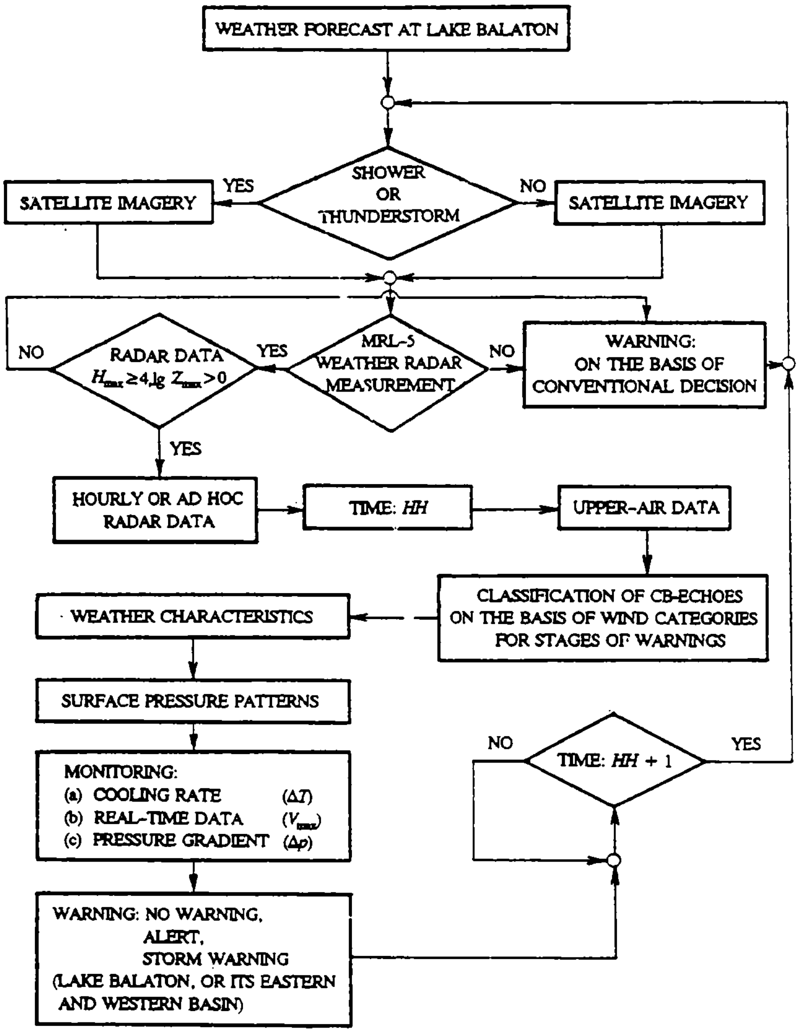

Figure 1: Block diagram of the objective decision system for forecasting the maximum wind gusts (V_{max})associated with max Cb echoes

The procedure using the computerized interpretation of manually digitized radar data has been working since 1988. The decision method was tested on the basis of an independent sample. Warnings issued by the use of computerized decision procedures and those based on conventional methods were compared in 548 cases from the years 1986, 1987 and 1989. The new procedure proved to be more reliable by 5% as compared to the one based on conventional data (the value of accuracy increased from 76% to 81%). At the same time the objective procedure reduced the cases of overestimation by 10% (Bartha and Zsikla, 1990).

3. DEVELOPMENT OF DECISION METHOD

The decision method used in the storm warning procedure requires a knowledge of the permanence of wind hazards during various weather conditions connected with Cb (Bartha et al.,1989). Therefore answers were required to the following questions:

- When does a Cb produce wind hazards at the surface ?
- Is there a difference between the permanence of wind hazards associated with Cb developed during various weather situations?
- How far ahead can wind hazards be estimated in various weather situations ?

3.1 DATA USED AS THE STARTING POINT FOR INVESTIGATION

In order to answer the questions about the permanence of wind hazards, some active cold fronts (I) and convective systems (C: convergence zone; H: instability line; MCC: mesoscale convective complex) were studied. These weather situations (36 frontal and 20 convective storms) were collected in 1986 and 1987 during the periods from May to September. The following data were used for the investigation:

- Hourly radar data (H_{max}; lgZ_3; $Y = H_{max}\ lgZ_3$) from the detection region with a radius of 150 or 200 km of the Szentgotthárd/Farkasfa weather radar station in West - Hungary.
- Synoptic observation of the Cb (SYNOP: $C_L = 3$ or 9) and some significant weather phenomena (showers; thunderstorms; hailstorms; wind gusts of 7m/s or stronger, associated with Cb) of 13 main synoptic surface weather stations in West Hungary.
- One or three hourly meso-synoptic charts for analysing the development and movement of frontal and convective systems over the region of West-Hungary.

3.2 RESULTS

It is known that the downdraught within a developed Cb starts approximately at the 0 °C level. The outflowing cold air spreads out at the surface under the Cb and produces a gust front at its boundary with the ambient air frequently associated with thunderstorm, shower or hailstorm. On that account, the maximum wind gusts connected with a Cb can be expected either simultaneously with the first observation of heavy shower respectively thunderstorm, or soon after. As a verification, the frequency distribution of $\Delta t = tv_{max} - t_{shower;thunderstorm}$ were investigated (figure 2) where tv_{max} is the development time of maximum wind gusts with shower or thunderstorm and $t_{shower;thunderstorm}$ the time of the surface observation of the same significant phenomena.

It follows from figure 2, that the overwhelming majority (84%) of maximum wind gusts associated with Cb developed either simultaneously with the first surface observation of a heavy shower or thunderstorm, or at a later time. The synoptic background of the cases for intervals $\Delta t < 0$ and $\Delta t \geq 2$ hours was also studied. The maximum wind gusts observed with interval $\Delta t < 0$ (in 16% of the cases) were the result of the Cb associated with a cold front (I) or instability line (H). This is in accordance with the fact that the gust front may propagate in the boundary layer for distances up to 80 - 100 km away from severe thunderstorm sources (Browning and Collier, 1982). In cases where $\Delta t \geq 2$ hours, the maximum wind gusts developed in pre- or post-frontal isobaric patterns with strong surface pressure gradient (in 9% of the cases). These wind gusts were the results of the Cb associated with frontal (I) or convective systems (C or H). On the basis of investigations, the maximum wind gusts developed either during the first surface observation of a heavy shower or thunderstorm, or soon after, within hours in 75% of the cases.

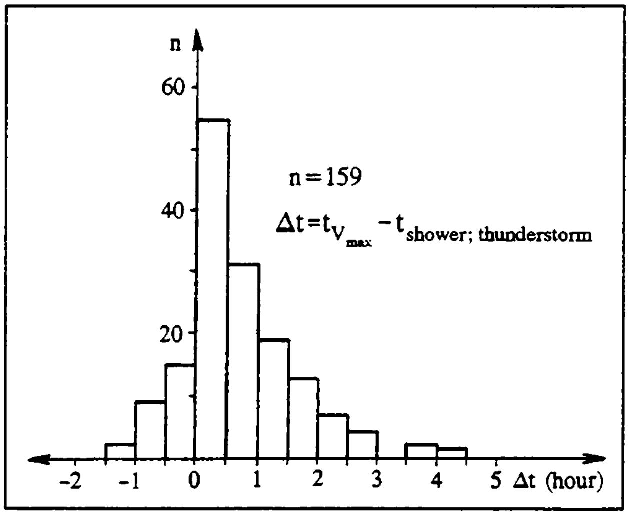

Figure 2: Frequency distribution of intervals $\Delta t = t_{V_{max}} - t_{shower;thunderstorm}$ (see text) in case of frontal and convective system in the region of West-Hungary, (1986-1987)

Further investigations required the introduction of the idea of potential and effective wind hazard periods:

- Potential wind hazard period (Δt_{pot}) is the time until the wind reaches its maximum value when the wind speed is rapidly and permanently increasing or the gusts are exceeding the value of 7 m/s, due to Cb or their significant weather phenomena. These wind gusts develop when the outflowing cold air from the downdraught spreads out at the surface under a Cb.

- Effective wind hazard period(Δt_{eff}) is the time taken for the wind to reach its maximum value when the wind speed is rapidly increasing or the gusts are exceeding 12 m/s, due to Cb or their significant weather phenomena. These wind gusts can be expected at the surface whenever the radar detects Cb echoes with the value of $Y = H_{max} \lg Z_3 \geq 10.9$ (Bartha, 1987).

Using these definitions an investigation was carried out in respect to the permanence of potential and effective wind hazard periods (Δt_{pot} and Δt_{eff}) during different synoptic situations connected with Cb.The results are shown in figures 3a, b and c.

Figures 3a and b show that if winds are observed to exceed 7 m/s there is about 40 to 45% probability of the maximum gusts occurring within the next two hours. However, if the wind exceeds 12 m/s the corresponding probability is about 65 to 70% whenever the radar detects Cb with value of $Y \geq 10.9$. On the basis of figures 3a and b it can be seen that the distribution functions for potential and effective hazardous periods of maximum wind gusts connected with non-frontal (C, MCC, H) thunderstorms are similar, but differ from the distribution function for the frontal (I) cases given in figure 3c. This figure shows a probability of 23% that the maximum gust within the next two hours if the wind exceeds 7 m/s.

However, if the wind exceeds 12m/s the corresponding probability is 85% whenever the radar detects Cb with the value of $Y \geq 10.9$. From figures 3a, b and c it can be seen that the effective wind hazard periods for the weaker convective systems (C, MCC) and instability lines (H) are shorter by 0,5-1 hour on the average as compared to the potential ones. Similarly, the same period proved to be shorter by about 2 hours in respect to cold fronts (I).

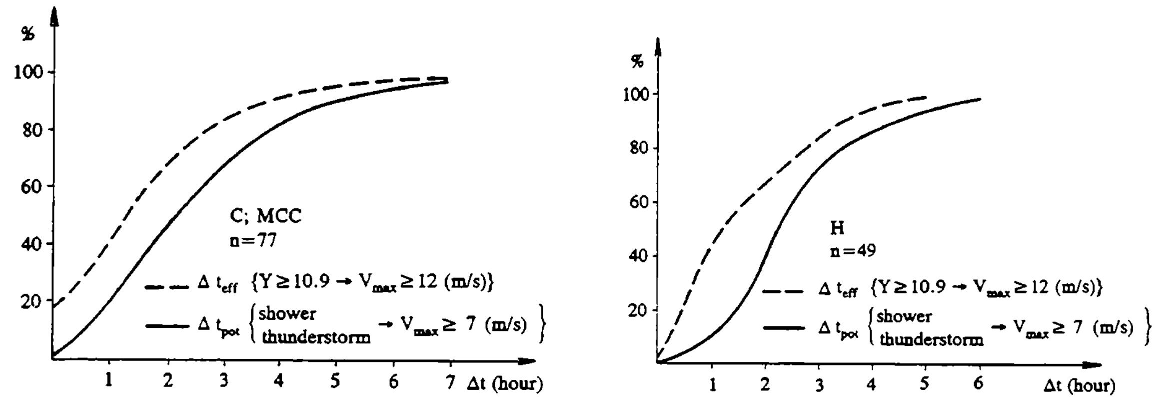

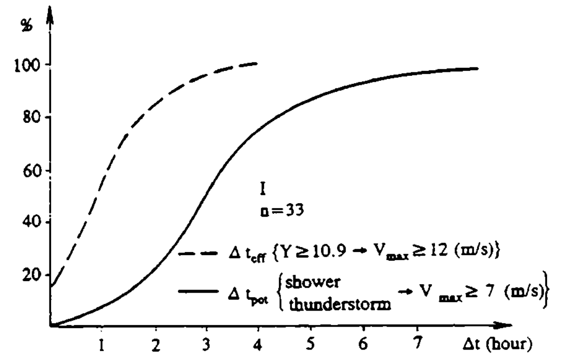

Figure 3:
Empirical probability distribution functions for the potential and effective hazardous periods (Δt_{pot} and Δt_{eff})of maximum wind gusts (V_{max}) associated with

(a): convergence zone (C) or meso-scale convective complex (MCC) and
(b): instability lines (H) and
(c): cold fronts (I) in the region of West-Hungary (1986-1987)

4. CONCLUSIONS

The following conclusions can be drawn:

a) Nowadays, weather radar and satellite data are available. The success of the so-called nowcasting warnings is largely dependent on the integration of non-conventional information into a complex meso-scale analysis (e.g. Horváth and Práger, 1990; Zwatz-Meise et al., 1993) included into the general synoptic framework.

b) In weak convective systems developed within the same air mass over West-Hungary, it is most likely that the maximum wind gusts occur either during the first surface observation of heavy shower or thunderstorm, or soon after within 2 hours.

c) For the production of storm warnings the subjective or objective recognition of instability lines must be performed before identifying this weather object by radar because the gust front may propagate in the boundary layer for distances up to 80 - 100 km away from the thunderstorm source.

d) The permanence of wind hazards associated with Cb can be increased by the strengthening surface pressure gradient during pre- and post-frontal weather situations.

e) The empirical probability distribution functions concerning the permanence of wind hazards indicate the periods for practical application of the warnings. For this reason these results can be used for a further optimization of the nowcasting decision method. In the near future, this decision method will be developed so that it uses digitized satellite information (Horváth et al., 1992) as well as digital radar data.

REFERENCES

BARTHA I.,1987: An objective decision procedure for prediction of maximum wind gusts associated with Cumulonimbus clouds. Idöjárás 91, 1330-346.

BARTHA I., HORVÁTH Á., KAPOVITS A., and VISSY K.,1989: Development of the forecasting methods using radar information for strong and stormy wind associated with convective activity (in Hungarian). Final Report on research work No.1-3-86-319 sponsored by the Hungarian Academy of Sciences.

BARTHA I. and Á. ZSIKLA, 1990: Use of radar echoes in stormwarning at Lake Balaton (in Hungarian). Idöjárás 94, 296-307.

BROWNING K.A. and COLLIER C.G.,1982: Nowcasting. Academic Press, 1/42.

FAWBUSH E.J. and MILLER R.C.,1954: A basis for forecasting peak wind gusts in non-frontal thunderstorms. Bull. Am. Met. Soc. 5,1.

HORVÁTH Á. and PRÁGER T.,1990: A meso-β-scale objective analysis for meteorological fields (in Hungarian). Idöjárás 94, 223/38.

HORVÁTH Á., H. ZSIKLA and M. PLATZ, 1992: Digitized satellite imagery for meso meteorological applications (in Hungarian). Meteorological Notes of Universities 6, I. 112-123.

ZWATZ-MEISE V., A. JANN and R. WINKLER, 1993: An analysis and forecast method including satellite images and parameters on isobaric and isentropic surfaces. Conference Documentation of the 1st European Conference on Applications of Meteorology. 27th September - 1st October 1993, Oxford, U.K.

Author's address:

IMRE BARTHA
8600 Siófok
P.O.Box. 80
HUNGARY
Phone: 84-310466
Fax: 225809

METEOTREND AND NOWCASTING

Slovak Hydrometeorological Institute, Bratislava, Slovakia

JÁN KAŇÁK

ABSTRACT

Meteotrend which was developed in the Slovak Hydrometeorological Institute as an implement for Very short-range Weather Forecasting and Nowcasting is described. The linear extrapolation used for forecasting cloud fields and an expert approach to a satellite image classification are discussed. A simple statistical method for the specification of rain fields as a part of Meteotrend is considered in this article. Meteosat infrared (IR) and water vapour (WV) data as well as radar measurements of precipitation intensities are used in this method. The results are included into the information about road weather conditions.

ZUSAMMENFASSUNG

In diesem Bericht wird Meteotrend beschrieben, ein Beitrag des Slovakischen Hydrometeorologischen Institutes zur sehr kurzfristigen Wettervorhersage und Nowcasting. Die lineare Extrapolation für die Vorhersage von Wolkenfeldern sowie ein Expertensystem zur Klassifikation von Satellitenbildern werden diskutiert ebenso wie eine einfache statistische Methode zur Bestimmung von Niederschlagsfeldern. Dafür werden Meteosat IR und WV Bilder sowie Radarmessungen von Niederschlagsintensitäten verwendet. Die Ergebnisse bilden einen Teil der Information für den Straßenwetterdienst.

1. INTRODUCTION

Meteotrend as a method using primarily satellite data to be meteorologically interpreted has been worked out in the past years at the SHMI Malý Javorník (Podhorský and Olsina, 1986; Podhorský, 1990). It comprises the very short-range forecast of the cloud field, the cloud types classification, and that of the meteorological phenomena related to them as well as the very short-range forecast of this classification.

The programme system realizing the Meteotrend method uses a PDP 11/34 computer, which is a part of the Malý Javorník WIRPS (Weather Images Receiving and Processing System) satellite reception equipment. The individual programmes are written in FORTRAN 77 programme language, and their release in the above-mentioned system is being carried out by a set of batch fields. The programme package can be started automatically, or by an operator, whereby the operator is enabled to change the primary system parameters if necessary at any time.

2. MPS PRIMARY OPERATIONAL CHARACTERISTICS

MPS (Meteotrend Programme System) is usually started automatically in accordance with the WIRPS operational scheme immidiately after receiving and primary processing of the Meteosat data. Besides, the operator may release it at any time he considers important, with regard to other operational tasks.

According to the output asked, the operation is ended between the 25th or 30th minute, where a primary output, the Meteosat IR-channel cloud field forecast (11.1 μm) and convective and advective tendencies available for the users already in the 25th minute. In the 30th minute another output, the classification of cloud types and that of the meteorological phenomena related as well as the very short-range forecast of this classification is given within the MPS. At present, the output is computed only if necessary, because the WIRPS is overburdened with other operational tasks. At present the MPS output covers the territory of Central Europe of 1024x1024 km^2 range with a resolution of 8x8 km^2.

3. MPS OUTPUT

3.1 CONVECTIVE AND ADVECTIVE TENDENCIES

Image output in false colour comprises a change of the object temperature (measured in the Meteosat IR-channel), within the time interval of two consecutive images (30 or 60 minutes), computed by the isodensities correspondence method (Podkorský and Vlcák, 1986). The meteorological interpretation of the change (the convective tendency) is from the physical point of view complicated. For instance in the case of cloudiness having an emissivity of 100%, the temperature change is related to the upper boundary of the cloudiness; a fact that is used in the case of convective cloudiness. In the case of layered cloudiness with an unchanged upper boundary the temperature change may be a consequence of an emissivity change.

The computation might be misled by a big change in the observed cloud shape within the interval of measurements because of an improper isodensity correspondence. The convective tendency imageries carried out by imaging only those cloud fields exceeding a pre-determined temperature change.

The advective tendency is pictured in the imagery as horizontal cloud movement vectors determined by the isodensity correspondence method. Movement direction and speed is determined for every square of 32x32 km^2 size. The convective and advective tendencies are a means for the recognition of the changes of the cloud field and are used for meteorological interpretation as well as a basis for the forecast computations in MPS.

3.2 CLOUDINESS FORECASTING

The actual cloudiness forecast yields an imagery set for a territory of 1024x1024 km^2 range with 8x8 km^2 resolution consistent with the Meteosat IR-channel. It comprises for every square IR-temperature forecasts, being determined by the method of the isodensities correspondence and linear extrapolation of cloud movement and temperature changes.

For better information the cloud field forecast is in a four image form which contains in the first three quadrants the real situation represented by the three last images, while the actual cloud field forecast is in the fourth quadrant.

3.3 CLASSIFICATION OF CLOUD TYPES AND THE METEOROLOGICAL PHENOMENA

The Central European territory is divided into squares of 8x8 km^2 range. To every square the numerical values of the cloud classes are attributed determined by the process of classification. Classes which can be classified at present are as follows:

a) Summer period
1. earth
2. As, Ns
3. Ci, Cs, Cc
4. shower
5. developing Cb
6. thunderstorm
7. thunderstorm with hail

b) Winter period
1. earth
2. fog or low cloudiness
3. As, Ns
4. stratus
5. cumulus

3.4 CLOUD TYPE CLASSIFICATION METHOD

During the first step the so-called sets of symptoms are prepared. These are the image matrices of the Central European territory which might consist of the Meteosat satellite primary data alone or a combination of these data with so-called supporting ones (TEMP or SYNOP), or products of the previous processed primary satellite data. It is essential to choose for the classification process those sets of symptoms which unambiguously specify cloud classes. Until now the following sets of symptoms have been used:

1. Meteosat IR-channel (11.1 µm)
2. Meteosat WV-channel (6.7 µm)
3. Convective tendency for IR-channel
4. Difference between the IR-temperature and that of the tropopause (from TEMP)
5. Convective tendency for WV-channel
6. Difference between the IR-temperature and that of the earth surface (from SYNOP)

The last symptom is used mainly in the winter period when fog and low cloudiness are classified.

So-called Etalon sets consisting of the symptom vectors for the individual classes have been prepared from unambiguous meteorological situations.

The method of the MPS classification is as follows: sets of symptoms for the time T_0 should be prepared as well as for T_1 in the case of a classification forecast. Then the data of the individual symptom sets are combined to make vectors of symptoms. The actual classification procedure uses a classification programme specified for it (classifier). The classifier has to find out the smallest deviation between the vectors of symptoms and those of the etalons. The class number belonging to the etalon, chosen from the classifier process, is attached to the relevant point of an image.

Primary intention of the classification of the cloud types with the help of satellite images, is to facilitate the meteorologial interpretations for the end-users.

3.5 PREPARATIONS OF ETALONS FOR THE CLASSIFICATION WITHIN THE MPS

Because of the character of the data which enter the process of classification in form of sets of symptoms, it is necessary to have an expert evaluation of the meteorological situation in order to pick out a convenient set of etalons. Substantial differences are found between the character of etalons determined for summer and winter situations. The convective cloudiness is dominant in the summer period and therefore the convective tendency symptom is playing a significant role. The earth surface temperature combined with the IR-channel has high priority in the winter period.

Preparation of the etalon sets is done by an expert evaluation of the meteorological situation and by visual interpretation of satellite images. For this purposes the expert must use an interactive graphic system to display images and to draw area borders of various cloud types. Then special software makes bit maps of these areas, which are statistically evaluated and values of etalons are computed. Etalon sets created in this way are used for automatic classification in real time.

Within the theories of pattern recognition one approach for such a problem is the so-called self-learning procedure. With regard to the meteorological phenomena and data which are at the disposal of the Institute, it is impossible to realize this approach, at present, and under the conditions of an operational service. Therefore, far more effective seems to be the expert approach which provides optimum symptoms, its number, as well as, an optimum number of etalons for any meteorological situation.

4. RAIN FIELD ESTIMATION BY MEANS OF METEOSAT DATA

The method for rain field estimation from Meteosat data was developed as an alternative method to the cloud type classification method used in Meteotrend. There was a strong requirement to estimate rain fields in the winter season for a specificiation of road weather conditions for the case that the Meteotrend method does not work successfully because of prevalent low cloudiness.

The principle of the method is based on the statistical evaluation of sufficient long series of satellite images and surface measurements of precipitation. The local comparison of these two data types led to the following empirical relation:

$$I^{V_{ir}}.\frac{W^{V_{wv}}}{10^4}=b \qquad (1)$$

where:	I	radiation temperature of IR-channel,
	W	radiation temperature of WV-channel,
	V_{ir}	exponent specifying weight of IR-channel and
	V_{wv}	exponent specifying weight of WV-channel with consideration of precipitation ability of cloudiness with radation temperature I and W

The values of weights must be chosen before the statistical evaluation of data.

The parameter b in the equation (1) called as parameter specifying the threshold for rain occurrence was obtained for values $V_{ir}= 1$ and $V_{wv}= 2$. The results of the statistical evaluation are for the winter period:

$15 < b < 30$ for rain

and $25 < b < 40$ for snow.

If these conditions are applied in relation (1), the conditions of the probable occurrence of precipitation can be derived:

$$I^{V_{ir}}.\frac{W^{V_{wv}}}{10^4}\langle b \qquad (2)$$

The method is not able to specify the probability of precipitation in a concrete location of the satellite image from the physical character of the used data (IR and WV channels). Therefore, this method is used in combination with radar data, which exactly specify the precipitation intensity. For areas, which are not covered by radar signal, only data from satellites are used. This fact is known to the users of this information and is exactly graphically displayed by means of various colours of signs.

The described method is used as a part of Meteotrend and applied on forecast IR and WV images. It serves as a nowcasting method for specifying the road weather conditions.

REFERENCES

PODHORSKÝ D. and O. OLSINA, 1986: System of Meteosat Data Processing at WMO Activity Centre for VSRF in Bratislava, Proceedings 6th Meteosat Scientific Users Meeting, ESA, Amsterdam.

PODHORSKÝ D. and VLCÁK L., 1986: Meteotrend Based on Meteosat Data. Report of the Proceedings 6th Meteosat Scientific Users Meeting. EUMETSAT, pp. 53-67.

PODHORSKÝ D., 1990: Lectures presented at the WMO Training Workshop on Observations and Forecast Methods for VSRF. WMO, T.d. No. 315, PSMP Report Series, No. 32.

Author's address:

JÁN KAŇÁK
Slovak Hydrometeorological Institute
Centre for Radar and Satellite Meteorology
835 15 Bratislava
SLOVAKIA
Phone: +42 7 281859
Fax: +42 7 281859

STUDY OF POSSIBILITY OF PRECIPITATION NOWCASTING USING DIGITAL RADAR AND METEOSAT DATA

Centre of Aerology, Institute of Meteorology and Water Management, Legionowo, Poland

STANISŁAW MOSZKOWICZ

ABSTRACT

Both radar and METEOSAT data are transformed in the same projection. Radar data are used to separate the satellite picture into zones of high, medium and low rain probability (satellite picture classification with radar data). Using cross-correlation of subsequent IR satellite pictures a field of cloud motion is determined. Motion vectors are determined for classified satellite pictures and a forecast of rain occurrence probability is given for 1, 1.5 and 2 hours ahead. The forecast pictures are compared with observed ones in order to determine the forecast quality.

ZUSAMMENFASSUNG

Sowohl Radar als auch Meteosat Daten werden auf dieselbe Projektion gebracht. Die Radardaten werden dazu benutzt, Satellitenbilder in Zonen mit hoher, mittlerer und niedriger Niederschlagswahrscheinlichkeit zu unterteilen (Satellitenbildklassifikation mittels Radardaten). Unter der Verwendung von Kreuzkorrelationsmethoden wird aus aufeinanderfolgenden Satellitenbildern ein Feld von Wolkenverlagerungen bestimmt. Werden Wolkenverlagerungen für klassifizierte Bilder bestimmt, so können Niederschlagswahrscheinlichkeiten für 1, 1.5 und 2 Stunden vorhergesagt werden. Zur Bestimmung der Qualität der Vorhersage werden die vorhergesagten mit aktuellen Bildern verglichen.

1. INTRODUCTION

The present study has the aim to clarify the possibilities of a joint use of digital radar and satellite data to predict the probability of rain occurrence up to 2 hours ahead (nowcasting).

First of all both types of data should be transformed into a common coordinate grid. It has been found convenient to transform satellite data into the local radar coordinate system. As a next step the radar data (precipitation and no-precipitation pixels) are used to construct a discriminative function, which is then used to divide satellite picture into region of high (≥50%), moderate (≥30%) and low (<30%) rain probability.

By moving regions of IR satellite pictures between successive images and calculating cross-correlation coefficients a field of cloud movements as seen by satellite is determined.

With the field of cloud motions a displacement of the classified parts of the satellite picture gives a prediction of rain occurrence probability. This picture has to be compared with observed pictures in order to determine the forecast quality. Such a comparison performed for one situation gives encouraging results.

2. DATA

The Automated Radar System (ASR) [Ciach et al., 1991] is composed of a MRL-5 radar, APOS equipment of radar control and radar signal digitising, IBM PC network and software. The system installed in the Centre of Aerology of the Institute of Meteorology and Water Management in Legionowo (Poland) has been operating every 10 minutes 24 hours a day since 3 June 1991. The radar observation comprises scans up to 250 km in range and 20 km in height. From radar data processing radar reflectivity maps on 6 levels, maps of echo tops, maps of precipitation intensity and maps of recognised meteorological phenomena are obtained. Full space scan data are archived every hour on a disk, two maps (echo tops and precipitation intensity) every 10 minutes.

A receiving station of METEOSAT digital data (UKWTechnik) is available at the Centre of Aerology since August 1992. Satellite data files are archived only sporadically when the situation is considered to be interesting.

The present work is based on both types of archive data.

3. ANALYSIS

3.1 COMBINING RADAR AND SATELLITE PICTURES

The satellite data are transformed with help of the IMAGE programme (part of the ASR system) into local radar coordinates using obvious geometrical considerations. Experience has shown that quite often a spatial discrepancy between radar (e.g. echo tops map) and satellite (e.g. IR) pictures is observed. As Poland is seen from METEOSAT at a rather inclined angle, it has been supposed that a parallax error may be at least partially responsible for this discrepancy. To account for the parallax the radiance temperature, determined from the IR satellite picture, is transformed into cloud top height using the standard atmosphere. The following approximate empirical formula for cloud top height [km] has been obtained:

$$h = \frac{p^2 - 260p + 19200}{960} \tag{1}$$

where p-value of IR pixel ($p<130$; if $p \geq 130$ it is rather ground than a cloud).

Then for a pixel with value *p*, the Earth radius is increased by the cloud top height derived and the geometrical transformation is performed. The satellite picture is transformed going from North and East, as in that direction the satellite is projecting its picture. Using this transformation some shadows (i.e. empty pixels) appear in the transformed satellite picture. The cloud top heights determined in this manner are stored to be used for a parallax correction in transformation of visible (VIS) and water vapour (WV) pictures. A subjective comparison of corrected and not corrected pictures with corresponding radar pictures shows that this parallax correction improves to some degree the spatial coincidence of both kinds of data.

Even after the parallax correction sometimes some discrepancy between radar and satellite picture is observed. Moving the radar (echo tops) against the satellite (IR) picture and searching for maximum cross-correlation between them one can determine an additional correction (displacement) for the satellite picture. These two corrections (parallax and shift according to correlation) permit to obtain sometimes a good coincidence of both pictures but unfortunately not every time.

Observing animated satellite pictures with some ground features well visible (e.g. the Alps, Balaton Lake, sea coast and mountains in Africa), one can observe that sometimes the features move and twist from picture to picture, too. Therefore this means that strict coincidence of both types of pictures is impossible. Consequently, there exist situations for which a prediction by this method is impossible, too. As for now it cannot be stated how often those situations appear.

3.2 CLASSIFICATION OF SATELLITE PICTURES USING RADAR DATA

The algorithm of satellite data classification is as follows:

1. Data:
   R(X,Y) - radar field of precipitation and no-precipitation pixels (1 and 0 values),
   IR(X,Y) - satellite infrared field (128 values),
   VIS(X,Y), or WV(X,Y) - satellite visible or water vapour field (128 values),
   X, Y - local radar coordinates,
   p1, p2 - threshold levels of precipitation probability (default 0.5 and 0.3).
2. Take (IR, VIS) or (IR,WV) as phase space and create frequency histograms HP for precipitation and HN for non-precipitation elements. Find highest IR value (IRmax) for precipitation.
3. Find centres of gravity CP = (UP, VP) and CN = (UN, VN) for both histograms in (IR, VIS) or (IR, WV) space.
4. If the distance D between CP and CN is small (< 2 units in IR, VIS or IR, WV space) - discrimination is impossible, go to END
5. Divide subsequently (k = 1, 2,..39) the phase space into two regions in such a way that an element belonging to the first region is k:(40-k) times closer to CP than to CN. Each time (for each k) find in the first region the number of precipitation (NP) and non-precipitation (NN) elements. If NP/(NP+NN) > p1 the first region is considered as discriminating precipitation with probability higher than p1. The highest k, fulfilling the condition, is stored as discriminating value (k1). Make the same with p2 to obtain k2. Thus 7 values (IRmax, UP, VP, UN, VN, k1, k2) form two discriminative functions for p1 and p2 probabilities.

6. Apply the discrimination to satellite data and create a picture in radar coordinates of high (>p1), medium (>p2) and low precipitation probability. The discrimination is performed as follows:

   If for some pixel IR<IRmax and the distance (in IR, VIS or IR,WV space) to CP is k1:(40-k1) smaller than the distance to CN - then the pixel is a precipitating one with p>p1.

   If not, but IR<IRmax and distance (in IR, VIS or IR,WV space) to CP is k2:(40-k2) smaller than distance to CN - then the pixel is precipitating with p>p2.

   If neither condition is satisfied, the pixel is considered as non-precipitating (probability of precipitation not greater than p2).
7. Store the discriminative values on disk for subsequent application to satellite picture in greater area than the radar coverage.
8. END.

The discriminative values can be applied to actual satellite data (used to create the discriminative function) or to past and future data, e.g. if there are not enough precipitation elements under radar coverage to create the actual discrimination function.

The visible (VIS) or water vapour (WV) data is used accordingly to its accessibility (e.g. there are no visible data in the night) and usefulness (e.g. in winter the visible data are not very informative).

3.3 FIELD OF CLOUD MOTION

As the precipitation forecast should be applied to the territory of Poland, the satellite picture is limited to this territory with some surroundings. 35 regions of 30 x 30 pixels have been chosen for cloud movement determination. They cover the area between approximately the south-western part of the Scandinavian Peninsula, the north-eastern part of Adriatic, the north-western part of the Black Sea and the Riga Golf.

Every 30 x 30 pixel region at time H (actual) is moved as far as 24 pixels in N, S, W and E direction and compared to the corresponding pixels at H30 min (previous). For each displacement the correlation coefficient between the two fields is calculated. The displacement resulting in the highest value of the coefficient is considered as actual cloud movement for the region. The correlation is not computed if the region contains too few cloud elements (< 100 in any of actual and previous region). The movement is expressed in number of pixels in N-S and E-W direction.

Having computed cloud motion in every region (where possible), the average motion vector is calculated. Then all regions are analysed: if a local vector differs in direction by more than 90^o from the average vector or from any vector from close surroundings, the vector is rejected as outstanding, and the region is treated as if the vector has not been calculated. As a next step, for all regions, where the motion vector is not determined, a mean motion vector from the surroundings is calculated, if possible.

Then a smoothing procedure is applied to the motion field: every vector is replaced by a weighted averaged vector from the region and surroundings, where the region is taken with weight 4, and neighbouring regions (with existing vectors) with weights 1. In such a way the field of motion is devoid of random fluctuations usually existing when cross-correlation procedures are used.

An animation of a time sequence of such smoothed fields shows a good continuity of the motion.

3.4 AN ATTEMPT OF PRECIPITATION PROBABILITY NOWCASTING

Areas of a satellite picture (IR, VIS) or (IR, WV), classified into regions of high, moderate and low precipitation probabilities, are displaced according to the motion determined as above for 60, 90 and 120 minutes ahead forming predicted pictures (nowcasting) of different levels of precipitation probability. They are then compared with actual pictures classified in the same way. A test of such a nowcasting technique has been performed for the territory of Poland (11 regions 30 x 30 pixels) using data of 10 August 1993. Every region has been divided into 36 sub-regions 5 x 5 pixels. In every sub-region the maximum precipitation probability both from predicted and actual pictures has been determined. A comparison between predicted and actual classes as of maximum precipitation has been calculated. The results are presented in table 1, 2 and 3. In the tables class 0 means low, class 1 moderate, and class 2 high precipitation probability.

Table 1: Comparison of predicted and actual class of maximum precipitation probability (number of cases in sub-regions of 5 x 5 image pixels).
Forecast for 1 hour - 4 situations of 10 August 1993

	Predicted		
Observed	Class 0	Class 1	Class 2
Class 0	182	70	0
Class 1	35	875	233
Class 2	0	105	102

Table 2: Comparison of predicted and actual class of maximum precipitation probability (number of cases in sub-regions of 5 x 5 image pixels).
Forecast for 1.5 hour - 4 situations of 10 August 1993

	Predicted		
Observed	Class 0	Class 1	Class 2
Class 0	168	92	1
Class 1	48	823	289
Class 2	0	111	52

Table 3: Comparison of predicted and actual class of maximum precipitation probability (number of cases in sub-regions of 5 x 5 image pixels).
Forecast for 2 hours - 3 situations of 10 August 1993

	Predicted		
Observed	Class 0	Class 1	Class 2
Class 0	123	76	4
Class 1	35	602	246
Class 2	0	82	20

The results seem to be encouraging. The greatest numbers tend to be close to the diagonal. When the class 0 is predicted, there does not exist any class 2, even for 2 hours forecast. Class 2 is not so well predicted, but the number of cases with observed class 0 is very small.

4. DISCUSSION

The results and algorithms presented above should only be considered as preliminary. There still remain a lot of problems to be resolved. First of all the coincidence of radar and satellite pictures is not always good enough to perform satellite data classification. It should be stressed that the lack of coincidence can be explained to some degree by the completely different type of teledetection by radar and satellite. One can say that radar makes a sort of X-raying of precipitating clouds while satellite gives a "flat" picture from above. The satellite detects e.g. Cirrus clouds which are nearly undetected by radar, so an attempt to correlate radar echo tops with cloud tops defined by their radiance temperature may lead to confusing results.

Nevertheless the comparison of predicted and observed pictures shows that at least in some cases such a forecast is possible and can be useful.

REFERENCES

CIACH C.G., P.M. DEWISZEK and Z.W. DZIEWIT, 1991: Automatic Meteorological Radar System Based on MRL-5 Radar and Network of IBM-PC Computers, 25th International Conference on Radar Meteorology, June 24-28 1991, Paris, France, AMS

Author's address

STANISŁAW MOSZKOWICZ
Centre of Aerology
Institute of Meteorology and Water Management
Legionowo
POLAND

ANALYSES OF VERTICAL CROSS SECTIONS AND THEIR COMBINATION WITH SATELLITE IMAGES

CEI PROJECT BETWEEN ZAMG (VIENNA) AND MHS (ZAGREB)

Subproject of the CEI Project "*Remote Sensing Methods in Meteorology and Their Application in Nowcasting*"

PART I:	**INTRODUCTION AND AIMS OF THE PROJECT**
PART II:	**HRID: THE CROSS SECTION METHOD AT THE MHS ZAGREB**
PART III:	**THE CROSS SECTION METHOD AT THE ZAMG (VIENNA)**

VERTICAL CROSS SECTIONS - A PROJECT BETWEEN AUSTRIA AND CROATIA

PART I: INTRODUCTION AND AIMS OF THE PROJECT

Central Institute of Meteorology and Geodynamics, Vienna, Austria

VERONIKA ZWATZ-MEISE

During the first meeting of the participants of the CEI project "Remote sensing methods in meteorology and their application in nowcasting" (Budapest, 1992) it was recognized that there are developments in the field of vertical cross sections at the ZAMG (Vienna) as well as at the MHS (Zagreb). Although the basic ideas about a use of those tools for synoptic research and operational work are very similar in both institutes, there are different mathematical approaches, different parameters and different data sources.

So the model used at Zagreb (HRID, see part II) has a physical basis while at ZAMG (see part III) a merely mathematical analysis method is used. At Zagreb, single station analyses, time and space cross sections (restricted to W-E and N-S directions) are available; at Vienna, only space cross sections but with an arbitrary orientation are computed.

At Zagreb the data basis are (for operational purposes) radiosonde measurements while at Vienna radiosonde measurements, ECMWF analysis and forecast data and satellite signals are used and combined operationally.

Besides parameters computed in both institutes (potential and equivalent-potential temperature, relative humidity) at Zagreb a couple of parameters in a local scale, mostly being a measure for stability, are used while at Vienna synoptic and meso-scale parameters are computed from ECMWF data and combined with satellite signals.

Thus this initial situation is a very lucky basis for a combination of both methods leading to a supplementation of results for both institutes.

The main aims of the project can be summarized as follows:

1) test and comparison of the mathematical models and a test of the quality of the derived parameters.

   The result should be a final combined model which is appropriate for the evaluation of tropospheric weather phenomena in different scales.

The test and comparison is made in several ways:

- with help of case studies stressing the abilities of the different models and parameters for determining weather phenomena.
- By theoretical and numerical investigations of different interpolation techniques including the one used in HRID, the Polynomial Hydrostatic Adjustment Technique (PHAT).
- By a test of the usefulness of one of the parameters derived by HRID, the Richardson number, for detecting Clear Air Turbulence (CAT). This test is planned in tight cooperation with the aviation weather service (Vienna) which contributes the pilot reports of observed CAT. This test can clarify the potential of this part of the HRID output for CAT warnings.

2) The study of tropospheric weather processes in different scales contained in the diverse parameters of the cross sections and the development of conceptual models. Interactions between stratospheric and tropospheric processes.

Besides new insights into the physical processes the output of this investigation shall lead to a basic manual for the use of vertical cross sections in synoptic research and operational service.

For this joint work 4 fixed cross sections have been chosen which are computed and archived twice daily and the features exhibited by the different programs are compared and the physical situation investigated.

A:	07145 Paris	07180 Nancy	10739 Stuttgart	10868 Munich	11035 Vienna	12843 Budapest		
B:	07510 Bordeaux	07481 Lyon	16080 Milan	16044 Udine	13130 Zagreb	15120 Cluj		
C:	06181 Kopenhagen	09184 Greifswald	09393 Lindenberg	09486 Wahnsdorf	11520 Prag	11035 Vienna	13130 Zagreb	16320 Brindisi
D:	10035 Schleswig	10338 Hannover	09548 Meiningen	10739 Stuttgart	16080 Milan	07761 Ajaccio	16560 Cagliari	

Besides the aims of the project mentioned before an additional important aim refers to the satellite material: the introduction of the remote sensing data in conventional data evaluation systems (the cross sections) and the combined use of three data sources (radiosondes, numerical model output, satellites). This is exactly the way the meteorological community has agreed to be the best one in respect to satellite information (Workshop on the Use of Satellite Data in Nowcasting and Very Short Range Forecasting, 1990). At present the numerical model used is the ECMWF model. It is intended to include in a second step data from limited area models like Aladin which will be available at the ZAMG from autumn 1994.

PART II:

HRID: THE CROSS SECTION METHOD AT THE MHS ZAGREB

METHODOLOGY AND APPLICATION OF THE HIGH RESOLUTION ISENTROPIC DIAGNOSTIC MODEL (HRID)

Meteorological and Hydrological Service, Zagreb, Croatia

DRAŽEN GLASNOVIĆ, IVAN ČAČIĆ and NATAŠA STRELEC

ABSTRACT

This paper gives a detailed review of the contribution of Croatian scientists to the CEI joint Project "Remote sensing methods in meteorology and their application in nowcasting". The high resolution isentropic diagnostic model (HRID) based on the polynomial hydrostatic adjustment technique (PHAT) represents a methodology to compute vertical cross-sections in time and space. In order to improve diagnostics of the atmospheric stratification a number of thermodynamic and stability parameters have been involved and related to the energy changes. Special attention has been paid to the interpretation of the meteorological phenomena in the cross-sections and particularly to the comparison of differences in their visualization in both the potential temperature and geometrical height coordinate systems. It is shown that such objectively derived cross-sections have a sensitivity and resolution good enough to resolve the processes not only on the synoptic, but also on the lower scales.

ZUSAMMENFASSUNG

Diese Abhandlung beabsichtigt einen ausführlichen Überblick über den Beitrag von kroatischen Wissenschaftlern zu dem CEI Gemeinschaftsprojekt "Remote Sensing Methoden in der Meteorologie und ihre Anwendung auf das Nowcasting" zu geben. Das hochauflösende Diagnosemodell HRID, das auf der Polynomial Hydrostatic Adjustment Technique (PHAT) basiert, repräsentiert eine Methode, um zusammengesetzte vertikale zeitliche und räumliche Querschnitte zu konstruieren und zu interpretieren. Um die Diagnostik der atmosphärischen Schichtung zu verbessern, wird eine Zahl von thermodynamischen und Stabilitätsparametern betrachtet und in Bezug zu den Energieänderungen gesetzt. Spezielle Aufmerksamkeit wird sowohl der Klärung und Erklärung von Phänomenen in den räumlichen und zeitlichen Querschnitten als auch dem Vergleich von Unterschieden in der Visualisierung geschenkt. Es wird gezeigt, daß solche objektiv abgeleiteten Querschnitte genügende Empfindlichkeit und Auflösung haben, um nicht nur die Prozesse des synoptischen, sondern auch kleinerer Bewegungs-Scales zu erfassen.

1. INTRODUCTION

Insight into the nature of atmospheric processes, as well as into the very complex mechanisms of their onset and development, strongly depends on the available objective methods. The elaboration of new, more sophisticated computational techniques and their proper integration into the overall diagnosis should result in better resolution of lower scale processes and more appropriate interpretation of series of objectively derived meteorological fields. At NMC Zagreb, a diagnostic model named "High Resolution Isentropic Diagnosis" (hereafter: HRID) was developed. Its main part consists of high resolution isentropic time and space cross-sections as well as "the isentropic high resolution 2+1D diagnosis" of combinations of various parameters or their changes. The methodology of HRID has been worked out in detail by Glasnović (1978,1983,1990; hereafter G78,G83,G90) and applied in Glasnović and Jurcec (1990) as well as in Jurcec and Glasnović (1991) to specific problems. Since June 1993, the further development of the considered model is a part of a bilateral research project undertaken by Croatia and Austria within the "Central European Initiative" (hereafter: CEI).

The basic method of the HRID is the "Polynomial Hydrostatic Adjustment Technique" (hereafter: PHAT). Its crucial point is related to the special subject of interest, where the key-question is: "How to achieve a broader and better application of the well-known thermodynamic and hydrodynamic principles in a computational procedure minimizing the influence of systematic computational errors?" Also, PHAT takes into account the fact that many changes in the atmosphere do not happen linearly so that nonlinear approximation of the meteorological parameters by polynomials would be a better way to calculate them. Accordingly, it includes a high resolution of input parameters on predetermined isentropic levels, where any of the polynomials from the first to the eighth degree as well as the uppermost level of the analysis and its vertical resolution degree may be chosen arbitrarily. Instead of applying the finite difference approximations PHAT involves both the isentropic hydrostatic relations and their derivatives of higher order. Another obvious difference between the present approach and the other interpolation routines is in the selection of the interpolation function. Although the Hermite interpolation scheme is used, here it is essentially modified.

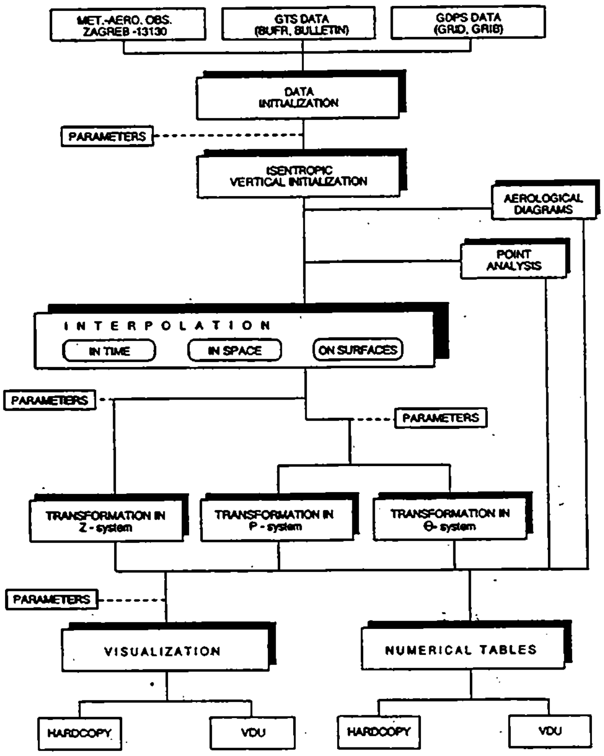

Figure 1.1: Flow diagram of the isentropic diagnostic model HRID

A detailed information on the flow diagram of the model is given in Figure 1.1. The HRID software structure is a modular one, enabling simple control, optimization and development. After the input data assimilation process, vertical initialization is started by defining the upper and lower analysis levels and determining the interpolation polynomial degree. As a next step, the interpolation and transformation into arbitrarily selected coordinate systems are performed. For interpretation, the user selects parameters and the form of the graphical presentation. During the operational application of HRID special attention will be paid to its objective interpretation in connection to satellite and radar products.

2. "HRID" - ISENTROPIC DIAGNOSTIC MODEL

Besides a detailed presentation of the existing atmospheric structure, the basic purpose of the high resolution isentropic model is a better calculation of the low scale and short duration processes. A good example to illustrate the former is upward frontal streaming, which is rather turbulent and not uncommon in the relatively narrow inclined zones. Taking into consideration the fact that the horizontal component of the frontal level surface inclination is significantly bigger than the vertical one, it becomes evident that the distance between two relevant points along the vertical line should necessarily be around 100 meters. Thorpe (1993) points out that for the optimal resolution of the sloping frontal zones the numerical grid should be constructed in such a way that the ratio of the vertical and horizontal distance between the points is close to the frontal inclination.

Basically, the objectively derived time and space cross-sections are two-dimensional using an isentropic coordinate system with time or space as horizontal axis and with the potential temperature in the vertical. A changeable grid depending on the prevailing atmospheric processes is usually obtained in construction of the isentropes. The spatial distribution of isentropes as well as their shape and associated grid-point values of parameters involved gives a powerful tool for a discussion of the physics of predominant atmospheric processes.

Default values are 1K in the vertical up to 100 hPa leading to about 120 - 180 isentropic levels. This means that an average distance between two adjacent isentropes is about 100 m or less than 50 hPa, depending on the prevailing atmospheric stability. The horizontal resolution default is one hour in the time scale and 10' for the space cross-section.

2.1 ANALYTICAL METHOD FOR VERTICAL INITIALIZATION

For vertical initialization, the modified Hermite polynomial interpolation routine is applied. Shapiro and Hastings (1973) were the first to introduce this computational procedure into meteorology, but it was successfully applied only in horizontal interpolation. The attempt of its application in the vertical resulted in a series of inconsistent phenomena, for instance formation of unrealistic superadiabatic gradients both in the free atmosphere and close to the ground and entwining of isentropes in certain parts of the numerical field. The failure, as was shown in G83, was a direct consequence of the approximation in finite differences and of the truncation error implicitly contained by such a calculation of vertical changes over the various thickness layers.

As shown in G83 and G90 these problems can be avoided by applying PHAT and by a modification of the Hermite interpolation routine. A simplified example of the so-defined computational scheme is given in the Figure 2.3.1 where the index i denotes end-points of the interpolation interval where input data are defined and the index j interpolation levels for the output values, vertical resolution being unambiguously determined by the previously defined series y_j (for j = 1, 2,...). The general form of the interpolation polynomial is given by the relation

$$y_n^{(m)}(x) = m!\sum_{k=m}^{n}\binom{k}{m}x^{k-m}a_k \tag{2.1.1}$$

where the index n indicates the polynomial degree, and the index m the derivative order.

Therefore, the basic polynomial (m=0) of the n-th degree may be expressed as

$$y_n(x) = \sum_{k=0}^{n}\binom{k}{0}x^k a_k \tag{2.1.2}$$

The interpolation routine is defined by the algebraic system of equations which includes a certain series of polynomial pairs of arbitrarily chosen degree n and their derivatives of a different order m. These polynomial pairs are formed in the end-points of the interpolation intervals. The first two equations are the basic polynomials defined by the relation (2.1.2) and each subsequent pair relates to the derivatives of a subsequently higher order m given by the general relation (2.1.1). In distinction to the original Hermite interpolation routine, the modified system of algebraic equations does not contain all of the basic polynomial derivatives. Therefore at selecting the fifth polynomial degree, for n=5, the basic system will contain six equations with six unknowns which are expressed in the form

$$\begin{aligned}
y_i(x) &= \sum_{k=0}^{5}\binom{k}{0}x_i^k a_k \\
y_{i+1}(x) &= \sum_{k=0}^{5}\binom{k}{0}x_{i+1}^k a_k \\
y_i^{(2)}(x) &= 2!\sum_{k=2}^{5}\binom{k}{2}x_i^{k-2}a_k \\
y_{i+1}^{(2)}(x) &= 2!\sum_{k=2}^{5}\binom{k}{2}x_{i+1}^{k-2}a_k \\
y_i^{(4)}(x) &= 4!\sum_{k=4}^{5}\binom{k}{4}x_i^{k-4}a_k \\
y_{i+1}^{(4)}(x) &= 4!\sum_{k=4}^{5}\binom{k}{4}x_{i+1}^{k-4}a_k
\end{aligned} \tag{2.1.3}$$

where only the second and fourth derivatives of the basic polynomial are taken into consideration, while the first and the third ones are left out.

The vertical interpolation procedure consists of two separate steps. The first step determines the system unknowns ak. For n=5 it amounts to a total of six coefficients, which are calculated on the basis of the available series of known values y (x) and x, but also of their derivatives in the end-points of the interpolation intervals. After the field of coefficients has been determined, by their substitution into the interpolation polynomial

$$y_j(x) = \sum_{k=0}^{5}\binom{k}{0}a_k x_j^k \tag{2.1.4}$$

interpolated values and their higher derivatives

$$y_j^{(m)}(x) = m!\sum_{k=m}^{5}\binom{k}{m}a_k x_j^{\,k-m} \qquad (2.1.5)$$

are calculated on predetermined interpolation levels x_j.

Modification of the original Hermite interpolation routine offers considerably more options for the formation of the symmetrical matrix of the basic algebraic system. In the case of selecting the polynomial of the seventh degree, the system should encompass a total of 8 equations which will, in their optimal combination, besides the basic pair of polynomials, include also their derivatives of the second, fourth and sixth order. At that, the first or any other subsequent derivative can be left out, on the condition that it preserves and implicitly contains the physical and mathematical properties of all of its lower grade predecessors.

2.2 POLYNOMIAL HYDROSTATIC ADJUSTMENT TECHNIQUE

A successful application of the modified Hermite interpolation routine requires an unambiguous answer to the following key issue: What is the way of calculating derivatives of the higher order in the end-points of the interpolation interval. As proposed in G83 and G90, PHAT is used for the calculation of the derivatives $y_i^{(n)}$ in (2.1.3). It is based on the isentropic hydrostatic equation

$$\frac{\partial M}{\partial \theta} = \varepsilon \qquad (2.2.1)$$

where the Montgomery's potential is defined by the relation

$$M = \varepsilon\theta + \phi \qquad (2.2.2)$$

and Exner's function, also called "modified pressure", by

$$\varepsilon = c_p(p/p_o)^{\kappa} \qquad (2.2.3)$$

where $\kappa = R/c_p$, with R as gas constant of air and c_p as specific heat at constant pressure. Choosing the pressure p as an interpolation function y(x) within the system of equations (2.1.3), and potential temperature Θ as an independent variable x, PHAT offers a possibility of a simple calculation not only of the first, but also of all higher order derivatives of p in respect to Θ. An alternative relation for the reciprocal value of the thermal stability is

$$\frac{\partial p}{\partial \theta} = -\frac{p}{\kappa\theta} \qquad (2.2.4)$$

By the multifold differentiation of the equation (2.2.4) a general functional relation for the m-th derivative of pressure is obtained in the form of a differential equation

$$p^{(m)}(\theta) = \frac{\partial^m p(\theta)}{\partial \theta^m} = (-1)^m \frac{\prod_{k=1}^{m}[1+(k-1)\kappa]}{\kappa^m}\frac{p}{\theta^m} \qquad (2.2.5)$$

derived in G83. On the basis of the relation (2.2.5) it can easily be concluded that for the calculation of pressure changes with potential temperature it is not necessary to use approximations in finite differences. This implies that the pressure values and potential temperatures in the end-points of each interpolation interval are sufficient to solve the algebraic equation system (2.1.3). An equally relevant and very useful feature of this relation can easily be discerned from its alternative form

$$p^{(m)}(\theta) = -\frac{1+(m-1)\kappa}{\kappa\theta}\frac{\partial^{m-1}p}{\partial\theta^{m-1}} \tag{2.2.6}$$

which has proved to be very convenient for writing computer programs. It shows that each higher derivative implicitly contains the physical and mathematical properties of its predecessors, entirely meeting the basic consistency condition of the modified Hermite interpolation routine application. Such a localization of mathematics on infinitesimal surroundings of interpolation points ensures to a large extent minimization of the influence of systematic numerical errors and, by that means, preserves the most subtle characteristics of atmospheric structure in the objective analysis. Although the considered objective technique is strictly hydrostatic, it is due to the mathematical localization that it can be successfully applied in a positively nonhydrostatic atmosphere, which is more than once shown in this paper.

In addition to that, PHAT offers the possibility of a transition from the isentropic into any other coordinate system, as well as the calculation of a series of derived thermodynamic parameters in this system. When selecting z as vertical coordinate, the model applies an alternative form of the isentropic hydrostatic equation

$$\frac{\partial z}{\partial\theta} = \frac{\varepsilon}{g} = \frac{c_p}{g}\left(\frac{p}{p_o}\right)^{\kappa} \tag{2.2.7}$$

by whose multifold differentiation a general equation for the calculation of its higher derivatives is obtained in the form of

$$z^{(m)}(\theta) = \frac{\partial^m z(\theta)}{\partial\theta^m} = (-1)^{m-1}\frac{\prod_{k=1}^{m-1}[1+(k-1)\kappa]}{\kappa^{m-1}\theta^{m-1}}\frac{\partial z}{\partial\theta} \tag{2.2.8}$$

Still, in order to reduce the calculation time, it is considerably more economical to use its alternative form

$$z^{(m)}(\theta) = -\frac{[1+(m-2)\kappa]}{\kappa\theta}\frac{\partial^{m-1}z}{\partial\theta^{m-1}} \tag{2.2.9}$$

implicitly containing the numerical values of lower derivatives calculated in the previous mathematical step.

For the interpolation of potential temperature onto the arbitrarily chosen geometrical height levels, PHAT applies the following relations

$$\theta^{(m)}(z) = \frac{\partial^m\theta(Z)}{\partial z^m} = \frac{1}{\theta^{m-1}}\left(\frac{g}{\varepsilon}\right)^m \tag{2.2.10}$$

or

$$\frac{\partial^m \theta(z)}{\partial z^m} = \frac{g}{\varepsilon\theta} \frac{\partial^{m-1}\theta}{\partial z^{m-1}} \tag{2.2.11}$$

which are used for transition from the isentropic into the geometrical height coordinate system. A similar approach can be applied for any basic thermodynamic parameters combination. For example, the change of the Exner function in respect to the temperature at any isentropic level could be presented as

$$\frac{\partial \varepsilon(T)}{\partial T} = \frac{1}{1-\kappa} \frac{\varepsilon}{T}, \quad \varepsilon = c_p T / \theta \tag{2.2.12}$$

at which its m-th derivative takes the form

$$\varepsilon^{(m)}(T) = \frac{\partial^m \varepsilon(T)}{\partial T^m} = \frac{\prod_{k=1}^{m} [(k-1)(k-2)+1]}{(1-\kappa)^m} \frac{\varepsilon}{T^m} \tag{2.2.13}$$

It is evident that PHAT is characterized by such features which enable a more economical and correct vertical initialization than application of any conventional numerical methods. Avoiding approximations in finite differences and any kind of averaging during calculation just ensures a better implementation of lower scale processes.

2.3 NUMERICAL ROUTINE FOR HORIZONTAL INTERPOLATION

The routine for interpolating in the horizontal coordinate, time or space, applied by the HRID model has been worked out in G90, and is based on Hermite's third degree polynomials. In order to preserve tendencies from the previous interval the successive interpolation method is used. On the contrary to PHAT, in computation of the derivatives finite differences are used. The initial algebraic system, created in the end-points of interpolation interval at coordinates t_i and t_{i+1}, consists of four equations in the following forms:

$$\begin{aligned} p_i(t) &= t_i^{\,2}A + t_i^{\,2}B + t_iC + D \\ (\frac{\partial p}{\partial t})_i &= 3t_i^{\,2}A + 2t_iB + C \\ p_{i+1}(t) &= t_{i+1}^{\,3}A + t_{i+1}^{\,2}B + t_{i+1}C + D \\ (\frac{\partial p}{\partial t})_{i+1} &= 3t_{i+1}^{\,2}A + 2t_{i+1}B + C \end{aligned} \tag{2.3.1}$$

By the successive shifting of the starting point during interpolation and positioning into the first, i.e. left-hand side point of each interpolation interval, the variable t becomes identically equal to zero, so the coefficients $C=(\partial p/\partial t)_i$ and $D=p_i$ can easily be determined directly from the input data. At the same time, by rearrangement, the algebraic system (2.3.1) is reduced to two equations

$$t_{i+1}^{\,3}A + t_{i+1}^{\,2}B = (p_{i+1} - p_i) - (\frac{\partial p}{\partial t})_{i+1} \tag{2.3.2}$$

$$3t_{i+1}^{2}A + 2t_{i+1}B = \left(\frac{\partial p}{\partial t}\right)_{i+1} - \left(\frac{\partial p}{\partial t}\right)_{i} \qquad (2.3.3)$$

with two unknowns A and B which are determined along the single isentropes between points p_i $(0,p_i)$ and p_{i+1} (t_{i+1}, p_{i+1}). Upon determining the coefficients A and B, knowing the values C and D, the interpolated pressure p is calculated for an arbitrarily chosen coordinate τ_k by their substitution into the interpolation polynomial

$$p_k(\tau) = A\tau_k^{3} + B\tau_k^{2} + C\tau_k + D \qquad (2.3.4)$$

and its changes with horizontal coordinate t according to the relation

$$\left[\frac{\partial p(\tau)}{\partial t}\right]_k = 3A\tau_k^{2} + 2B\tau_k + C \qquad (2.3.5)$$

The Figure 2.3.1 gives a simplified illustration of the above described numerical scheme, which comprises successive interpolations with the changeable left-hand side "end-point" of the time or space interval along a particular isentrope.

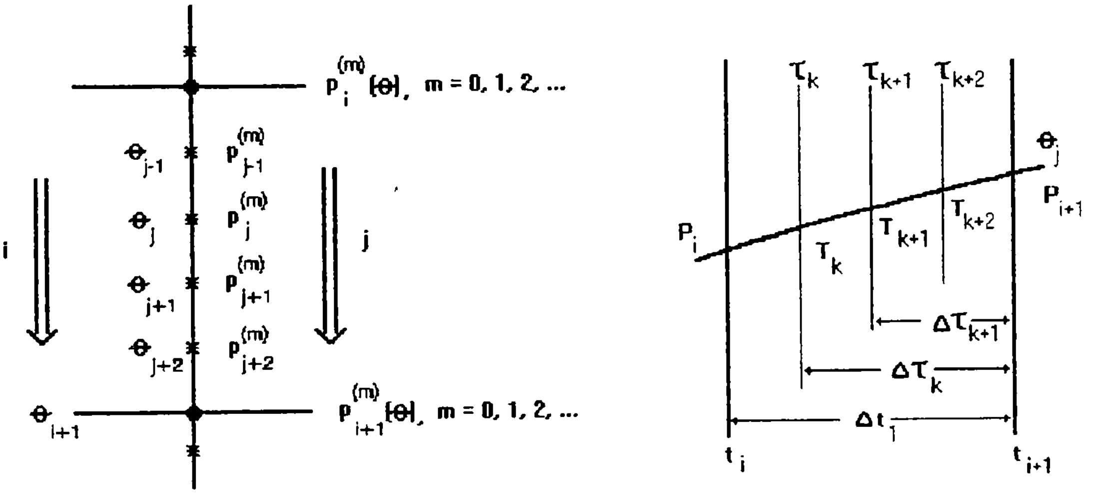

Figure 2.3.1: Left side: illustration of a scheme for vertical interpolation of parameters
Right side: a scheme for horizontal (time or space) interpolation

3. PACKAGE OF DIAGNOSTICS

One of the aims of the project is to produce a package of diagnostic tools for a deeper insight into the vertical structure of the atmosphere. Accordingly, a number of thermodynamic and stability parameters has been choosen and their vertical profiles were calculated by use of PHAT. The resulting curves consist of more than one hundred points with every numerical value being strictly related to the infinitesimal neighbourhood of its location.

The considered package combines the thermal and dynamic as well as energy and stability features of the atmospheric structure in the unsaturated and saturated air. Besides the basic meteorological variables, the following derived parameters are computed: real and hydrostatic

Brunt-Vaisala frequency, Scorer parameter, Richardson number, dimensionless energy number, temperature and potential temperature lapse rates, vertical acceleration, specific and relative humidity, the mixing ratio and the equivalent potential temperature.

3.1 BRUNT-VAISALA FREQUENCY

Many studies (see Turner,1973) concerning the atmospheric static stability involve an important quantity which has the dimension of a squared frequency and may be expressed in the form

$$N^2 = \frac{g}{\theta}\frac{\partial\theta}{\partial z} \tag{3.1.1}$$

containing the gravity acceleration, the potential temperature and its lapse rate. This quantity represents the governing term in a differential equation which describes the motion of an element of inviscid fluid displaced to a small distance vertically from its equilibrium position. The square root of the expression (3.1.1) defines a parameter often called the Brunt-Vaisala frequency or, more descriptively, the buoyancy frequency. The characteristic period $2\pi/N$ of the considered bouyancy oscillations is usually of the order of a few minutes in the statically stable stratified layers of the atmosphere, and of many hours in the deep ocean.

In general, the physical meaning of this stability parameter enables to lay down an appropriate stability criterion. There are three possible states of stability which can clearly be indicated by the Brunt-Vaisala frequency. Any positive value of its square indicates a statically stable state, negative is unstable and for $N=0$ there is a neutral equilibrium.

Introducing the hydrostatic relation (2.2.8) and the Exner function (2.2.3), a hydrostatic Brunt-Vaisala frequency can be derived as

$$N_h = \frac{g}{\sqrt{\varepsilon\theta}} = \frac{g}{\sqrt{c_p T}} \tag{3.1.2}$$

Any point of its vertical profile corresponds to the observed temperature at the given pressure and height representing the frequency of the buoyancy oscillation of an infinitesimal isothermal atmosphere in hydrostatic balance. The combination of the two considered parameters enables the basic stability criterion to be extended as follows

$$\begin{array}{ll} N > N_h & \text{very stable} \\ N = N_h & \text{hydrostatic equilibrium} \\ 0 < N < N_h & \text{relatively stable} \end{array} \tag{3.1.3}$$

which gives an additional information about the existence of very stable layers characterized by temperature inversions as well as the position of hydrostatic equilibrium.

The basic idea is to make comparisons of both, the actual and hydrostatic Brunt-Vaisala frequency curves. According to (3.1.3) figure 3.1.1 clearly indicates five stable layers in the left picture where N is much greater than N_h. At about 16 km a tropopause can be located and a strong temperature inversion at about 11 km. On the other hand, the unstable superadiabatic layers can be recognized as the layers between two points where the solid curve reaches the neutral stability line for $N=0$. At the moment, the vertical profile is restricted to positive values, because the buoyancy frequency N is not a real number when its square is negative. Therefore, an unstable state characterized by superadiabatic layers should be represented as a complex number in the imaginary part of the complex plane.

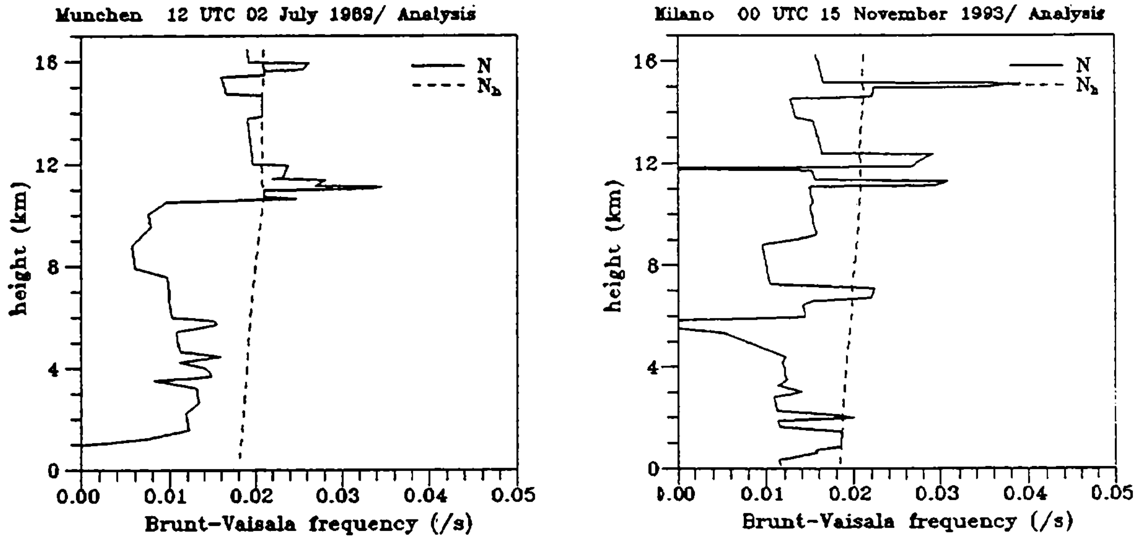

Figure 3.1.1: An example of the high resolution vertical profile of the actual Brunt-Vaisala frequency (solid line) in respect to its hydrostatic form (dashed line). Two cases are shown: München, 2 July 1989 12 UTC on the left and Milano, 15 November 1993 00 UTC on the right.

3.2 SCORER PARAMETER

Another important quantity, usually called the Scorer parameter, has been involved to describe spatial characteristics of the buoyancy oscillations. The square of considered parameter is expressed by the relation

$$l^2 = \frac{N^2}{u^2} - \frac{1}{u}\frac{\partial^2 u}{\partial z^2} \qquad (3.2.1)$$

with the wind velocity u and its vertical shear and atmospheric stability expressed by the Brunt-Vaisala frequency. Since the non-linear term in (3.2.1) is often neglected, the Scorer parameter may be defined as a ratio of the buoyancy frequency N and the wind velocity taking the form

$$l = \frac{N}{u} \qquad (3.2.2)$$

This parameter has a dimension of the wave number. Its reciprocal $L=2\pi/l$ enables an evaluation of the wave length for buoyancy oscillations of a fluid element in an environment with stable stratification. Following the same approach as for N, the hydrostatic Scorer parameter l_h has been defined by substituting N by N_h in (3.2.2).

So, each one of vertical profiles in Figure 3.2.1 gives an opportunity to make speculations about the wave length of the oscillation which could have occurred. For instance, small values of l refer to possible large oscillations and reduced static stability. Conversely, the large Scorer parameter indicates small oscillation as well as enlarged stability. In addition, having in mind the fact that the fluid elements oscillate only in stably stratified environment any unstable layer characterized by superadiabatic conditions can be identified between two adjacent neutral points for $l=0$. On the other hand, a comparison of the relative position of two considered curves clearly enables identification of the temperature inversions. Such very stable layers exist where the solid curve is located to the right of the dashed one.

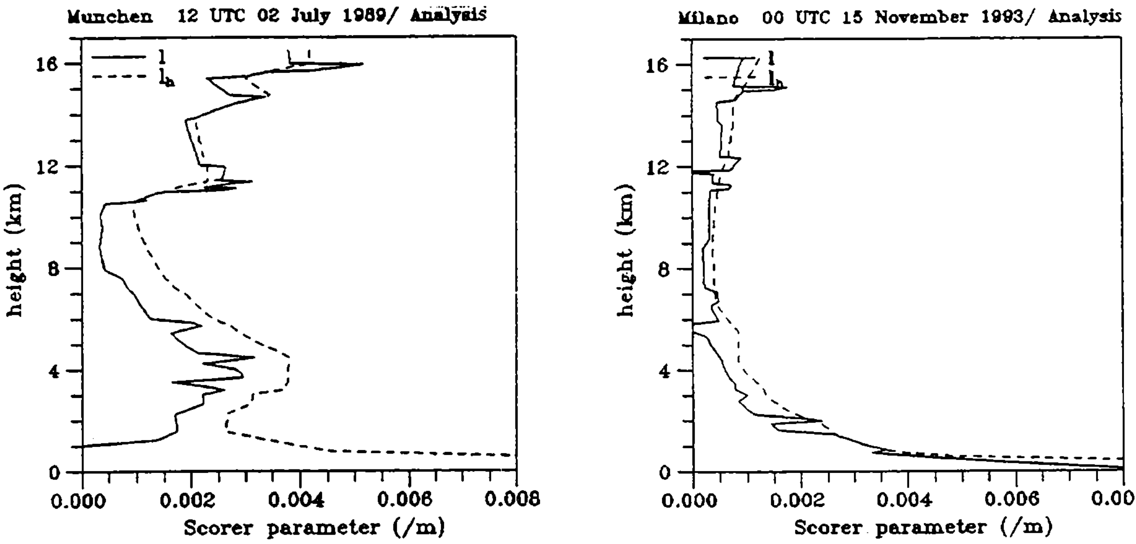

Figure 3.2.1: The high resolution vertical profiles of the actual Scorer parameter (solid line) compared to their hydrostatic curves (dashed line) for the same cases as shown in Figure 3.1.1

According to this, many interesting features in figure 3.2.1 may be clearly recognized. On the right picture for Milano the large wavelengths prevail even at the tropopause level and in the stratosphere including an unstable superadiabatic layer without oscillations from 5.4 to 5.9 km. Very small wavelengths are related to the large values of the Scorer parameter from the ground up to 1 km. The same feature exists for München, but only in the hydrostatic case represented by the dashed line, while the solid curve indicates a superadiabatic layer just above the surface level.

3.3 RICHARDSON NUMBER

The dimensionless Richardson number has been derived by considering the parametrization of the wave problem and it is usually expressed in the form

$$Ri = \frac{\dfrac{g\partial\theta}{\theta\partial z}}{\left[\left|\dfrac{\partial u}{\partial z}\right|\right]^2} \tag{3.3.1}$$

where g is the acceleration of gravity, Θ is the potential temperature, u is the horizontal wind speed and z is the geopotential height. Following the definitions given in the WMO Technical Note No.155, the Richardson number is basically the ratio of the rate of destruction of turbulent energy by the negative buoyancy of the stable layer to the rate of production of turbulent energy by the vertical wind shear. Ri decreases with decreasing static stability and increasing vertical wind shear.

One of the atmospheric phenomena related to the Richardson number is the Kelvin-Helmholtz instability. This is a process of turbulence associated with strong vertical wind shear in a statically stable layer . The energy source for this type of instability is the mechanical energy produced by the vertical wind shear. In the free atmosphere, Kelvin-Helmholtz instability occurs in thin, stable layers, where strong vertical wind shear is present, and is usually called Clear Air Turbulence (CAT). The Richardson number must be lower than a certain critical value to satisfy the conditions for production or intensification of the turbulence. Theoretical predictions and observations agree that $Ri \leq 0.25$ is a necessary, but not sufficient condition for shear induced instability to occur.

An example of the Richardson number profile is given in Figure 3.3.1. Values of Ri less then zero stand for statically unstable layers in the atmosphere. In the figure shown here there is a superadiabatic layer, at about 1 km above the ground, which is represented by $Ri > 0$. Values between 0 and 0.25 (or according to some authors 0.5) represent the layers where CAT occurrence is possible.

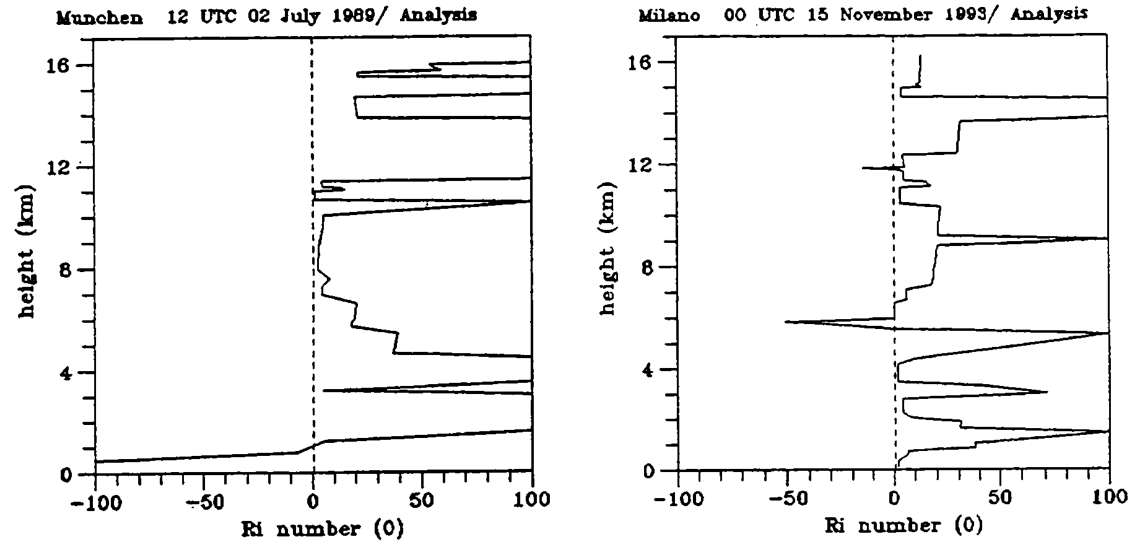

Figure 3.3.1: Profile of dimensionless Richardson number. The dashed line stands for Ri = 0.25 which is the critical value under which turbulence forms and intensifies.

3.4 LAPSE RATES OF TEMPERATURE AND POTENTIAL TEMPERATURE

Another means to examine the stability properties of the atmosphere are the lapse rates of temperature and potential temperature. In Figure 3.4.1 the temperature lapse rate γ is shown by the solid curve. The thicker, vertical solid line stands for a temperature lapse rate equal to the dry-adiabatic lapse rate Γ_d.If the curve of γ is on the right of the Γ_d line it means that the temperature is decreasing faster than in dry-adiabatic air which then represents an unstable layer. On the other hand, if the γ curve is far to the left of Γ_d $(\gamma<<\Gamma_d)$ it represents a very stable layer.

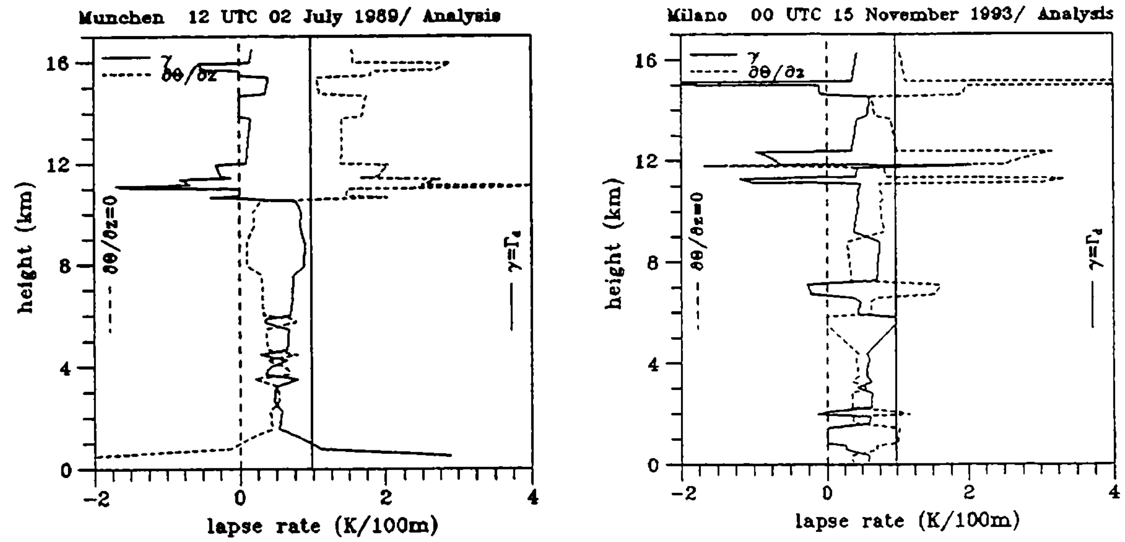

Figure 3.4.1: Lapse rates of temperature and potential temperature for the same cases as shown in Figure 3.1.1

The dashed curve shows the potential temperature lapse rate which can be compared to the vertical dashed line that stands for $\partial\Theta/\partial z=0$. In case of $\partial\Theta/\partial z >> 0$ the layer is very stable, and it is unstable for $\partial\Theta/\partial z < 0$. It can also be seen that the profiles of γ and $\partial\Theta/\partial z$ are reversely proportional (in fact they are almost mirror reflected) whereby the $\partial\Theta/\partial z$ curve shows more sensitivity to changes.

3.5 DIMENSIONLESS ENERGY NUMBER

In order to relate the atmospheric stability and possible static energy changes an attempt was made in G83 to derive an appropriate dimensionless parameter. A differentiation of the original expression for the Montgomery potential function (2.2.2) in respect to the geopotential gives a relation

$$\frac{\partial M}{\partial \phi} = \frac{\partial M / \partial \theta}{\partial \phi / \partial \theta} = \frac{\frac{\partial}{\partial \theta}(\varepsilon\theta + \phi)}{\partial \phi / \partial \theta} \tag{3.5.1}$$

which by its rearrangement takes the form

$$\frac{\partial M}{\partial \phi} = 1 + \frac{\varepsilon(1 + \frac{\partial \ln \varepsilon}{\partial \ln \theta})}{\partial \phi / \partial \theta} \tag{3.5.2}$$

and enables a further discussion of the thermodynamic state in an infinitesimal neighborhood of any point. In the case of hydrostatic equilibrium, when the surfaces of constant θ and M coincide $\partial M/\partial\theta$ equals 1 and therefore the second term on the right side in (3.5.2) must be zero. Obviously, it may be formulated as a condition

$$1 + \frac{\partial \ln \varepsilon}{\partial \ln \theta} = 0 \tag{3.5.3}$$

However, in the general nonhydrostatic case, when there is a deviation from hydrostatic equilibrium, the above condition may be reexpressed by defining a dimensionless parameter such as

$$\hat{E} = 1 + \frac{\partial \ln \varepsilon}{\partial \ln \theta} \tag{3.5.4}$$

By additional rearrangements using the isentropic relations (3.5.4) can be written as

$$\hat{E} = 1 + \kappa \frac{\partial \ln p}{\partial \ln \theta} = \frac{\partial \ln T}{\partial \ln \theta} \tag{3.5.5}$$

or alternatively

$$\hat{E} = \frac{1}{\varepsilon} \frac{\partial (\varepsilon\theta)}{\partial \theta} = \frac{\theta}{T} \frac{\partial T}{\partial \theta} \tag{3.5.6}$$

It can easily be seen from (3.5.6) that the so defined dimensionless energy number indicates the change of the specific enthalpy with potential temperature in respect to the Exner function. Also, taking into account the hydrostatic equation (2.2.1), it becomes obvious that the equation (3.5.6) compares the more general changes of this specific enthalpy with a change of the Montgomery potential in the hydrostatic equilibrium.

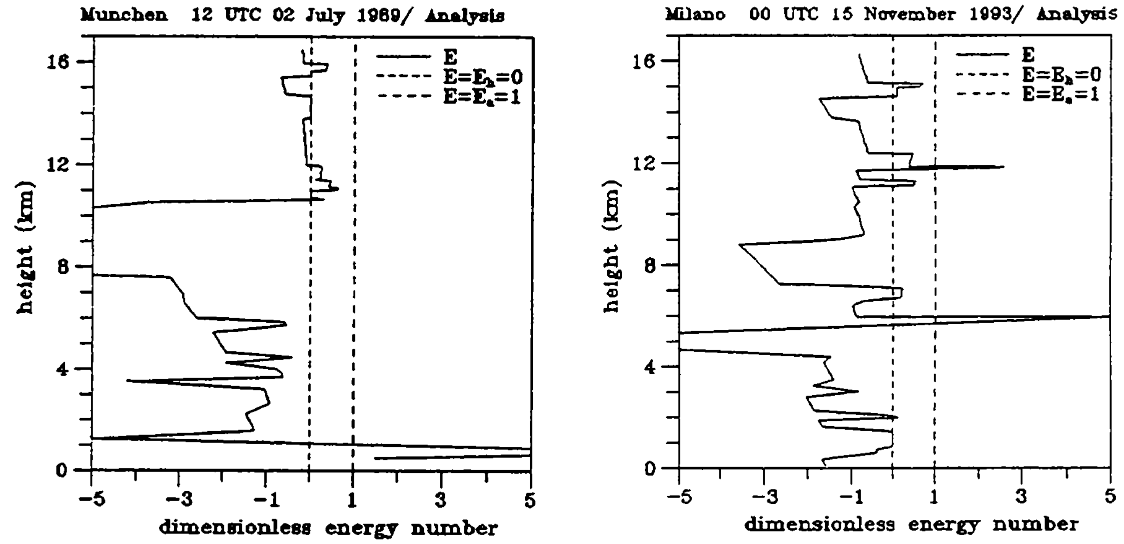

Figure 3.5.1: The vertical profiles of the dimensionless energy number Ê for the same situations shown in Figure 3.1.1

In practice, the usefulness of the considered parameter for an extraction of very detailed stability features involved in the real atmospheric structure is demonstrated in figure 3.5.1. Its high resolution vertical profile is drawn in respect to the auxiliary lines which indicate an isothermal state and the hydrostatic equilibrium for Ê = 0 as well as the neutral equilibrium for Ê = 1. In such a way, the figure is divided in three regions of interest. There is a very stable region characterized by temperature inversion between the neutral and isothermal line, a statically stable region on the left of the neutral line and on the right of it the unstable one. Such a design of the figure offers a better visualization and many features are much more recognizable, for instance, the intensity of superadiabatic layers as well as the position and thickness of any temperature inversion.

3.6 VERTICAL ACCELERATION

The vertical acceleration is derived here as a parameter proportional to atmospheric stability including the dimensionless energy number defined by equation (3.5.4). It can be written as

$$\frac{dw}{dt} = -\frac{g\Delta z}{T}(1+\hat{E})\Gamma_d \qquad (3.6.1)$$

where Γ_d is the dry-adiabatic lapse rate and Ê is the dimensionless energy number.

It should be emphasized that the vertical acceleration itself does not give the information whether there is ascending or descending motion but only whether the vertical motion that exists is accelerated or decelerated due to stability or unstability of the layer.

As shown by the profile on the left side of figure 3.6.1 the vertical acceleration for Munich takes positive values about 0.5 km above the ground. That means that in this layer acceleration of vertical motion can be observed. This itself is not an evidence of accending motion but its comparison to any other parameter, for example Ê indicating a superadiabatic layer there leads to such a conclusion.

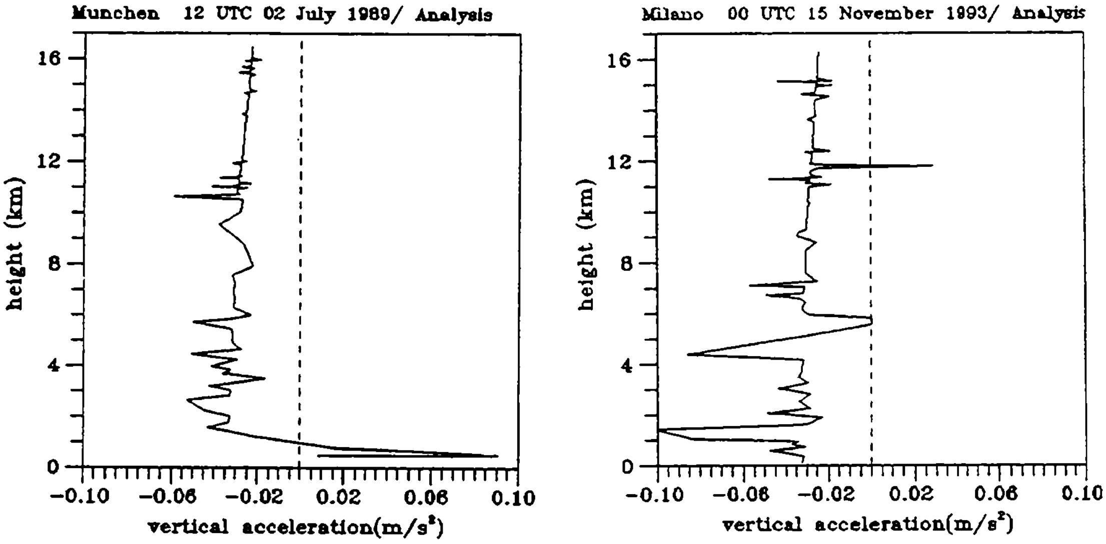

Figure 3.6.1: The vertical acceleration profiles for the same cases as in previous parameter figures. The dashed line stands for dw/dt = 0.

3.7 EQUIVALENT POTENTIAL TEMPERATURE

Equivalent potential temperature is a parameter that gives the information about the water content in the air. It is well known that humidity triggers the most intense processes in the atmosphere, therefore the information given by equipotential temperature profiles or cross-sections could be of vital importance.

Equivalent potential temperature is the temperature that an air particle has after being lifted dry-adiabatically to the condensation level, then pseudo-wet- adiabatically high up, losing all the water that was condensed during this upward motion, and then lowered dry-adiabatically down to the 1000 hPa level.

The form that is used in HRID for expressing the equipotential temperature was given by Bolton (1980). It is partly empirical and can be written as

$$\theta_e = \theta' \exp\{[3.376 / T_L - 0.00254]\, r(1 + 0.00081r)\} \qquad (3.7.1)$$

where T_L stands for the condensation level temperature, r is the mixing ratio and θ‘ can be written as

$$\theta' = T_K \left[\frac{1000}{p}\right]^{\frac{R}{c_p}[1-0.00028r]} \qquad (3.7.2)$$

where T_K is the absolute temperature.

4. BASIC PRINCIPLES OF INTERPRETATION

4.1 SOME BASIC FEATURES OF THE CROSS-SECTIONS

The elementary HRID tool is the field of isentropes, which are, in fact, the isoplets of the potential temperature. Their vertical crowding ($\partial\Theta/\partial z$) is directly proportional to the atmospheric static stability N^2 with high values indicating the very stable layers such as temperature inversions, while vice versa, wide vertical spacing of the isentropes indicates relatively unstable regions usually related to the free convection, cloudiness or precipitation. Horizontal crowding of isentropes is a very good indication of the frontal zones.

This is valid for both time and space-cross sections. Under the assumption that the atmospheric motions are mostly adiabatic, the isentropic surfaces in the space cross-sections may be considered as "material surfaces". On the other hand isentropes in the time cross-sections enable monitoring of diabatic flow, as a consequence of the time change of the potential temperature ($\partial\Theta/\partial t$).

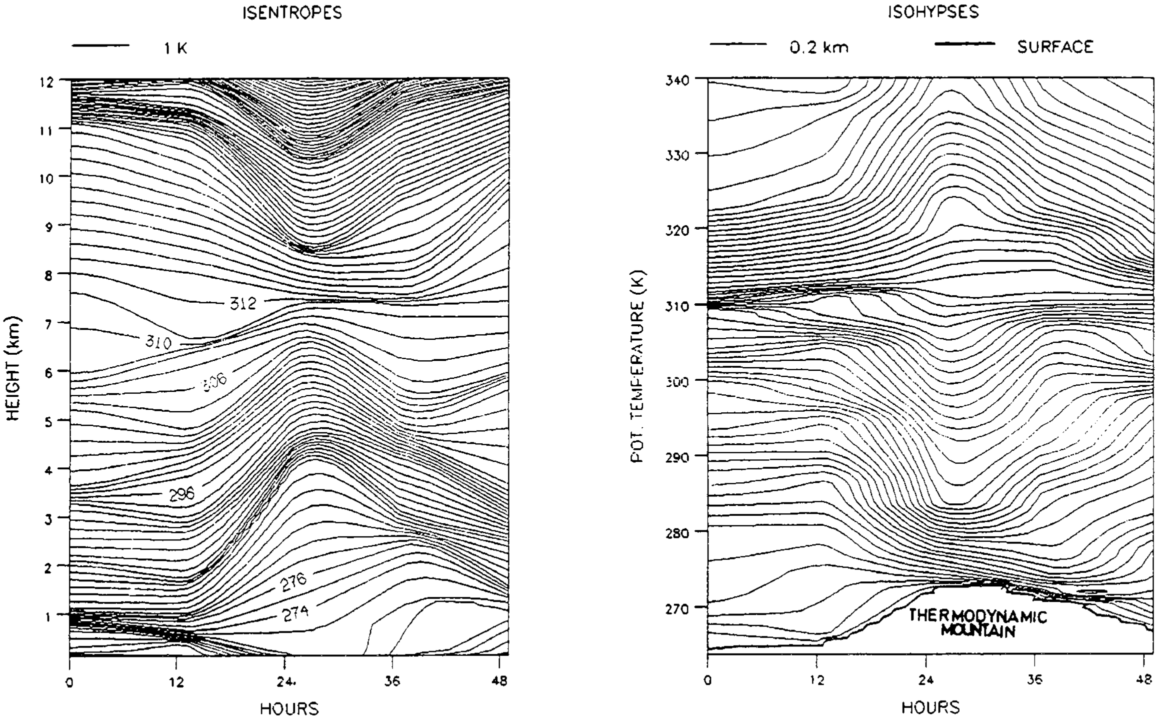

Figure 4.1.1: Time cross-section of isentropes in z coordinates and the corresponding isohypses in Θ coordinate system on the 27^{th} of December 1992, 00 UTC+48, at Zagreb

The configuration of the isohypses in Θ coordinate system is inversely proportional to the isentropic configuration in the z system. This follows from the reversed functions $\partial\Theta/\partial z$ and $\partial z/\partial\Theta$. As shown in figure 4.1.1, the descending part of the tropospheric wave between 24 and 48 hours in z coordinates corresponds to the ascending part of the wave in Θ coordinates. On the other hand the ascending part in z coordinates corresponds to the descending part of the wave in Θ coordinates.

It must be emphasized that the Θ coordinate system comprehends some special features such as the so called "Thermodynamic Mountain" (TM) which is the ground value of the potential temperature Θ.

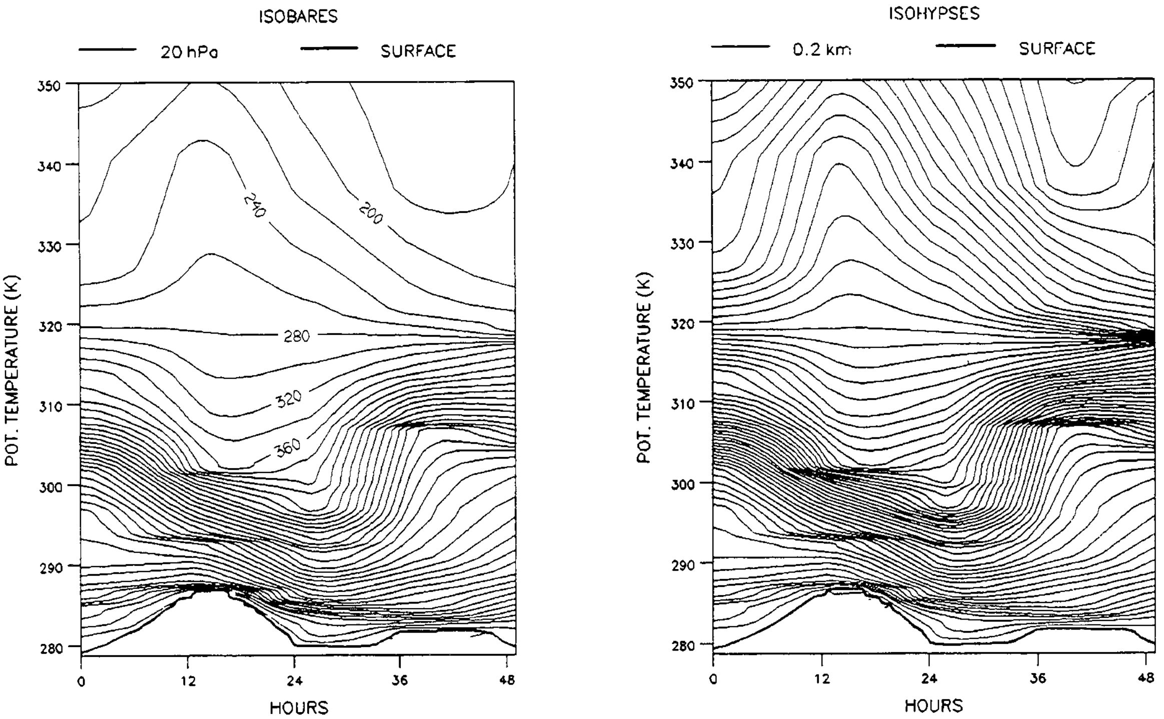

Figure 4.1.2: Time cross-section of isohypses and the corresponding isobars in Θ coordinates on the 27th of December 1992, 00 UTC+48, at Zagreb

Figure 4.1.2 very clearly expresses the fact that in the Θ coordinate system isohypses may satisfactorily replace isobars. This indicates that the high similarity in the configuration of the isoplets also exists in the corresponding z (geometrical height) and p (pressure) coordinate system. Therefore there is no reason to use both of them. In the paper, z is chosen as a relevant coordinate because of a simple visualisation of orography in the cross-sections.

4.2 BASIC ATMOSPHERIC FEATURES INTERPRETED FROM CROSS-SECTIONS

Position, sloping and crowding of isentropes characterize the basic features of the atmosphere such as atmospheric fronts, temperature inversions and the tropopause. Their correspondence in space and time cross-sections exists only if the time cross-sections are based on measurements in the downstream flow relative to the incoming features. Consequently the basic atmospheric features in the time and space have a mirror reflection.

The figures 4.2.1 and 4.2.2 illustrate schematically the mirror reflection phenomena of a warm and a cold front in the space and time cross sections. The position of the air sounding measurements for a time cross-section of the incoming atmospheric front is drawn by the dashed line.

Corresponding frontal types basically differ in the mirror reflection of the inclination of their isentropes. In respect to the propagation direction upward inclined isentropes of a warm front in the space cross-sections appear as declined isentropes in the time cross-sections. On the other hand declined isentropes of a cold front in the space cross-sections correspond to upward inclined isentropes in the time cross-sections.

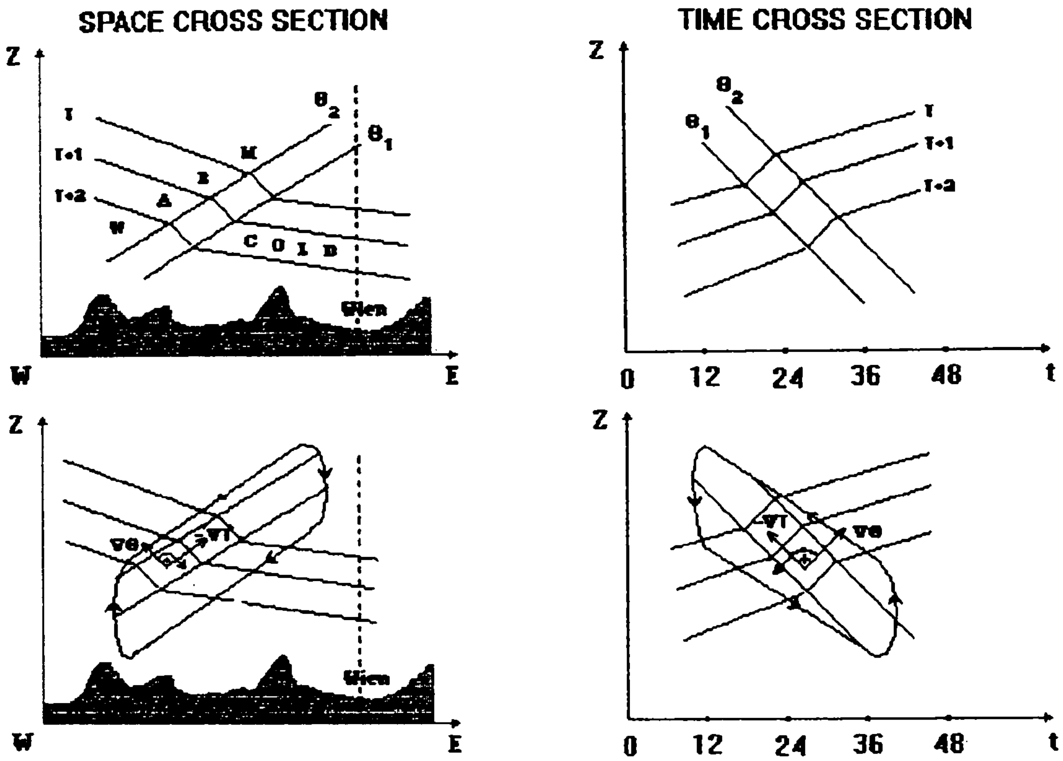

Figure 4.2.1: Comparison of the space and time cross-section of a warm front presented by isentropes and isotherms with solenoids marked. The dashed line indicates the position of the air sounding measurements of the incoming atmospheric front with a movement direction drawn by the arrow.

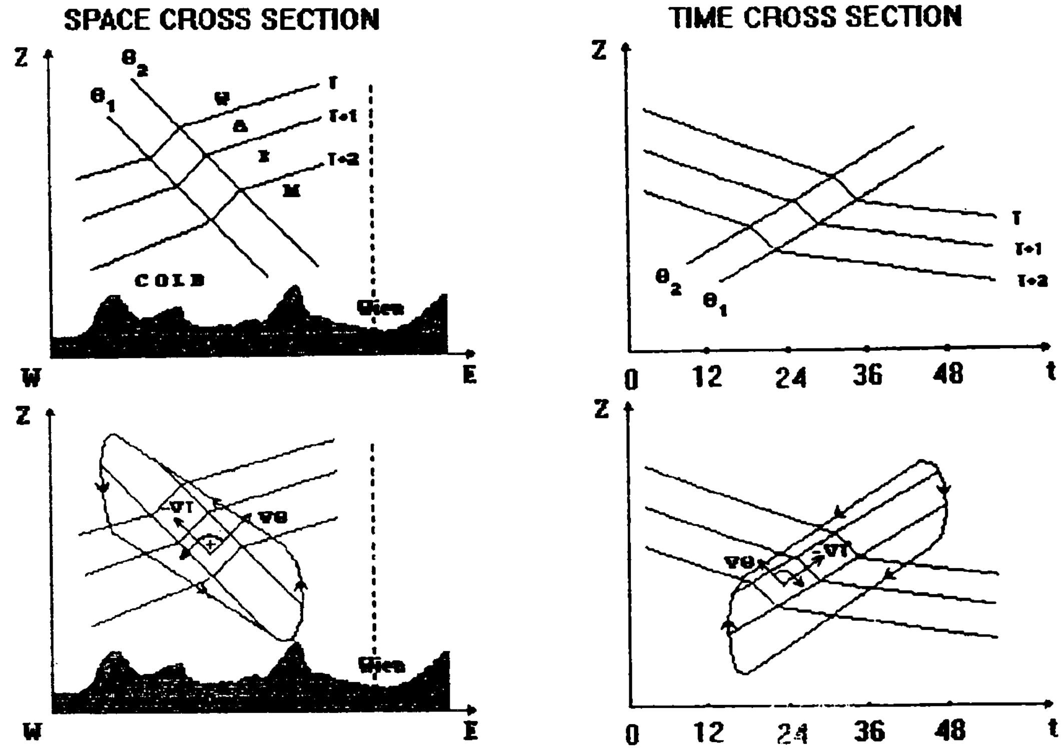

Figure 4.2.2: Comparison of the space and time cross-section of a cold front presented by isentropes and isotherms and with solenoids marked. The dashed line indicates the position of the air sounding measurements of the incoming atmospheric front with movement direction drawn by the arrow.

As shown in the figures 4.2.1 and 4.2.2, the deflection of the isotherms at the border of the frontal layer produces solenoids with a resultant solenoidal circulation which tends to level the frontal layer no matter what the type of the cross-section is. For both types this circulation produces ascending motion on top of and descending motion below of the frontal surface.

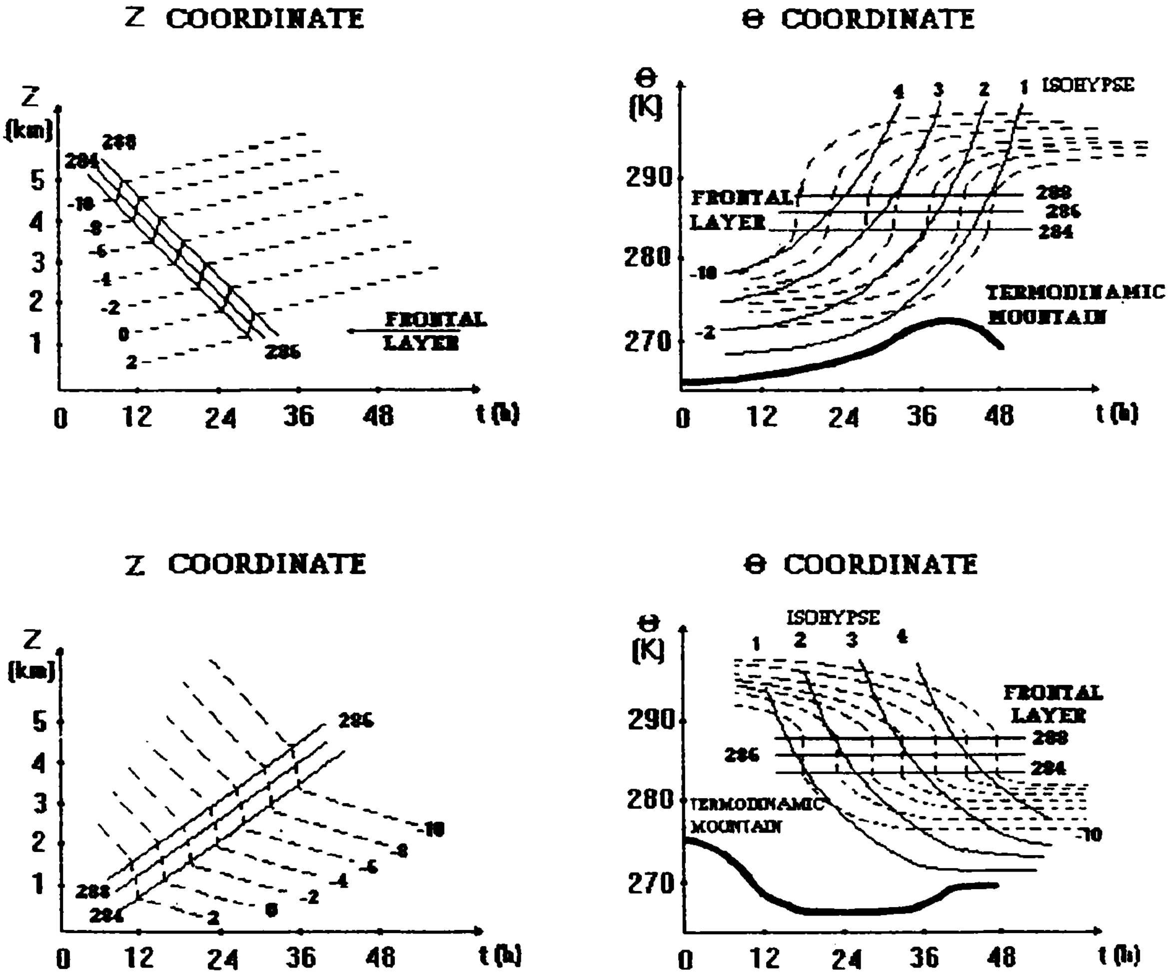

Figure 4.2.3: Comparison of the time cross-section in z and Θ coordinates of a warm (upper panels) and a cold (lower panels) front presented by isentropes, isohypses and isotherms.

It should be noted that, in most of the cases, time cross-sections with Θ coordinates offer a better resolution of the thermodynamic structure. This particularly corresponds to the thermal (figure 4.2.3) and wind (figure 4.2.4) structure of the frontal layers and the tropopause (figure 4.2.5) as well as to the thermal structure of temperature inversions (figure 4.2.6). The deflection of isotherms and isotachs at the frontal boundary is in most of the cases much better in Θ coordinates, too.

In the Θ coordinate system the frontal boundaries are deflecting the isohypses, too. Inclined isohypses, with values decreasing in time correspond to the warm front, while declined isohypses, with values increasing in time, denote the cold front.

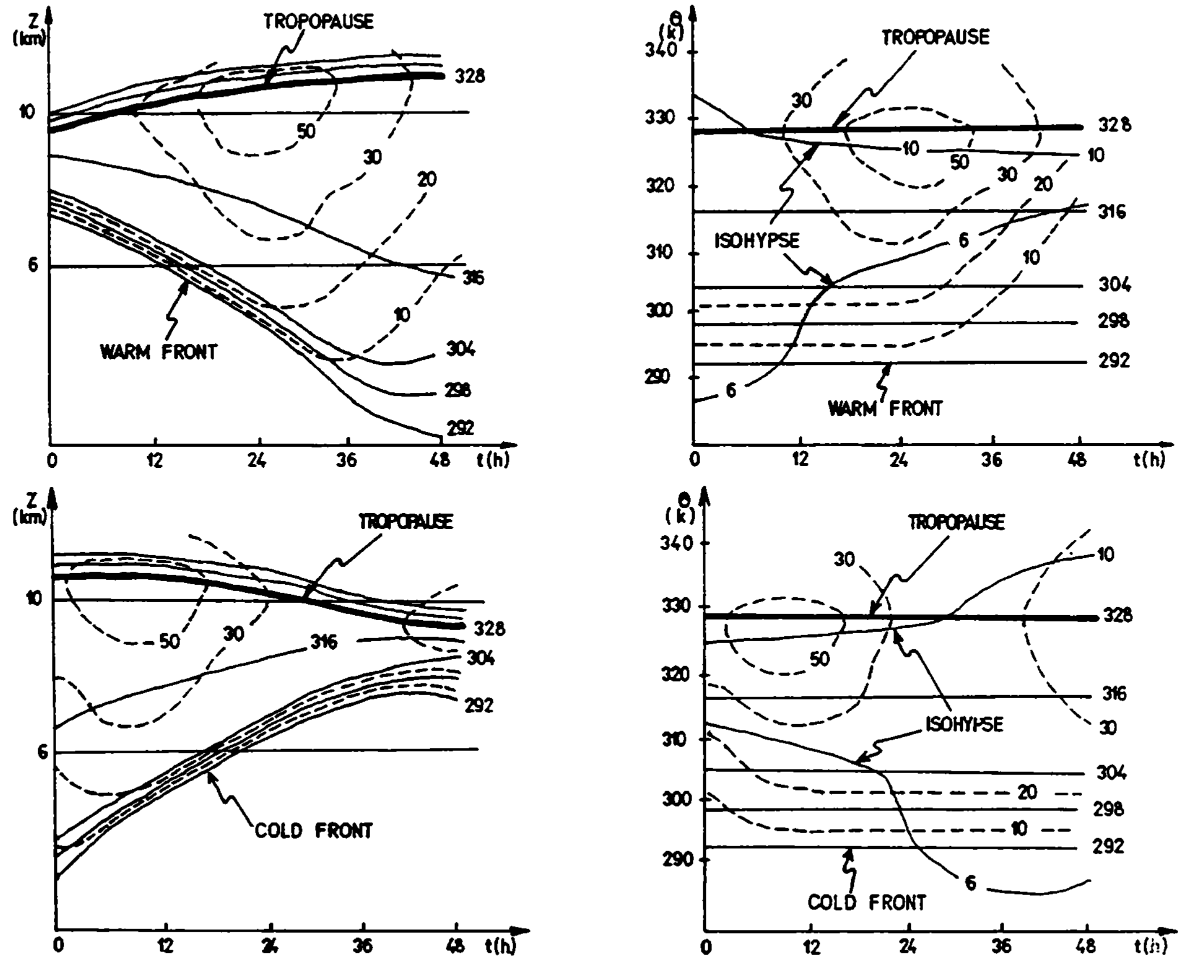

Figure 4.2.4: Comparison of the time cross-sections in z and Θ coordinates of a warm and a cold front presented by isentropes, isohypses and isotachs

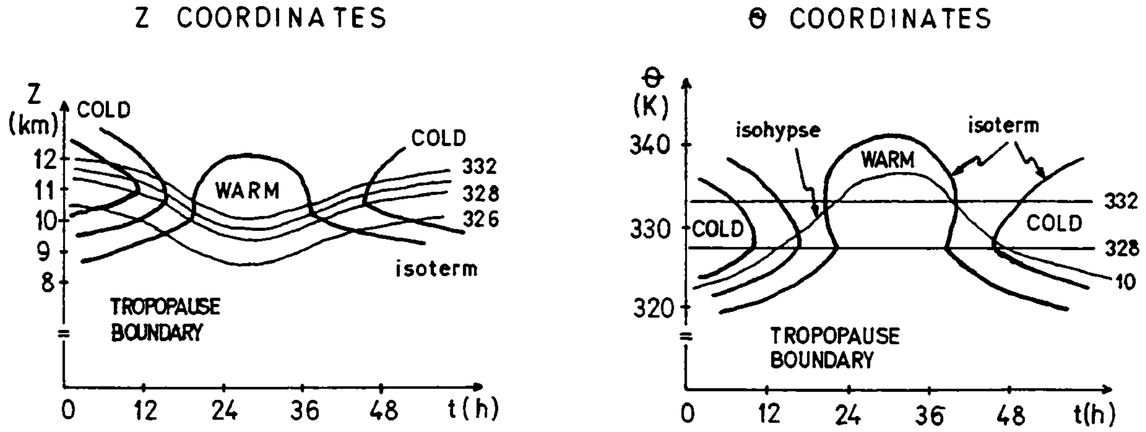

Figure 4.2.5: Time cross-sections in z and Θ coordinates of a tropopause presented by isentropes, isohypses and isotherms

In many cases tropopauses have long, continuous wave-shaped lines, which is a common feature in space cross sections (figure 4.2.7). Similar pattern can also be seen in time cross-sections (figure 4.2.5). Because of a strong deflection of isotherms, solenoidal circulation also tends to level all sloping parts of the tropopause - no matter what the cross-section type is.

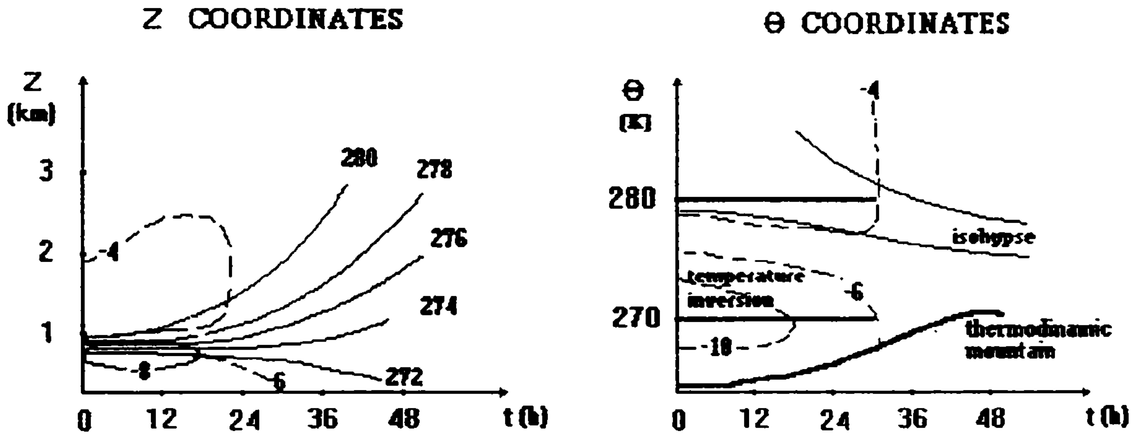

Figure 4.2.6: Time cross-sections in z and Θ coordinates of a temperature inversion presented by isentropes, isohypses and isotherms.

In space as well as in time cross-sections temperature inversions are quasihorizontal layers of high static stability with the lack of solenoids. Generally, a dominant factor is the evolution of inversion layers, which can be seen in time cross sections.

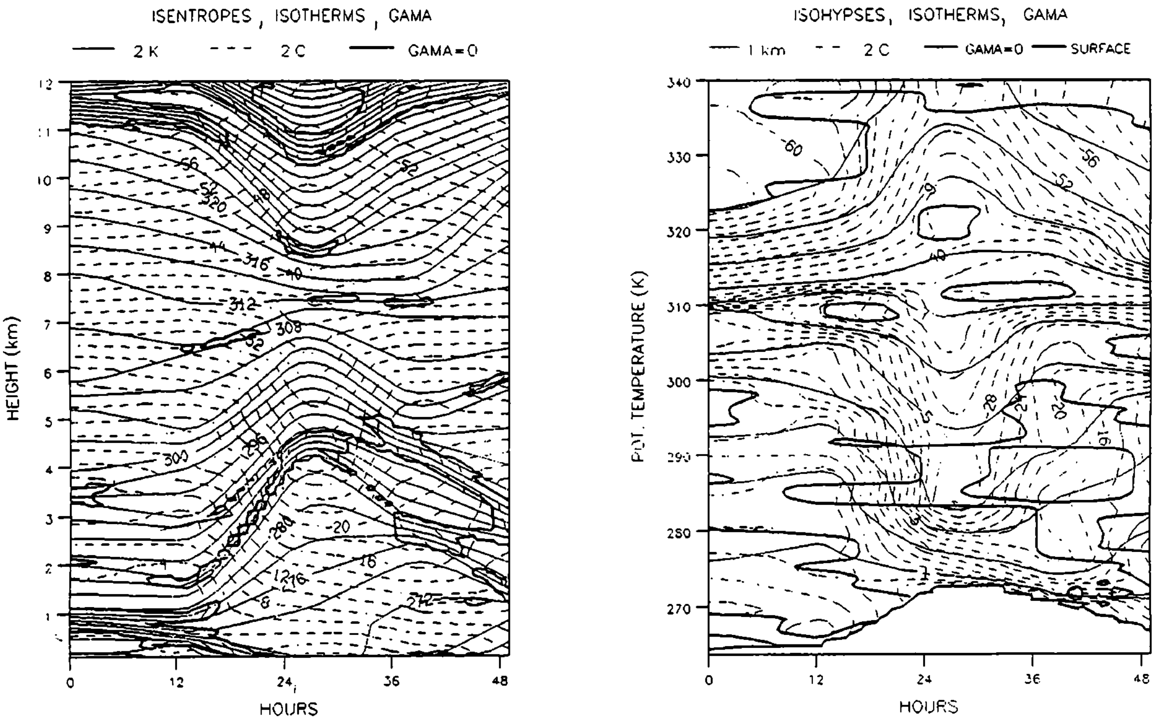

Figure 4.2.7: Time cross-section of a cold front passing over a low tropospheric inversion defined by isentropes or isohypses, isotherms, and zero-value of lapse rate temperature in z and Θ coordinates on the 27th of December 1992, 00 UTC, at Zagreb. Heavy line denotes the values of the zero value temperature lapse rate, GAMMA=0.

Figure 4.2.7 comprehends the considered basic atmospheric features in time cross-sections in z and Θ coordinates based on a real case: the cold front passage over a low tropospheric inversion on the 27th of December 1992, 00 UTC, at Zagreb.

Both cross-sections show the wave patterns of isentropes and isohypses. Figure 4.2.7 shows the cold front (between approx. 15 and 27 hours) that appears on the ascending part of the wave of isentropes in z coordinates (the descending part of the wave of isohypses in Θ coordinates). The frontal layer is characterized by strong baroclinity along the sloped and most crowded isentropes. It must be noted that in most cases this part of the wave embodies a cold front. Vice versa, the descending part of the wave in z coordinates (the ascending part of the wave in Θ coordinates) between approx. 27 and 48 hours in most cases embodies a warm front.

Due to a high static stability, a good objective indicator of frontal zones and a very helpful tool for the atmospheric front visualization and an objective interpretation is the isoplet of the zero value temperature lapse rate, GAMMA=0. Figure 4.2.7 presents that tropopause and inversion layers are well marked with the isoplet of zero-value temperature lapse rate too.

Figure 4.2.7 is also an example of monitoring a temperature inversion dissipation in the boundary layer which is described in the next paragraph in more detail. This phenomenon is also well known as masked cold front. In such cases the arrival of the cold front coincides with the formation of the thermal mountain; and its maximal development is connected with the final dissipation of the inversion layer. Usuallly, the beginning of the dissipation corresponds to the appearance of a thermodynamic mountain (figure 4.2.7 right side, from 12 hours on). Simultaneously, the dissipation of the low tropospheric inversion layer (between 7 and 23 hours) results in an isotherm deflection. The beginning of the temperature inversion dissipation also corresponds to a slight descending of isentropes (figure 4.2.7 left side). Such sloped isentropes act as a very shallow "false warm front".

4.3 EXAMPLES OF SPECIAL ATMOSPHERIC PROCESSES AND PHENOMENA IN THE TIME CROSS-SECTIONS

4.3.1 Inversion Splitting and Dissipation

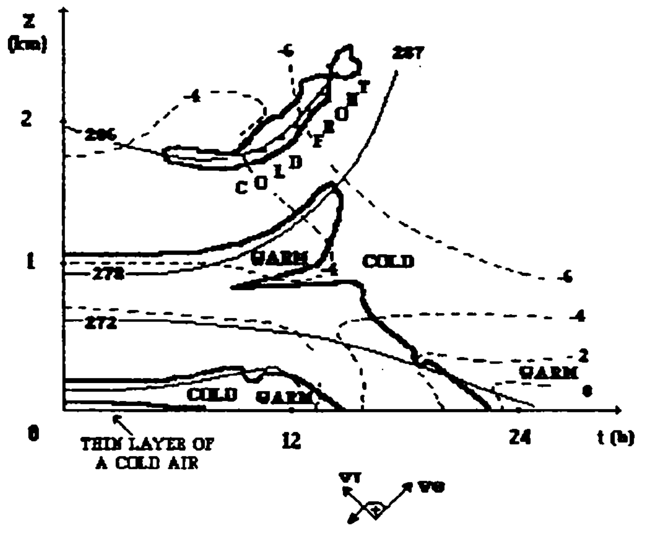

One of the possible mechanisms for the dissipation of a low tropospheric temperature inversion is a cold front passage describes on base of figures 4.2.7. and 4.3.1. The schematic presentation figure 4.3.1 is extracted from the time cross-section of 27th of December, 1992, at Zagreb (figure 4.2.7).

Figure 4.3.1: Schematic presentation of a low tropospheric inversion dissipation during the passage of a cold front

4.3.2 Conditions of a Thermodynamic Mountain Growth

The appearance of a thermodynamic mountain (TM) primarily corresponds to the temperature increase. The influence of the pressure decrease is one order of magnitude less. There are numerous complex conditions for increasing and decreasing of a TM. These conditions depend not only on the atmospheric features but also on the season of a year. From experience it is known that the following dominant factors contribute to the shape of a TM.

a) warm front passing cloudiness,
night cooling and warm advection (in winter),
heating and warm advection (in summer).

b) cold front passing inversion dissipation,
cold advection and night cooling (in winter),
cold advection and daily heating (in summer).

4.3.3 Tropopause Funnel

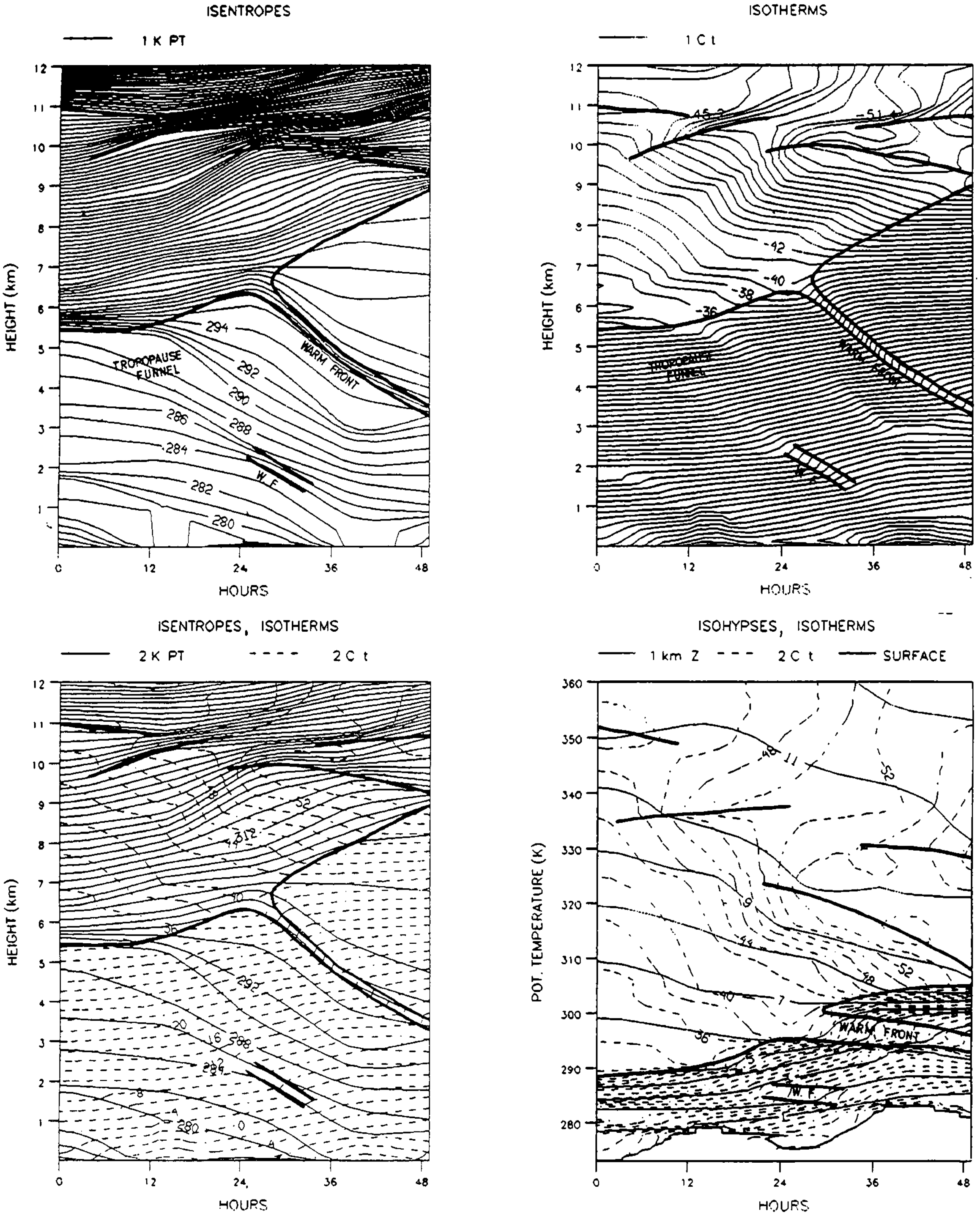

Fig 4.3.2: Tropopause funnel in time cross-section in z and Θ coordinates on the 3rd of January 1993 at Brindisi defined by isentropes or isohypses and isotherms

A tropopause funnel is the case of a "false tropopause" in a deep cyclone which is described by Palmen and Newton (1969) using space cross sections. Here a tropopause funnel is presented in the time cross-section in z and Θ coordinates (figure 4.3.3.1) corresponding to the real situation on 3rd of January 1993, at Brindisi.

It must be emphasized that the air just above the "tropopause" depression could not have originated in the stratosphere and moved down to 500 hPa because in that case the temperature of "tropopause" would have been too high compared to usual values (-36°C) The real tropopause can be located much higher. In the present case it is split in several layers between 9 and 11 km with temperatures between -42°C and -56°C.

4.4. SOME ADDITIONAL TOOLS AND PARAMETERS OF THE CROSS-SECTIONS

4.4.1 Equivalent Potential Temperature and Relative Humidity

The further products involve the moist atmospheric processes and the monitoring of their evolution. The products also implement the diagnosis of the available parameters in "2+1D" dimensional time cross-section.

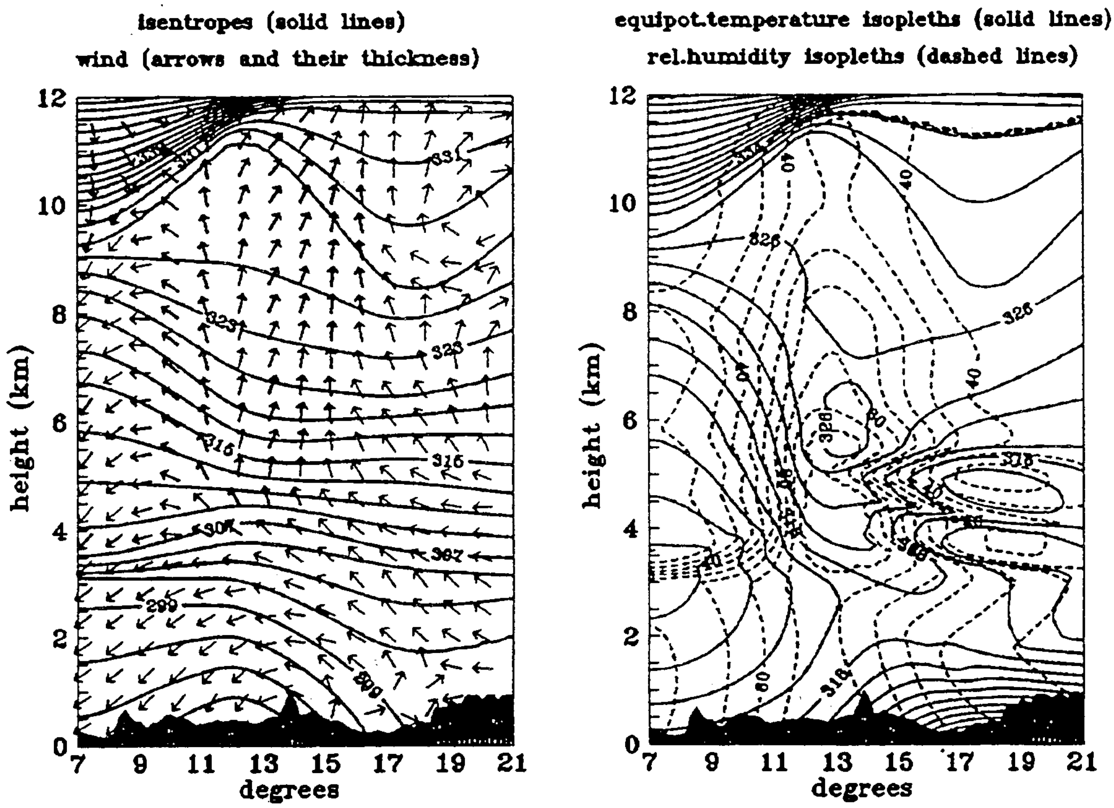
**isentropes (solid lines)
wind (arrows and their thickness)**

**equipot.temperature isopleths (solid lines)
rel.humidity isopleths (dashed lines)**

Figure 4.4.1: Latitudinal space cross-section along 48.75 N (corresponding to cross section A in part I) of isentropes, horizontal wind vector, equivalent- potential temperature and relative humidity in z coordinates on the 3rd of July 1989 at 12 UTC

The moisture in the cross-sections can be visualized by the equivalent potential temperature and specific humidity as quasi-conservative and conservative parameters, and relative humidity. The last parameter is a significant measure whether the thermodynamic process will be dry or wet.

Figure 4.4.1 is an example for a weather situation with conditional instability throughout the troposphere which is a common stability condition in summer weather (Cacic, 1984, 1986). The drastic differences in the static stability in dry and moist air in a summer period are evident by comparing the configuration of the equivalent potential temperature and potential temperature isoplets that are completely different. The influence of moisture clearly is reflected by the coincidence of the relative humidity and equivalent potential temperature maxima. Assuming that regions where the relative humidity maxima exceed the value of 80% are accompanied by condensation, the equivalent potential temperature describes well the thermodynamical processes in the atmosphere.

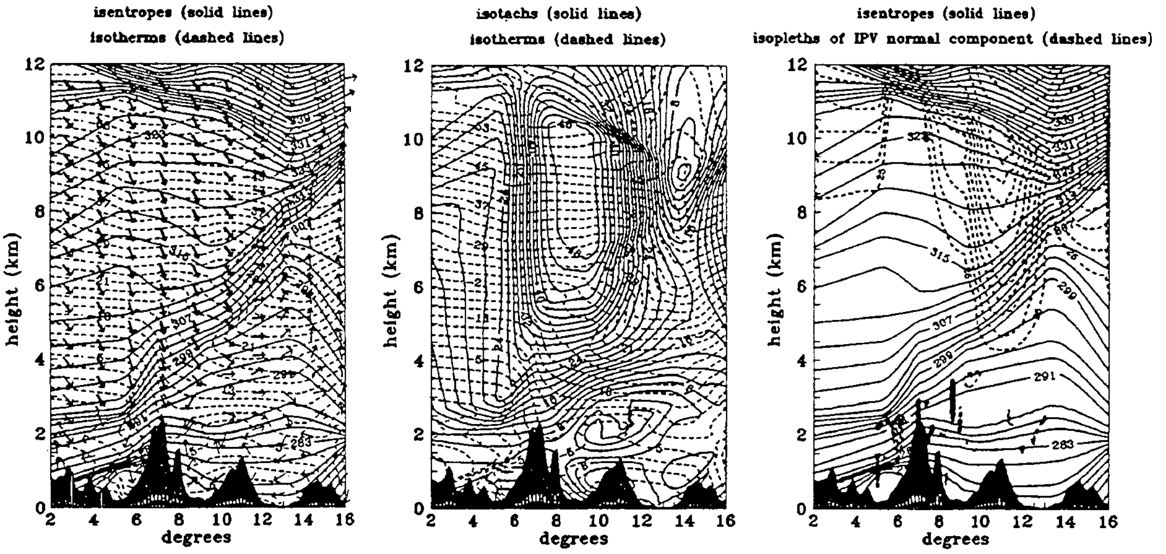

Fig 4.4.2: Latitudinal space cross-section along 45.75 N (corresponding to cross-section B in part I) of isentropes, horizontal wind vector, isotachs, equivalent potential temperature, relative humidity and IPV normal component isoplets in z coordinates on the 29th of November 1993, 12 UTC

4.4.2 Isentropic Potential Vorticity

The isoplets of the isentropic potential vorticity component normal to the cross-section (hereafter: IPV) are presented in figure 4.4.2. As stated by Reed and Danielsen (1959) as well as by Hoskins (1985), the IPV component may be successfully utilized as an air-mass tracer. So, because of its quasi-conservative property, the considered field enables speculations about an injection of the cold and dry stratospheric air into the middle troposphere through a break or fold in the tropopause. Such a process is clearly detected in figure 4.4.2 by very strong stratospheric-tropospheric interactions during a pronounced upper-level frontogenesis above the Alps, Stratospheric air has been advected downwards to even 4 km along sloping isentropes. Owing to the similar conservative characteristics, it seems very promising to connect the IPV-field and the water-vapor (WV) satellite images.

4.4.3 "2 + 1D" Presentation

Another approach in the presentation of the atmospheric processes, which enables a slightly different view into their development in time, has been defined here as "the high resolution isentropic 2+1D diagnosis". This is a fictitious three-dimensional Cartesian coordinate system with time as one of the axis. Any two other parameters can be chosen for the two other axis. The resulting surface has a very characteristic shape and its topography strongly depends on the prevailing atmospheric structure and the processes involved at any time interval.

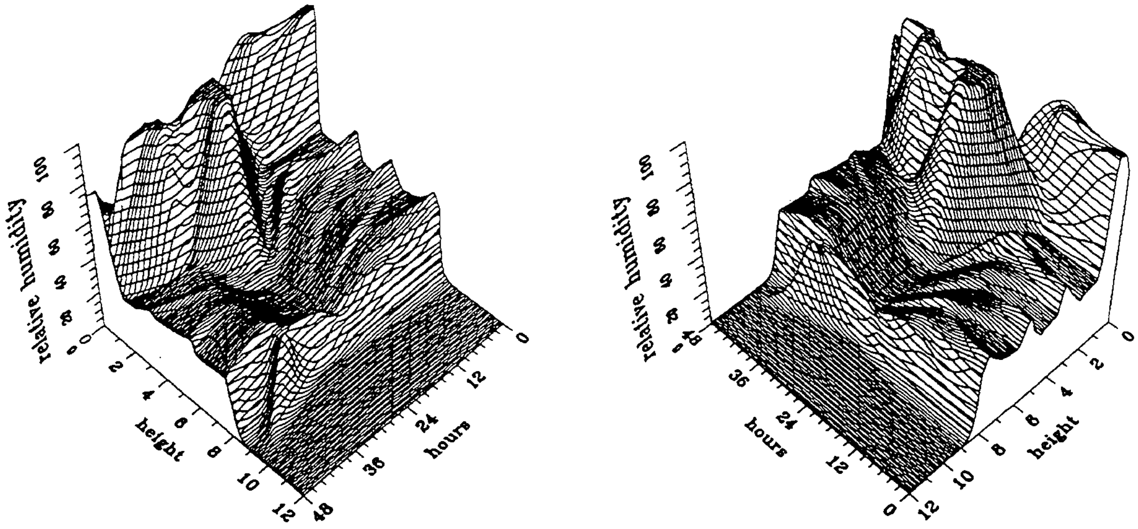

Figure 4.4.3: The "2+1D" time cross-sections of the relative humidity isoplets and isohypses in z coordinates on the 27th of December 1992, at Zagreb, viewed from two opposite positions

An interesting example of the considered "2+1D"-diagnostics is presented in figure 4.4.3, where the surface f(r,z,t)=0 is viewed from two opposite positions. Such a visualization involves not only an important information of the time-changes of the relative humidity distribution, but also consequently the time-changes of cloudiness wich may be connected. It seems reasonable to compare this diagnostic tool with satellite data. The "2+1D" diagnosis in figure 4.4.3 referring to figure 4.2.7 clearly indicates the main part of the available moisture, and frontal passages can be identified.

5. CONCLUSION

The results indicate the capability of the model to resolve meteorological phenomena not only of the synoptic, but also of the lower scales between two input data groups. The high vertical resolution of the model is realized by application of PHAT. This analytical method implies quite a new approach in respect to the conventional numerical schemes in finite differences. Instead of such an approximation of the derivative, PHAT prefers the derivative itself and the inclusion of thermodynamic and hydrodynamic principles in the computational procedure.

The theoretical basis of PHAT are the hydrostatic isentropic relations and their derivatives of higher order as well as a modification of the Hermite polynomial interpolation routine. The most important result of its application asserts that this "hydrostatically adjusted" technique always gives a satisfactory approximation of an actual, generally nonhydrostatic state in the infinitesimal neighbourhood of a point: On the first impression a paradox. The hydrostatic adjustment of the basic algebraic system is related to derivatives of higher order of the so-called "end-point conditions". For instance, the meaning of the second derivative of the pressure in respect to the potential temperature is the rate of change of the reciprocal of thermal stability parameter, where the hydrostatic properties of the first derivative are implicitly contained. Conversely, the basic pair of "end-point conditions" comprehends "a nonhydrostatic reality" involving the actual values of observed pressure and potential temperature or any other combination of input parameters. The hydrostatic assumption is only an appropriate and very useful physical approximation of the actual and generally nonhydrostatic thermodynamic state. Accordingly, the hydrostatic solution of PHAT may, under hydrostatic circumstances, appear as a particular solution of the basic algebraic system. In general case, the solution must be nonhydrostatic. The rearrangement of Eq.(3.5.5) defining the dimensionless energy number and its theoretical consideration affirm this fact clearly. It states that, for any combination of the pressure and potential temperature, the first derivative of the polynomial tends to its hydrostatic value when the dimensionless energy number tends simultaneously to zero.

Nevertheless, the present state of PHAT contains some generally unanswered questions. The most important of them is related to the determination of an optimal algebraic system to approximate the function, where the key issue is: "How best to choose the degree of approximating polynomial and an order of its higher derivatives". As stated by Bakhvalov (1977), this is a generally unresolved problem. Therefore, he pointed out the necessity of the experiments in elaboration of computational methods, where the first reliable evidence of its successfulness or failure is clearly indicated by resulting numerical values.

ACKNOWLEDGMENTS

The authors would like to thank the colleagues Miss Dijana Klaric and Mr Mladen Govorcin for their help in the optimization of the software and particularly Miss Dijana Klaric for the contribution in designing the graphical output by MAGICS software.

REFERENCES

BAKHVALOV, N. S., 1977: Numerical methods. Mir Publishers Moscow, 663 pp.

BOLTON, D., 1980: The computation of equivalent potential temperature. Mon. Weather Rev., 108, 1046-1053.

BRUNT, D., 1952: Physical and dynamical meteorology. Cambridge Univ. Press, 428 pp.

ČAČIĆ, I., 1984: Conditions of a storm motion over Medvednica. Proceedings of the XVIII Inter. Conference for Alpine Meteor, Opatija, Sept., 25-29, 175-177.

ČAČIĆ, I., 1986: Utjecaj orografije u mezorazmjeru na ponaanje Cb oblaka i razdiobu oborine: Slukaj 28. srpnja 1980 na podrucju Medvednice (Cb cloud behavior and rain distribution by the mesoscale orography: Case 28 July 1980 on the area of Medvednica. Rasprave - Papers 21 DHMZ, Zagreb, 69-76.

GLASNOVIĆ, D., 1978: Objective cross-section analysis. Proceedings of the XV Inter.Meeting on Alpine Meteor., Grindelwald, Sept., 19-23, 1978, 192-195.

GLASNOVIĆ, D.,, 1983: Dijagnosticki izentropski model za istrazivanje vertikalne strukture atmosfere. (A diagnostic isentropic model for an investigation of the vertical atmospheric structure - Summary in English), Monography I, 33 pp.

GLASNOVIĆ, D., 1990: Isentropic high resolution time cross-section based on polynomial hydrostatic adjustment technique. Rasprave - Papers 25, DHMZ, Zagreb, 37-47.

GLASNOVIĆ, D. and V. JURCEC, 1990: Determination of upstream bora layer depth. Meteor. Atmos. Phys., 43, 137-144.

JURCEC, V. I D. and GLASNOVIĆ, 1991: Application of the hydraulic theory to naturally occuring bora flow, Hrvatski meteorol. Casopis, 26, DHMZ, Zagreb, 19-40

HOSKINS, B.J., M.E. MCINTYRE and A.W. ROBERTSON, 1985: On the use of isentropic potential vorticity maps. Quart.J.R.Met.Soc., 111, 877-946.

PALMEN, E. and C. W. NEWTON, 1969: Atmospheric Circulation Systems. Academic Press, 603 pp

REED, R.J. and E.F. DANIELSEN, 1959: Fronts in vicinity of the tropopause. Arch. Met. Geophys. Biokl., A11, 1-17.

SHAPIRO, M.A. and J.T. HASTINGS, 1973: Objective cross-section analyses by Hermite polynomial interpolation on isentropic surfaces. J.Appl.Met., 12, 753-762.

THORPE, A.J., 1993: The representation of fronts. Proceedings of a seminar held at ECMWF, Reading, 7-11 Sept. 1992, 237-246.

TURNER, J.S., 1973: Buoyancy effects in fluids. Cambridge University Press, 368 pp,

Author's address:

DRAŽEN GLASNOVIĆ, IVAN ČAČIĆ and NATAŠA STRELEC
Meteorological and Hydrological Service
Gric 3
41000 Zagreb
CROATIA
Phone: +385 41 421 222/279
Fax: +385 41 278 703
E-mail: glasnovic@cirus.dhz.hr
cacic@cirus.dhz.hr
strelec@cirus.dhz.hr

PART III:

THE CROSS SECTION METHOD AT THE ZAMG (VIENNA)

COMPUTATION AND EVALUATION OF VERTICAL CROSS SECTIONS AT THE CENTRAL INSTITUTE FOR METEOROLOGY AND GEODYNAMICS IN VIENNA

Central Institute for Meteorology and Geodynamics, Vienna, Austria

VERONIKA ZWATZ-MEISE, ALEXANDER JANN, ROLAND WINKLER

ABSTRACT

The paper presents the cross section analysis used operationally for diagnosis and forecast as well as for research. First the analysis algorithm is introduced and the data sources and parameters used in the cross sections are mentioned. Three data sources are combined: radiosonde data, derived parameters from the ECMWF model and satellite signals. All parameters can be superimposed and visualized as necessary.

In a second part several examples of cross section analyses for typical weather systems are discussed.

A third part presents some results of the scientific cross section project between Austria and Croatia. Of special interest is the combination of time cross sections with satellite data.

ZUSAMMENFASSUNG

Der Bericht befaßt sich mit den Querschnittsanalysen, die operationell für Diagnose und Vorhersage ebenso wie für die Forschung verwendet werden. Es werden drei Datenquellen kombiniert: Radiosondendaten, abgeleitete Parameter des EZMW- Modells und Satellitendaten. Alle Parameter können je nach Bedarf überlagert werden.

In einem zweiten Teil werden mehrere Beispiele von Querschnittsanalysen typischer Wettersysteme diskutiert.

In einem dritten Teil werden die ersten Ergebnisse des internationalen Querschnittsprojektes zwischen Österreich und Kroatien präsentiert. Davon ist eine Kombination zwischen zeitlichen Querschnitten und Satellitenbildern besonders zu erwähnen.

A. FUNDAMENTALS OF CROSS-SECTION VISUALIZATION

1. INTRODUCTION

For a couple of years, objectively calculated cross-sections are being available at the Zentralanstalt für Meteorologie und Geodynamik in Vienna. As experience with the products has confirmed, they provide a deeper insight into synoptic systems.

2. DATA SOURCES, ANALYSIS METHODS, AVAILABLE PARAMETERS

2.1 CROSS-SECTIONS FROM RADIOSONDE DATA

Cross-sections from radiosonde data are realized for 4 parameters:

- potential temperature
- relative humidity
- two slightly different forms of the equivalent-potential temperature (see part B.).

The number of incorporated radiosonde stations and the direction of the cross-section can be chosen arbitrarily. The radiosonde data, projected onto the line connecting the two outer sonde stations, is transformed into a regular grid point field (which is necessary for the visualization software) by bilinear interpolation. The horizontal gridpoint distance is, depending on the cross-section, between 50 and 100 km, the vertical gridpoint distance is approximately 20 hPa. The layers near the earth's surface are subjected to a special treatment as they are modified by values provided by synoptic stations. Only those synoptic stations are considered which are close enough to the polygon connecting the radiosonde stations; usually the maximum distance from that line is chosen to be 50 km, a value empirically found to be adequate. The inclusion of synoptic stations makes a more accurate location of the surface front feasible.

2.2 CROSS-SECTIONS FROM ECMWF DATA

For this type of cross-section, gridpoint data provided by the European Centre for Medium-Range Weather Forecast (ECMWF) are used. The data may be taken from analysis fields as well as from forecast fields (based on analysis of 12 UTC of the preceding day). A special product comprises the forecast field for 00, 06, 12, and 18 UTC. At present, the data are available only on a few pressure levels, but the situation shall improve in the near future. Interpolation to the regular grid is Lagrangian in the vertical and linear in the horizontal direction. The vertical gridpoint distance is larger than in the case of radiosonde cross-sections: between 50 and 100 hPa (depending on the parameter).
The user can choose among the following parameters:

- potential temperature
- relative humidity
- equivalent-potential temperature
- relative vorticity
- vorticity advection
- divergence of the horizontal wind field
- wind speed
- ω (=dp/dt)
- divergence of the Q-vector
- normal component of the Q-vector

An explanation of the meaning of the last two parameters is given below.

2.3 "CROSS-SECTIONS" OF SATELLITE INFORMATION

Pixel values of satellite images along a section line can be visualized, either from IR-, VIS-, or WV-images. Visualization of the IR temperature (=surface or cloud top temperature) and WV temperature (=brightness temperature of WV signal) is also possible.

2.4 SUPERPOSITION

All types of cross-sections can be superimposed on each other.

B. DISCUSSION OF PARAMETERS AND EXAMPLES

The whole cross section diagnostic done in Vienna is based on the combination of the different data sets mentioned before: radiosonde, ECMWF model and satellite images. Therefore the next sections deal with a useful combination of these parameters respectively data.

Most of the parameters described in the next chapters belong to basic synoptic knowledge, therefore only those mathematical relations will be reproduced which are not commonly used.

1. POTENTIAL TEMPERATURE, EQUIVALENT-POTENTIAL TEMPERATURE AND RELATIVE HUMIDITY

1.1 BASIC CONCEPT AND IDEAS

Equivalent-potential temperature is computed by (1):

$$\theta_{EK} = \theta \exp\left(\frac{rq_m}{c_p T_k}\right) \tag{1}$$

where θ is the potential temperature, r the latent heat of condensation, q_m the mixing ratio and c_p the specific heat at constant pressure. As is pointed out in Mahringer and Zwatz-Meise (1993) this form of equivalent-potential temperature contains in the exponent T_k, which is the temperature of the condensation level; the advantage of this form of the equivalent-potential temperature is that it can be used for dry and wet atmospheres and therefore for cloudy as well as cloudless parts of the satellite image; in the dry case isentropes of potential and equivalent-potential temperature differ only by a factor, while in the wet case equation (1) computes the equivalent potential temperature.

To take into account these problems, a block of four panels containing potential, both forms of equivalent-potential temperature and relative humidity with the actual radiosonde measurements is visualized (figure 1a). The comparison of potential and equivalent-potential temperature fields clearly shows the influence of humidity resulting in a much more pronounced frontal gradient in the equivalent-potential temperature cross section. Although a comparison of both types of equivalent-potential temperature indicates some (rather small) deviations in the values itself, especially in the lower layers, no differences in the isoline pattern can be recognized.

Typical features in the cross sections are (Zwatz-Meise and Hufnagl 1990; Zwatz-Meise 1991; Zwatz-Meise 1987):

- Frontal surfaces which show up as inclined zones of crowded isentropes some of them reaching the ground, others being merely upper level fronts. These are phenomena connected with cloudbands respectively cloudshields in satellite images.
- Non-frontal, mostly meso-scale, features like for instance phenomena in the cold air. These are phenomena connected with comma clouds or enhanced cumuli cloudiness in the satellite images.
- Special stratifications of the troposphere apart from the features just mentioned. To this group there belong labile areas as well as very stable boundary layers or tropopause layers. These are phenomena which can be accompanied by cloudiness in satellite images (for instance convective cells or fog) but this is not necessarily the case.

The combination of isentropes, relative humidity and satellite signals shows a wide variety. Some typical examples are :

- High humidity values on top of the frontal layer (representing upgliding wet air) and low humidity values below of it (representing sinking dry air).
- High humidity values also below the frontal zone from the ground level upward.
- Upper level fronts with high humidity on top of the isentropic surface.
- Cold air features like comma and enhanced cumuli (EC) can be connected either with a thick layer of high humidity or high humidity only in upper layers.

1.2 EXAMPLES

1.2.1 Cold Front

Figure 2 shows an example of a cold front. The cloud band in figure 2a has a zonal orientation and the cross section leading from north to south is indicated. Figure 2b shows a distinct frontal surface with a multiple structure. One branch reaches the surface south of Meiningen (09548) and is connected with high humidity from the surface up to about 500 hPa while dry air below the frontal surface has moved downward to about 800 hPa. A thick zone of crowded isentropes is horizontally oriented southward across the Alps. South of the Alps it separates a wet ground layer from a dry layer above. In the satellite image cloudiness within an upper zone of high humidity connected with an upper level front between 300 hPa above Schleswig (10035) down to about 500 hPa above Milan (16080) is superimposed.

1.2.2 Warm Front

Figure 3a shows the rather patchy cloud shield of a warm front. The zonally oriented cross section (figure 3b) reaches from the very open warm sector at approximately Paris (07145) across the surface warm front near Nancy (07180) eastward.

There is a second warm frontal surface in higher layers from about 600 hPa above Paris (07145) up to 300 hPa above Munich (10868). This seems very similar to a warm front shield type (Zwatz-Meise 1991) where the higher frontal zone indicates the upgliding air of the warm conveyor belt while the lower zone belongs to the more classical warm front type.

1.2.3 Cold Air Cloud Feature

The satellite image (figure 4a) shows several cloud features along the cross section. The cloudband with cold tops east of Vienna (11035) belongs to the cold front; the cloud structure between Stuttgart (10739) and Munich (10868) is therefore a typical cold air feature which could be diagnosed as comma or EC (enhanced cumuli). The cross section (figure 4b) indicates the cold front east of Vienna and a warm front-like zone in the west over France. In between these two configurations, the cloud mass is within a layer without any gradients of the isentropes reaching from the ground surface up to 500 - 400 hPa. It represents a thick, wet, may be labile layer.

2. EQUIVALENT-POTENTIAL TEMPERATURE COMBINED WITH TEMPERATUR ADVECTION

2.1 BASIC CONCEPT AND IDEAS

Temperature advection is computed from thickness values in all available layers from ECMWF analysis as well as forecast data.

Temperature advection is a parameter contained in the omega equation and therefore connected with upward motion and the formation of typical cloudiness. Warm air advection (WAA) indicates rising, cold air advection (CAA) sinking.

Therefore this parameter is used for the determination of different front types, cold air phenomena and non-frontal WAA cloudiness. Waves on fronts are characterised by a contiguity of WAA and CAA maxima.

Some typical configurations shall be mentioned.

- Cold fronts with a zone of WAA on top of the frontal zone, indicating the upgliding warm air and CAA below the frontal zone, being connected with sinking cold air.
- Warm fronts of different types (Zwatz-Meise 1991) with a broad zone of WAA within and on top of the frontal layer.
- Comma and EC-cloudiness within CAA.
- Waves on fronts showing the movement of warm and cold air around the depression in contrary to jet streak waves which have only the cloud appearance of waves but are within CAA (Zwatz-Meise 1991b).

2.2 EXAMPLES

2.2.1 Cold Front

In figure 2c there is WAA on top of the main cold front surface but CAA within and below of it which is a very classical distribution. However south of the Alps CAA is already in front of the cold front.

Satellite signals show a very abrupt northern cloud edge followed by a broad area with high greyshades reaching as far as south of Milano (16080). The peak immediately north of Ajaccio (07761) is much more pronounced in the IR than in the VIS signals, therefore it consists of rather high thin cloudiness.

2.2.2 Warm Front

In figure 3c, WAA within and on top of both frontal surfaces is dominant. The satellite signals especially from IR are very high along the whole cross section. This indicates that a high level cloud shield perhaps connected with the warm conveyor belt of the higher frontal surface is superimposed on the classical warm front band belonging to the surface warm front.

2.2.3 Cold Air Cloud Feature

From figure 4d it is clear that the EC cloudiness is situated within CAA. The IR signals rise immediately west of Stuttgart (10739) and remain high until east of Munich (10868) with a rather ragged appearance which is typical for convective clusters. The highest VIS signals can be found in this area, too. The still higher IR values east of Vienna belong to the cold front cloudiness.

2.2.4 Wave Development

Figure 5a shows two satellite images 12 hours apart with a classical wave development. At 12 UTC, it can be seen between Udine (16044) and Zagreb (13130), and 12 hours later this feature has moved to Brindisi (16320). The development is rather slight during this period but becomes more rapid from then on.

Figure 5b shows the temperature advection for both points of time. At 12 UTC WAA can be found from the ground up to about 800 hPa between Udine and Zagreb (16044 - 13130); this is the boundary for cloudiness shown by an increase in the IR as well as VIS curve. 12 hours later the area of warm air advection can be found nearly through the whole troposphere east of Brindisi (16320). This is the area of the brightest cloud signals which are now extended also more to the west as a consequence of the cyclonic circulation existing there.

3. EQUIVALENT-POTENTIAL TEMPERATURE COMBINED WITH DIVERGENCE AND VERTICAL MOTION (OMEGA)

3.1 BASIC CONCEPTS AND IDEAS

Although in work with satellite images it has proved to be useful to look at the single contributors to vertical motion in the omega equation (vorticity advection, temperature advection etc), there is of course also high interest in the fields of vertical motion and divergence itself. Vertical motion (represented by omega) and divergence are linked by the Richardson equation and have a direct connection to the cloud fields.

Certain situations of interest shall be mentioned:

- Classical fronts often show upward motion on top of the frontal surface and sinking below of it which is another sign for the relative motion at frontal surfaces and has already been mentioned in connection with humidity and temperature advection.
- Deviation from this distribution can be connected with old or weakly developed fronts.
- In the classical front cases fhe field of divergence accompanies the frontal surface by a zone of convergence while divergence prevails above this zone.

- A special distribution of vertical motion and divergence is also connected with the vertical circulation cells in the entrance and exit region of jet streaks. In the left exit region as well as in the right entrance region there is convergence in lower layers with upward motion in middle and upper layers and divergence in the jet level. Especially in the left exit region cloud configurations like EC-cloudiness or commas can be found due to the mentioned processes (Zwatz- Meise 1991b).

3.2 EXAMPLES

3.2.1 Cold Front

Figure 2e shows vertical motion (omega) with rising between Meiningen (09548) and Milano (16080) which is the area of the coldest cloud tops (peaks are colder than -70^{o}C). Sinking prevails in the lower part of the frontal zone north of Meiningen (09548). The double structure of the vertical motion field again draws attention to the thick ground layer south of the Alps mentioned already in 1.2.1. The front seems to move across the Alps as well as further southward on top of this ground layer.

Figure 2f shows a classical distribution for the divergence field. There is a zone of convergence within the main frontal zone from the surface over Stuttgart (10739) up to approximately 400 hPa above Hannover (10338); above this convergence zone divergence prevails. Such a distribution confirms the idea of vertical circulation cells.

3.2.2 Cold Air Cloud Features

Figure 4e confirms the idea of vertical circulation for the cold air cloudiness which can be located between the gridpoints (31/24 and 34/23). Very similar to the mentioned jet streak circulation there is convergence in the lower troposphere up to about 700 hPa and divergence aloft; upward motion has its maximum between 850 and 500 hPa. The VIS signals show, apart from a ragged appearance, the highest reflectivities in this area.

4. EQUIVALENT-POTENTIAL TEMPERATURE COMBINED WITH VORTICITY, VORTICITY ADVECTION AND ISOTACHS

4.1 BASIC CONCEPTS AND IDEAS

Vorticity and vorticity advection are parameters responsible for development and formation of special cloud systems. The vertical change of vorticity advection is a part of the omega equation whereby an increase of cyclonic vorticity advection with height contributes to upward motion and may play therefore a role in cloud development. Vorticity is responsible for the formation of a more or less distinct spiral structure within the cloud mass. Thereby the two contributors to vorticity, curvature and shear vorticity have an important influence on the configuration.

In satellite meteorology a simple identification method for vorticity advection has been introduced. Assuming that wind usually increases with height the pronounced maxima of positive vorticity advection (PVA) at 500 and/or 300 hPa are evaluated instead of its vertical change. Although this assumption may not be fulfilled everywhere the method has proved to be very useful.

The following situations are typical for the parameter combinations under discussion (Zwatz-Meise and Mahringer 1990, Zwatz-Meise 1991):

- cold air cloud phenomena within a deep layer of isentropes without remarkable gradients are connected with a PVA maximum in high levels downstream from a vorticity maximum in this layer.
- In the case of cloud phenomena in the left exit region of jet streaks an isotach maximum at high levels is connected with the PVA maximum.

Increased frontal cloudiness in connection with wave developments or in connection with the crossing of a jet streak are characterised by a PVA maximum in high levels superimposed on the frontal zone.

4.2 EXAMPLES

4.2.1 Cold Air Cloud Features

Figure 4c contains the just mentioned connection between vorticity and vorticity advection in the layer 500 to 300 hPa above the gridpoint 31/24 which is just at the western edge of the enhanced cloud configuration.

4.2.2 Wave Development

Figure 5c shows an intensive PVA maximum in the height which is area of the wave cloudiness between Udine (16044) and Zagreb (13130). This was the point of time where cyclonic circulation just had started with WAA in a low layer. The PVA maximum is a sign for the deepening of the cyclonic depression.

12 hours later there is still PVA east of Brindisi (16320).

5. EQUIVALENT POTENTIAL TEMPERATURE AND FRONTOGENESIS PARAMETER

5.1 BASIC CONCEPT AND IDEAS

The normal-component Q_n of the Q-vector can be derived from:

$$Q_n = -\frac{\partial Vn}{\partial n}\frac{\partial \theta}{\partial n} \qquad (2)$$

with n representing the direction normal to the isotherms and V_n the wind component in this direction. It can be used as frontogenesis parameter (Hoskins and Pedder 1980; Kurz 1989). Therefore its evaluation together with frontal zones is useful.

The following topics are of much interest for an evaluation:

- The existence of frontogenesis or frontolysis within the frontal surface which may lead to conclusions about an increase or decrease of the frontal strength and weather activity.
- Connection between the areas of frontogenesis and other parameters like upward motion and humidity.

5.2. EXAMPLES

5.2.1 Cold Front

Figure 2d shows intensive frontogenesis within the main frontal zone north and a secondary maximum with much weaker values south of the Alps. Again the coincidence with the brightest satellite signals is evident.

5.2.2 Cold Air Cloud Features

The frontogenesis parameter in figure 4f clearly confirms the diagnosis of the cloud systems along the cross section. There are high values of frontogenesis within the cold front east of Vienna while there are no remarkable values of this parameter connected with the non-frontal cloud system of the EC between Stuttgart (10739) and Munich (10868).

For further examples see also the paper "The use of satellite images in operational and research work at the Central Institute of Meteorology and Geodynamics in Vienna" (Zwatz-Meise et al.) in this volume.

6. SOME AIMS OF THE CROSS SECTION EVALUATION

As already mentioned it is intended in this project to make a collection of cases for one year.

There are several aims for the case study evaluations:

- to get much more knowledge about the physical state of synoptic and meso scale systems;
- to derive a relation between the distribution of parameters in cross section and actual weather;
- special weight shall be given to differences between the classical situations and their deviations;
- to use cross sections for forecast. At present, forecast fields of ECMWF parameters are already computed and operationally available. Figure 1b, c shows two examples. From equivalent-potential temperature and relative humidity (figure 1b) a very fast propagation of the cold front zone from grid point 32/24 at 00 UTC (which is between Stuttgart and Munich) to grid point 36/23 at 06 UTC (which is very near to Vienna) and further to 37/23 at 12 UTC (which is very near to Budapest) can be concluded. A zone of high humidity in front of the very steeply inclined frontal surface retains its values and position relative to the frontal surface during these 12 hours.

The cold front is followed by a warm front-like baroclinic zone; at 12 UTC its zone of crowded isentropes extends from about 800 hPa above gridpoint 28/24 (which is very close to Paris) up to about 450 hPa above gridpoint 34/23 (which is very close to Salzburg). A maximum of high humidity on top of this baroclinic zone reaches Switzerland. Figure 2c supplements these prognostic considerations with the propagation of the forecast WAA maxima on top as well as within the frontal zone.

7. FIGURES AND UNITS

For the description of the examples see paragraphs 2-5.
For a list of units for the parameters used in the legends see Appendix A.2.

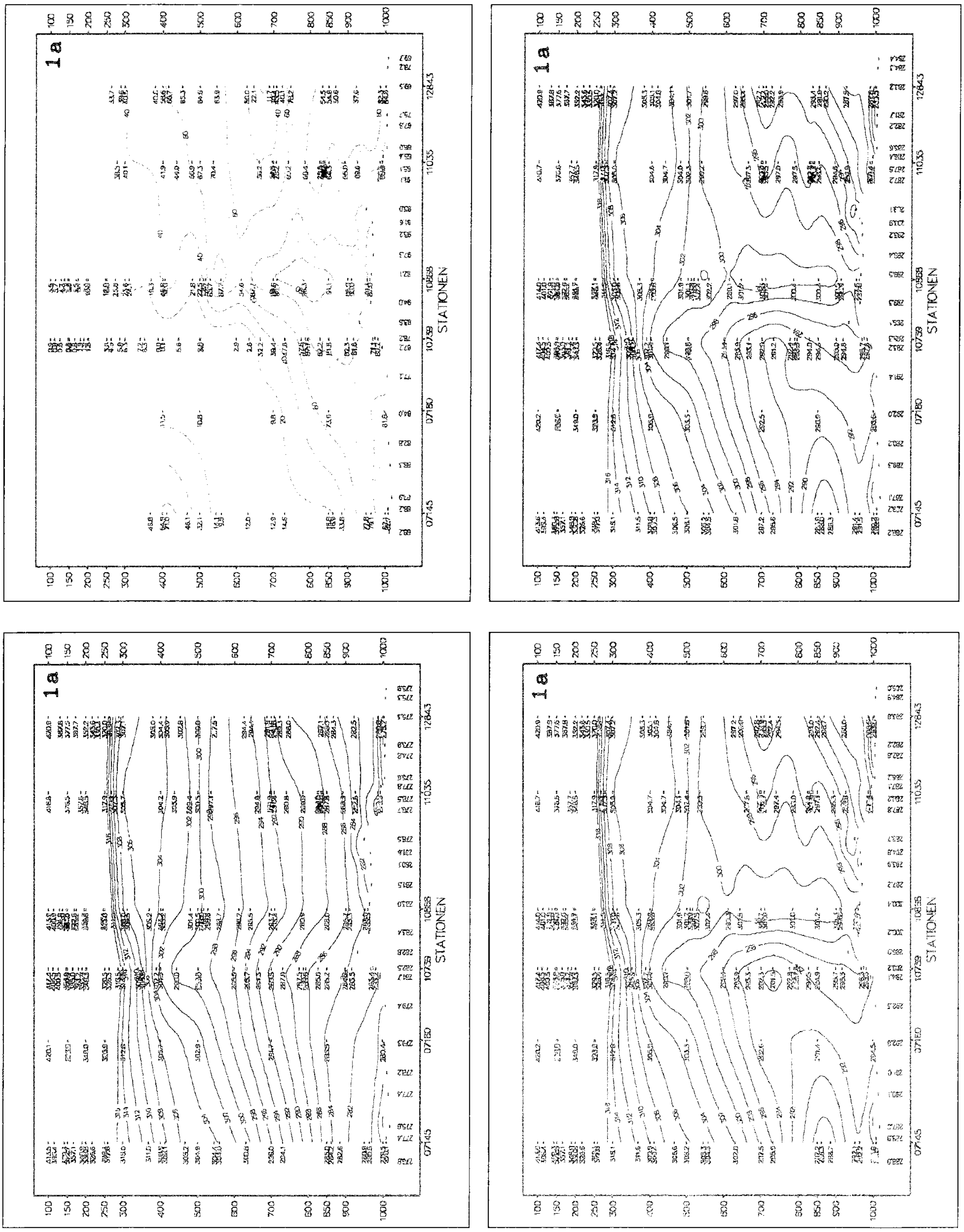

Figure 1:

4 March 1994/00 UTC

1a: Cross sections from radiosonde data, relative humidity (u.r.); potential temperature (u.l.), equivalent - potential temperature - cond (l.r.) with radiosonde measurements; l.l.: equivalent potential temperature.

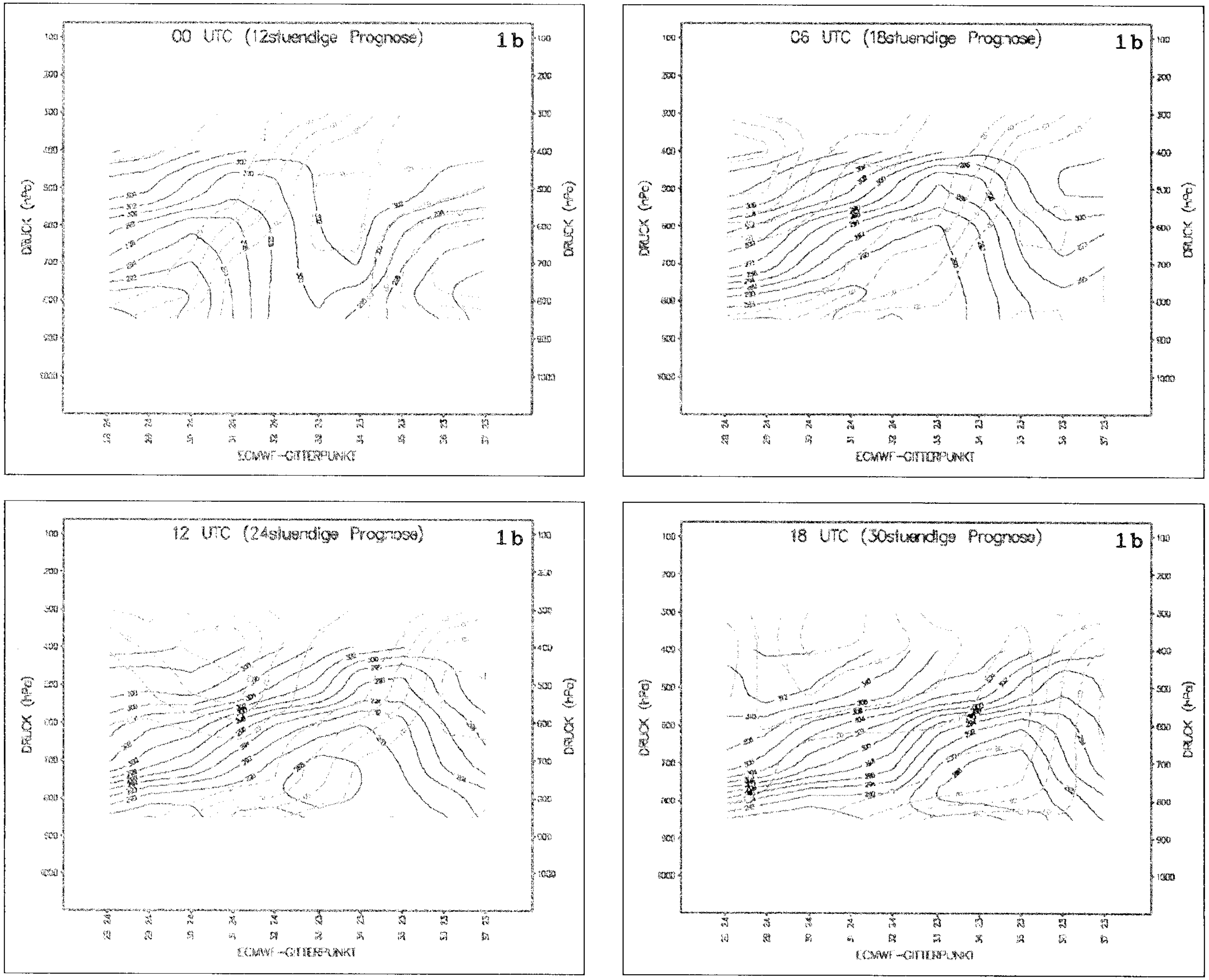

Figure 1:

4 March 1994/00 UTC

1b: Forecast block from ECMWF data for 00, 06, 12, 18 UTC (based on the initial field of 12 UTC of the previous day); solid black: equivalent-potential temperature, solid green: relative humidity.

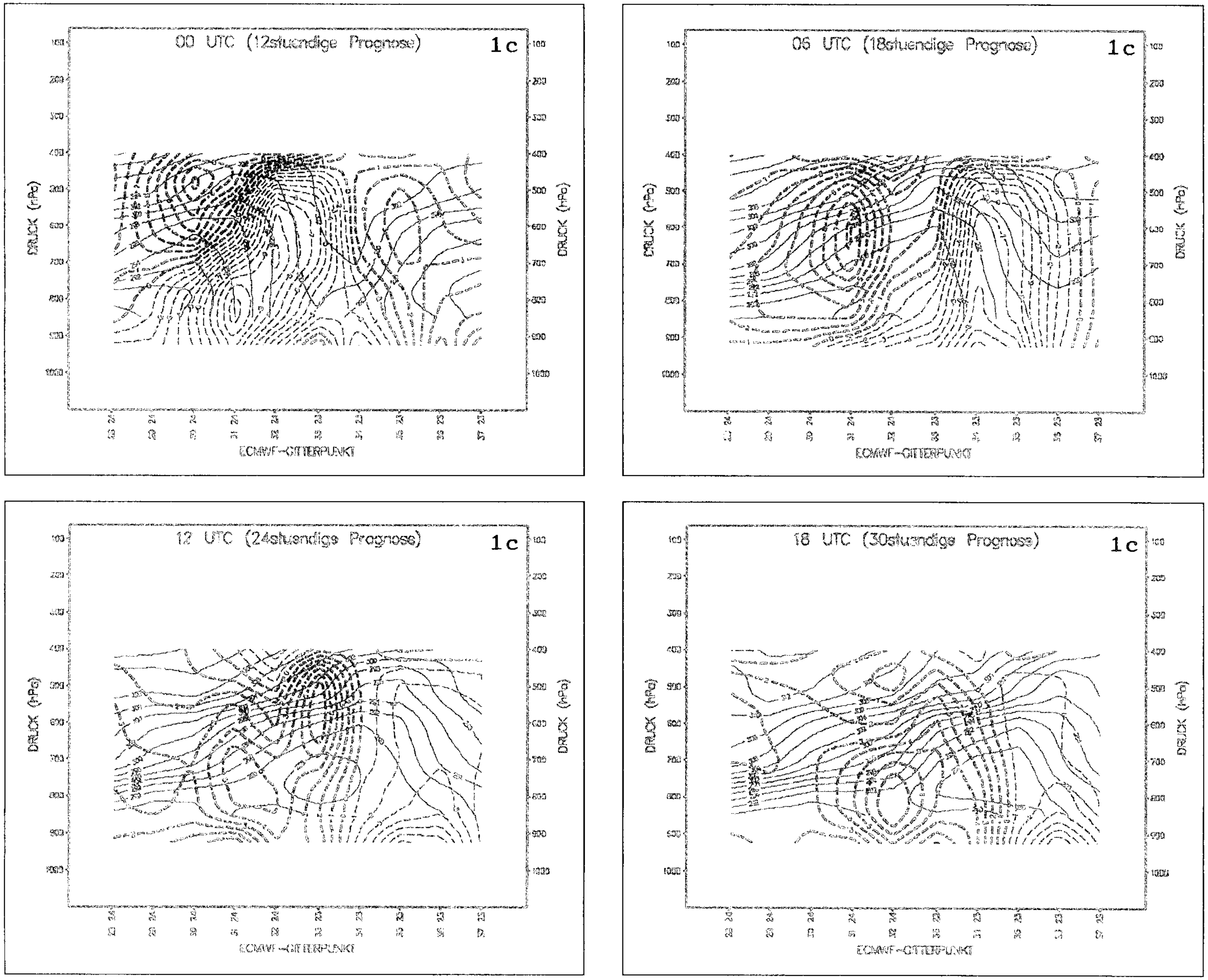

Figure 1:

4 March 1994/00 UTC

1c: same as 1b; solid black: equivalent-potential temperature, dashed blue: temperature advection.

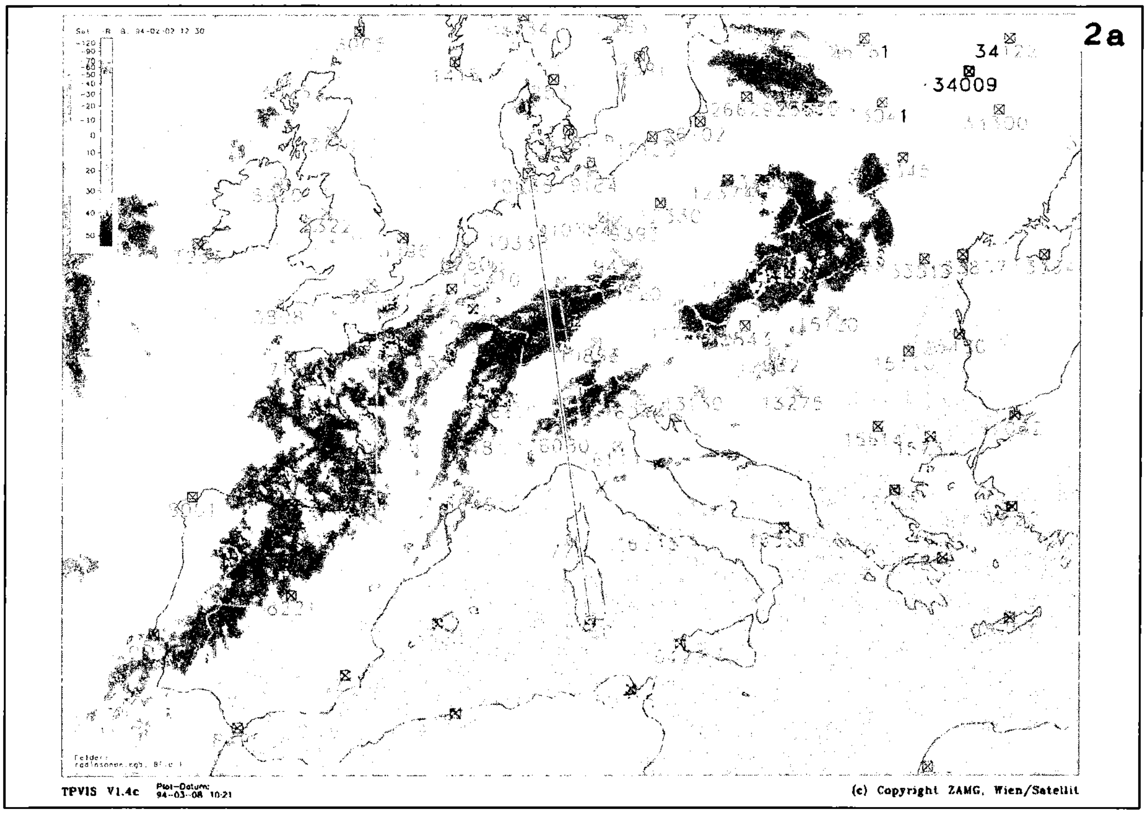

Figure 2a: IR, Meteosat, numbers of radiosonde stations, cross section indicated

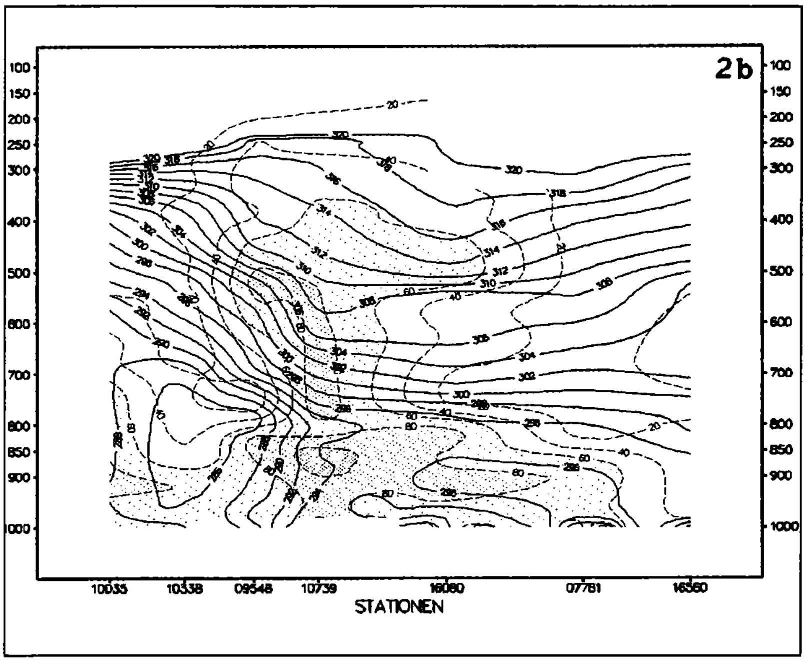

2b:
radiosonde data, solid black: equivalent-potential temperature dashed and shaded green: relative humidity

Figure 2: 2 February 1994/12 UTC; cold front with multiple structure

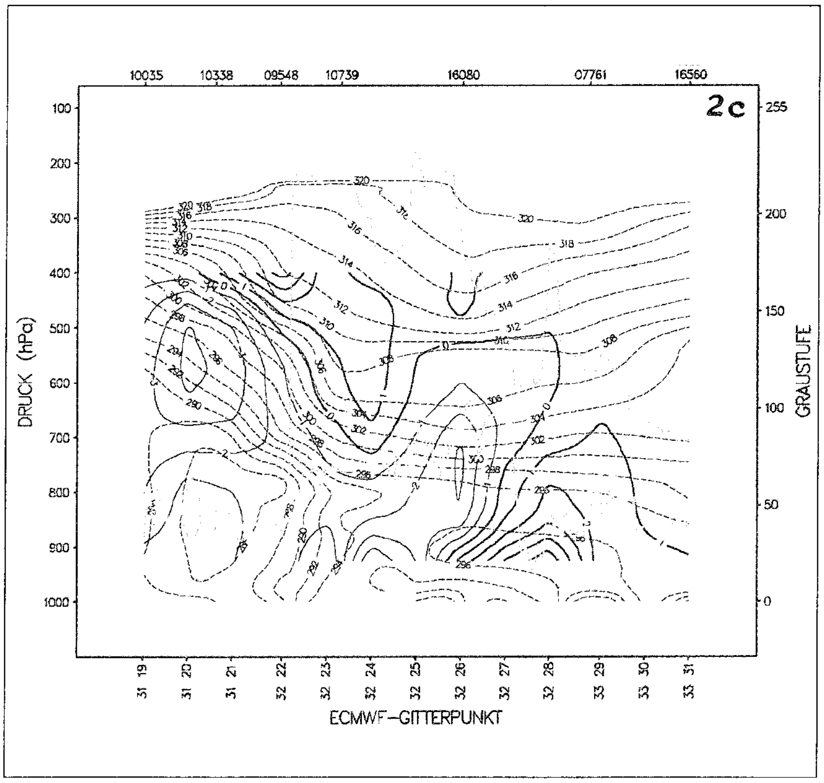

2c:
black dashed: equivalent-potential temperature from radiosonde data; solid blue: temperature advection from ECMWF data (heavy: WAA, light:CAA); orange: satellite signals (light: IR, heavy: VIS)

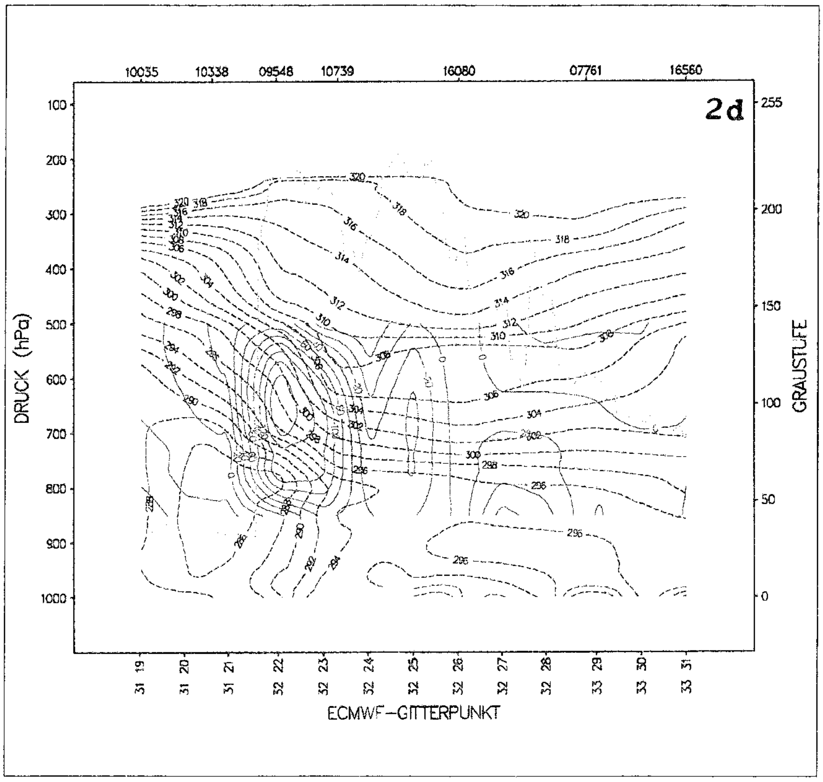

2d:
black dashed: equivalent-potential temperature from radiosonde data; violet: normal component of Q-vector (frontogenesis parameter) from ECMWF data (negative: frontogenesis, positiv: frontolysis); orange: IR-signals

Figure 2: 2 February 1994/12 UTC; cold front with multiple structure

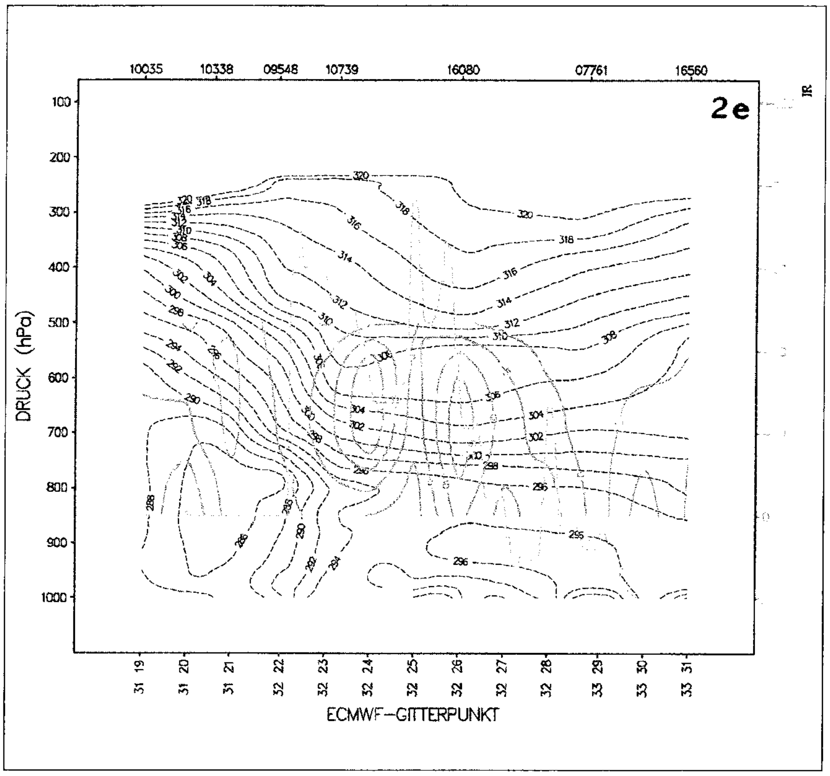

2e:
black dashed: equivalent-potential temperature from radiosonde data; solid brown: vertical motion from ECMWF data (omega: heavy: rising, light: sinking); orange: IR-signals (temperature)

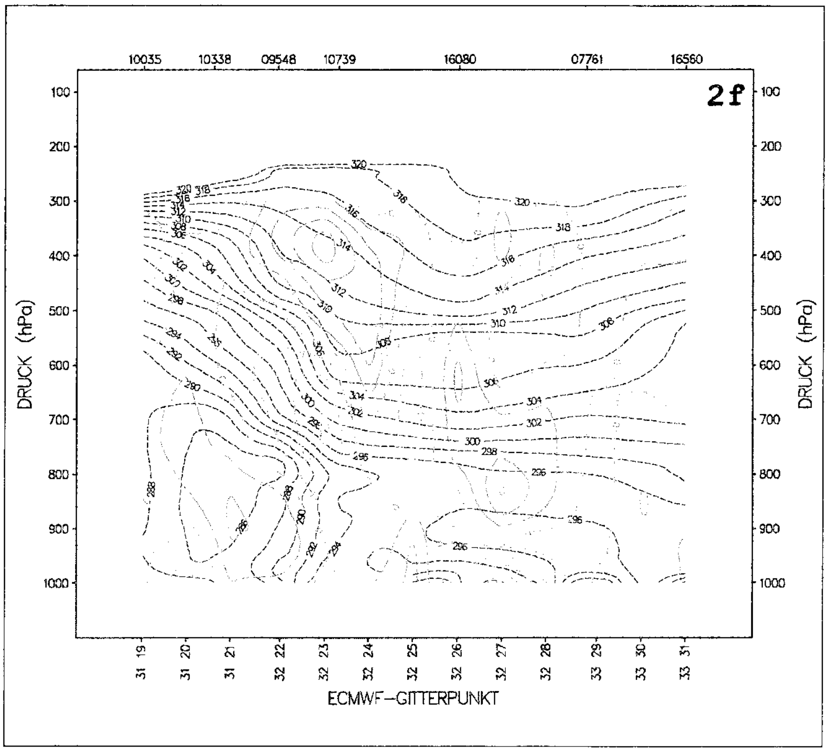

2f:
black dashed: equivalent-potential temperature from radiosonde data; solid red: divergence from ECMWF data (heavy: convergence, light: divergence)

Figure 2: 2 February 1994/12 UTC; cold front with multiple structure

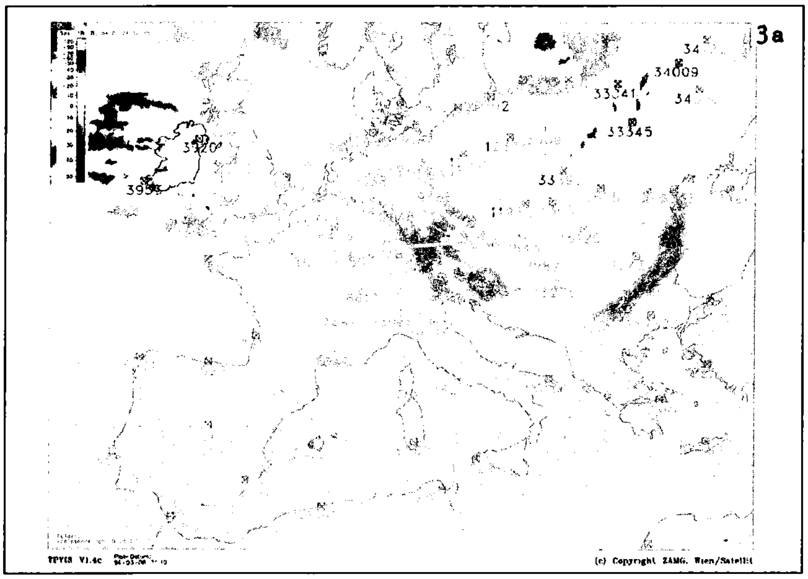

3a:
IR, Meteosat, numbers of radiosonde stations, cross section indicated

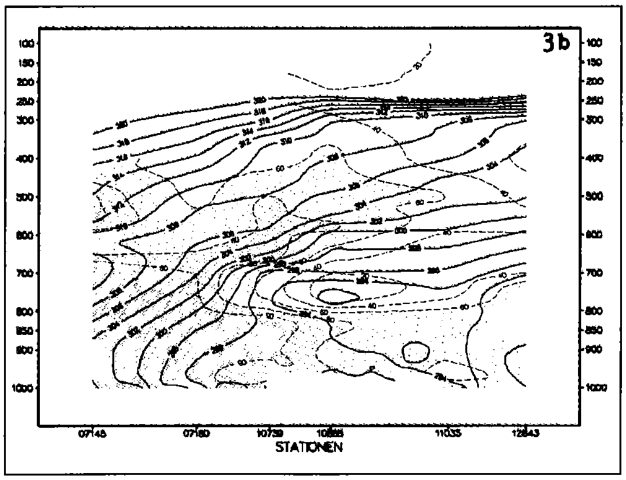

3b:
radiosonde data, solid black: equivalent-potential temperature dashed and shaded green: relative humidity

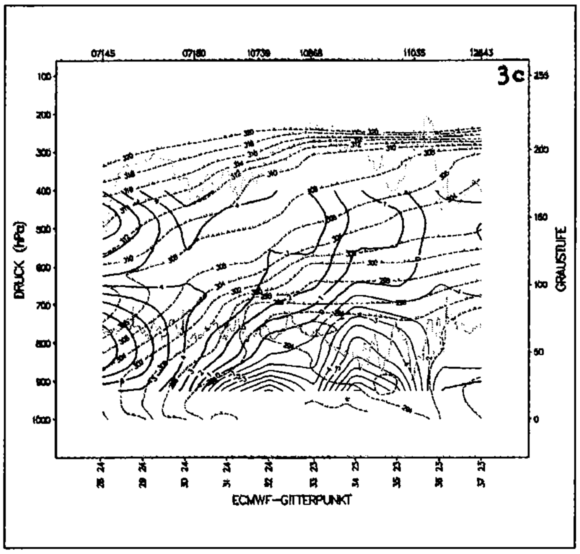

3c:
black dashed: equivalent-potential temperature from radiosonde data; solid blue: temperature advection from ECMWF data (heavy: WAA, light:CAA); orange: satellite signals (light: IR, heavy: VIS)

Figure 3: 24 January 1994,12 UTC; baroclinic zones with warm front character

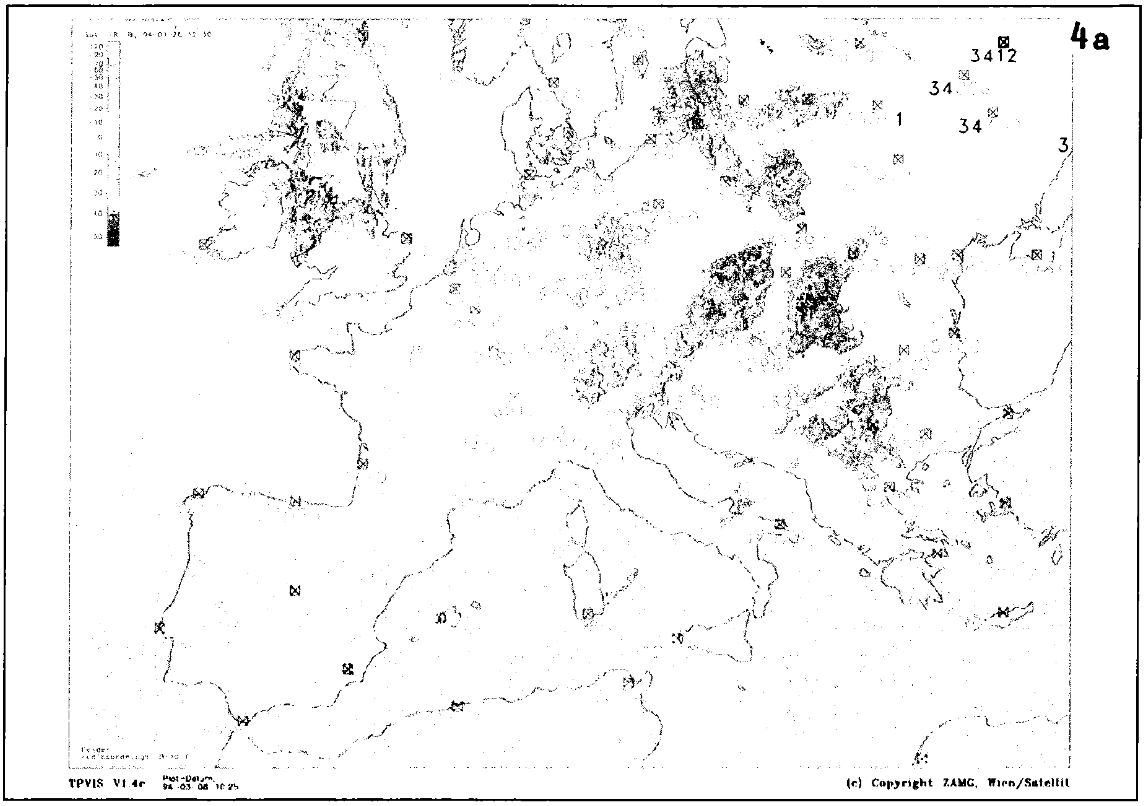

Figure 4a: IR, Meteosat, numbers of radiosonde stations, cross section indicated

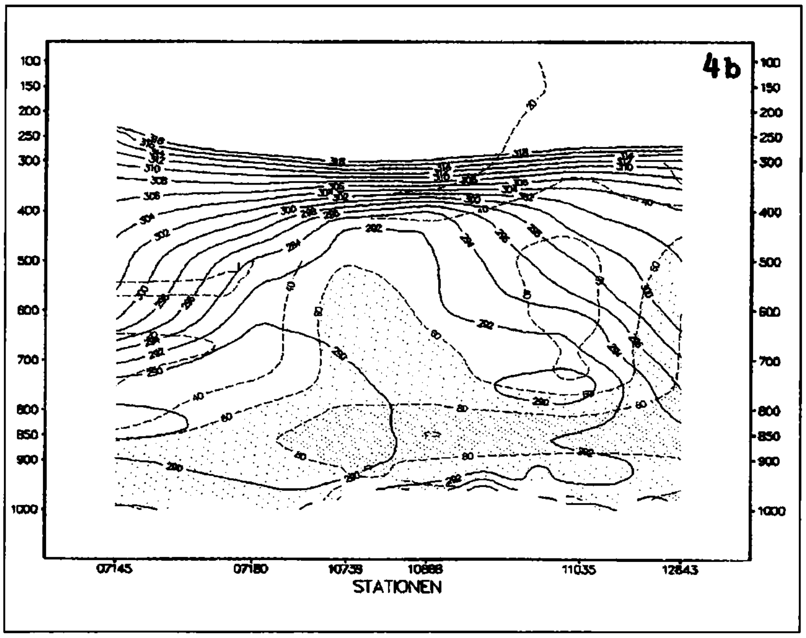

4b:
radiosonde data, solid black: equivalent - potential temperature dashed and shaded green: relative humidity

Figure 4: 26 January 1994/12 UTC; cold front and cold air cloud feature

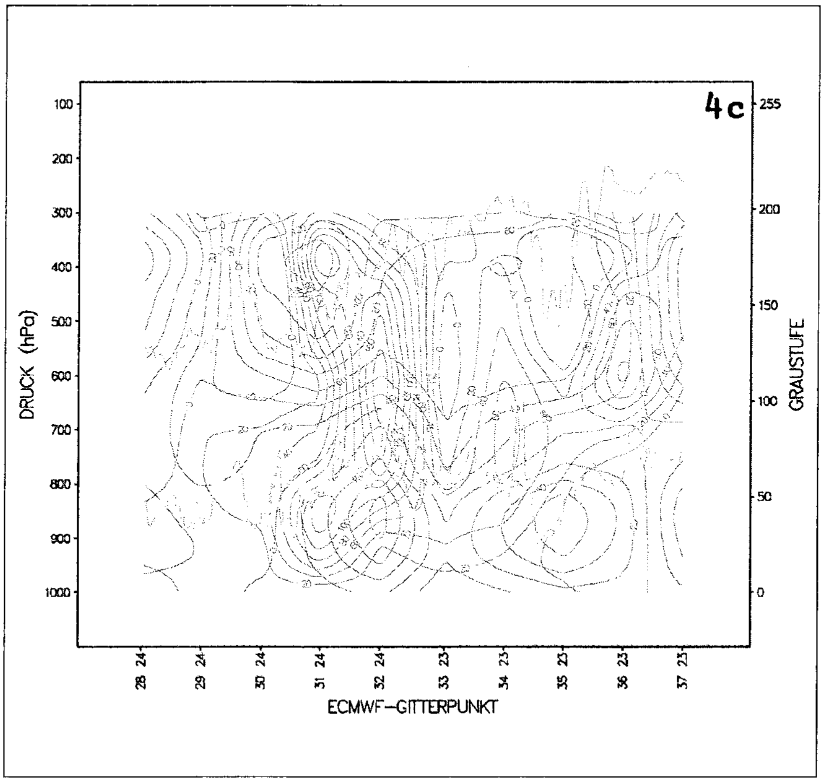

4 c:
solid blue: rel.vorticity from ECMWF data; solid turquoise: positive abs. vorticity advection from ECMWF data; orange: satellite signals (light: IR; heavy: VIS)

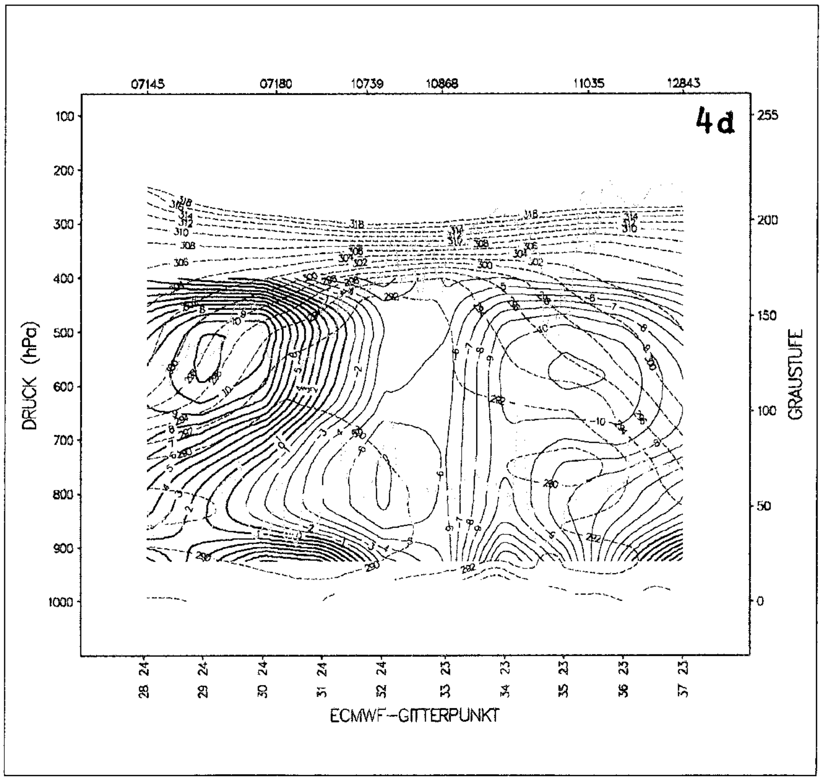

4d:
black dashed: equivalent-potential temperature from radiosonde data; solid blue: temperature advection from ECMWF data (heavy: WAA, light:CAA); orange: satellite signals (light: IR, heavy: VIS)

Figure 4: 26 January 1994/12 UTC; cold front and cold air cloud feature

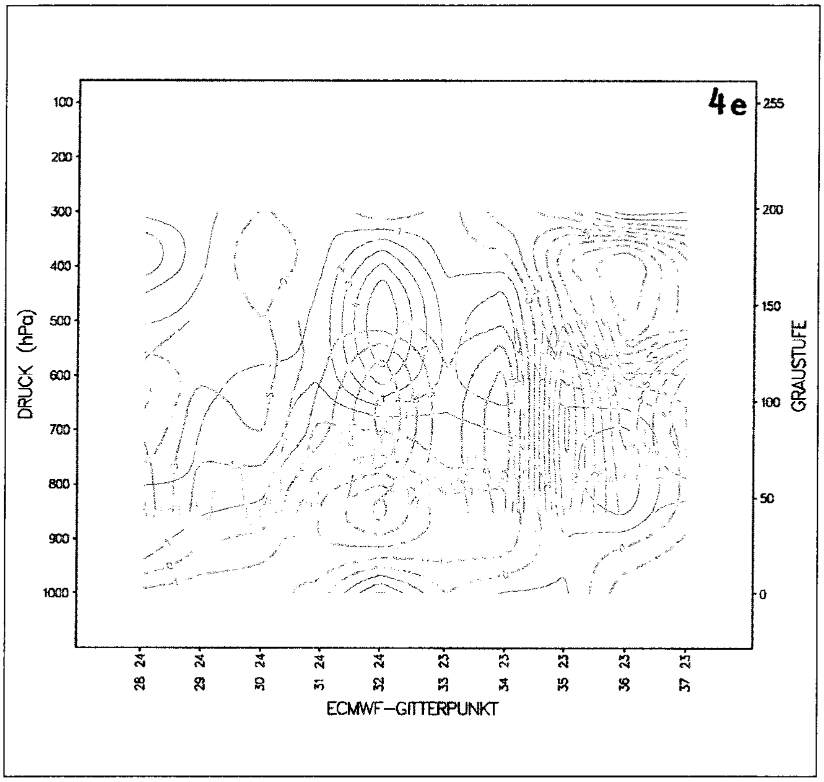

4e:
solid red: divergence from ECMWF data (heavy: convergence, light: divergence); solid brown: vertical motion from ECMWF data (omega: heavy: rising, light: sinking); orange: VIS-signals

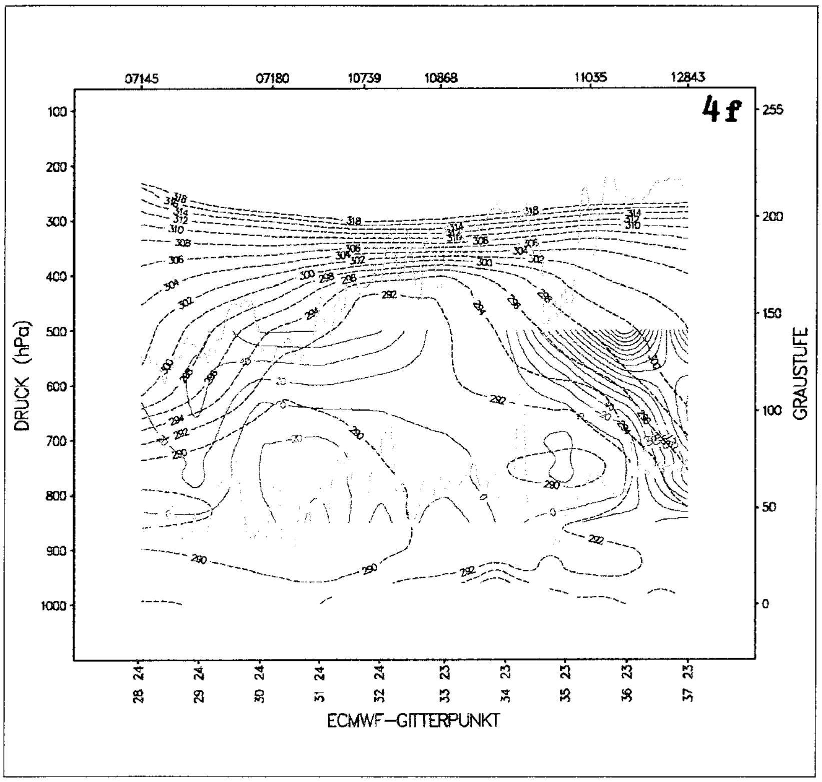

4f:
black dashed: equivalent-potential temperature from radiosonde data; violet: normal component of Q-vector (frontogenesis parameter) from ECMWF data (negative: frontogenesis, positiv: frontolysis); orange: satellite signals (heavy: VIS, light: IR)

Figure 4: 26 January 1994/12 UTC; cold front and cold air cloud feature

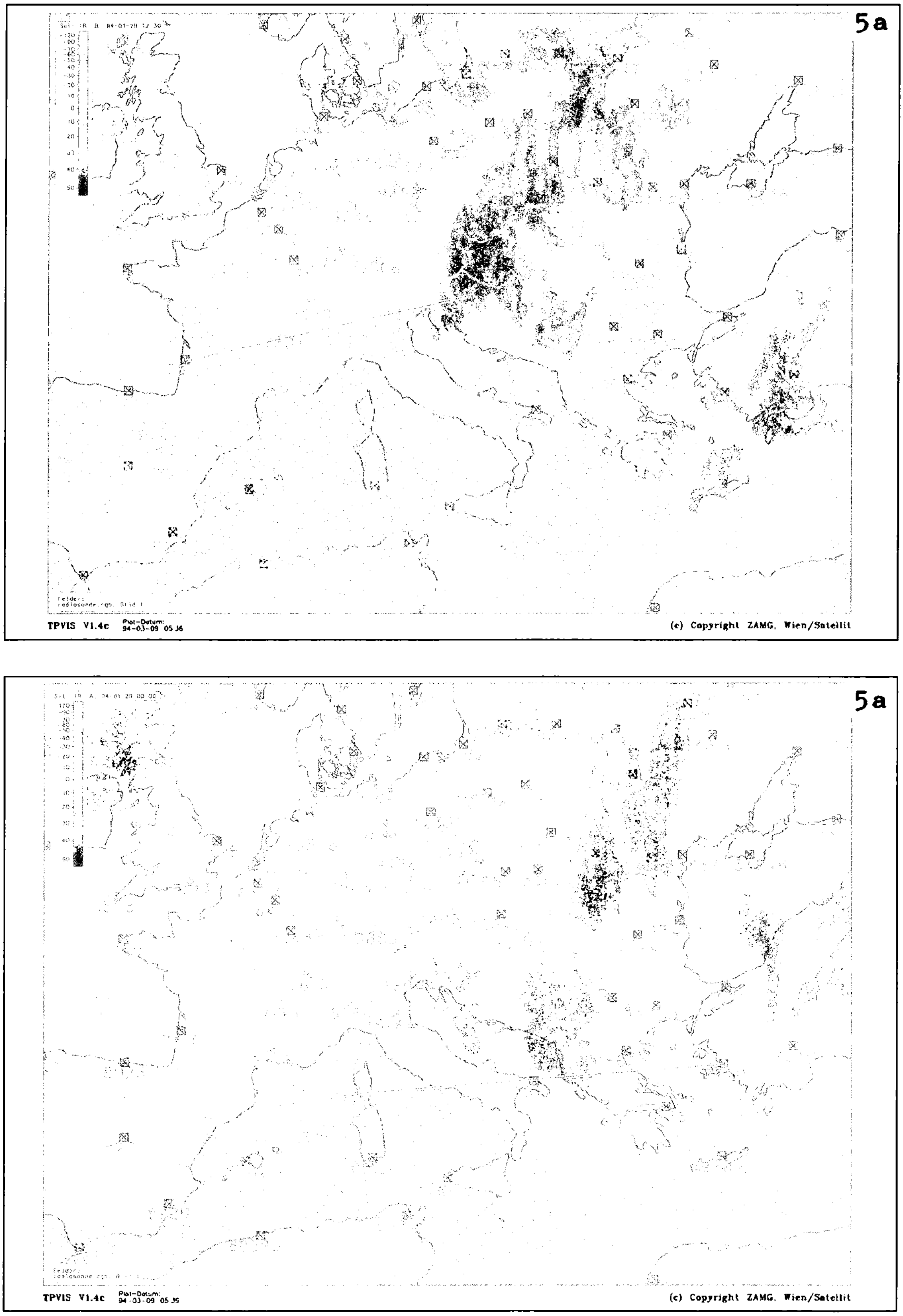

Figure 5a: 28 January 1994/12 UTC - 29 January 1994/00 UTC; wave development IR, Meteosat, numbers of radiosonde stations, cross section indicated (upper panel: 28/12 UTC; lower panel: 29/00 UTC)

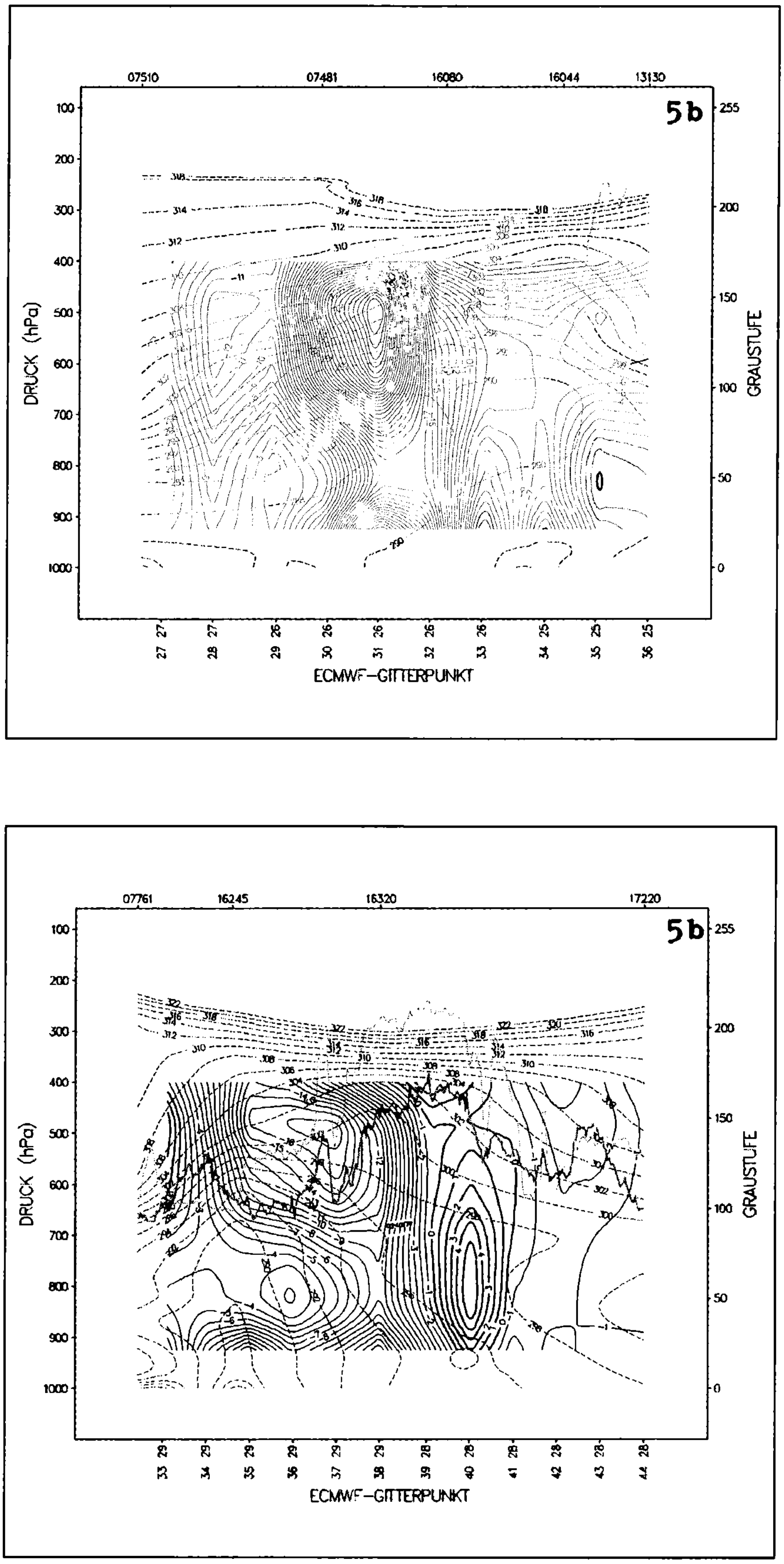

Figure 5b: 28 January 1994/12 UTC - 29 January 1994/00 UTC; wave development
black dashed: equivalent-potential temperature from radiosonde data; solid blue: temperature advection from ECMWF data (heavy: WAA, light:CAA); orange: satellite signals (light: IR, heavy: VIS); (upper panel: 28/12 UTC; lower panel: 29/00 UTC)

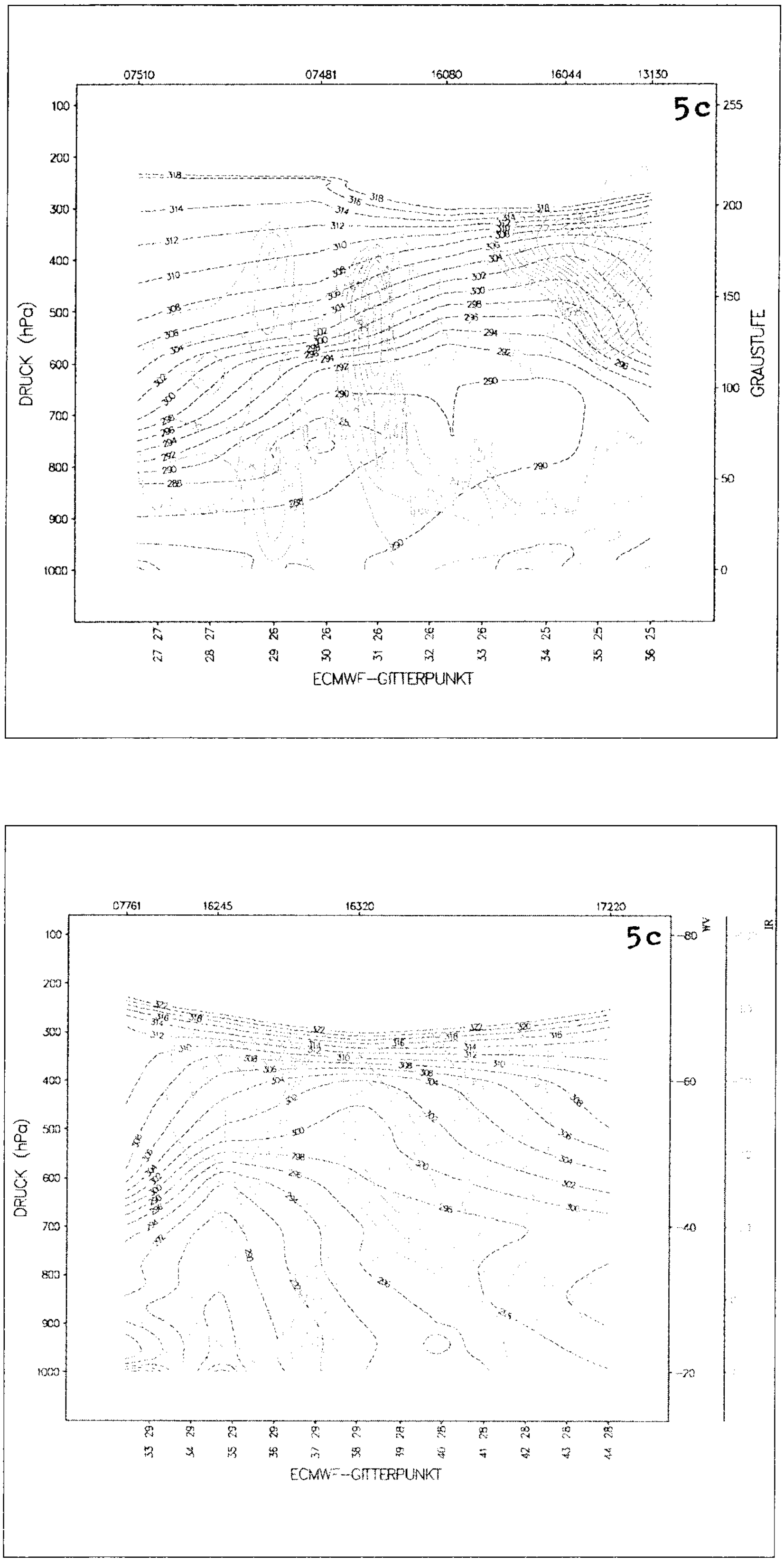

Figure 5c: 28 January 1994/12 UTC - 29 January 1994/00 UTC; wave development black dashed: equivalent-potential temperature from radiosonde data; solid turquoise: positive abs. vorticity advection from ECMWF data; orange: satellite signals (light: IR, heavy: VIS); (upper panel: 28/12 UTC; lower panel: 29/00 UTC)

ZAMG VIENNA

Radiosonde cross section: 20 December 1993, 12 GMT
Equivalent-potential temperature

Meridional 20 December 1993 12 UTC/Analysis along 15.55 E
Equivalent-potential temperature

MHS CROATIA

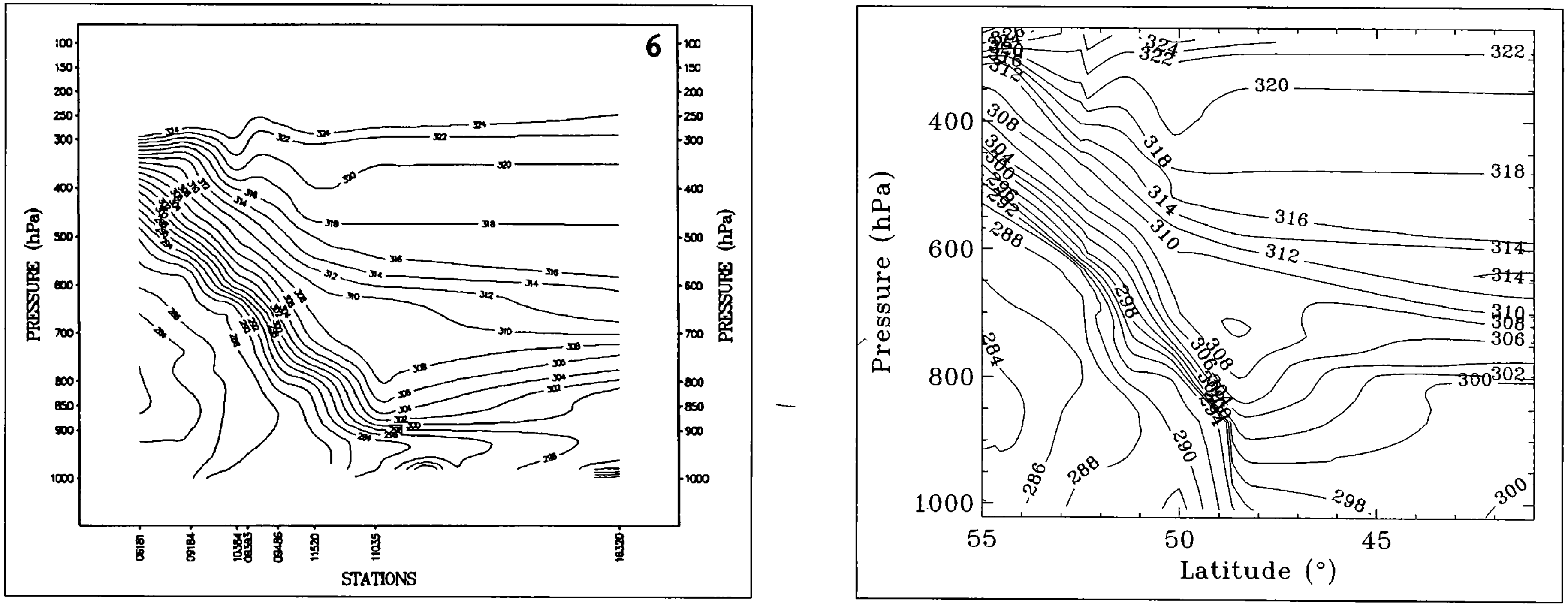

Figure 6: Space cross-sections from Copenhagen to Brindisi for December, 20th, 1993. Left: Method ZAMG; right: Method HRID.

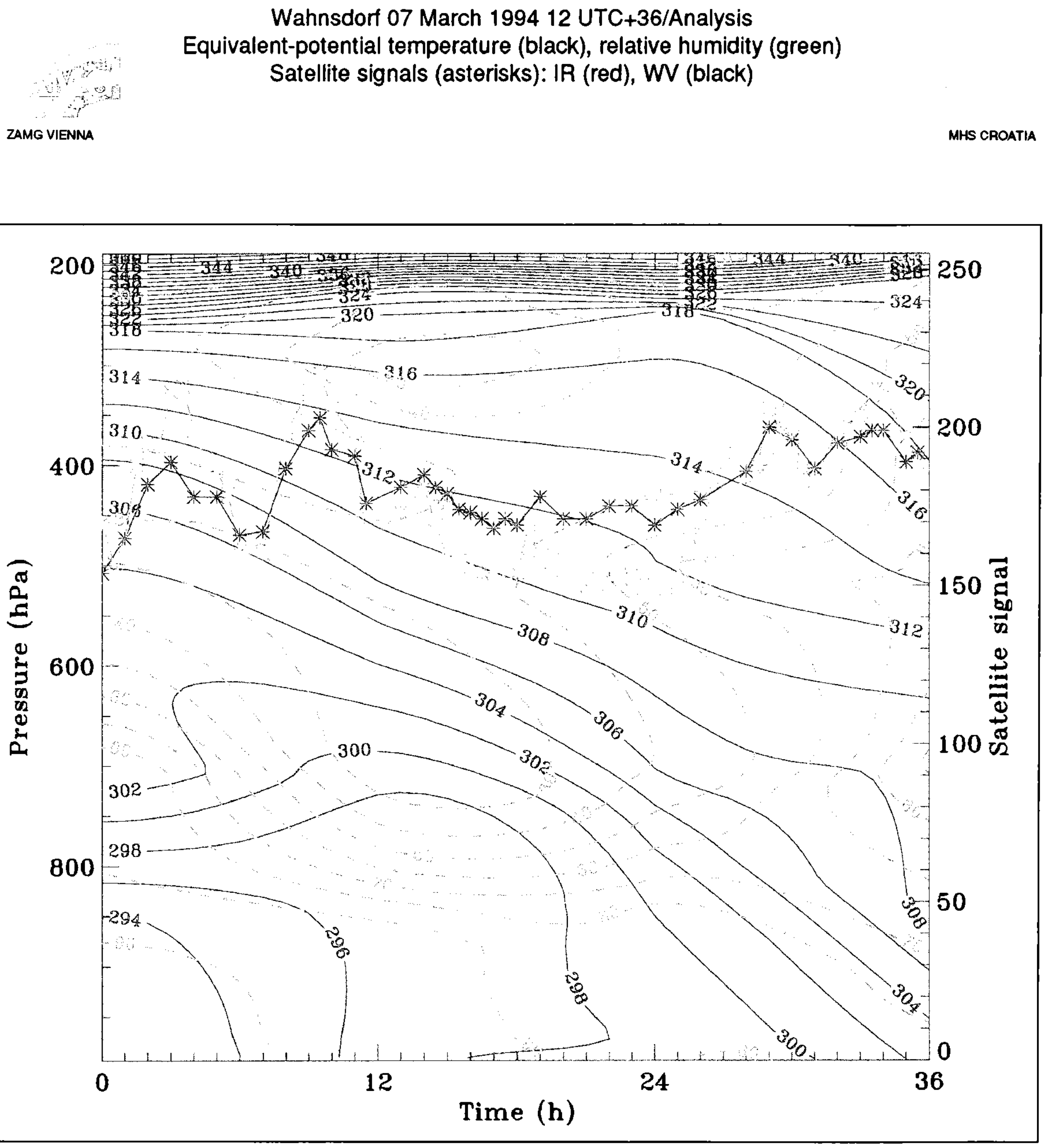

Figure 7: HRID time cross-section with superimposed time series of satellite signals, at Wahnsdorf, Germany

Appendix A.1

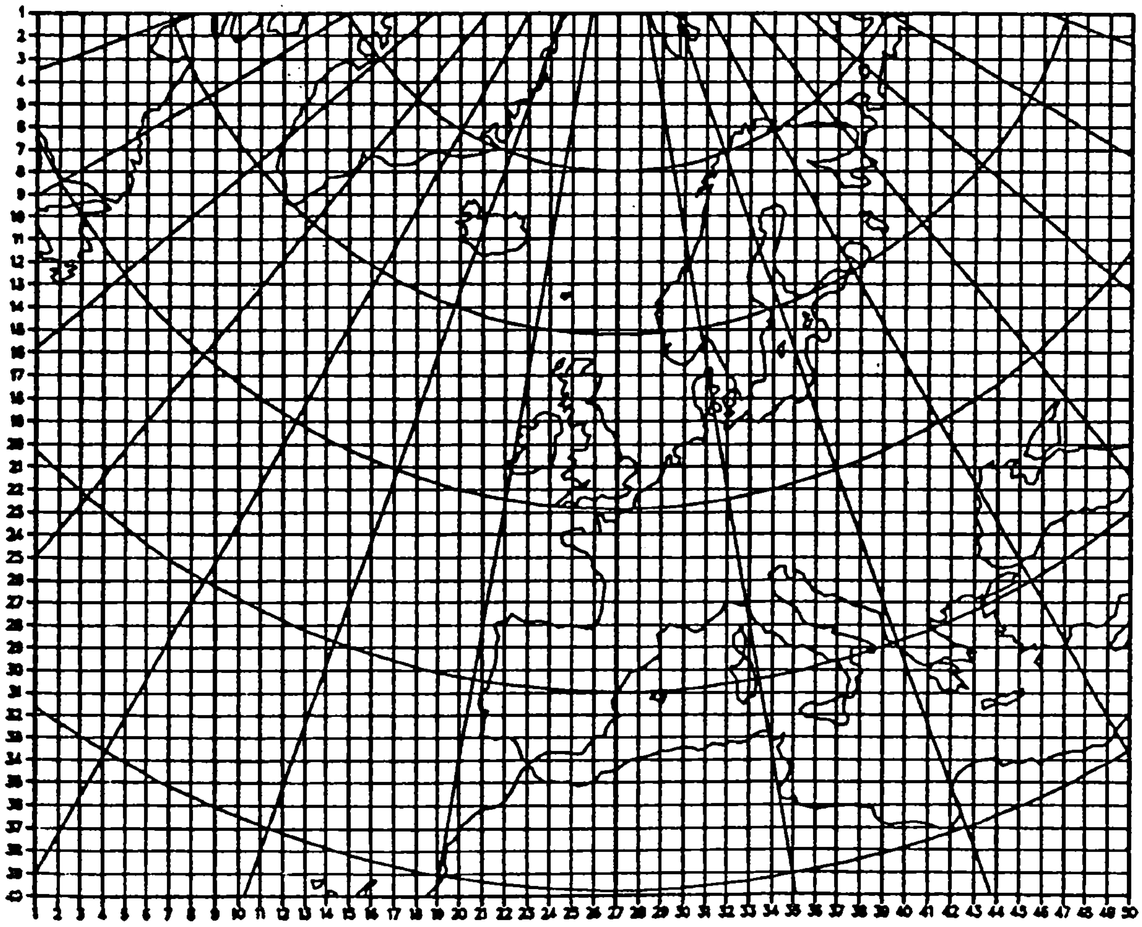

The Mesh of Gridpoints on which ECMWF Data are available

Appendix A.2

List of units and isoline distances:

Parameter: unit ; isoline distance
Potential temperatures: K ; 2
relative humidity: % ; 20
temperature advection: (K/12h) ; 1
vorticity advection: (1.E-10s**-2) ; 20
vorticity: (1.E-6s**-1) ; 20
omega: (hPa/h) ; 5
divergence: (1.E-5s**-1) ; 1
isotachs: (m/s) ; 20
Qn: (1.E-11 K/(m*s)) ; 20

C. COMBINATION OF THE TWO DIFFERENT ANALYSIS METHODS

The cross-section programs developed at the NMC Zagreb, Croatia, have been implemented at the ZAMG. For the time being, radiosonde data is investigated in single station analyses, time cross-sections and space cross-sections. In operational use, the vertical coordinate is pressure, but there is an option to use z-system. Several comparisons with the cross-section visualization system developed at the ZAMG have already been made (Figure 6).

Recently, an option to superimpose time series of satellite information on the time cross-sections of the parameters calculated in HRID has been added (Figure 7).

Theoretical considerations have been initiated, final results will be published elsewhere.

REFERENCES

HOSKINS, B.J. and M.A.PEDDER, 1980: The diagnosis of middle latitude synoptic development. Quart. J. R. Met. Soc, 106, 707-719.

KURZ, M., 1989: Zur Analyse und Diagnose der ersten beiden Fronten des Frontenexperiments der Deutschen Forschungsgemeinschaft. Meteorol. Rdsch. 41, 147-160.

MAHRINGER, G. and V. ZWATZ-MEISE, 1993: A semi-operational diagnosis method. Contributions to Atmospheric Physics, Vol. 66, No. 1-2, 89-106.

ZWATZ-MEISE, V. and G. MAHRINGER, 1990: SATMOD: An Interactive System Combining Satellite Images and Model Output Parameters. Wea. and Forecasting, Vol. 5, No. 2, 233-246.

ZWATZ-MEISE, V. and F. HUFNAGL, 1990: Some Results about the Relation between an objective Front Parameter and Cloud Bands in Satellite Images and its Connection to Classical Cold Front Models. Meteorol. Atmos. Phys., 42, 77-89.

ZWATZ-MEISE, V., 1991: Satellite-synoptic aspects of warm fronts. Proceedings of the 8th Meteosat Scientific Users Meeting. EUMETSAT; EUM P08.

ZWATZ-MEISE, V., 1987: Satelliten-synoptische Aspekte im Bereich Front-Höhentrog. Wetter und Leben 39, 101-115.

ZWATZ-MEISE, V., 1991: Satelliten-synoptische Jet-Streak Phänomene und ihre Einbeziehung in die Wettervorhersage. Publikationen der Österr. Akademie der Wissenschaften, math.-nat. Kl., Abt.I 198. Bd, 5. bis 10. Heft.

ZWATZ-MEISE, V. and K. BENDL, 1992: PVA-Maxima and their connection to cloud systems in satellite images and to precipitation. Meteorol. Atmos.Phys. 47, 145-164.

Author's address:

VERONIKA ZWATZ-MEISE, ALEXANDER JANN, ROLAND WINKLER
Central Institute for Meteorology and Geodynamics
Synoptical Division
Hohe Warte 38, A-1190 Vienna, AUSTRIA
Phone: +43 1 36 44 53/2315, 2316, Fax: +43 1 36 45 70
E-mail: zwa@zassun3.zamg.ac.at
jann@zassun3.zamg.ac.at

Arbeiten aus der Zentralanstalt für Meteorologie und Geodynamik

bisher erschienen:

Heft	Publ.Nr.	Fachgebiet	Autor	Titel und Umfang	Preis in öS
1	184	Geophysik	ECKEL, O.:	*Über die vertikale Temperaturverteilung im Traunsee.* Wien 1967, 42 S., 4 Tab., 24 Abb.	80,--
2	186	Meteorologie	STEINHAUSER, F.:	*Ergebnisse von Pilotballon - Höhenwindmessungen in Österreich,* Wien 1967, 44 S., 16 S. Tab., 28 Abb.	70,--
3	487	Geophysik	TOPERCZER, M.:	*Die Verteilung der erdmagnetischen Elemente in Österreich zur Epoche 1960.0.* Wien 1968, 18 S., 3 Tab., 10 Kartenbeilagen	vergriffen
4	190	Geophysik	BRÜCKL, E., G. GANGL und P. STEINHAUSER:	*Die Ergebnisse der seismischen Gletschermessungen am Dachstein im Jahre 1967.* Wien 1969, 24 S., 11 Abb.	50,--
5	191	Meteorologie	HADER, F.:	*Durchschnittliche extreme Niederschlagshöhen in Österreich. Wien 1969,* 19 S., 6 Tab., 1 Kartenbeilage	50,--
6	192	Meteorologie	STEINHAUSER, F.:	*Der Tagesgang der Bewölkung und Nebelhäufigkeit in Österreich.* Wien 1969, 22 S., 4 Tab., 16 Abb.	50,--
7	193	Geophysik	GANGL, G.:	*Die Erdbebentätigkeit in Österreich 1901-1968.* Wien 1970, 36 S., 11 Abb., 1 Kartenbeilage	vergriffen
8	195	Meteorologie	STEINHAUSER, F.:	*Die Windverhältnisse im Stadtgebiet von Wien.* Wien 1970, 17 S., 52 Tab., 47 Abb.	120,--
9	196	Geophysik	BRÜCKL, E., G. GANGL und P. STEINHAUSER:	*Die Ergebnisse der seismischen Gletschermessungen am Dachstein im Jahre 1968.* Wien 1971, 31 S., 7 Tab., 13 Abb.	vergriffen
10	198	Geophysik	BRÜCKL, E., G. GANGL:	*Die Ergebnisse der seismischen Gletschermessungen am Gefrorne Wand Kees im Jahre 1969.* Wien 1972, 13 S., 8 Abb., 3 Karten	50,--
11	201	Geophysik	BITTMANN, O., E. BRÜCKL, G. GANGL und F. J. WALLNER:	*Die Ergebnisse der seismischen Gletschermessungen am Obersten Pasterzenboden (Glocknergruppe) im Jahre 1970.* Wien 1973, 21 S., 9 Abb., 3 Karten	60,--
12	202	Meteorologie	STEINHAUSER, F.:	*Tages- und Jahresgang der Sonnenscheindauer in Österreich 1929-1968.* Wien 1973, 12 S., 98 Tab., 5 Abb.	110,--
13	203	Meteorologie		*Klimadaten des Neusiedlerseegebietes, I. Teil. Tabellen der Stundenwerte der Lufttemperatur, 1966-1970,* 105 Tab.	90,--
14	205	Geophysik	PÜHRINGER, A., W. SEIBERL, E. TRAPP und F. PAUSWEG:	*Die Verteilung der erdmagnetischen Elemente in Österreich zur Epoche 1970.0.* Wien 1975, 18 S., 3 Tab., 9 Kartenbeilagen	90,--
15	206	Meteorologie		*Klimadaten des Neusiedlerseegebietes, II. Teil. Tabellen der Stundenwerte der Relativen Feuchte, 1966-1970,* 105 Tab.	100,--
16	207	Meteorologie		*Hundert Jahre Meteorologische Weltorganisation und die Entwicklung der Meteorologie in Österreich.* Wien 1975, 50 S.	100,--

Heft	Publ.Nr.	Fachgebiet	Autor Titel und Umfang	Preis in öS
17	208	Geophysik	TORPERCZER, M.: *Die Geschichte der Geophysik an der Zentralanstalt für Meteorologie und Geodynamik.* Wien 1975, 24 S.	50,--
18	209	Meteorologie	CHALUPA, K.: *Ergebnisse der Registrierung der Schwefeloxid-Immission in Wien - Hohe Warte, Okt. 1967-Dez. 1974.* Wien 1976, 62 S., 19 Tab., 24 Abb.	80,--
19	210	Geophysik	GUTDEUTSCH, R. und K. ARIC: *Erdbeben im ostalpinen Raum.* Wien 1976, 23 S., 3 Karten	80,--
20	211	Meteorologie	TOLLNER, H., W. MAHRINGER und F. SÖBERL: *Klima und Witterung der Stadt Salzburg.* Wien 1976, 176 S., 29 Abb.	220,--
21	214	Geophysik	SEIBERL, W.: *Das Restfeld der erdmagnetischen Totalintensität in Österreich zur Epoche 1970.0.* Wien 1977, 8 S., 1 Kartenbeilage	vergriffen
22	216	Meteorologie	SABO, P.: *Ein Vergleich deutscher und amerikanischer Höhenvorhersagekarten für den Alpenraum.* Wien 1977, 34 S., 11 Tab., 5 Abb.	60,--
23	217	Meteorologie	CEHAK, K.: *Die Zahl der Tage mit Tau und Reif in Österreich.* Wien 1977, 17 S., 6 Tab., 1 Abb., 6 Karten	80,--
24	218	Meteorologie	CHALUPA, K.: *Ergebnisse der Registrierung der Schwefeloxid- und Summenkohlenwasserstoff - Immission in Wien - Hohe Warte 1975.* Wien 1977, 40 S., 13 Tab., 12 Abb.	70,--
25	219	Geophysik	BRÜCKL, E. und O. BITTMANN: *Die Ergebnisse der seismischen Gletschermessungen im Bereich der Goldberggruppe (Hohe Tauern) in den Jahren 1971 und 1972.* Wien 1977, 30 S., 2 Tab., 34 Abb., 2 Karten	80,--
26	222	Geophysik	FIEGWEIL, E.: *Die Nachbebenserie der Friauler Beben vom 6. Mai und 15. September 1976.* Wien 1977, 20 S., 7 Tab., 5 Abb.	60,--
27	223	Meteorologie	MACHALEK, A.: *Prognosenprüfung im Österreichischen Wetterdienst.* Wien 1977, 55 S., 4 Tab., 5 Abb.	80,--
28	224	Meteorologie	SKODA, G.: *Kinematisch-Klimatologische Verlagerung von Kaltfronten und Troglinien.* Wien 1977, 32 S., 7 Tab., 10 Abb.	70,--
29	225	Geophysik	TRAPP, E. und D. ZYCH: *Verteilung der Vertikalintensität im Raum Wien - Salzburg nach Meßergebnissen der Zentralanstalt und der ÖMV-AG.* Wien 1977, 15 S., 3 Tab., 1 Karte, 2 Kartenbeilagen	50,--
30	226	Meteorologie	*Klimadaten des Glocknergebietes, I. Teil: Tabellen und Stundenwerte der Lufttemperatur und der Relativen Luftfeuchte 1974-1976 (Wallack-Haus, Hochtor-Süd, Hochtor-Nord, Fuscher-Lacke).* 117 Tab.	150,--
31	227	Meteorologie	*Bericht über die 14. Internationale Tagung für Alpine Meteorologie vom 15.-17. Sept. 1976 in Rauris, Salzburg, 1. Teil.* Wien 1978, 323 S.	250,--
32	228	Meteorologie	*Bericht über die 14. Internationale Tagung für Alpine Meteorologie vom 15.-17. Sept. 1976 in Rauris, Salzburg, 2. Teil.* Wien 1978, 347 S.	250,--
33	229	Meteorologie	CHALUPA, K.: *Ergebnisse der Registrierung der Schwefeloxid-, Summenkohlenwasserstoff- und Ozon-Immission in Wien - Hohe Warte, 1976.* Wien 1978, 53 S., 20 Tab., 17 Abb.	90,--

Heft	Publ.Nr.	Fachgebiet	Autor Titel und Umfang	Preis in öS
47	251	Meteorologie	CHALUPA, K.: *Ergebnisse der Registrierung der Schwefeloxid-Immission in Wien - Stephansplatz, 1975-1979.* Wien 1981, 50 S., 13 Tab., 21 Abb.	vergriffen
48	252	Meteorologie	LAUSCHER, F.: *Säkulare Schwankungen der Dezennienmittel und extreme Jahreswerte der Temperatur in allen Erdteilen.* Wien 1981, 42 S., 8 Tab.	50,--
49	254	Meteorologie	CHALUPA, K.: *Ergebnisse der Registrierung der Schwefeloxid-Immission in Wien - Hohe Warte und in Wien - Stephansplatz, 1980.* Wien 1981, 46 S., 24 Tab., 13 Abb.	100,--
50	255	Geophysik	MELICHAR, P.: *Ergebnisse der vergleichenden geomagnetischen Absolutmessungen an den Observatorien Tihany - Ungarn und Wien - Kobenzl.* Wien 1981, 35 S.	50,--
51	256	Geophysik	BRÜCKL, E. und K. ARIC: *Die Ergebnisse der seismischen Gletschermessungen am Hornkees in den Zillertaler Alpen im Jahre 1975.* Wien 1981, 20 S., 5 Tab., 5 Abb., 1 Karte	vergriffen
52	257	Meteorologie	*Klimadaten des Glocknergebietes, VII. Teil: Tabellen der Stundenwerte der Windgeschwindigkeit und der Windrichtung 1977-1979 (Fusch, Fuscher Lacke, Wallack-Haus, Guttal).* Wien 1982, 82 Tab.	120,--
53	260	Meteorologie	STEINHAUSER, F.: *Verteilung der Häufigkeiten der Windrichtungen und der Windstärken in Österreich zu verschiedenen Tages- und Jahreszeiten.* Wien 1982, 140 S., 131 Tab., 4 Kartenbeilagen	120,--
54	261	Meteorologie	DOBESCH, H. und F. NEUWIRTH: *Wind in Niederösterreich, insbesondere im Wiener Becken und im Donautal.* Wien 1982, 212 S., 183 Abb.	vergriffen
55	266	Meteorologie	*Klimadaten des Glocknergebietes, VIII. Teil: Tabellen der Stundenwerte der Globalstrahlung 1975-1980 (Fuscher-Lacke und Wallack-Haus).* Wien 1983, 39 S.	50,--
56	268	Geophysik	WEBER, F. und R. WÜSTRICH: *Ergebnisse der refraktionsseismischen Messungen am Hochkönigsgletscher.* Wien 1983, 50 S., 3 Tab., 7 Abb., 11 Beilagen	100,--
57	278	Meteorologie	*Klimadaten des Glocknergebietes, IX. Teil: Tabellen der Niederschlagsmeßergebnisse 1974-1980.* 48 S., 41 Tab.	70,--
59	283	Meteorologie	KAISER, A.: *Inversionen in der bodennahen Atmosphäre über Klagenfurt.* Wien 1984, 79 S., 13 Tab., 22 Abb.	80,--
60	284	Meteorologie	LAUSCHER, F.: *Ozonbeobachtungen in Wien von 1853-1981. Zusammenhänge zwischen Ozon und Wetterlagen.* Wien 1984, 29 S., 13 Tab. 3 Abb.	40,--
61	289	Meteorologie	*Klimadaten von Österreich Mittelwerte 1971-1980.* Teil I (Vorarlberg) und Teil II (Tirol). 71 S.	60,--
62	299	Geophysik	DRIMMEL, J.: *Seismische Intensitätsskala 1985 (SIS-85).* Vorschlag einer Neufassung der Intensitätsskala MSK-64. 28 S., 8 Tab., 2 Abb.	40,--
63	300	Meteorologie	*Klimadaten von Österreich Mittelwerte 1971-1980.* Teil III (Salzburg) und Teil IV (Oberösterreich). 107 S.	80,--
64	302	Meteorologie	LAUSCHER, F.: *Klimatologische Synoptik Österreichs mittels der ostalpinen Wetterklassifikation.* Wien 1985, 65 S., 32 Tab., 5 Abb.	90,--

Heft	Publ.Nr.	Fachgebiet	Autor	Titel und Umfang	Preis in öS
34	231	Meteorologie		*Klimadaten des Glocknergebietes, II. Teil: Tabellen der Stundenwerte der Lufttemperatur und der Relativen Luftfeuchte 1974-1976 (Fusch, Ferleiten, Piffkaralm).* Wien 1978, 62 Tab.	80,--
35	233	Meteorologie		*Klimadaten des Glocknergebietes, III. Teil: Tabellen der Stundenwerte der Lufttemperatur und der relativen Luftfeuchte 1974-1976 (Guttal, Seppenbauer, Margaritze, Glocknerhaus, Schneetälchen, Polsterpflanzenstufe).* Wien 1978, 100 Tab.	130,--
36	234	Meteorologie	CHALUPA, K.:	*Ergebnisse der Registrierung der Immission von Stickoxiden, Summenkohlenwasserstoffen, Ozon und Schwefeldioxid in Wien - Hohe Warte, 1977.* Wien 1979, 74 S., 31 Tab., 24 Abb.	115,--
37	235	Meteorologie	MACHALEK, A.:	*Analyse von Fehlprognosen im Österreichischen Wetterdienst und Diskussion ihrer potentiellen Entstehungskriterien.* Wien 1979, 45 S., 2 Tab., 35 Abb.	100,--
38	236	Geophysik	DRIMMEL, J., E. FIEGWEIL und G. LUKESCHITZ:	*Die Auswirkung der Friauler Beben in Österreich. Makroseismische Bearbeitung der Starkbeben der Jahre 1976/77 samt historischem Rückblick.* Wien 1979, 83 S., 47 Abb., 3 Karten	150,--
39	238	Geophysik	FIEGWEIL, E.:	*Über die Vorkommen von Wiederholungsbeben in Mitteleuropa.* Wien 1979, 20 S., 9 Abb.	50,--
40	239	Meteorologie		*Klimadaten des Glocknergebietes, IV. Teil: Tabellen der Stundenwerte der Windgeschwindigkeit und der Windrichtung 1973-1976 (Fusch, Wallack-Haus, Guttal, Glocknerhaus, Margaritze, Fuscher-Lacke).* Wien 1979, 94 Tab.	120,--
41	242	Meteorologie	CHALUPA, K.:	*Ergebnisse der Registrierung der Immission von Stickoxiden, Ozon und Schwefeloxid in Wien - Hohe Warte, 1978.* Wien 1980, 58 S., 30 Tab., 15 Abb.	130,--
42	241	Meteorologie	CHALUPA, K.:	*Ergebnisse der Registrierung der Immission von Stickoxiden, Ozon und Schwefeloxid in Wien - Hohe Warte, 1979.* Wien 1980, 65 S., 32 Tab., 20 Abb.	130,--
43	246	Meteorologie	RAGETTE, G.:	*Methoden zur Berechnung großräumigen Niederschlages.* Wien 1980, 47 S., 1 Tab., 2 Abb.	70,--
44	247	Meteorologie		*Klimadaten des Glocknergebietes, V. Teil: Tabellen der Stundenwerte der Lufttemperatur und der Relativen Luftfeuchte, 1977-1979 (Wallack-Haus, Hochtor-Süd, Hochtor-Nord, Fuscher-Lacke).* Wien 1980, 135 Tab.	vergriffen
45	248	Geophysik	BRÜCKL, E., G. GANGL, W. SEIBERL und Chr. GNAM:	*Seismische Eisdickenmessungen auf dem Ober- und Untersulzbachkees in den Sommern der Jahre 1973 und 1974.* Wien 1980, 23 S., 2 Tab.	50,--
46	249	Meteorologie		*Klimadaten des Glocknergebietes, IV. Teil: Tabellen der Stundenwerte der Lufttemperatur und der Relativen Luftfeuchte, 1977-1979 (Fusch, Piffkaralm, Guttal, Seppenbauer, Margaritze, Glocknerhaus, Schneetälchen, Obere Grasheide, Polsterpflanzenstufe).* Wien 1981, 110 Tab.	120,--

Heft	Publ.Nr.	Fachgebiet	Autor Titel und Umfang	Preis in öS
65	303	Geophysik	ZYCH, D.: *Messungen der erdmagnetischen Vertikalintensität und Suszeptibilitätsuntersuchungen durch die ÖMV-AG als Beitrag zur Kohlenwasserstoffexploration in Österreich.* Wien 1985, 14 S., 2 Tab., 2 Abb., 3 Kartenbeilagen	60,--
66	304	Meteorologie	HOJESKY, H.: *Langjährige Radiosonden- und Höhenwindmessungen über Wien 1952-1984.* Wien 1985, 219 S., 64 Tab., 13 Abb.	120,--
67	306	Geophysik	*Results of the Austrian Investigations in the International Lithosphere Program from 1981-1985.* Wien 1986, 79 S., 4 Tab., 28 Abb.	80,--
68	308	Hydrometeorologie	ECKEL, O. und H. DOBESCH: *Mittelwerte der Wassertemperatur von Traunsee und Millstätter See nach mehrjährigen Registrierungen in verschiedenen Tiefen.* Wien 1986, 87 S., 74 Tab.	70,--
69	309	Meteorologie	KOLB, H., G. MAHRINGER, P. SEIBERT, W. SOBITSCHKA, P. STEINHAUSER und V. ZWATZ-MEISE: *Diskussion meteorologischer Aspekte der radioaktiven Belastung in Österreich durch den Reaktorunfall in Tschernobyl.* Wien 1986, 63 S., 4 Tab., 20 Abb.	vergriffen
70	312	Geophysik	ARIC, K., E. BRÜCKL: *Ergebnisse der seismischen Eisdickenmessungen im Gebiet der Stubaier Alpen (Daunkogelferner), der Venedigergruppe (Schlatenkees und Untersulzbachkees) und der Silvrettagruppe (Vermunt-Gletscher).* Wien 1987, 18 S., 4 Tab., 10 Abb., 4 Kartenbeilagen	80,--
71	314	Meteorologie	CHALUPA, K.: *Ergebnisse der Registrierung der Schwefeloxid-Immission in Wien - Hohe Warte und in Wien - Stephansplatz, 1981.* Wien 1987, 67 S., 41 Tab., 11 Abb.	100,--
72	315	Meteorologie	CHALUPA, K.: *Ergebnisse der Registrierung der Schwefeloxid-Immission in Wien - Hohe Warte und in Wien - Stephansplatz, 1982-1985.* Wien 1987, 76 S., 27 Tab., 15 Abb.	100,--
73	317	Geophysik	ARIC, K. et al: *Structure of the Lithosphere in the Eastern Alps Derived from P-residual Analysis.* Wien 1988, 35 S., 3 Tab., 17 Abb.	60,--
74	322	Meteorologie	CHALUPA, K.: *Ergebnisse der Registrierung der Schwefeloxid-Immission in Wien - Hohe Warte und in Wien - Stephansplatz 1986-1987 sowie eine Übersicht der 20jährigen Reihe 1968-1987.* Wien 1988, 80 S., 38 Tab., 20 Abb.	100,--

Berichte über den Tiefbau der Ostalpen

Herausgegeben von H. W. FLÜGEL und P. STEINHAUSER
bisher erschienen:

Heft	Publ.Nr.	Fachgebiet	Autor	Titel und Umfang	Preis in öS
1				*Jahresbericht 1973.* Verhandlungen der Geologischen Bundesanstalt. Jahrgang 1974, H. 4, S. A138-A148	
2				*Jahresbericht 1974.* Zentralanstalt für Meteorologie und Geodynamik, Wien 1975, 21 S., 5 Abb.	vergriffen
3				*Jahresbericht 1975.* Zentralanstalt für Meteorologie und Geodynamik, Wien 1976, 74 S., 14 Abb.	115,--
4	215		WALACH, G.:	*Geophysikalische Arbeiten im Gebiet des Nordsporns der Zentralalpen I: Magnetische Traverse 1 (Neunkirchen-Hochwechsel-Pöllauer Bucht).* Zentralanstalt für Meteorologie und Geodynamik, 22 S., 5 Abb., 4 Beilagen	40,--
5	221			*Jahresbericht 1976.* Zentralanstalt für Meteorologie und Geodynamik, Wien 1977, 101 S., 21 Abb.	130,--
6	230			*Jahresbericht 1977, Teil 1.* Zentralanstalt für Meteorologie und Geodynamik, Wien 1978, 54 S., 9 Abb.	85,--
7	240			*Jahresbericht 1977, Teil 2.* Zentralanstalt für Meteorologie und Geodynamik, Wien 1979, 60 S., 19 Abb.	90,--
8	244			*Tagungsbericht über das 1. Alpengravimetrie Kolloquium - Wien 1977.* Herausgeber: P. STEINHAUSER, Zentralanstalt für Meteorologie und Geodynamik, Wien 1980, 129 S., 35 Abb.	90,--
9	245		GÖTZE, H. J., O. ROSENBACH und P. STEINHAUSER:	*Die Bestimmung der mittleren Geländehöhen im Hochgebirge für die topographische Reduktion von Schweremessungen.* Zentralanstalt für Meteorologie und Geodynamik, Wien 1980, 16 S., 2 Tab., 5 Abb.	25,--
10	264		ROSENBACH, O., P. STEINHAUSER, W. EHRISMANN, H. J. GÖTZE, O. LETTAU, D. RUESS und W. SCHÖLER:	*Tabellen der mittleren Geländehöhen der Ostalpen und ihrer Umgebung für Rasterelemente $\Delta\varphi = 0.75'$. $\Delta\lambda = 1.25'$.* 1. Lieferung. Zentralanstalt für Meteorologie und Geodyna-mik, Wien 1982, 23 S., 20 Tab.	100,--
11	273			*Tagungsbericht über das 2. Internationale Alpengravimetrie Kolloquium - Wien 1980.* Herausgeber: B. MEURERS und P. STEINHAUSER, Zentralanstalt für Meteorologie und Geodynamik, Wien 1983, 168 S., 85 Abb.	200,--
12	288			*Tagungsbericht über das 3. Internationale Alpengravimetrie Kolloquium - Leoben 1983.* Herausgeber: B. MEURERS, P. STEINHAUSER und G. WALACH, Zentralanstalt für Meteorologie und Geodynamik, Wien 1985, 222 S.	270,--
13	323			*Tagungsbericht über das 4. Internationale Alpengravimetrie Kolloquium - Wien 1986.* Herausgeber: B. MEURERS und P. STEINHAUSER, Zentralanstalt für Meteorologie und Geodynamik, Wien 1988, 200 S., 77 Abb.	250,--

Österreichische Beiträge zu Meteorologie und Geophysik

bisher erschienen:

Heft	Publ.Nr.	Fachgebiet	Autor Titel und Umfang	Preis in öS
1	329	Meteorologie	*Tagungsbericht EURASAP, Wien, 14.-16. Nov. 1988, Evaluation of Atmospheric Dispersion Models Applied to the Release from Chernobyl.* Wien 1989, 20 Beiträge, 198 S., 100 Abb., 17 Tab.	200,--
2	332	Geophysik	*Tagungsbericht über das 5. Internationale Alpengravimetrie Kolloquium - Graz 1989.* Herausgeber: H. LICHTENEGGER, P. STEINHAUSER und H. SÜNKEL, Wien 1989, 256 S., 100 Abb., 17 Tab.	vergriffen
3	336	Geophysik	*Schwerpunktprojekt S47-GEO: Präalpidische Kruste in Österreich, Erster Bericht.* Herausgeber: V. HÖCK und P. STEINHAUSER, Wien 1990, 15 Beiträge, 257 S., 104 Abb., 17 Tab., 23 Fotos	280,--
4	338	Meteorologie	LANZINGER, A. et al: *Alpex-Atlas.* FWF-Projekt P6302 GEO, Wien 1991, 234 S., 23 Abb., 2 Tab., 200 Karten	250,--
5	341	Meteorologie	BÖHM, R.: *Lufttemperaturschwankungen in Österreich seit 1775.* Wien 1992, 95 S., 34 Abb., 24 Tab.	vergriffen
6	343	Geophysik	MEURERS, B.: *Untersuchungen zur Bestimmung und Analyse des Schwerefeldes im Hochgebirge am Beispiel der Ostalpen.* Wien 1992, 146 S., 72 Abb., 9 Tab.	160,--
7	351	Meteorologie	AUER, I.: *Niederschlagsschwankungen in Österreich seit Beginn der instrumentellen Beobachtungen durch die Zentralanstalt für Meteorologie und Geodynamik.* Wien 1993, 73 S., 18 Abb., 5 Tab., 6 Farbkarten	330,--
8	353	Umwelt	STOHL, A., H. KROMP-KOLB: *Analyse der Ozonsituation im Großraum Wien.* Wien 1994, 135 S., 73 Abb., 8 Tab.	330,--
9	356	Geophysik	*Tagungsbericht über das 6. Internationale Alpengravimetrie-Kolloquium, Leoben 1993.* Herausgeber: P. STEINHAUSER und G. WALACH, Wien 1993, 251 S., 146 Abb. [Korrektur der irrtümlichen Nummerierung Heft 8/Publ. 353]	330,--
10	357	Meteorologie	ZWATZ-MEISE, V.: *Contributions to Satellite and Radar Meteorology in Central Europe.* Wien 1994, 169 S., 25 Farbabb., 42 SW-Abb., 13 Tab.	330,--